TRAJECTORY DESIGN AND TARGETING
FOR APPLICATIONS TO THE EXPLORATION PROGRAM
IN CISLUNAR SPACE

by

Emily M. Zimovan Spreen

A Dissertation

Submitted to the Faculty of Purdue University

In Partial Fulfillment of the Requirements for the Degree of

Doctor of Philosophy
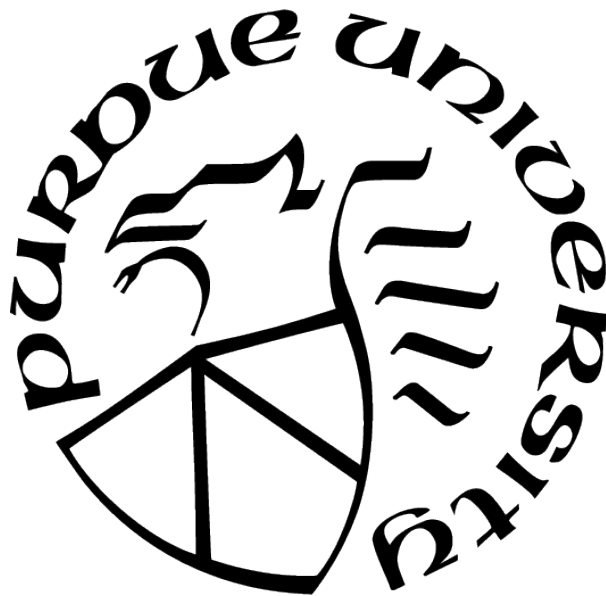
School of Aeronautics and Astronautics

West Lafayette, Indiana

May 2021

THE PURDUE UNIVERSITY GRADUATE SCHOOL
STATEMENT OF COMMITTEE APPROVAL

Prof. Kathleen C. Howell, Chair

School of Aeronautics and Astronautics

Dr. Diane C. Davis

a.i. solutions, Inc.

Prof. James M. Longuski

School of Aeronautics and Astronautics

Prof. Carolin E. Frueh

School of Aeronautics and Astronautics

Approved by:

Prof. Gregory A. Blaisdell

To my family,

for always believing in me.

ACKNOWLEDGMENTS

First, I want to thank my husband, Chris. Chris, you've been a source of constant support, understanding, and love throughout my time in graduate school. You've helped me celebrate the victories and push through the tough times. Thank you for supporting my ambitions. I am so grateful to have you as my husband and best friend.

I also want to thank my parents. I am so grateful that you supported my sense of wonder and curiosity as I was growing up. You have always encouraged me to ask questions and then search for the answers–and look where it has lead me! Without you, I would not be where I am today.

I am so thankful to the other members of my family, as well. To my brothers, Steve, Eric, and Kevin–thank you for teaching me that I belong anywhere, regardless of whether there are other women in the room. To my grandparents, your love and support throughout my life has helped me to succeed. Grandpa Frank, I'll always be your 'clinging vine.'

I also want to thank my in-laws, Kathy and Russ. Thank you for supporting me and encouraging me throughout this entire process. I'm so thankful for your generosity and kindness.

Next, I want to extend my gratitude to my advisor, Prof. Kathleen Howell. Thank you for supporting me, encouraging me, and providing me with endless opportunities throughout my time in the research group (and even as an undergraduate student). Thank you for helping me to learn all that I have and contribute to the field of astrodynamics in a meaningful way.

Thank you to the members of the Multi-Body Dynamics research group. You've listened to me present hundreds of times over the past six years. I am thankful for the advice you've given me, questions you've asked me, and thoughts you've shared with me. Outside of the office, you've also become my closest friends. I will always cherish the time we've spent in West Lafayette together. I want to extend a special thank you to Kenza,

TABLE OF CONTENTS

7

LIST OF TABLES

LIST OF FIGURES

17

19

ABSTRACT

A dynamical understanding of orbits in the Earth-Moon neighborhood that can sustain long-term activities and trajectories that link locations of interest forms a critical foundation for the creation of infrastructure to support a lasting presence in this region of space. In response, this investigation aims to identify and exploit fundamental dynamical motion in the vicinity of a candidate 'hub' orbit, the L_2 southern 9:2 lunar synodic resonant near rectilinear halo orbit (NRHO), while incorporating realistic mission constraints. The strategies developed in this investigation are, however, not restricted to this particular orbit but are, in fact, applicable to a wide variety of stable and nearly-stable cislunar orbits. Since stable and nearly-stable orbits that may lack useful manifold structures are of interest for long-term activities in cislunar space due to low orbit maintenance costs, strategies to alternatively initiate transfer design into and out of these orbits are necessary. Additionally, it is crucial to understand the complex behaviors in the neighborhood of any candidate hub orbit. In this investigation, a bifurcation analysis is used to identify periodic orbit families in close proximity to the hub orbit that may possess members with favorable stability properties, i.e., unstable orbits. Stability properties are quantified using a metric defined as the stability index. Broucke stability diagrams, a tool in which the eigenvalues of the monodromy matrix are recast into two simple parameters, are used to identify bifurcations along orbit families. Continuation algorithms, in combination with a differential corrections scheme, are used to compute new families of periodic orbits originating at bifurcations. These families possess unstable members with associated invariant manifolds that are indeed useful for trajectory design. Members of the families nearby the L_2 NRHOs are demonstrated to persist in a higher-fidelity ephemeris model.

Transfers based on the identified nearby dynamical structures and their associated manifolds are designed. To formulate initial guesses for transfer trajectories, a Poincaré mapping technique is used. Various sample trajectory designs are produced in this investigation to demonstrate the wide applicability of the design methodology. Initially, designs are based in the circular restricted three-body problem, however, geometries are demonstrated

to persist in a higher-fidelity ephemeris model, as well. A strategy to avoid Earth and Moon eclipse conditions along many-revolution quasi-periodic ephemeris orbits and transfer trajectories is proposed in response to upcoming mission needs. Lunar synodic resonance, in combination with careful epoch selection, produces a simple eclipse-avoidance technique. Additionally, an integral-type eclipse avoidance path constraint is derived and incorporated into a differential corrections scheme as well. Finally, transfer trajectories in the circular restricted three-body problem and higher-fidelity ephemeris model are optimized and the geometry is shown to persist.

1. INTRODUCTION

Over the past century, humans have sent numerous robotic probes and flagship missions into space in pursuit of new discovery and an increased understanding of the universe. A permanent presence in Low Earth Orbit (LEO) has been established through multi-national cooperation. However, expanding beyond LEO to embrace a far-reaching permanent presence–a shift beyond exploration missions–is a near-term goal. An increasingly permanent presence in the regions beyond LEO necessitates the strategic development of supporting infrastructure and an implementation strategy in cislunar space.

1.1 Motivation

A dynamical understanding of orbits in the Earth-Moon neighborhood that can sustain long-term activities and trajectories that link locations of interest forms a critical foundation for the creation of infrastructure to support a lasting presence in this region of space. A future long-term habitat or hub in an orbit near the Moon is expected to serve as a staging location for activities and missions within cislunar space; one such concept is offered by NASA's Lunar Gateway. The Gateway is currently planned to be maintained over a long duration in a Near Rectilinear Halo Orbit (NRHO) to serve as both a proving-ground for deep space activities and a stepping-stone for exploration within the Earth-Moon neighborhood and beyond [1].

Expanding from a hub near the Moon, NASA and a variety of private organizations aim to develop a robust space economy through the creation of a transportation network that allows for the transport of spacecraft between locations in cislunar and translunar space within the next decade using both electric and chemical propulsion [1], [2]. Due to an interest in long-term activities, stable or nearly-stable periodic orbits (e.g., NRHOs and Distant Retrograde Orbits or DROs), offer potential utility. However, transfer design between these types of orbits presents challenges. In particular, stable and unstable invariant manifolds, typically leveraged for initial guess generation for transfer design in multi-body regimes, are

either non-existent, not well-defined, or may be too slowly departing for some applications. In response, alternative strategies for transfer design between stable and nearly-stable orbits require more extensive investigation.

Previous point solutions suggest that an improved understanding of complex behaviors in the neighborhood of stable orbits (particularly the current Gateway baseline orbit, the NRHO) enables more effective techniques to design transfers in this regime. Therefore, rather than focusing solely on mass- or time-optimized point solutions derived from an extensive grid search, further exploration of the dynamical structures in the region provides a dynamical framework to alternatively initiate the design process. Once knowledge of the dynamical terrain surrounding the hub orbit is available, potential transfer pathways are constructed by combining arcs from various types of known periodic orbits within the Earth-Moon system and, if applicable, their manifold structures. Design flexibility, as well as predictable, intentional solution geometries, allows for wider exploration and exploitation of available motions, contingencies in response to mission requirement modifications, and transfer solutions rooted in well-understood characteristic behaviors.

1.2 Objectives

To enable the expansion of a human presence beyond low Earth orbit, a further understanding of the cislunar regime is critical. Currently, many trajectories in this region are offered as point-solutions that are output from optimization algorithms. Gaps in the understanding of the multi-body foundational dynamics in cislunar space leads to a lack of intuition and, therefore, limited trajectory options for missions in this neighborhood. Additionally, due to highly sensitive dynamics, challenges in implementation regularly arise. Finally, mission constraints, such as eclipse duration limitations, restrict the allowable design space, further increasing the challenge of trajectory design in the Earth-Moon vicinity. This investigation aims to contribute to the development of a trajectory design approach, relevant to hub activities, that utilizes an understanding of fundamental dynamical structures rather than focusing on point designs, as well as a strategy to incorporate realistic

mission constraints into the targeting process along the way. This goal is addressed through the following questions:

1. *Are there structures nearby stable or nearly-stable orbits (candidates for a long-duration cislunar hub) that have favorable stability characteristics for transfer design (i.e., possess unstable/stable manifolds into/out of the vicinity)?*

   Stable or nearly-stable orbits predominately lack useful manifold structures that are typically employed for transfer design in multi-body dynamical regimes. Other strategies to traverse the dynamical terrain in the vicinity of these orbits, therefore, aids in the process of generating initial guesses for transfer arcs. These initial guesses are then transitioned to a converged solution using a differential corrections scheme.

2. *Can invariant manifolds from these nearby structures be incorporated, along with other known periodic orbits and manifolds, into a design technique for transfers into/out of a hub orbit and to other destinations of interest?*

   A strategy to incorporate nearby periodic orbits with other structures in cislunar space (e.g., other periodic libration point orbits, resonant orbits, primary body-centered orbits) along with their manifolds potentially offers an initial guess generation technique that is more familiar to multi-body trajectory designers. Poincaré maps and other dynamical systems tools deliver insight into connections within cislunar space that originate near the hub orbit, thereby providing a roadmap of readily-available pathways and offering insight into potential destinations of interest.

3. *Do designs based on these fundamental structures (found in the CR3BP) persist in a higher-fidelity dynamical model?*

   Initial designs are typically constructed in a simplified multi-body model that allows for time-invariance and symmetries that reveal fundamental structures. For transfer designs based on these structures to be useful for actual mission implementations, verification that these structures (and their favorable characteristics) are maintained in a higher-fidelity ephemeris model is necessary.

4. *Can challenging mission constraints (e.g., eclipse avoidance) be implemented in the initial design process to yield a more cohesive transition from design to application?*

   Often, a trajectory is incrementally modified to meet various mission constraints within an optimization scheme. If initial designs are generated that meet various mission constraints from the beginning, more design options may arise and the final optimized solution is likely to be more predictable.

In this investigation, the hub is assumed to be moving along an L_2 NRHO, that is, the current baseline for the NASA Lunar Gateway. This type of orbit presents unique challenges (e.g., stable or nearly-stable, out-of-plane orientation, close proximity to the Moon, etc.). The techniques developed in this investigation are applicable to this type of orbit and also to a wide variety of other trajectory design applications in cislunar space.

1.3 Previous Contributions

1.3.1 Multi-Body Dynamics

In 1687, with the publication of the *Principia*, Sir Isaac Newton recorded the laws that govern the motion of N-bodies moving under the Universal Law of Gravitation. Thus began the search for an analytical solution to the complex motion that governed the heavens [3]. Years later, in 1722, Leonhard Euler simplified a model representing the N-body problem with the formulation of the Circular Restricted Three-Body Problem (CR3BP) [4]. A truly key innovation, the view of the problem from the perspective of a rotating frame enabled significant progress. With the assumption of an infinitesimal third body and primary bodies in circular orbits about their common barycenter, this simplification of the N-body problem allowed for the understanding of orbital motion to drastically increase. Joseph-Louis Lagrange demonstrated the existence of the triangular equilibrium solutions to the CR3BP in 1772, the same year that Euler recognized the existence of the collinear libration points. The emergence of these equilibrium points led to additional understanding and insight into

the problem. Over sixty years later, in 1836, an integral of the motion in the CR3BP, now known as the Jacobi integral or Jacobi constant, was noted by Carl Gustav Jacob Jacobi [5]. This integral, or constant of the motion, bolstered insight into this dynamical regime and led to the recognition of the existence of bounding surfaces of allowable third body motion, the zero velocity surfaces, shown by Hill in 1878 [6].

Within the second volume of *Les Méthodes Nouvelles de la Mécanique Céleste*, Henri Poincaré identified that no additional algebraic integrals of the motion exist in the CR3BP [7]. Since then, countless authors have explored the complex motion in this dynamical regime. In 1881, a technique to visualize complex solutions in the CR3BP was contributed by Henri Poincaré, now recognized as a Poincaré map [5]. This tool, not directly utilized by Poincaré due to computational limitations in the early 1900s, offers invaluable insight into dynamical systems. However, not until 1978 was a mission proposed to exploit multi-body dynamical motion; the International Sun-Earth Explorer-3 (ISEE-3) spacecraft was inserted into a Sun-Earth L_1 halo orbit and was maintained there for almost four years [8]. Since then, an increasing number of missions are incorporating these types of orbits including ARTEMIS (a mission to Earth-Moon L_1 and L_2); SOHO, ACE, Genesis, and WIND (missions to Sun-Earth L_1); and WMAP (a mission to Sun-Earth L_2) [9], [10].

1.3.2 Differential Corrections

Differential corrections methods, which date back to Newton's *Principia*, are a fundamental aspect of multi-body trajectory design [3]. Many different formulations of differential corrections algorithms exist within the context of solving two-point boundary value problems. Authors such as Keller [11], as well as Roberts and Shipman [12], [13], produced shooting method formulations in which a solution to a two-point boundary value problem is determined by integrating an appropriate initial value problem [14]. The advent of modern computers enabled the application of shooting methods to solve complex problems, e.g., trajectory design in a multi-body dynamical regime. A free-variable and constraint method,

one specific formulation of a shooting scheme, as detailed by Pavlak, is implemented in this investigation [15].

1.3.3   Periodic Orbits

As early as 1881, Poincaré demonstrated the existence of an infinite number of periodic solutions in the three-body problem [7]. Since then, many authors have focused on the construction and characterization of these orbits. As an example, Moulton's collection of analytical methods for approximating periodic motion near the libration points in 1920 inspires continuing efforts [16]. However, large computational advances within the last half-century have allowed many periodic solutions to be computed formally. As recent samples of such efforts, families of periodic solutions in the CR3BP are characterized and defined in an application to lunar south pole coverage by Grebow [17] and an algorithm to identify many previously unknown planar periodic solutions is developed by Schlei [18]. Grebow's detailed overview of the development of periodic orbit solutions in the circular restricted three-body problem is particularly useful and many additional references are supplied [17].

Near Rectilinear Halo Orbits

'Halo' orbits, a term to describe a specific type of three-dimensional periodic orbit possessing an uninterrupted line of sight to the Earth, first appeared in the literature in work by Farquhar in 1968 [19]. Later, Breakwell and Brown, in 1979, demonstrated the existence of a family of related solutions, the family denoted as the L_2 halo orbits; a similar family bifurcating from an L_1 Lyapunov orbit also emerged. The L_1 halo family is characterized in the work by Breakwell and Brown and is also continued with representative periodic orbits from the planar Lyapunov orbit towards the increasingly three-dimensional orbits in the vicinity of the smaller primary [20]. Howell extended the families of L_1 and L_2 halo orbits to other systems in addition to offering a characterization of the L_3 halo family [21]. Notable for the current investigation, Howell and Breakwell, in 1983, developed an approximation for the

stable "almost rectilinear halo orbits" within the L_1 and L_2 halo families for computational ease and, perhaps more significantly, also expand the understanding of this orbit type at the time [22]. Favorable stability properties of these halo orbits nearest the Moon suggest their suitability for long-duration applications. These orbits are now termed Near Rectilinear Halo Orbits, or NRHOs. An in-depth investigation into the characteristics and defining qualities of the NRHOs is offered in the author's M.S. thesis [23].

1.3.4   Multi-Body Trajectory Design

Typically, when designing trajectories in a multi-body regime, initial guess formulation relies on invariant manifold structures, or ballistic pathways that lead into/out of unstable periodic orbits. In response to the need for trajectory design strategies to meet mission demands despite a lack of usable manifolds flowing to/from stable periodic orbits, various alternative approaches for both impulsive and low-thrust transfers between stable and nearly-stable orbits have been produced by multiple authors. Examples include work by Capdevila et al. to generate a network of impulsive transfers between stable periodic orbits in cislunar space [24]. In addition, Parker et al. and Herman investigated low-thrust transfers from Earth to Distant Retrograde Orbits (DROs) [25], [26], and Parrish et al. introduced low-thrust transfers between DROs and L_2 halo orbits (beyond the region of NRHOs) [27].

Goals for a number of current NASA mission scenarios have recently motivated investigations into both low-thrust and impulsive transfers into and out of the L_2 NRHOs in particular. McGuire et al. examined a strategy to produce transfers into NRHOs and between cislunar multi-body orbits with a 40kW low-thrust engine using a trajectory design and optimization tool [28]. McCarty and McGuire utilized parallel monotonic basin hopping to mass-optimize a low-thrust NRHO-to-DRO transfer [29]. Also in 2017, Lantoine produced efficient impulsive NRHO-to-DRO transfers using a scheme that blends Earth-Moon-Sun ephemeris departure and arrival segments with a Moon-to-Moon transfer arc modeled in the Sun-Earth CR3BP [30]. Loucks et al. investigated a strategy to access L_2 NRHOs using a powered lunar swingby to accomplish the large plane change–a strategy first proposed by the

General Electric Company in 1969 and Farquhar in 1971 to access the L_2 region for a lower cost than a direct two-burn solution from Earth to L_2 [31]–[33]. Similar three-burn solutions to access L_2 halo orbits, constructed by linking natural arcs in the CR3BP, were proposed by Folta et al. in 2012 [34]. A form of this three-burn solution now forms the Artemis III baseline mission trajectory [35]. Davis et al. determined that a small departure burn is sufficient to predictably initiate departure from the NRHO baseline orbit into heliocentric space. However, it was determined that uncontrolled perturbations also potentially lead to departures from the NRHO when orbit maintenance is not active [36], [37]. Davis et al. also investigated low ΔV magnitude lunar impactor trajectories originating from the NRHO in the CR3BP [36].

Transitioning lower-fidelity solutions into higher-fidelity models is an important step in the verification of a design prior to a mission. Work by Zimovan, Howell, and Davis aimed to quantify the changes incurred geometrically when the NRHO is transitioned to a higher-fidelity model [38]. Pritchett et al. transitioned impulsive transfers between stable and nearly-stable orbits in the CR3BP to the Earth, Moon, Sun, Jupiter ephemeris model and demonstrated that the geometry of the transfers is maintained, indicating that the lower-fidelity model did indeed offer a useful design tool [39]. In 2019, Boudad et al. investigated how the geometry and stability of NRHOs evolves as they are transitioned from the CR3BP to an intermediate higher-fidelity model, the bicircular four-body problem [40].

Incorporation of challenging mission constraints into the trajectory design process has been examined by various authors. A particular challenge, relevant to the eclipse avoidance constraint, is offered by the formulation of a constraint along the path (i.e., not enforced *at* a patchpoint in a multiple-shooting scheme [23]). Ojeda Romero and Howell investigated a strategy to enforce a solar exclusion zone constraint along transfers from a GTO to a Sun-Earth libration point orbit [41]. An eclipse avoidance constraint is enforced along many-revolution low-thrust spiral trajectories in work done in 2018 by Aziz [42]. Finally, Pritchett et al. investigated strategies to transition transfers between stable and nearly-stable orbits

from low-thrust to impulsive engine models and vice versa; offering a strategy to enforce engine constraints on a trajectory design [39].

1.4   Current Work

This research effort aims to develop a methodology to move through cislunar space between destinations of interest while implementing innovative strategies to incorporate realistic mission constraints. The development of this trajectory design approach will allow for an understanding of fundamental motion in cislunar space that applies across many missions enabling a more informed design approach, rather than focusing on a point solution for each mission. A focus on transitioning between stable and nearly-stable orbits, particularly NRHOs, is relevant to NASA Gateway operations. The investigation also aims to enhance current trajectory targeting approaches within a framework that is applicable to various missions by incorporating various types of mission constraints. The document is organized as follows:

- **Chapter 2: Dynamical Models**
  In this chapter, the dynamical models and coordinate frames used in this investigation are introduced. The circular restricted three-body model serves as an approximation of higher-fidelity dynamics. The N-body model allows for an accurate consideration of the influence of multiple gravitational bodies on a particle of interest. Assumptions for each model are described. Additionally, derivations for techniques to transition states between coordinate frames of interest are provided.

- **Chapter 3: Trajectory Construction and Numerical Processes**
  Differential corrections strategies to produce trajectories and orbits that satisfy constraints are described. In particular, free-variable and constraint multi-dimensional Newton's methods, in the form of single- and multiple-shooting corrections algorithms, are used throughout this investigation. Details for transitioning solutions between the circular restricted three-body model and the higher-fidelity ephemeris model are pro-

vided. A constraint to avoid the penumbral shadow cone of an occluding body, e.g., the Earth or Moon, is derived. This shadow constraint is used to produce Moon and Earth eclipse-free solutions throughout the analysis. In this chapter, two options for solution continuation processes are described and derived. Finally, a description and illustrations of a dynamical systems tool that simplifies visualization of complex flow, a Poincaré mapping technique, is offered.

- **Chapter 4: Orbital Stability and Bifurcations**

  Orbital stability plays a key role in the characteristics of the dynamical flow in the vicinity of a periodic orbit. Strategies to quantify the stability of an orbit using eigenvalues of the monodromy matrix are described including time constant and stability index. If an orbit is unstable, it possesses stable and unstable invariant manifold structures that offer pathways for ballistic arrival at and departure from the orbit. A method to compute trajectories that lie along the manifold surfaces is presented. As stability characteristics evolve along a periodic orbit family, bifurcations can occur. Bifurcation theory as well as specific bifurcation types that are of interest to the investigation are described, as are strategies to identify bifurcations along orbit families. Broucke stability diagrams and bifurcation diagrams offer effective visualization techniques of evolving stability characteristics and bifurcation occurrences along orbit families.

- **Chapter 5: Near Rectilinear Halo Orbits and Nearby Dynamical Structures**

  This chapter begins with a description and various quantifications of the Near Rectilinear Halo Orbits (NRHOs). Nearby dynamical structures are identified using a Broucke stability diagram and families of nearby periodic orbits are computed. Eclipse avoidance techniques that rely on favorable geometry that arises from synodic resonance are described. The analysis is repeated for the Distant Retrograde Orbit (DRO) family.

- **Chapter 6: Transfer Design Methodology and Applications**

  A strategy to design transfer trajectories linking an NRHO and DRO that utilize intermediate higher-period orbits is described and numerous sample trajectories in the CR3BP and higher-fidelity ephemeris model are offered. Next, a method to recover

from inadvertent departures from an NRHO using nearby dynamical structures is explored. This analysis relies on manifold trajectories that originate at cislunar orbits in the vicinity of the NRHOs. A fundamental structure relevant to long-duration transfer trajectories between cislunar orbits, the 1:4 resonant orbit family, is identified. Heteroclinic and homoclinic connections involving the 9:2 lunar synodic resonant northern and southern NRHOs are described. Optimization of transfer trajectories in both the CR3BP and ephemeris model is included throughout this chapter.

- **Chapter 7: Concluding Remarks**

  A summary of the results presented in preceding chapters is provided along with recommendations for future work and responses to the four posed fundamental questions.

Portions of this work have been presented at various conferences and published elsewhere prior to incorporation into this dissertation document. The original papers are available in References [23], [38], [43]–[49].

2. DYNAMICAL MODELS

Dynamical models that supply different levels of fidelity are employed in the investigation. The Circular Restricted Three-Body Problem (CR3BP) provides an autonomous approximation of Earth-Moon dynamics, enabling an understanding of underlying dynamical structures. The ephemeris model allows for higher-fidelity simulations.

2.1   The Circular Restricted Three-Body Problem (CR3BP)

The dynamical model in the CR3BP serves as a reasonable approximation to higher-fidelity dynamical models in the Earth-Moon system, including those that also incorporate solar gravity. Within this application of the CR3BP, the motion of a massless spacecraft, P_3, under the gravitational influence of two primary bodies, the Earth (P_1) and Moon (P_2) is explored. These two primary bodies, modeled as point-masses, are assumed to move in circular orbits about their common barycenter. The motion of the spacecraft is then described relative to a coordinate frame, $\hat{x}$-$\hat{y}$-$\hat{z}$, that rotates with the motion of the Earth and Moon and is centered at the Earth-Moon barycenter, as portrayed in Figure 2.1(a). In this frame, the spacecraft is located by the nondimensional coordinates x, y, and z. By convention, quantities in the CR3BP are nondimensionalized such that the Earth-Moon distance, as well as the mean motion of the primaries, are both equal to a constant value of unity. In addition, the Earth and Moon masses are nondimensional and equal to $1 - \mu$ and μ, respectively, where the parameter μ equals the ratio of the mass of P_2 to the total mass of the system ($P_1 + P_2$). In the rotating frame, the scalar equations of motion for the spacecraft are written as

$$\ddot{x} - 2\dot{y} = \frac{\partial U}{\partial x}, \ \ddot{y} + 2\dot{x} = \frac{\partial U}{\partial y}, \ \ddot{z} = \frac{\partial U}{\partial z} \tag{2.1}$$

where the pseudo-potential function, $U = \frac{1}{2}(x^2 + y^2) + \frac{1-\mu}{d} + \frac{\mu}{r}$, while $d = \sqrt{(x + \mu)^2 + y^2 + z^2}$, and $r = \sqrt{(x - 1 + \mu)^2 + y^2 + z^2}$.

The CR3BP admits five relative equilibrium (or Lagrange) points: the collinear points L_1, L_2, and L_3, located along the Earth-Moon line, and two equilateral points, L_4 and L_5, that form equilateral triangles with the two primaries. An energy-like integral of the motion, denoted the Jacobi constant, exists in the rotating frame such that $JC = 2U - \dot{x}^2 - \dot{y}^2 - \dot{z}^2$. Detailed derivations of CR3BP equations of motion, the location of the equilibrium points, and derivation of the Jacobi constant expression are available in Chapter 2.1 of Zimovan, 2017 [23].

2.2 The Ephemeris Model

For mission design applications where higher-fidelity modeling accuracy is required, N-body differential equations and planetary ephemerides are employed. In this higher-fidelity ephemeris model, the motion of the particle of interest (e.g., a spacecraft), P_i, is rendered relative to a central body, P_q, in an inertial frame described in terms of the coordinates $\hat{X}$-$\hat{Y}$-$\hat{Z}$. The particle P_i is influenced by the gravity of P_q as well as other perturbing particles, P_j. Such an N-body system is depicted in Figure 2.1(b). The well-known dimensional N-body relative vector equation of motion is written as

$$\ddot{\mathbf{r}}_{q\mathrm{i}} = -\tilde{G}\frac{(m_\mathrm{i} + m_q)}{r_{q\mathrm{i}}^3}\mathbf{r}_{q\mathrm{i}} + \tilde{G}\sum_{\substack{\mathrm{j}=1 \\ \mathrm{j}\neq \mathrm{i},q}}^{N} m_\mathrm{j}\left(\frac{\mathbf{r}_{\mathrm{ij}}}{r_{\mathrm{ij}}^3} - \frac{\mathbf{r}_{q\mathrm{j}}}{r_{q\mathrm{j}}^3}\right) \tag{2.2}$$

where $\tilde{G}$ denotes the universal gravitational constant, $m_{(\cdot)}$ is the mass of $P_{(\cdot)}$, and the definition of vector quantities is consistent with Figure 2.1(b). Note that a bold letter indicates a vector entity, while an identical non-bold symbol refers to the modulus of the corresponding vector. For this analysis, the relative position of each perturbing body with respect to the central body, $\mathbf{r}_{q\mathrm{j}}$, is instantaneously computed by employing NASA's NAIF (Navigation and Ancillary Information Facility) SPICE ephemeris data tool[50]. Since the trajectories used in this analysis are in close proximity to the Moon, selecting the Moon as a central body is reasonable and convenient for numerical integration. For this application, the mass m_q represents the Moon; the target mass, m_i, is the spacecraft, and the additional masses m_j
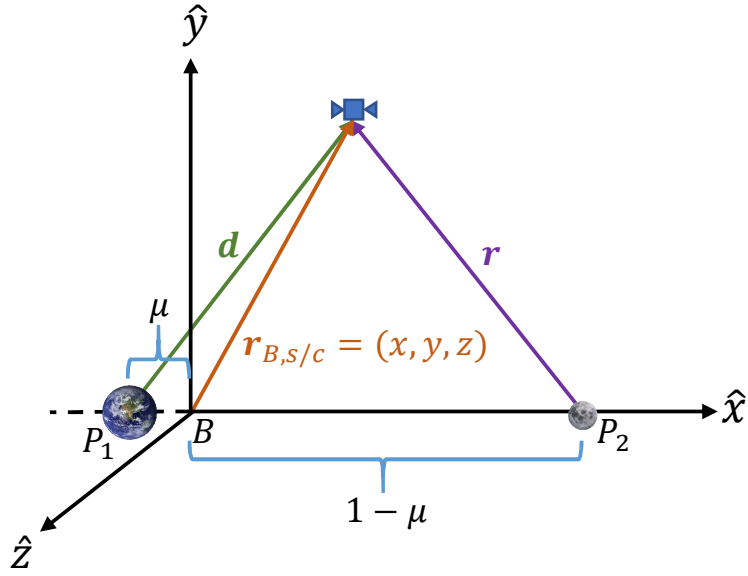
(a) Geometry of the CR3BP in the Earth-Moon rotating frame
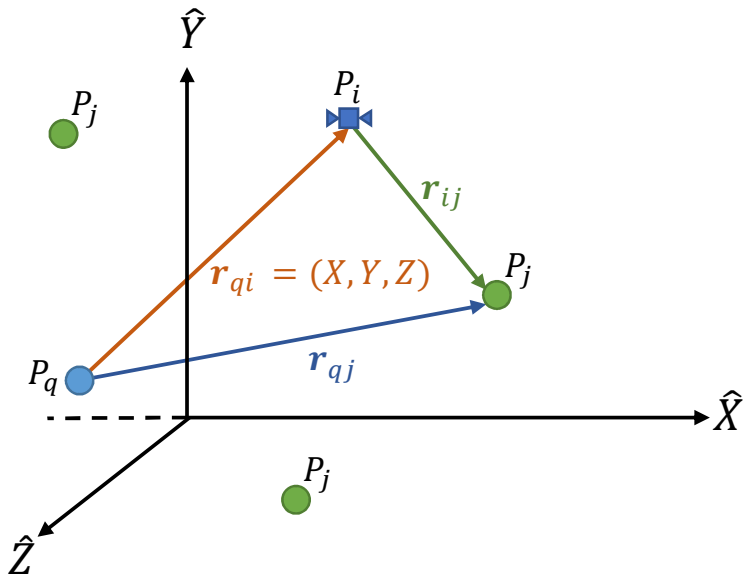
(b) Geometry of an N-body system in an arbitrary inertial frame

Figure 2.1. : Reference frame definitions

correspond to additional bodies that exert a non-negligible gravitational attraction. The N-body vector differential equation is propagated in the J2000 inertial reference frame and includes the Earth, Moon, and Sun as celestial bodies of influence.

2.3 Coordinate Frame Transformations

An important aspect of multi-body trajectory design is the ability to transform state vectors between coordinate frames. Coordinate frame transformation allows trajectories to be viewed from various perspectives to gain insight into the design and to allow for solutions to be transitioned between models of various levels of fidelity, e.g., between the CR3BP and the N-body ephemeris model. The methodologies required to switch between a rotating frame and an arbitrary inertial frame, as well as a rotating frame and the primary-centered J2000 inertial frame, are detailed.

2.3.1 Coordinate Frame Transformation Between a Rotating Frame and an Arbitrary Inertial Frame

To gain insight into a trajectory design concept constructed in the CR3BP, it is beneficial to view the solution in both the traditional rotating frame and in a general inertial frame, as defined in Figure 2.2. Recall, the rotating frame is defined by unit vectors $\hat{x}$-$\hat{y}$-$\hat{z}$ and the general inertial frame is defined by unit vectors $\hat{X}$-$\hat{Y}$-$\hat{Z}$. The rotating frame and an arbitrary inertial frame are assumed to be equivalent at time zero (arbitrarily defined in the autonomous CR3BP), and the orientation of the rotating frame with respect to the inertial frame is described simply by the angle $\theta = t$, where t is the nondimensional time elapsed since the frames were equivalent at time zero. Here, $\dot{\theta}$ is assumed constant due to the assumptions in the CR3BP. Both frames are centered at the barycenter of the primary system, and the rotating $\hat{z}$-axis is parallel to the orbital angular momentum of the primaries and is aligned with the inertially fixed $\hat{Z}$-axis. Note, the arrow labeled $\mathbf{r}_{3_p}$ is the planar projection of the vector from the barycenter to P_3 (which is denoted $\mathbf{r}_3$). P_3 is free to move
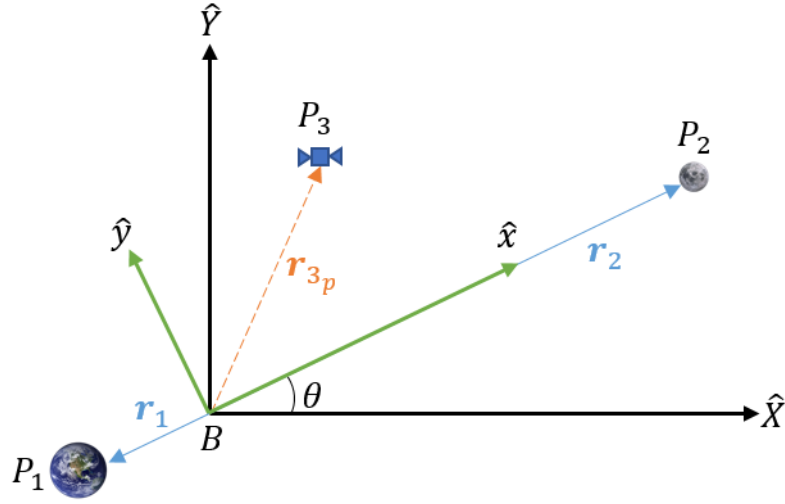
Figure 2.2. : Definitions of inertial and rotating coordinate frames

in all three spatial dimensions. Since the $\hat{x}\hat{y}$-plane and the $\hat{X}\hat{Y}$-plane coincide for all time, a rotating position vector is transformed to an inertial position vector with a simple rotation matrix

$$\begin{bmatrix} X \\ Y \\ Z \end{bmatrix} = \begin{bmatrix} \cos\theta & -\sin\theta & 0 \\ \sin\theta & \cos\theta & 0 \\ 0 & 0 & 1 \end{bmatrix} \begin{bmatrix} x \\ y \\ z \end{bmatrix} \tag{2.3}$$

or

$$\begin{bmatrix} X \\ Y \\ Z \end{bmatrix} = {}^{\mathbf{I}}\mathbf{C}^{\mathbf{R}} \begin{bmatrix} x \\ y \\ z \end{bmatrix} \tag{2.4}$$

where the superscript R indicates a vector expressed in terms of rotating frame coordinates relative to a rotating observer and I denotes a vector expressed in inertial frame coordinates

relative to an inertial observer. To compute the velocity with respect to an inertial observer in the rotating frame, the basic kinematic equation,

$$\dot{\boldsymbol{\rho}} = \frac{{}^I d\boldsymbol{\rho}}{dt} = \frac{{}^R d\boldsymbol{\rho}}{dt} + {}^I\boldsymbol{\omega}^R \times \boldsymbol{\rho} \qquad (2.5)$$

is used. Here, $\boldsymbol{\rho}$ represents the nondimensional position of P_3 with respect to the barycenter expressed in terms of rotating coordinates, i.e., $\boldsymbol{\rho} = x\hat{x} + y\hat{y} + z\hat{z}$. The angular velocity relating the frames has magnitude equal to unity (since the mean motion of the orbit of the primary bodies is defined as unity in this formulation). Thus, ${}^I\boldsymbol{\omega}^R = \hat{z} = \hat{Z}$. The velocity relative to an inertial observer expressed in the rotating frame is then defined as

$$\dot{\boldsymbol{\rho}} = (\dot{x} - y)\hat{x} + (\dot{y} + x)\hat{y} + \dot{z}\hat{z}. \qquad (2.6)$$

Combining the relationship between the inertial and rotating frames in Equation (2.3) with the expression for the inertial velocity expressed in terms of rotating coordinates in Equation (2.6) yields an expression for the inertial velocity expressed in terms of inertial coordinates, i.e.,

$$\frac{{}^I d\boldsymbol{\rho}}{dt} = \dot{\boldsymbol{\rho}} = ((\dot{x} - y)\cos\theta - (\dot{y} + x)\sin\theta)\hat{X} + ((\dot{x} - y)\sin\theta + (\dot{y} + x)\cos\theta)\hat{Y} + \dot{z}\hat{Z}. \qquad (2.7)$$

Combining the simple rotation matrix in Equation (2.3) with Equation (2.7) and writing in matrix form, the total transformation matrix that relates a state with respect to a rotating

observer expressed in rotating frame coordinates to a state with respect to an arbitrary inertial observer expressed in inertial frame coordinates is then written as

$$
\begin{bmatrix} X \\ Y \\ Z \\ \dot{X} \\ \dot{Y} \\ \dot{Z} \end{bmatrix} = \begin{bmatrix} \cos\theta & -\sin\theta & 0 & 0 & 0 & 0 \\ \sin\theta & \cos\theta & 0 & 0 & 0 & 0 \\ 0 & 0 & 1 & 0 & 0 & 0 \\ -\sin\theta & -\cos\theta & 0 & \cos\theta & -\sin\theta & 0 \\ \cos\theta & -\sin\theta & 0 & \sin\theta & -\cos\theta & 0 \\ 0 & 0 & 0 & 0 & 0 & 1 \end{bmatrix} \begin{bmatrix} x \\ y \\ z \\ \dot{x} \\ \dot{y} \\ \dot{z} \end{bmatrix} \tag{2.8}
$$

or

$$
\begin{bmatrix} X \\ Y \\ Z \\ \dot{X} \\ \dot{Y} \\ \dot{Z} \end{bmatrix} = \begin{bmatrix} \mathbf{^I C^R} & \mathbf{0} \\ \mathbf{^I \dot{C}^R} & \mathbf{^I C^R} \end{bmatrix} \begin{bmatrix} x \\ y \\ z \\ \dot{x} \\ \dot{y} \\ \dot{z} \end{bmatrix}. \tag{2.9}
$$

The transformation matrix given in Equation (2.9) transforms a full six-dimensional state vector with respect to a rotating observer expressed in rotating coordinates, i.e., $[x\ y\ z\ \dot{x}\ \dot{y}\ \dot{z}]^T$, to a six-dimensional state vector with respect to an inertial observer expressed in terms of inertial coordinates, i.e., $\left[X\ Y\ Z\ \dot{X}\ \dot{Y}\ \dot{Z}\right]^T$.

Although state vectors are typically defined as originating at the barycenter in the rotating frame, other basepoints possess some advantages as well. For example, if a primary-centered inertial state is desired, a simple translation in the rotating frame from the barycen-

ter of the primary bodies to the desired basepoint is a first step. Then, the transformation matrix is applied to the translated vector. To transform from an inertial state to a rotating state, the inverse of the transformation matrix is multiplied by the inertial state to yield the state as expressed in terms of the rotating coordinates. As an overview, the steps to transform a six-dimensional state with respect to a rotating observer expressed in the rotating frame to a state with respect to an inertial observer expressed in the inertial frame are:

1. If desired, translate the rotating state that originates at the barycenter of the primaries such that its basepoint is at a different desired location

2. Apply the transformation matrix in Equation (2.9) to the rotating state

This methodology is applied throughout the analysis for transforming a rotating trajectory state into an arbitrary inertial frame to gain additional insight. The steps to transform a six-dimensional state with respect to an inertial observer to a state with respect to a rotating observer expressed in the rotating frame are:

1. Apply the **inverse** of the transformation matrix in Equation (2.9) to the inertial state

2. If desired, translate this rotating state such that its basepoint is at the barycenter of the primaries, as is typical for a classically defined rotating frame

Again, this methodology is applied throughout the analysis for transforming a state defined in an arbitrary inertial frame to a state defined in the rotating frame with respect to a rotating observer.

2.3.2 Coordinate Frame Transformation Between a Rotating Frame and the J2000 Inertial Frame

Transitioning a state from a rotating frame to the J2000 inertial frame is similar to the procedure to transition a state from the rotating frame to an arbitrary inertial frame

from Section 2.3.1. However, planetary ephemerides for a specific epoch date must be incorporated into the transformation. Since the barycenter is not fixed relative to either of the primaries in the N-body ephemeris model, this transformation is typically implemented with the basepoint at one of the primary bodies. To begin, a rotating position vector is translated such that the basepoint is at one of the primary bodies and is dimensionalized using the instantaneous characteristic quantities $\tilde{t}^*$ and $\tilde{l}^*$, which are defined as

$$\tilde{l}^* = r_{12} \tag{2.10}$$

and

$$\tilde{t}^* = \frac{\tilde{l}^{*3}}{\sqrt{\tilde{G}m_1 + \tilde{G}m_2}} \tag{2.11}$$

where $\mathbf{r_{12}}$ is the dimensional position vector of P_2 with respect to P_1, available from ephemeris data for a given epoch, $\tilde{G}$ is the dimensional gravitational constant, m_1 is the mass of P_1, and m_2 is the mass of P_2. The dimensional position vector in the rotating frame that originates at a primary, $\mathbf{r_p}$, is then defined as

$$\mathbf{r_p} = \begin{bmatrix} x_p \\ y_p \\ z_p \end{bmatrix} \tag{2.12}$$

where the subscript p denotes values centered at a primary body. Next, an instantaneous, primary-centered rotating frame is constructed using ephemeris data. This instantaneous frame is defined in terms of unit vectors parallel to axes in the J2000 inertial frame. The corresponding axes are defined as

$$\hat{\tilde{x}} = \frac{\mathbf{r_{12}}}{\tilde{l}^*} \tag{2.13}$$

$$\hat{\tilde{z}} = \frac{\mathbf{r_{12}} \times \mathbf{v_{12}}}{|\mathbf{r_{12}} \times \mathbf{v_{12}}|} \tag{2.14}$$

$$\hat{\tilde{y}} = \hat{\tilde{z}} \times \hat{\tilde{x}} \tag{2.15}$$

42

A rotation matrix is defined using these instantaneous rotating axes as

$$
{}^{\mathbf{I}}\tilde{\mathbf{C}}^{\mathbf{R}} = \begin{bmatrix} \hat{\tilde{x}} & \hat{\tilde{y}} & \hat{\tilde{z}} \end{bmatrix} = \begin{bmatrix} \tilde{C}_{11} & \tilde{C}_{12} & \tilde{C}_{13} \\ \tilde{C}_{21} & \tilde{C}_{22} & \tilde{C}_{23} \\ \tilde{C}_{31} & \tilde{C}_{32} & \tilde{C}_{33} \end{bmatrix} \tag{2.16}
$$

where $\hat{\tilde{x}}$, $\hat{\tilde{y}}$, and $\hat{\tilde{z}}$ are column unit vectors. Using this instantaneous rotation matrix, a primary-centered dimensional position vector expressed in the rotating frame can be transformed to a primary-centered dimensional position vector that is expressed in terms of the J2000 inertial coordinates, i.e.,

$$
\begin{bmatrix} X_p \\ Y_p \\ Z_p \end{bmatrix} = {}^{\mathbf{I}}\tilde{\mathbf{C}}^{\mathbf{R}} \begin{bmatrix} x_p \\ y_p \\ z_p \end{bmatrix}. \tag{2.17}
$$

Since the mean motion of the primaries and, therefore, the angular velocity of the rotating frame with respect to the inertial frame, is no longer constant in the N-body ephemeris model, the instantaneous angular velocity ${}^{I}\tilde{\boldsymbol{\omega}}^{R} = \dot{\tilde{\theta}}\hat{\tilde{z}}$ must be computed as well. The instantaneous angular velocity is evaluated by using the two-body problem definition, i.e.,

$$
\dot{\tilde{\theta}} = \frac{|\mathbf{r_{12}} \times \mathbf{v_{12}}|}{r_{12}^2} \tag{2.18}
$$

with units of rad/sec. To construct the velocity relative to an observer in the J2000 inertial frame, but expressed in terms of rotating frame coordinates, the basic kinematic equation is leveraged. Recall the kinematic relationship,

$$
\frac{{}^{I}d\boldsymbol{r_p}}{dt} = \frac{{}^{R}d\boldsymbol{r_p}}{dt} + {}^{I}\tilde{\boldsymbol{\omega}}^{R} \times \boldsymbol{r_p} \tag{2.19}
$$

that yields

$$
\frac{{}^{I}d\boldsymbol{r_p}}{dt} = (\dot{x}_p - \dot{\tilde{\theta}}y_p)\hat{\tilde{x}} + (\dot{y}_p + \dot{\tilde{\theta}}x_p)\hat{\tilde{y}} + \dot{z}_p\hat{\tilde{z}}. \tag{2.20}
$$

Equation (2.20) is combined with Equation (2.17) to produce an expression for the instantaneous inertial velocity expressed in inertial coordinates, i.e.,

$$
\frac{{}^I d\boldsymbol{r_p}}{dt} = ((\dot{x}_p - \dot{\tilde{\theta}} y_p)\tilde{C}_{11} + (\dot{y}_p + \dot{\tilde{\theta}} x_p)\tilde{C}_{12} + \dot{z}_p \tilde{C}_{13})\hat{X}
$$
$$
+ ((\dot{x}_p - \dot{\tilde{\theta}} y_p)\tilde{C}_{21} + (\dot{y}_p + \dot{\tilde{\theta}} x_p)\tilde{C}_{22} + \dot{z}_p \tilde{C}_{23})\hat{Y}
$$
$$
+ ((\dot{x}_p - \dot{\tilde{\theta}} y_p)\tilde{C}_{31} + (\dot{y}_p + \dot{\tilde{\theta}} x_p)\tilde{C}_{32} + \dot{z}_p \tilde{C}_{33})\hat{Z} \quad (2.21)
$$

Finally, the total transformation matrix that relates the six-dimensional state given in rotating frame coordinates with respect to a rotating observer to the state expressed in J2000 inertial coordinates with respect to an observer in the J2000 inertial frame, produced by combining Equations (2.21) and (2.17) is given as

$$
\begin{bmatrix} X_p \\ Y_p \\ Z_p \\ \dot{X}_p \\ \dot{Y}_p \\ \dot{Z}_p \end{bmatrix} = \begin{bmatrix} \tilde{C}_{11} & \tilde{C}_{12} & \tilde{C}_{13} & 0 & 0 & 0 \\ \tilde{C}_{21} & \tilde{C}_{22} & \tilde{C}_{23} & 0 & 0 & 0 \\ \tilde{C}_{31} & \tilde{C}_{32} & \tilde{C}_{33} & 0 & 0 & 0 \\ \dot{\tilde{\theta}}\tilde{C}_{12} & -\dot{\tilde{\theta}}\tilde{C}_{11} & 0 & \tilde{C}_{11} & \tilde{C}_{12} & \tilde{C}_{13} \\ \dot{\tilde{\theta}}\tilde{C}0_{22} & -\dot{\tilde{\theta}}\tilde{C}_{21} & 0 & \tilde{C}_{21} & \tilde{C}_{22} & \tilde{C}_{23} \\ \dot{\tilde{\theta}}\tilde{C}_{32} & -\dot{\tilde{\theta}}\tilde{C}_{31} & 0 & \tilde{C}_{31} & \tilde{C}_{32} & \tilde{C}_{33} \end{bmatrix} \begin{bmatrix} x_p \\ y_p \\ z_p \\ \dot{x}_p \\ \dot{y}_p \\ \dot{z}_p \end{bmatrix}. \quad (2.22)
$$

As previously stated, the rotating position and velocity state *must* first be dimensionalized before a transformation into the J2000 inertial frame using Equation (2.22) can be performed since the 6×6 transformation matrix includes dimensional elements in the lower left quadrant. Additionally, note that to transform a state relative to an observer in the J2000 inertial frame expressed in inertial frame coordinates to a state relative to a rotating observer expressed in rotating frame coordinates, the inverse of the transformation matrix in Equation (2.22) is applied.

As it is beneficial to integrate the *N*-body equations of motion using nondimensional quantities due to numerical challenges, the dimensional states in the J2000 inertial frame resulting from the application of Equation (2.22) must be nondimensionalized as a final step in the transformation process from a state relative to a rotating observer expressed in rotating coordinates to a state relative to a J2000 inertial frame observer expressed in inertial coordinates. Typically, the standard characteristic quantities from the CR3BP are used to nondimensionalize the resulting state, $\left[X_p \ Y_p \ Z_p \ \dot{X}_p \ \dot{Y}_p \ \dot{Z}_p \right]^T$, which is defined as relative to an observer in the J2000 inertial frame and is expressed in inertial coordinates. As an overview, the steps to transform a state relative to a rotating observer that is expressed in the rotating frame to a state relative to an observer in the J2000 inertial frame that is expressed in the J2000 inertial frame are:

1. Translate the rotating state that has a basepoint at the barycenter of the primaries such that its basepoint is located at the center of a primary

2. Dimensionalize the translated primary-centered rotating state with the instantaneous characteristic quantities

3. Apply the transformation matrix given in Equation (2.22) to the rotating frame state

4. Nondimensionalize the primary-centered J2000 inertial state using the characteristic quantities from the CR3BP

This methodology is used throughout the analysis for transforming a rotating frame trajectory solution (states expressed in rotating frame coordinates relative to a rotating observer) into states expressed in the J2000 inertial frame relative to an observer in the J2000 inertial frame in order to gain additional insight and to prepare for transitioning a state from the CR3BP to the higher-fidelity *N*-body ephemeris model.

The steps to transform a state relative to an observer in the J2000 inertial frame that is expressed in the J2000 inertial frame to a state relative to a rotating observer that is expressed in the rotating frame are:

1. Dimensionalize the primary-centered J2000 inertial state using the characteristic quantities from the CR3BP

2. Apply the **inverse** of the transformation matrix given in Equation (2.22) to the inertial state

3. Nondimensionalize the new primary-centered rotating state using the instantaneous characteristic quantities

4. If desired, translate the rotating state (that currently has its basepoint located at the center of a primary) such that it has a basepoint at the barycenter of the primaries

This methodology is used throughout the analysis for transforming states expressed in the J2000 inertial frame relative to an observer in the J2000 inertial frame (e.g., ephemeris propagation) into states expressed in a rotating frame relative to a rotating observer to gain additional insight and aid in visualization of higher-fidelity N-body ephemeris model solutions in a classical rotating frame. Note, the primary bodies here can be any two bodies of interest–the Earth-Moon frame is useful to compare ephemeris solutions to the classical Earth-Moon CR3BP, while the Sun-Earth and Sun-Moon rotating frames are useful for eclipse visualization since the shadows of the smaller primaries are fixed in these frames.

3. TRAJECTORY CONSTRUCTION AND NUMERICAL PROCESSES

Keplerian analysis of orbital motion is available through analytic solutions to the two-body problem equations of motion. In higher-fidelity models, closed-form solutions to the governing equations of motion are not known to exist due to the lack of sufficient integrals of the motion. Numerical strategies are employed to propagate trajectories in these models. However, arbitrary sets of initial conditions rarely yield the desired behavior. In response, differential corrections techniques are necessary to produce trajectories and orbit solutions that meet various mission requirements. Additionally, numerical continuation strategies offer methods to identify additional solutions. Since the motion of a spacecraft modeled in the CR3BP or higher-fidelity ephemeris model is quite complex, Poincaré mapping offers a well-known strategy to simplify the visualization of dynamical flow. Mapping techniques are used extensively in this analysis.

3.1 Differential Corrections

Due to the fact that there is currently no known analytical solution to the CR3BP equations of motion or the higher-fidelity N-body equations of motion, some form of differential corrections processes are necessary to yield solutions that meet various constraints.

3.1.1 State Transition Matrix

Any corrections strategy is based on an assessment of the sensitivities. Thus, to implement various shooting methods, a scheme to relate variations in the initial state, $\mathbf{x}(t_0)$, to variations in the downstream state, $\mathbf{x}(t, \mathbf{x}(t_0))$, is required. Using a first-order Taylor

series expansion relative to the nominal path, the linear variational equations, derived from the equations of motion are written in the form

$$\delta \dot{\mathbf{x}}(t) = \mathbf{A}(t)\delta \mathbf{x}(t) \tag{3.1}$$

where the matrix $\mathbf{A}(t)$ is the Jacobian matrix comprised of the partials of the equations of motion with respect to the states evaluated at time t, i.e., $\mathbf{A}(t) = \frac{\partial \mathbf{f}(t, \mathbf{x}(t), \boldsymbol{\kappa})}{\partial \mathbf{x}(t)}$. Here, the equations of motion are represented in first order form as $\dot{\mathbf{x}}(t) = \mathbf{f}(t, \mathbf{x}(t), \boldsymbol{\kappa})$ where the state vector is $\mathbf{x}(t) = [x(t) \quad y(t) \quad z(t) \quad \dot{x}(t) \quad \dot{y}(t) \quad \dot{z}(t)]^T$ and $\boldsymbol{\kappa}$ represents a vector of additional variables or parameters. The vector $\mathbf{x}(t)$ represents the state vector of interest for both the CR3BP and the ephemeris model.

The solution to Equation (3.1), in a linear sense, is written in the form of the matrix derivative that relates variations in the initial state to variations in the downstream state, i.e.,

$$\delta \mathbf{x}(t) = \left(\frac{\partial \mathbf{x}(t)}{\partial \mathbf{x}(t_0)} \right) \delta \mathbf{x}(t_0). \tag{3.2}$$

By expanding and rearranging Equation (3.2), the definition of the state transition matrix (STM), $\boldsymbol{\Phi}(t, t_0)$, is

$$\boldsymbol{\Phi}(t, t_0) = \frac{\partial \mathbf{x}(t)}{\partial \mathbf{x}(t_0)}. \tag{3.3}$$

The first-order matrix differential equation governing the evolution of the STM can be reduced to the form

$$\dot{\boldsymbol{\Phi}}(t, t_0) = \mathbf{A}(t)\boldsymbol{\Phi}(t, t_0). \tag{3.4}$$

The initial conditions for propagation of Equation (3.4) are $\boldsymbol{\Phi}(t_0, t_0) = \mathbf{I}_{6 \times 6}$. The elements of the STM are determined from the integration of Equation (3.4) along with the equations of motion. A detailed derivation of the equations presented in this section, as well as specific derivations of the particular STMs associated with both the CR3BP and the N-body ephemeris models are available in Zimovan, 2017, Chapter 3.1.

3.1.2 Free-Variable and Constraint Method

In this investigation, corrections strategies based on multi-variable Newton's methods are applied to solve boundary value problems while satisfying a given set of constraints. From among numerous types of implementation strategies, this analysis employs a free-variable and constraint method within a single-shooting or multiple-shooting scheme. Let the free-variable vector be defined as

$$\mathbf{X} = \begin{bmatrix} X_1 \\ X_2 \\ \vdots \\ X_n \end{bmatrix} \tag{3.5}$$

where the elements of $\mathbf{X}$ are the n design variables (i.e., the set of variables that are allowed to be modified in the problem). Typically, $\mathbf{X}$ contains state elements, integration times, epochs, and other quantities. The design variables can evolve subject to m scalar constraint equations satisfying $\mathbf{F}(\mathbf{X}) = \mathbf{0}$, or,

$$\mathbf{F}(\mathbf{X}) = \begin{bmatrix} F_1(\mathbf{X}) \\ F_2(\mathbf{X}) \\ \vdots \\ F_m(\mathbf{X}) \end{bmatrix} = \mathbf{0}. \tag{3.6}$$

The constraints are typically position, time of flight, or velocity constraints, although many other types of constraints are possible. Sample constraint formulations and the corresponding derivations are available in Chapter 3.2.3 of Zimovan, 2017 [23].

A scheme to determine a free-variable vector, $\mathbf{X}^*$, such that $\mathbf{F}(\mathbf{X}^*) = \mathbf{0}$ (that is, all of the constraint equations are satisfied simultaneously) is derived. An iterative process to solve

for $\mathbf{X}^*$, given an initial guess for the free-variable vector, i.e., $\mathbf{X}^0$, is derived by expanding the constraint vector in a Taylor series about the initial guess and truncating to first order. The first order Taylor series expansion about the initial guess is given as

$$\mathbf{F}(\mathbf{X}) = \mathbf{F}(\mathbf{X}^0) + D\mathbf{F}(\mathbf{X}^0)\left(\mathbf{X} - \mathbf{X}^0\right) \tag{3.7}$$

where $\frac{\partial \mathbf{F}(\mathbf{X}^0)}{\partial \mathbf{X}^0}$ is denoted as $D\mathbf{F}(\mathbf{X}^0)$, an $m \times n$ Jacobian matrix that is comprised of the partial derivatives of the constraints with respect to the free-variables. Noting that a solution implies $\mathbf{F}(\mathbf{X}) = \mathbf{0}$, Equation (3.7), can be rearranged and written in an iterative update form as

$$\mathbf{X}^{j+1} = \mathbf{X}^j - D\mathbf{F}(\mathbf{X}^j)^{-1}\mathbf{F}(\mathbf{X}^j) \tag{3.8}$$

where $\mathbf{X}^j$ is the current iteration of the free-variable vector, $\mathbf{X}^{j+1}$ is the next iteration of the free-variable vector, and $\mathbf{F}(\mathbf{X}^j)$ is the value of the current constraint vector as evaluated after propagating the equations of motion from the initial condition $\mathbf{X}^j$. Since the current free-variable vector and value of the current constraint vector are known, $D\mathbf{F}(\mathbf{X}^j)$ is also available. An iteration process is initiated by employing Equation (3.8) as the update equation. Iterations continue until $\mathbf{F}(\mathbf{X}^{j+1}) = \mathbf{F}(\mathbf{X}^*) = \mathbf{0}$ to some acceptable tolerance.

If the design vector includes more free-variables than the constraint vector $(n > m)$, which is typically the case, there are infinitely many solutions to the update equation. In this investigation, the minimum norm solution is selected. The minimum norm update equation is given by

$$\mathbf{X}^{j+1} = \mathbf{X}^j - D\mathbf{F}(\mathbf{X}^j)^T\left(D\mathbf{F}(\mathbf{X}^j)D\mathbf{F}(\mathbf{X}^j)^T\right)^{-1}\mathbf{F}(\mathbf{X}^j). \tag{3.9}$$

The minimum norm solution is used because it seeks a solution, $\mathbf{X}^{j+1}$, that is closest to the initial guess, $\mathbf{X}^j$. This yields a solution, $\mathbf{X}^*$, that is as close as possible to $\mathbf{X}^0$ and will likely retain characteristics of the initial free-variable vector.

Simple Targeting Scheme Formulation

One of the most basic corrections strategies is a simple targeting scheme. Sometimes termed a single-shooting method, a single trajectory arc with the appropriate initial state vector is the solution to a two-point boundary value problem. The formulation of the free-variable vector and constraint vector is problem dependent, however, the elements of the algorithm are consistent. Let the spacecraft initial state be defined as

$$\mathbf{x}(t_0) = [x(t_0) \quad y(t_0) \quad z(t_0) \quad \dot{x}(t_0) \quad \dot{y}(t_0) \quad \dot{z}(t_0)]^T. \tag{3.10}$$

In the CR3BP, $\mathbf{x}(t)$ represents the state vector, i.e., P_3 with respect to the barycenter. In the N-body ephemeris model, $\mathbf{x}(t)$ reflects the state of P_i relative to P_k. From the initial time, the first-order equations of motion, $\dot{\mathbf{x}}(t) = \mathbf{f}(t, \mathbf{x}(t), \boldsymbol{\kappa})$, are propagated to some later time, $t_0 + T$, such that the spacecraft arrives at some point downstream at the state $\mathbf{x}(t_0 + T)$. By modifying the initial state values (position and/or velocity), the spacecraft arrives at an alternative downstream location. To determine an initial state such that the final state of the spacecraft is equal to some desired final position state, $\mathbf{x}_d$, a shooting scheme employs the update equation in Equation (3.8) or Equation (3.9). Note, in a single-shooting approach, the design variable vector, $\mathbf{X}$, includes initial state elements; then, the constraint equation, $\mathbf{F}(\mathbf{X})$, incorporates constraints to enforce some desired final state.

Since a simple targeter is a basic application for a corrections strategy, an example is useful. Figure 3.1 illustrates a targeting algorithm in which only the initial velocity is adjusted to reach some final desired position. For this example, the design variable vector
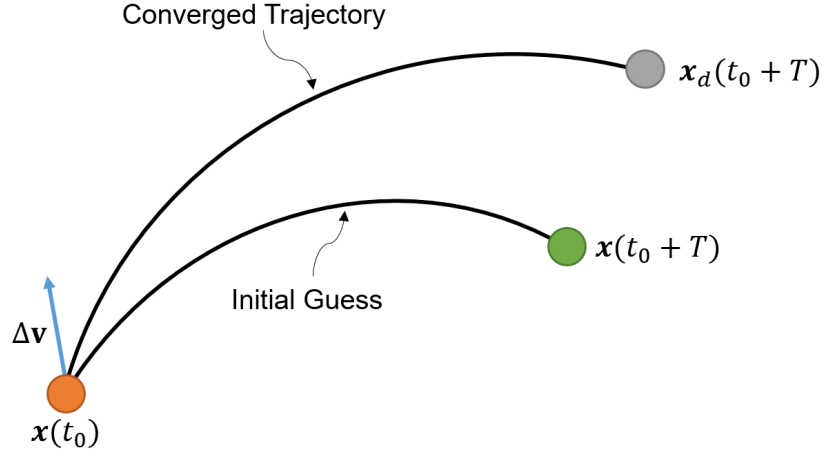
Figure 3.1. : Single-shooter corrections algorithm schematic

is comprised of the initial velocity components and the integration time along the segment. The design variable vector is written as

$$
\mathbf{X} = \begin{bmatrix} \dot{x}(t_0) \\ \dot{y}(t_0) \\ \dot{z}(t_0) \\ T. \end{bmatrix}
\tag{3.11}
$$

The constraint vector includes the constraints on the final position along the trajectory, i.e., the final position is equal to some desired position, and is expressed as

$$
\mathbf{F}(\mathbf{X}) = \begin{bmatrix} x(t_0 + T) - x_d \\ y(t_0 + T) - y_d \\ z(t_0 + T) - z_d \end{bmatrix} = \mathbf{0}.
\tag{3.12}
$$

Therefore, the partials in the matrix $D\mathbf{F}(\mathbf{X})$ are

$$D\mathbf{F}(\mathbf{X}) = \begin{bmatrix} \frac{\partial x(t_0+T)}{\partial \dot{x}(t_0)} & \frac{\partial x(t_0+T)}{\partial \dot{y}(t_0)} & \frac{\partial x(t_0+T)}{\partial \dot{z}(t_0)} & \frac{\partial x(t_0+T)}{\partial T} \\[2mm] \frac{\partial y(t_0+T)}{\partial \dot{x}(t_0)} & \frac{\partial y(t_0+T)}{\partial \dot{y}(t_0)} & \frac{\partial y(t_0+T)}{\partial \dot{z}(t_0)} & \frac{\partial y(t_0+T)}{\partial T} \\[2mm] \frac{\partial z(t_0+T)}{\partial \dot{x}(t_0)} & \frac{\partial z(t_0+T)}{\partial \dot{y}(t_0)} & \frac{\partial z(t_0+T)}{\partial \dot{z}(t_0)} & \frac{\partial z(t_0+T)}{\partial T} \end{bmatrix}. \tag{3.13}$$

Noting that some of the elements of $D\mathbf{F}(\mathbf{X})$ are, in fact, elements of the STM (where ϕ_{ij} is the (i, j) component of the STM), and others are velocity components, $D\mathbf{F}(\mathbf{X})$ is evaluated straightforwardly as

$$D\mathbf{F}(\mathbf{X}) = \begin{bmatrix} \phi_{14} & \phi_{15} & \phi_{16} & \dot{x}(t_0 + T) \\[2mm] \phi_{24} & \phi_{25} & \phi_{26} & \dot{y}(t_0 + T) \\[2mm] \phi_{34} & \phi_{35} & \phi_{36} & \dot{z}(t_0 + T) \end{bmatrix}. \tag{3.14}$$

In this example, since the integration time along the segment is a design variable, velocity components evaluated at the final time, $t_0 + T$, indicate the impact of time on the states at the final position. When integration time, T, is a free-variable, the corrections scheme is denoted a variable-time shooting method. If the time along the segment is not allowed to vary, the shooting method is labeled fixed-time.

Multi-Segment Corrections Algorithm Formulation

In more complex design problems, or for longer integration times, a multi-segment corrections algorithm is better suited. A multiple-shooting method simultaneously solves several two-point boundary value problems to meet design constraints. To formulate a multiple-shooting procedure, a trajectory must be discretized into $(n-1)$ segments, or arcs, that are separated by n patchpoints, or nodes, as illustrated in Figure 3.2. Here, $\mathbf{x}_j^0$ refers to the full six-dimensional state corresponding to patchpoint j at the epoch time τ_j (where $\mathbf{x}_j^0$ is not a function of τ_j), and T_j refers to the integration time along segment j. The final
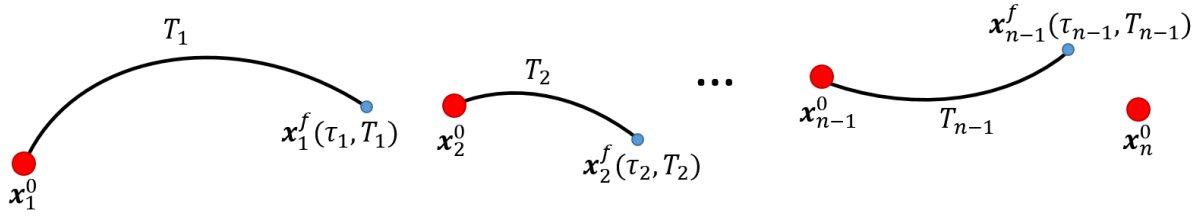
Figure 3.2. : Multiple-shooter corrections algorithm schematic

state along a trajectory arc is written as $\mathbf{x}_j^f(\tau_j, T_j)$ and is a function of the initial epoch along the segment, τ_j, and the integration time, T_j. Note, the epoch is only required in the time-dependent N-body ephemeris model; in the CR3BP, the epoch is not incorporated since the system is autonomous or time-invariant. The initial guess for the six-dimensional state at the patchpoints and the resulting arcs do not necessarily yield a continuous path. Thus, continuity constraints, in the form $\mathbf{x}_{j-1}^f(\tau_{j-1}, T_{j-1}) - \mathbf{x}_j^0 = \mathbf{0}$, enforce full state continuity along the converged trajectory. In the non-autonomous ephemeris model, epoch continuity must also be enforced, i.e., the epoch date at the end of one arc must equal the epoch date at the beginning of the subsequent arc. As a note, if an impulsive maneuver is allowed at a patchpoint, position continuity is enforced, while velocity continuity is omitted from the constraint vector. Any additional path constraints are applied at patchpoints.

As an example of a multi-segment corrections process, i.e., a multiple-shooter, full state continuity is enforced over a trajectory in the N-body ephemeris model with n patchpoints. The free-variable vector, in this example, includes the position and velocity states at all of the patchpoints, the time along each of the integrated segments, and the epoch times at the patchpoints, i.e.,

$$\mathbf{X} = \begin{bmatrix} \mathbf{x}_1^0 & \dots & \mathbf{x}_n^0 & T_1 & \dots & T_{n-1} & \tau_1 & \dots & \tau_n \end{bmatrix}^T. \tag{3.15}$$

54

The constraint vector then includes state and epoch continuity constraints for each segment, i.e.,

$$
\mathbf{F}(\mathbf{X}) =
\begin{bmatrix}
\mathbf{x}_1^f(\tau_1, T_1) - \mathbf{x}_2^0 \\[2ex]
\vdots \\[2ex]
\mathbf{x}_{n-1}^f(\tau_{n-1}, T_{n-1}) - \mathbf{x}_n^0 \\[2ex]
\tau_1 + T_1 - \tau_2 \\[2ex]
\vdots \\[2ex]
\tau_{n-1} + T_{n-1} - \tau_n
\end{bmatrix}
= \mathbf{0}.
\tag{3.16}
$$

Considering $\mathbf{X}$, and $\mathbf{F}(\mathbf{X})$, the Jacobian matrix, $D\mathbf{F}(\mathbf{X})$, is written as

$$
D\mathbf{F}(\mathbf{X}) =
\begin{bmatrix}
\frac{\partial \mathbf{x}_1^f}{\partial \mathbf{x}_1^0} & -\frac{\partial \mathbf{x}_2^0}{\partial \mathbf{x}_2^0} & & & \frac{\partial \mathbf{x}_1^f}{\partial T_1} & & \frac{\partial \mathbf{x}_1^f}{\partial \tau_1} & \\[2ex]
& \ddots & \ddots & & & \ddots & & \ddots & \\[2ex]
& & \frac{\partial \mathbf{x}_{n-1}^f}{\partial \mathbf{x}_{n-1}^0} & -\frac{\partial \mathbf{x}_n^0}{\partial \mathbf{x}_n^0} & & \frac{\partial \mathbf{x}_{n-1}^f}{\partial T_{n-1}} & & & \frac{\partial \mathbf{x}_{n-1}^f}{\partial \tau_{n-1}} \\[2ex]
& & & & \frac{\partial T_1}{\partial T_1} & & & \frac{\partial \tau_1}{\partial \tau_1} & -\frac{\partial \tau_2}{\partial \tau_2} \\[2ex]
& & & & & \ddots & & & \ddots & \ddots \\[2ex]
& & & & \frac{\partial T_{n-1}}{\partial T_{n-1}} & & & \frac{\partial \tau_{n-1}}{\partial \tau_{n-1}} & -\frac{\partial \tau_n}{\partial \tau_n}
\end{bmatrix}.
\tag{3.17}
$$

By simplifying the partial derivatives and substituting STM elements where appropriate, Equation (3.17) is rewritten as

$$
D\mathbf{F}(\mathbf{X}) =
\begin{bmatrix}
\mathbf{\Phi_1} & -\mathbf{I_{6\times6}} & & & \dot{\mathbf{x}}_1^f & & \frac{\partial \mathbf{x}_1^f}{\partial \tau_1} & \\
& \ddots & \ddots & & & \ddots & & \ddots \\
& & \mathbf{\Phi_{n-1}} & -\mathbf{I_{6\times6}} & & \dot{\mathbf{x}}_{n-1}^f & & \frac{\partial \mathbf{x}_{n-1}^f}{\partial \tau_{n-1}} \\
& & & & 1 & & 1 & -1 \\
& & & & & \ddots & & \ddots & \ddots \\
& & & & & & 1 & & 1 & -1
\end{bmatrix}
\tag{3.18}
$$

where $\mathbf{\Phi_j}$ refers to the STM along segment j or $\mathbf{\Phi_j}(\tau_j + T_j, \tau_j)$, and $\frac{\partial \mathbf{x}_j^f}{\partial \tau_j}$ is the partial derivative of the final state along the jth segment with respect to the epoch corresponding to the jth patchpoint.

Partials with respect to epoch time, τ_j, and any constraints on epoch time are *only* applicable in the N-body ephemeris model. In the CR3BP, these partials and constraints are not applicable and are omitted from $\mathbf{F}(\mathbf{X})$ and $D\mathbf{F}(\mathbf{X})$. The design variables for a similar example in the CR3BP would include patchpoint states and segment integration times (in the case of a variable-time multiple-shooter), while the constraints would simply enforce state continuity. Similar to the fixed-time, single-shooter, if times between patchpoints remain fixed, integration time does not appear in the design variable vector. A multiple-shooting scheme is used throughout this investigation for converging trajectories that meet design constraints in both the CR3BP and in the N-body ephemeris model.

3.1.3 Periodic Orbit Computation

As discussed in detail in Zimovan, 2017 (Reference [23]), a simple type of periodic motion appears in the form of symmetric orbits in the CR3BP. Although other types of non-symmetric periodic motion exist, xz-symmetric orbits are the primary focus in this investigation and, therefore, a strategy to numerically compute this type of periodic motion is briefly introduced. Due to symmetry, a variable-time single- or multiple- shooting algorithm is used in which a half revolution of a periodic orbit is solved for. Typically, a single-shooting algorithm is sufficient, although for longer period orbits or orbits that are in a highly sensitive dynamical regime (i.e., an orbit that passes nearby a primary) a multiple-shooting algorithm is useful. To solve for xz-symmetric periodic orbits, solutions are constructed by constraining the departure and arrival condition at the xz-plane crossing to be perpendicular. In other words, the initial condition vector is of the form

$$\mathbf{x}_0 = \begin{bmatrix} x_0 & 0 & z_0 & 0 & \dot{y}_0 & 0 \end{bmatrix}^T. \tag{3.19}$$

Similarly, the constraints on the state variables used to enforce a downstream crossing perpendicular to the xz-plane are defined as

$$\mathbf{F}(\mathbf{X}) = \begin{bmatrix} y(T) \\ \dot{x}(T) \\ \dot{z}(T) \end{bmatrix} = \mathbf{0}. \tag{3.20}$$

The elements of the Jacobian matrix, $D\mathbf{F}$, are composed of elements of the STM and velocity values at the end of each trajectory segment.

3.1.4 Transitioning CR3BP Solutions to the Ephemeris Model

Often, when a higher-fidelity model is necessary for certain applications, preliminary trajectory design is first accomplished in the CR3BP and then transitioned to the higher-fidelity N-body ephemeris model. Building a solution in the CR3BP, prior to working within the N-body ephemeris model, is beneficial due to the simplifying assumptions in the CR3BP, the predictable repeating behavior (especially in the case of periodic motion), and the lack of dependence on the epoch. Designing trajectories to meet mission requirements directly in the N-body ephemeris model is possible as well, although it is generally challenging without an *a priori* solution. In this investigation, trajectory solutions and periodic orbits are computed within the context of the CR3BP and then transitioned to the N-body ephemeris model for further analysis of the effects of higher-order perturbations.

Once a suitable solution is available in the CR3BP, transitioning the solution to the ephemeris model is, in theory, straightforward. Recall that the CR3BP is formulated in a barycenter-centered rotating frame and the N-body ephemeris model is formulated in the J2000 inertial frame. The strategy presented in Section 2.3.2 is used to transition CR3BP patchpoints, i.e., six-dimensional states at intervals along a trajectory arc, from the rotating frame to patchpoints in the J2000 inertial frame at a given epoch. Then, the transformed patchpoints, or state vectors, are converged to a continuous path via a differential corrections technique to enforce continuity and other constraints within the N-body force model. In practice, however, the transformed patchpoints may not supply a sufficient initial guess for the differential corrections process, resulting in convergence challenges. Additional efforts focused on the numerical process may be necessary. For example, some benefit may be gained by introducing elements of the higher-fidelity model one at a time. As a starting point, the trajectory can first be converged in the N-body ephemeris model with only the primary bodies from the CR3BP influencing the motion of the body of interest. Such a solution differs from the CR3BP solution because the eccentricity of the orbits of the primary bodies as well as epoch date dependence is accommodated within the higher-fidelity model. Then, additional perturbing bodies or other constraints can be added, one at a time, with the

previous solution serving as an initial guess for the next trial. Additionally, attempting to enforce too many constraints simultaneously is challenging in the N-body ephemeris model. Adding constraints one at a time or relaxing certain constraints in preliminary corrections iterations can aid convergence.

3.1.5 Eclipse Constraint Formulation

Transitioning a trajectory from the CR3BP to an ephemeris model presents challenges in maintaining a favorable geometry, especially for eclipse avoidance purposes [23]. A minimum norm targeting scheme produces a solution that is maintained close to the initial CR3BP design [23]. The addition of a path constraint to the differential corrections process, one that forces the trajectory to remain outside the shadows of the Earth and Moon, is one strategy that enables convergence of eclipse-free geometries in a higher-fidelity model [41]. The eclipse avoidance path constraint is based on the geometry of the shadow of an occluding celestial body [45]. Varying levels of shadow fidelity are available–a cone model is relatively simple and reasonably accurate [51]. Parameters to compute the shadow geometry are defined in Figure 3.3 [23]. The Sun, denoted S, has a radius defined as R_S, R_O is the radius of the occluding body, O (the Earth or the Moon, i.e., the orange sphere), and r_{SO} is the distance between the Sun and the occluding body, at a given instant in time. Using geometry, the dimensions of the shadow cones are computed as

$$l = \frac{R_O * r_{SO}}{R_S - R_O} \tag{3.21}$$

$$p = \frac{R_O * r_{SO}}{R_S + R_O} \tag{3.22}$$

$$\alpha = \tan^{-1}\left(\frac{R_O}{p}\right) \tag{3.23}$$

$$\theta = \tan^{-1}\left(\frac{R_O}{l}\right). \tag{3.24}$$

Using these expressions and defining $\mathbf{r}_{Ssc}$ as the vector from the Sun to the spacecraft, $\mathbf{r}_{SO}$ as the vector from the Sun to the occluding body, and $\mathbf{r}_{Osc}$ as the vector from the occluding body to the spacecraft, the location of the spacecraft, sc, relative to the shadow is determined. The spacecraft is located within the penumbra if

$$r_{Osc}\sin(\zeta) \leq \left(p + \frac{\mathbf{r}_{SO}}{r_{SO}} \bullet \mathbf{r}_{Osc}\right)\tan\alpha \tag{3.25}$$

and

$$r_{Ssc} > r_{SO}. \tag{3.26}$$

To avoid any eclipsing event, maintaining the spacecraft outside the penumbra is generally sufficient.
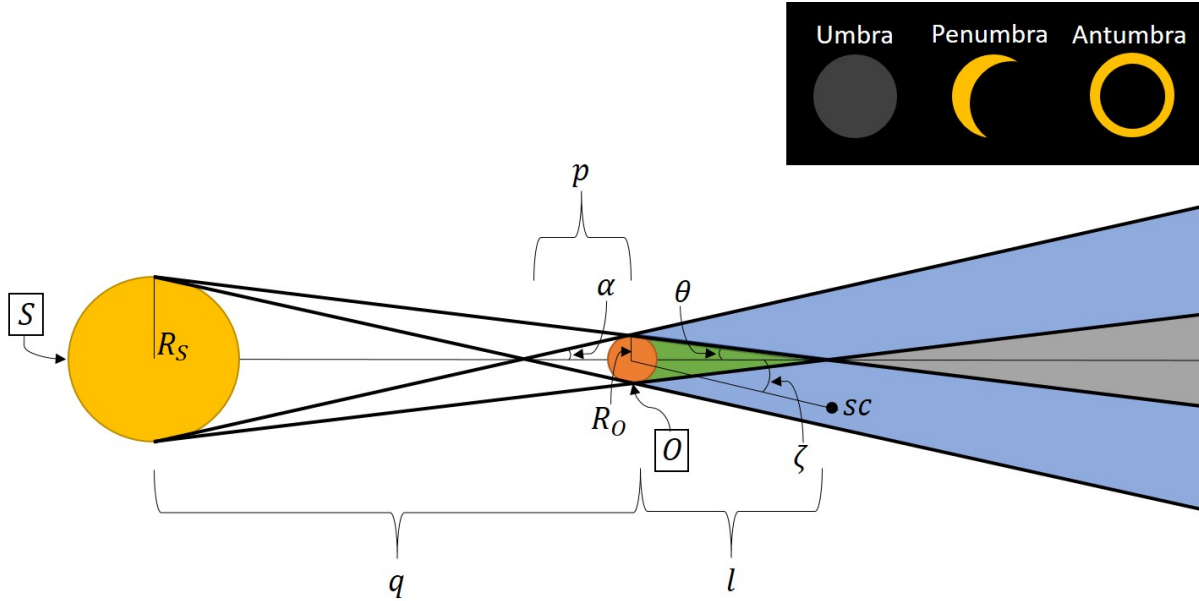
Figure 3.3. : Eclipse geometry definitions

The mathematical expressions in Equations (3.25) and (3.26) are manipulated to formulate a path constraint for the ephemeris differential corrections multiple-shooting scheme [23]. This constraint, along with continuity constraints, guides the transition of periodic tra-

jectories between the CR3BP and the ephemeris model. This constraint is enforced within the ephemeris model since the Sun, and therefore eclipses, are generally not considered in the time-invariant CR3BP. The eclipsing path constraint is formulated as an expression, F_j, that is appended to the constraint vector for each of the segments, j, in the multiple-shooting scheme [41]

$$F_j = \int_{\tau_j}^{\tau_j + T_{seg}} H(r_{Ssc} - r_{SO}) * (f - |f|) dt \tag{3.27}$$

where

$$f = r_{Osc} \sin(\zeta) - \left(p + \frac{\mathbf{r}_{SO}}{r_{SO}} \bullet \mathbf{r}_{Osc} \right) \tan(\alpha) \tag{3.28}$$

and $H(r_{Ssc} - r_{SO})$ is a Heaviside function used to activate the constraint when the spacecraft is located on the shadowed side of the occluding body from the Sun. The expression in Equation (3.27) is evaluated using a Riemann sum. The time step used in the evaluation of the Riemann sum must be sufficiently small to capture eclipse crossings. In this analysis, a fixed step of 0.001 nondimensional time units (approximately 6 minutes) is used to evaluate the eclipse constraint with sufficient accuracy. In practice, the radius of the occluding body (i.e., the Earth or Moon) is artificially scaled up within the constraint to account for errors in modeling (e.g., lack of atmosphere model for Earth) or to provide a margin for eclipse avoidance to account for other uncertainties.

The path constraint formulation for eclipse avoidance is flexible and, thus, applicable in a variety of scenarios beyond eclipse-free transfer trajectory generation. As an example, this constraint proves useful in producing long-duration eclipse-free baseline orbits in a higher-fidelity model [45]. The path constraint aids in designing solutions that meet mission constraints, e.g., power and thermal requirements may limit the allowable duration of shadow passages.

3.2   Continuation Processes

Single-shooting and multiple-shooting schemes are employed to compute a single point solution for a trajectory or periodic orbit based on one given set of initial conditions. In

general, it is useful to construct a range of related solutions, or a family, if possible. Families of periodic orbits deliver insight into the dynamical characteristics across an entire region and offer various options for trajectory design. Additionally, since a family of orbits spans a range of characteristics, an individual orbit, or family member, is then able to be selected more carefully to meet mission requirements. Figure 4.2(a) depicts the southern portion of the L_2 halo family of orbits computed in the CR3BP and plotted in the Earth-Moon rotating frame. Multiple strategies to compute families of orbits and trajectories exist; for example, a natural parameter continuation scheme offers a straightforward approach to compute a new trajectory based on a previously converged solution. Additionally, a strategy that requires less intuition, the pseudo-arclength continuation scheme, is also an option.

3.2.1   Natural Parameter Continuation

Natural parameter continuation offers a simple strategy to construct a family of related solutions. To begin, a single converged solution is determined by implementing a numerical corrections process given some initial guess. Then, one parameter associated with the converged solution is incremented by a small, but specified, amount. This parameter typically possesses some physical significance, e.g., x_0, y_0, z_0, Jacobi constant, or time of flight, among many other possibilities. The previously converged solution, now with one varied parameter, is then employed as an initial guess for a new trajectory in a differential corrections scheme. Once converged, the new trajectory maintains some characteristics of the previous trajectory, however, the solutions are independent but related across values of the varied parameter. The natural parameter continuation process is then repeated to construct additional related trajectories. This continuation scheme applies to both periodic orbits and non-periodic trajectory arcs.

3.2.2 Pseudo-Arclength Continuation

An alternative continuation scheme is offered by the pseudo-arclength method [52], [53]. Pseudo-arclength differs from natural parameter continuation in the selection of the increment quantity to advance to the next solution in the family. The increment, or step size, Δs, in the pseudo-arclength continuation strategy is defined in a direction tangent to the family. All free-variables are then updated simultaneously. By stepping in a tangent direction, prior knowledge of the evolution in the solution space is not necessary. Additionally, larger increments are possible and, in many applications, fewer iterations are required for convergence. However, in this continuation scheme, the step size, Δs, is not an intuitive physical parameter which leads to less insight into the relative distance between solutions.

In any continuation scheme, including pseudo-arclength continuation, a new member of the family is computed based on a previous solution. A previously converged solution is defined by a free-variable vector denoted $\mathbf{X_j^*}$, where $\mathbf{F}(\mathbf{X_j^*}) = \mathbf{0}$. The free-variable vector denoted as $\mathbf{X_{j+1}^0}$ represents the initial guess for the next family member that may not yet meet the constraints. Given $\mathbf{X_j^*}$, a unit vector tangent to the family at $\mathbf{X_j^*}$ is constructed from the null vector, denoted $\Delta \mathbf{X_j^*}$, of the Jacobian matrix, $D\mathbf{F}(\mathbf{X_j^*})$. The null vector of $D\mathbf{F}(\mathbf{X_j^*})$ is selected since adding a multiple of the null space vector does not change the solution to the first-order iterative update equation given in Equation (3.7), $\mathbf{F}(\mathbf{X}) = \mathbf{F}(\mathbf{X^0}) + D\mathbf{F}(\mathbf{X^0})(\mathbf{X} - \mathbf{X^0})$. To ensure that the next solution, $\mathbf{X_{j+1}}$, is shifted by the scalar step Δs along the family tangent vector, an additional constraint is added to the original constraint vector, $\mathbf{F}(\mathbf{X_{j+1}})$. This pseudo-arclength constraint is a scalar expressed as

$$(\mathbf{X_{j+1}} - \mathbf{X_j^*})^T \Delta \mathbf{X_j^*} - \Delta s = 0. \tag{3.29}$$

The augmented constraint vector is then

$$
\mathbf{G}(\mathbf{X_{j+1}}) = \begin{bmatrix} \mathbf{F}(\mathbf{X_{j+1}}) \\ (\mathbf{X_{j+1}} - \mathbf{X_j^*})^T \Delta \mathbf{X_j^*} - \Delta s \end{bmatrix} = \mathbf{0}. \tag{3.30}
$$

The derivative of the augmented constraint vector, $\mathbf{G}(\mathbf{X_{j+1}})$ with respect to the free-variables, $\mathbf{X_{j+1}}$, yields an augmented Jacobian matrix given by

$$
D\mathbf{G}(\mathbf{X_{j+1}}) = \frac{\partial \mathbf{G}(\mathbf{X_{j+1}})}{\partial \mathbf{X_{j+1}}} = \begin{bmatrix} D\mathbf{F}(\mathbf{X_{j+1}}) \\ \Delta \mathbf{X_j^*}^T. \end{bmatrix} \tag{3.31}
$$

Once the augmented constraint vector and the Jacobian matrix are constructed, a differential corrections scheme is employed to converge upon the next family member, $\mathbf{X_{j+1}^*}$.

3.3 Poincaré Mapping Technique

Poincaré mapping, a technique first introduced by Henri Poincaré in 1881, is an approach that allows for concise visualization of the flow and an effective reduction of dimensionality of the transfer design problem [54]. To construct a Poincaré map, a smooth surface of section, or hyperplane, at which trajectory crossings are recorded, is selected. This hyperplane, Σ, can be physical (such as the $y = 0$ plane in configuration space) or can be nonphysical (such as periapsis or apoapsis occurrences). Then, a variety of initial conditions are propagated; if the map is generated in the CR3BP, these initial conditions typically each possess an identical Jacobi constant. Each time the propagated trajectories cross the hyperplane, information concerning the trajectory is recorded. Mathematically, an initial condition $\mathbf{x_0}$ on Σ is mapped forward in time to $P(\mathbf{x_0})$; both points appear discretely on the map. The mapping $\mathbf{x_0} \rightarrow P(\mathbf{x_0})$, termed the Poincarè map, preserves both stability and periodicity [54]. If an orbit is precisely periodic, then $P(\mathbf{x_0}) = \mathbf{x_0} = \mathbf{x^{PO}}$, and the process

yields a single point on the hyperplane, i.e., a 'fixed point.' A schematic illustrating a general Poincaré mapping process is provided in Figure 3.4.

Significant insight into the six-dimensional flow of a trajectory is gained by reducing the dimension of the system through the use of a Poincaré map. Additionally, Poincaré mapping allows for the comparison of many trajectories simultaneously and more completely than in configuration space, dramatically increasing the understanding of the design space. A sample departure trajectory from a periodic orbit is propagated in an ephemeris model
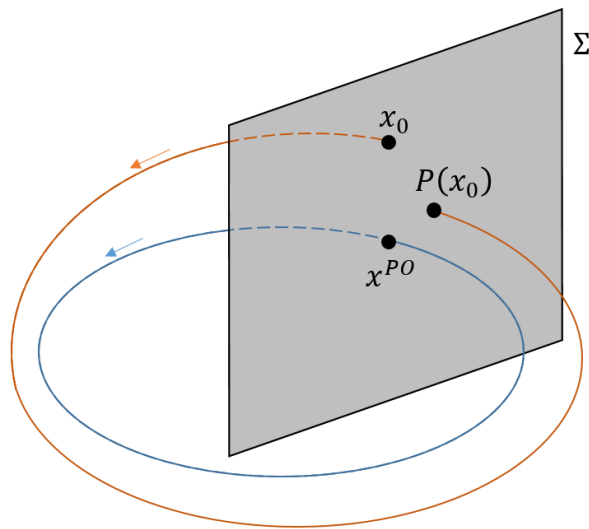
Figure 3.4. : Poincaré map schematic, adapted from Perko [54]

and is plotted in Figure 3.5(a) in the nondimensionalized Earth-Moon rotating frame. A hyperplane at $y = 0$ in the Earth-Moon rotating frame is selected to generate the Poincaré map. Figure 3.5(b) depicts the geometric hyperplane in grey where trajectory intersections with the hyperplane, denoted as 'events,' are highlighted as green stars. At each event, the full spacecraft state (position and velocity) is recorded. In Figure 3.5(c), the Earth-Moon rotating (x, v_x) coordinates for the events are plotted as green stars; each star is numbered to indicate the order of the event, i.e., event 1 is the first intersection of the departing trajectory with the hyperplane, event 2 is the second intersection, and so on. The events are considered as snapshots along the departure trajectory [44]. The Poincaré map in Figure

is termed a 'double-sided' map since intersections piercing the hyperplane from both the positive and negative directions are recorded.
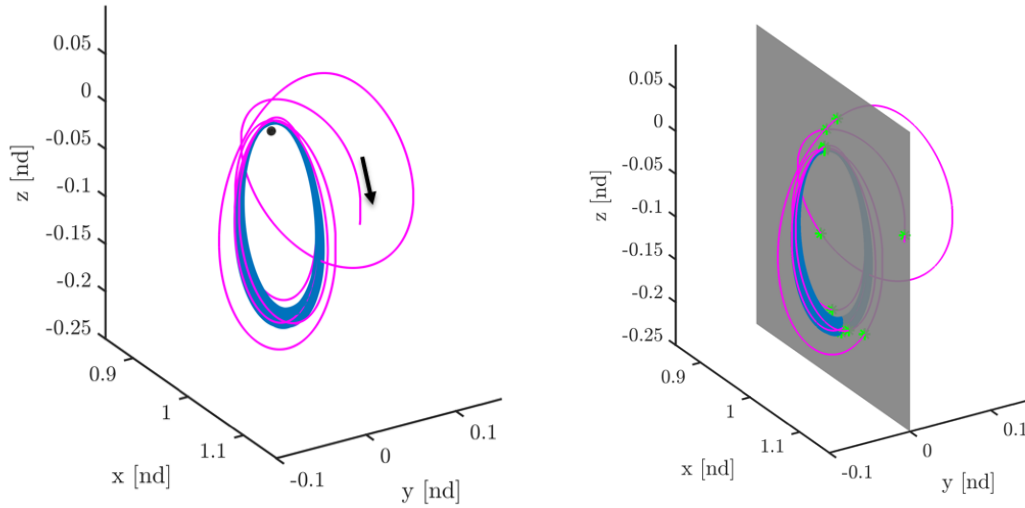
(a) Sample ephemeris trajectory (magenta) departing from a quasiperiodic orbit (blue) plotted in the Earth-Moon rotating frame

(b) Hyperplane at the Earth-Moon rotating $y = 0$ plane (grey) and crossings of the hyperplane (green)
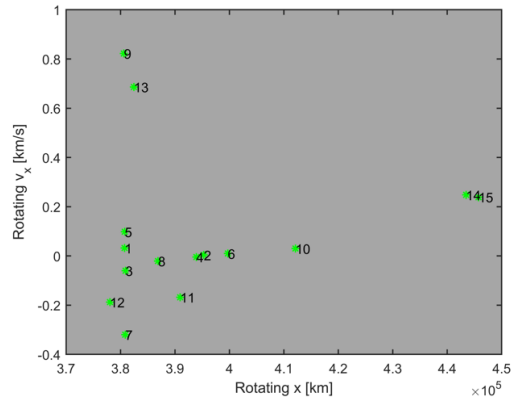
(c) An x-v_x Poincaré map depicting hyperplane crossings of the departing flow from (a) marked with green stars

Figure 3.5. : Departing trajectory in the Earth-Moon rotating frame (a) and an associated Poincaré map used to identify candidate recovery options (b)

4. ORBITAL STABILITY AND BIFURCATIONS

Orbital stability plays a key role in understanding characteristics of the dynamical flow in the vicinity of a periodic orbit. It also impacts design processes, for example, transfer design to and from the orbit can be more efficient due to the existence of unstable and stable manifolds that ballistically lead away from and toward a periodic orbit, respectively. Stability of an orbit also influences orbit maintenance costs, e.g., spacecraft in linearly stable orbits may require less total Δv to maintain their motion. For a long-duration mission, such as the NASA Gateway or other hub, the ability to maintain an orbit for a long-duration at a low cost is crucial. Insertion options and access to a range of other cislunar orbits, however, must also be considered. Thus, orbital stability is a key consideration.

4.1 Monodromy Matrix

The stability of a periodic orbit is deduced through the eigenvalues of the monodromy matrix. The monodromy matrix, denoted $\mathbf{\Phi}(t_0 + P, t_0)$, is equivalent to the STM evaluated over precisely one orbital period, P, and corresponds to a discrete linear mapping. The monodromy matrix has the following properties:[55]

1. The eigenvalues of the monodromy matrix are always in reciprocal pairs.

2. The determinant of $\mathbf{\Phi}(t_0 + P, t_0)$ must equal unity.

3. The monodromy matrix is symplectic.

For a precisely periodic orbit, the set of eigenvalues from the monodromy matrix occur in the form: $(1,\ 1,\ \lambda_1,\ 1/\lambda_1,\ \lambda_2,\ 1/\lambda_2)$. The two unit eigenvalues are referred to as the trivial pair. Since the mondoromy matrix refers to a discrete time system, the stability bound for the eigenvalues of this matrix is the unit circle. Stable eigenvalues have magnitude less than unity and unstable eigenvalues have magnitude greater than unity. This concept is illustrated in Figure 4.1. Eigenvalues of the monodromy matrix that are within the blue

region are deemed 'stable' and flow along the eigenvector direction associated with these eigenvalues will approach the fixed point as time progresses. Eigenvalues that are within the red region are deemed 'unstable' and flow along the eigenvector direction associated with these eigenvalues will depart away from the fixed point. Note that since eigenvalues of the monodromy matrix always come in reciprocal pairs, if there is an unstable eigenvalue, there will also always be a stable eigenvalue (and vice versa). The monodromy matrix, among many applications, is used to assess orbit stability, compute manifold arcs, and detect bifurcations within this investigation.
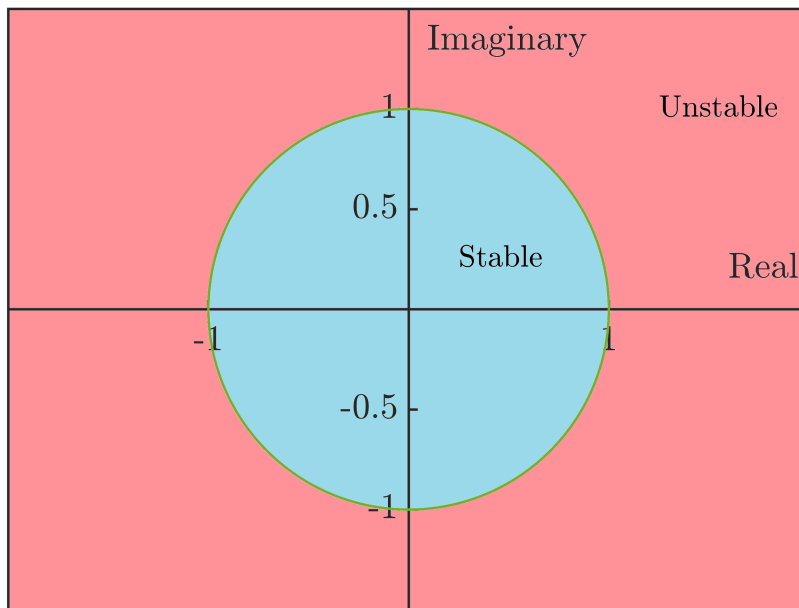
Figure 4.1. : Illustration of stability bound for eigenvalues of the monodromy matrix

4.2 Stability Properties in the CR3BP

4.2.1 Stability Index

Stability indices provide a useful measure of stability for periodic orbits. This metric is defined as

$$\nu_j = \frac{1}{2}\left(||\lambda_j|| + \frac{1}{||\lambda_j||}\right), \tag{4.1}$$

where λ_j represents the eigenvalues of the monodromy matrix, $\boldsymbol{\Phi}(t_0 + P, t_0)$ [23]. If all of the stability indices are equal to unity, an orbit is linearly stable and possesses no unstable subspace. If any nontrivial stability index has magnitude greater than unity, the orbit is unstable and natural flow exists into and out of the orbit. The magnitude of the stability index is directly related to the rate of the departing/arriving flow. For example, the stability indices of the L_2 NRHOs range from 1 to 1.69, as is apparent in Figure 4.2(b), while the stability index of the halo orbit that bifurcates from the L_2 Lyapunov family is larger at 606.11. As demonstrated by the magnitude of the stability indices for the NRHOs, natural flow into and out of these orbits is either nonexistent or may be too slow to offer utility for some transfer applications.

Orbital stability is employed to delineate the region along the family of halo orbits denoted the NRHOs [38]. The NRHOs are defined as the subset of the halo orbits with bounded linear stability, i.e., the NRHOs are stable or nearly-stable. In the Earth-Moon system, an L_2 NRHO is defined as a halo orbit between the first and third members of the family that reflect stability changes in the region near the smaller primary, highlighted in maroon and purple in Figure 4.2(a) and marked with maroon and purple asterisks (*) in Figure 4.2(b). The southern L_2 halo family is plotted in Figure 4.2(a); these orbits are denoted as 'southern' since the majority of the trajectory lies below the rotating xy-plane. The stability changes defining the bounds of the L_2 NRHOs occur at halo orbits possessing perilune radii of 1832 km and 17390 km, respectively [23].

An alternative formulation of the stability index as $\tilde{\nu}_j = \frac{1}{2}\left(\lambda_j + \frac{1}{\lambda_j}\right)$ is presented in Reference [23]. This formulation provides insight into the evolution of each of the nontrivial pairs of eigenvalues as well as the order of instability of each family member. Although this alternative formulation does provide valuable information, it is *not* used in this investigation because, in the case of a monodromy matrix of a periodic orbit possessing complex eigenvalues with magnitude greater than 1, $\tilde{\nu}_j$ is complex.
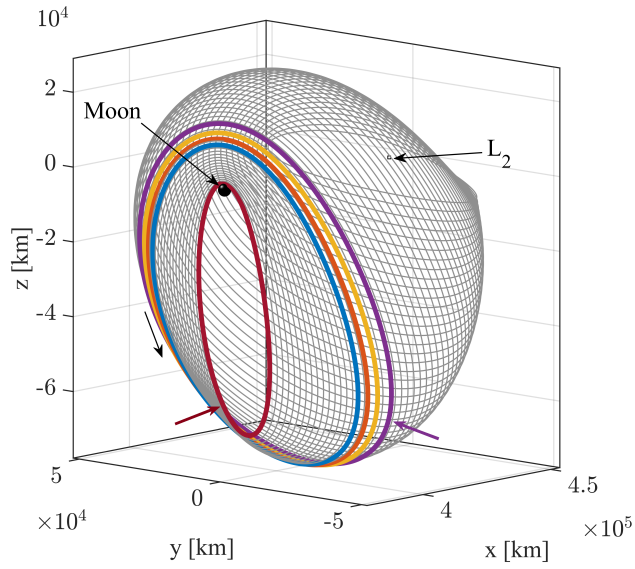
(a) Southern L_2 halo family, NRHOs are the subset be-
tween the maroon and purple highlighted orbits marked
by maroon and purple arrows
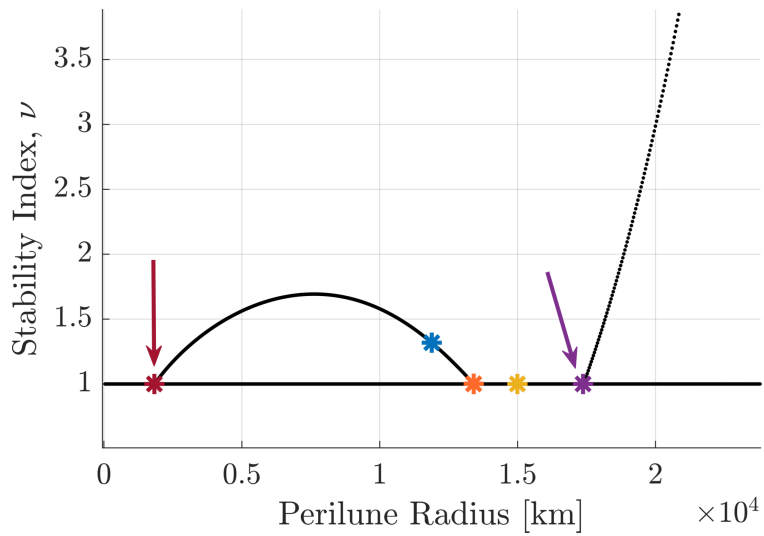
(b) NRHO stability indices

Figure 4.2. : NRHOs in the Earth-Moon rotating frame (a) and NRHO stability indices
(b)

4.2.2 Time Constant

For unstable orbits, a useful metric corresponding to the temporal scale of the dominant divergent motion is derived by considering the time constant, Υ, as measured in terms of the number of revolutions along the nominal orbit, that is

$$\Upsilon = \frac{1}{|\text{Re}(\ln(\lambda_{\max}(\boldsymbol{\Phi}(t_0 + P, t_0))))|} \frac{1}{P} \tag{4.2}$$

where $\lambda_{\max}(\ )$ is an operator that returns the largest magnitude eigenvalue of the argument matrix. Note that the time constant is infinite for a marginally stable orbit, i.e., $\lambda_{\max}(\boldsymbol{\Phi}(t_0 + P, t_0)) = 1$. The value $\tau[rev]$ is physically interpreted as the number of revolutions along the nominal orbit necessary to amplify a given initial perturbation in the dominant direction by a factor of e [38]. The time constant for the NRHOs ranges from approximately one revolution (for nearly stable orbits) to infinite revolutions (for stable NRHOs) while the time constant for the halo orbit that bifurcates from the L_2 Lyapunov family is much smaller at 0.0412 revolutions.

4.3 Computation of Invariant Manifolds

Often leveraged to generate initial guesses for transfer design in the CR3BP, manifolds offer pathways for ballistic arrival at and departure from unstable periodic orbits. To compute stable and unstable manifold structures, or, more specifically, trajectories that lie along these manifold surfaces, a step in the direction of a stable or unstable mode of a fixed point, $\mathbf{x_i^{PO}}$, along the periodic orbit must first be taken. The directions of the stable and unstable modes corresponding to a fixed point are determined by the eigenvectors of the monodromy matrix, $\boldsymbol{\Phi}(t_0 + P, t_0)$, that correspond to stable and unstable eigenvalues, respectively. States in which a step has been taken in the direction of a stable or unstable eigenvector, are written as

$$\mathbf{x_S} = \mathbf{x_i^{PO}} \pm \epsilon \boldsymbol{\nu}_S, \quad \mathbf{x}_U = \mathbf{x_i^{PO}} \pm \epsilon \boldsymbol{\nu}_U \tag{4.3}$$

where $\boldsymbol{\nu}$ is an eigenvector of $\boldsymbol{\Phi}(t_0 + P, t_0)$ that has been normalized with respect to the position coordinates and ϵ is a small perturbation amount, defined in terms of distance, that allows for the numerical computation of the manifold structure [23], [56]. The value for ϵ used in this investigation is between 15 and 50 km. The perturbed states, $\mathbf{x_S}$ and $\mathbf{x_U}$, are integrated in the CR3BP using the equations of motion. For a stable manifold, in which the manifold trajectory approaches the fixed point, numerical integration is accomplished in reverse time. In contrast, an unstable manifold departs the fixed point in forward time. The collection of all manifold trajectories from each fixed point along a periodic orbit comprise the manifold surface. A more detailed explanation of manifold theory is offered in Perko and Koon et al. [54], [56].

4.4   Bifurcations

Bifurcation theory is the study of changes in the qualitative structure of flow associated with a dynamical system of differential equations as a result of parameter variations [57]. If the change in flow is large for a small change in a significant parameter, a bifurcation point is reached. On the other hand, if the change in flow is small for a corresponding small change in a parameter, the system is structurally stable at that parameter value and a bifurcation does not occur. As applied to the dynamical system of the CR3BP, bifurcation theory allows for the detection of orbits (bifurcation points) that 'branch' or 'grow' into new families of periodic solutions with behavior that is unique from the originating family. Additionally, bifurcation theory allows for the detection of changes in order of instability along an orbit family (i.e., how many unstable/stable modes are associated with each member of an orbit family).

4.4.1   Bifurcation Types

Considered in this investigation are the following bifurcation types:

1. **Tangent Bifurcation:** As a general rule, a transition in stability characteristics along an orbit family denotes a bifurcation (as noted by changes in the value of the stability index). In the case of a change in family stability occurring simultaneously with two nontrivial eigenvalues of the monodromy matrix going to unity, $\lambda_j = 1/\lambda_j = +1$, a tangent bifurcation has occurred. There is a change in the order of instability along a family as a tangent bifurcation occurs [55], [57]. A tangent bifurcation is further delineated as either a cyclic fold, pitchfork bifurcation, or transcritical bifurcation:

   - Cyclic Fold Bifurcation: The orbits along a single periodic orbit family change order of instability but do not intersect with any other family at a cyclic fold [55]. A cyclic fold occurs at an extremum in Jacobi constant value [57].

   - Pitchfork Bifurcation: At a change in stability characteristics along a family, two new families are formed that both possess the same stability as members of the original family prior to the bifurcation.

   - Transcritical Bifurcation: At a transcritical bifurcation, a stable and unstable orbit family intersect; at this intersection, the stability characteristics of the families are swapped.

2. **Period-Doubling Bifurcations:** At a period-doubling bifurcation, two nontrivial monodromy matrix eigenvalues collide at -1 and depart from the unit circle to the negative real line or vice versa [57]. The stability characteristics (i.e., order of instability) of an orbit family changes at a period-doubling bifurcation.

3. **Period-Multiplying Bifurcations:** A period-multiplying bifurcation (of multiplying factor m where m is an integer greater than 2) occurs when two nontrivial monodromy matrix eigenvalues evolve such that $\lambda_j, 1/\lambda_j = \sqrt[m]{1} = \cos(2\pi/m) \pm i\sin(2\pi/m)$ [55]. Note, these are the first and $(m-1)^{th}$ complex roots of unity. As an example, when two nontrivial eigenvalues of the monodromy matrix, $\lambda_j, 1/\lambda_j = \sqrt[3]{1} = -0.5 \pm 0.8660i$, a period-tripling bifurcation occurs. Period-multiplying bifurcations do not require a collision of eigenvalues on the unit circle and thus there is not necessarily a corresponding change in orbital stability along the family.

4. **Secondary Hopf and Modified Secondary Hopf Bifurcations:** A less typical
   type of bifurcation is described as a secondary Hopf bifurcation; this type occurs when
   two eigenvalues collide on the unit circle and depart into the complex plane at a
   location other than ± 1 along the real axis (therefore, a change in stability also occurs).
   A modified secondary Hopf bifurcation is triggered when two eigenvalues collide on
   the real line and depart into the complex plane (other than at ± 1), however, this
   scenario does not occur with a change in stability. In the special case of a secondary
   Hopf bifurcation (modified or regular), after departure from the unit circle or real line,
   eigenvalues are complex but with magnitude greater than unity, indicating the existence
   of spiral manifolds (oscillatory and departing/approaching flow) [57]. In some special
   cases, periodic solutions are produced from secondary Hopf bifurcations, however, in
   general, invariant tori surrounding the periodic orbit are formed [57]–[59].

In the case of tangent bifurcations (other than the cyclic fold type), period-doubling, and
period-multiplying bifurcations, a new family of periodic orbits intersects with the current
family; it is in this new family, which possesses members nearby in both energy and geometry,
that useful unstable structures may arise. An additional detailed description of bifurcation
types is available in Reference [57].

4.4.2   Detection of Bifurcations Using a Broucke Stability Diagram

In 1969, Broucke introduced an alternative method to identify bifurcations based
on changes in the eigenstructure of the monodromy matrix [60]. In this technique, the
nontrivial eigenvalues of the monodromy matrix for each family member are recast in terms
of two parameters, α and β

$$\alpha = -\left(\lambda_1 + \frac{1}{\lambda_1} + \lambda_2 + \frac{1}{\lambda_2}\right) = 2 - Tr\left(\mathbf{\Phi}(t_0 + P, t_0)\right) \tag{4.4}$$

$$\beta = \frac{1}{2}\left(\alpha^2 - \left(\lambda_1^2 + \frac{1}{\lambda_1^2} + \lambda_2^2 + \frac{1}{\lambda_2^2}\right)\right) = \frac{1}{2}\left(\alpha^2 + 2 - Tr\left(\mathbf{\Phi}(t_0 + P, t_0)^2\right)\right). \qquad (4.5)$$

The scalars α and β fully define the set of four nontrivial eigenvalues, thereby reducing the set of parameters to be monitored from four to two. The derivation of α and β is available in Appendix B. Additionally, using α and β to detect bifurcations eliminates the need to compute eigenvalues, thereby reducing numerical inaccuracies and computation time. The set (α, β) is plotted for each member of a family of periodic orbits on a Broucke stability diagram resulting in a curve that illustrates the evolution of the eigenstructure across the family [57], [61]. The Broucke stability diagram in Figure 4.3 offers insight into the eigenvalue configuration in the complex plane. In this figure, the small graphic in each region illustrates the unit circle and the general arrangement of the four nontrivial eigenvalues. By noting changes in the eigenstructure over the evolution of the family based solely on the values of (α, β), bifurcations are detected. If an (α, β) pair is within the orange region, note that the corresponding orbit is stable, otherwise it is unstable. The bifurcations of interest (and their relation to the Broucke stability diagram) are described in Table 4.1. The derivation of the curves delineating the regions on the Broucke stability diagram is detailed in B.

4.4.3 Bifurcation Diagram

A bifurcation diagram is a tool that is used to capture the relationship between bifurcating families as a parameter of the system is varied [57]. The bifurcation diagram is a more detailed form of a hodograph that illustrates the structure of the solutions along a family, in combination with information about the order of instability along a family and details about connections between families. A two-dimensional plot of Jacobi constant (or some parameter that varies smoothly along an orbit family) and a non-zero parameter at a mirror configuration (symmetry point at which the rotating $y = 0$ plane is crossed perpendicularly) is plotted to generate a bifurcation diagram. The non-zero parameters at the mirror configuration that are typically used in a bifurcation diagram are the x, z, or $\dot{y}$ coordinates. Since there is a loss of information when plotting a hodograph (i.e., not all
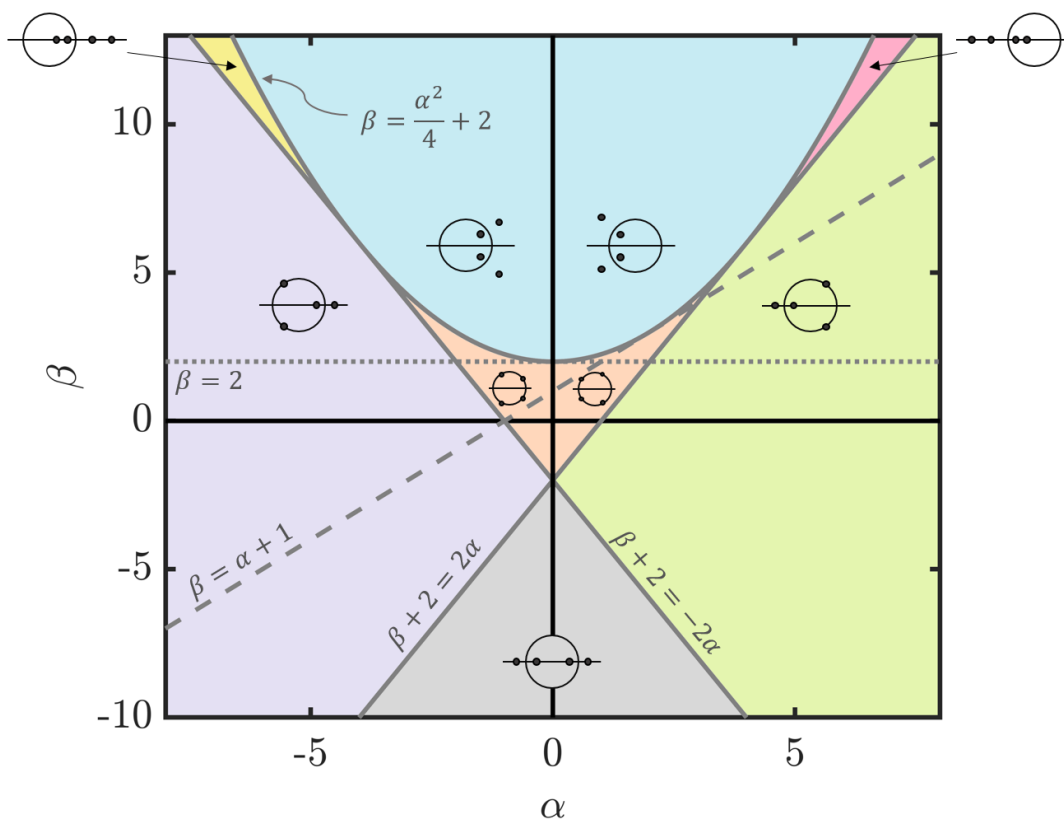
Figure 4.3. : Broucke stability diagram [60]

states are fully represented) an intersection in a bifurcation diagram is necessary, but not sufficient, to identify a bifurcation between families.

A sample bifurcation diagram, one depicting two solution families, is plotted in Figure 4.4. The solid curve corresponds to the 'original' orbit family; the dashed hodograph corresponds to a 'new' orbit family that is continued from the denoted bifurcation. Changes in the order of instability are marked by black triangles. The color of the curve corresponds to the number of unstable modes, i.e., a teal-colored curve corresponds to a solution with zero unstable modes (a stable orbit), a blue-colored curve corresponds to a solution that possesses one unstable mode, while a magenta-colored curve corresponds to a solution that has two unstable modes. The order of instability corresponds to the dimension of the stable/unstable subspaces associated with the fixed point. An orbit that has an order of instability equal to

Table 4.1. : Classification of bifurcations of interest based on a Broucke stability diagram

Bifurcation Type	Eqn. of Line Crossed	Color Transitions	Stab. Change?
Tangent	$\beta + 2 = -2\alpha$	Orange $\leftrightarrow$ Purple Green $\leftrightarrow$ Grey Yellow $\leftrightarrow$ Purple	Yes
Period-Doubling	$\beta + 2 = 2\alpha$	Orange $\leftrightarrow$ Green Purple $\leftrightarrow$ Grey Pink $\leftrightarrow$ Green	Yes
Period-Tripling	$\beta = \alpha + 1$	N/A	No
Period-Quadrupling	$\beta = 2$	N/A	No
Secondary Hopf	$\beta = \frac{\alpha^2}{4} + 2$ $\alpha \in (-4, 4)$	Orange $\leftrightarrow$ Blue	Yes
Modified Secondary Hopf	$\beta = \frac{\alpha^2}{4} + 2$ $\alpha \in (-\infty, -4] \bigcup [4, \infty)$	Pink $\leftrightarrow$ Blue Yellow $\leftrightarrow$ Blue	No

zero or unity possesses a center subspace; if imaginary components of the unit magnitude eigenvalues are non-zero, quasi-periodic orbits can be computed on a torus surrounding the periodic solution [62]. A change in the order of instability along a family corresponds to a bifurcation. Bifurcations *can* occur without a change in order of instability, however, as is often the case with period-multiplying bifurcations.

4.4.4 Switching Families at Bifurcations

In this investigation, a modified pseudo-arclength scheme is used to continue a new family at a bifurcation. In the case of a tangent bifurcation, if the bifurcating orbit is precisely identified, the eigenvalues of the monodromy matrix will take the form $(1, 1, 1, 1, \lambda, 1/\lambda)$. The null space of $D\mathbf{F}(\mathbf{X_j^*})$ in this case is two-dimensional. One of the null space vectors, $\Delta\mathbf{X_j^*}$, is associated with continuing along the current family in a pseudo-arclength scheme; this vector points in a direction that is interpreted to be along the family. The other null space vector, denoted $\tilde{\Delta}\mathbf{X_j^*}$, points along the *new* family. If the vector $\tilde{\Delta}\mathbf{X_j^*}$ is able to be
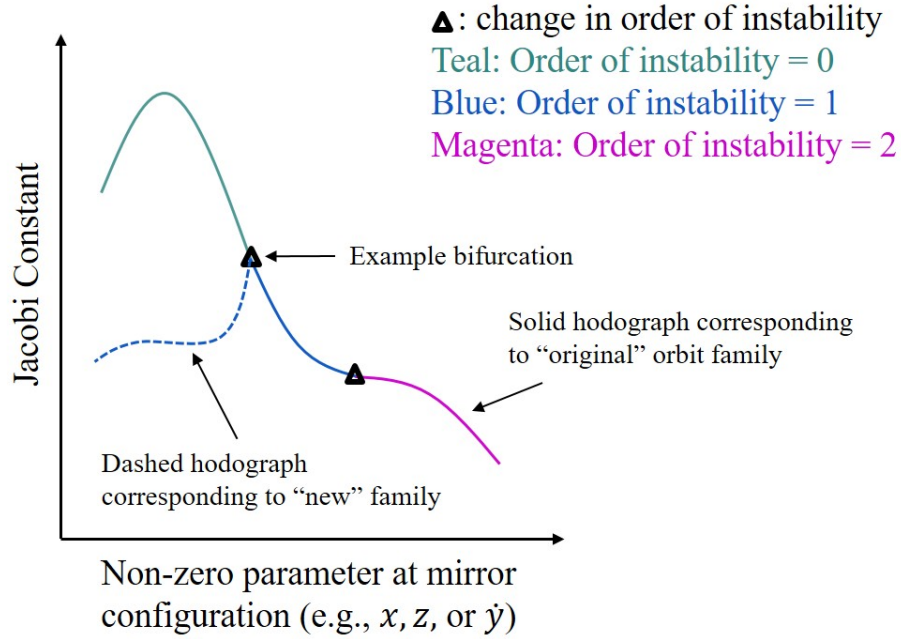
Figure 4.4. : Sample bifurcation diagram

precisely identified, it is simply substituted into the pseudo-arclength constraint, given in Equation 3.29, and the first member along the new family can be obtained using a single- or multiple-shooting differential corrections scheme. Then, the new family can be continued as normal with a natural parameter or pseudo-arclength continuation method.

In practice, however, the bifurcating orbit within a family is not identified precisely, but is located to within some reasonable tolerance. An approximation for the second dimension of the null space of $D\mathbf{F}(\mathbf{X}_\mathbf{j}^*)$, denoted the vector $\tilde{\Delta}\mathbf{X}_\mathbf{j}^*$, is used to locate the new family in the modified pseudo-arclength scheme. This approximation is provided by the right singular vectors associated with a singular value decomposition of $D\mathbf{F}(\mathbf{X}_\mathbf{j}^*)$. Let the singular value decomposition of $D\mathbf{F}(\mathbf{X}_\mathbf{j}^*) = \mathbf{U}\mathbf{S}\mathbf{V}^*$ where the '$[\,\cdot\,]^{*}$' operator indicates a complex conjugate transpose. The diagonal elements of $\mathbf{S}$ correspond to the singular values of $D\mathbf{F}(\mathbf{X}_\mathbf{j}^*)$. The *rows* of $\mathbf{V}^*$ are the right singular vectors of $D\mathbf{F}(\mathbf{X}_\mathbf{j}^*)$. In general, the right singular vectors that correspond to singular values equal to zero (or near zero) span (or approximately span) the null space of the original matrix. Identifying the second smallest singular value and the

corresponding right singular vector provides an approximation for $\tilde{\Delta}\mathbf{X}_{\mathbf{j}}^{*}$ which is then simply substituted into the pseudo-arclength constraint, given in equation 3.29. In Matlab, the `[U,S,V]=svd([·])` command provides the singular value decomposition of the matrix inside the argument. Carefully note that the returned matrix, `V`, is the complex conjugate transpose of the matrix used in the decomposition, i.e., the argument matrix, `[·]` = `U*S*V'` in Matlab. The approximation for $\tilde{\Delta}\mathbf{X}_{\mathbf{j}}^{*}$ is the *column* of `V` associated with the second smallest singular value of $D\mathbf{F}(\mathbf{X}_{\mathbf{j}}^{*})$ [63].

In the case of a period-multiplying bifurcation of multiplying factor m, the bifurcating orbit in the original, minimal period family (denoted the period-1 family) must be propagated for m revolutions prior to implementing the modified pseudo-arclength continuation scheme to find the new family. The monodromy matrix associated with the period-m orbit at the bifurcation, $\mathbf{\Phi}(t_0 + mP, t_0)$ is equivalent to the monodromy matrix of the original period-1 orbit at the bifurcation, raised to the mth power, i.e., $\mathbf{\Phi}^m(t_0 + P, t_0)$. Equivalently, the eigenvalues of the monodromy matrix of the period-m orbit are equal to the eigenvalues of the period-1 orbit monodromy matrix raised to the mth power. Thus, for m revolutions along a period-1 orbit at a bifurcation, eigenvalues associated with the period-multiplying bifurcation (of the form $\sqrt[m]{1} = \cos(2\pi/m) \pm i\sin(2\pi/m)$ when the period-1 orbit is propagated for one revolution) are instead equal to unity. A period-m bifurcation from the original family can then be treated as a tangent bifurcation from an m-revolution orbit in the original family and the modified pseudo-arclength scheme described above can be used to continue this new family. The same scheme applies to continuing period-doubling bifurcations.

5. NEAR RECTILINEAR HALO ORBITS AND NEARBY DYNAMICAL STRUCTURES

Near rectilinear halo orbits (NRHOs) are being increasingly considered for missions in cislunar space. The NRHOs are a subset of the L_1 and L_2 families of halo orbits identified by their favorable stability characteristics. Due to the stable and nearly-stable nature of the NRHOs, nearby dynamical structures in the vicinity of the orbits offer alternative means to initiate transfer design in the vicinity of these orbits. Long-duration eclipse avoidance for spacecraft in NRHOs must be considered due to thermal limitations, line-of-sight requirements, and power needs. Orbits in resonance with the lunar synodic period offer predictable geometries that, when paired with careful epoch selection, avoid the shadows of the Earth and Moon.

5.1 Near Rectilinear Halo Orbit Characteristics

The near rectilinear halo orbits are of particular interest to the exploration program. The L_2 halo family is comprised of three-dimensional orbits that originate from a tangent bifurcation along the planar Lyapunov family associated with the L_2 equilibrium point [35]. The halo family evolves out of the Earth-Moon rotating xy-plane and approaches the vicinity of the Moon. Note that the halo family is mirrored across this plane; orbits that possess a majority positive z-component are referred to as 'northern' while 'southern' members are defined by a negative z-component.

As described in Section 4.2.1, the NRHOs are defined as the subset of the halo orbits with bounded linear stability, i.e., the NRHOs are stable or nearly-stable. Thus, in the Earth-Moon system, the subset of the L_2 halo family denoted as the NRHOs is defined between the first and third members of the family that reflect stability changes in the region near the smaller primary, highlighted in maroon and purple in Figure 4.2(a) and marked with maroon and purple asterisks (*) in Figure 4.2(b). The southern L_2 halo family is plotted in

Figure 5.1; the NRHO subset of the family is highlighted in green. Note, there are L_2 halo orbits with smaller perilune radii than those in the defined NRHO region; these orbits are denoted the NRHO+ subset by Boudad et al. [64].
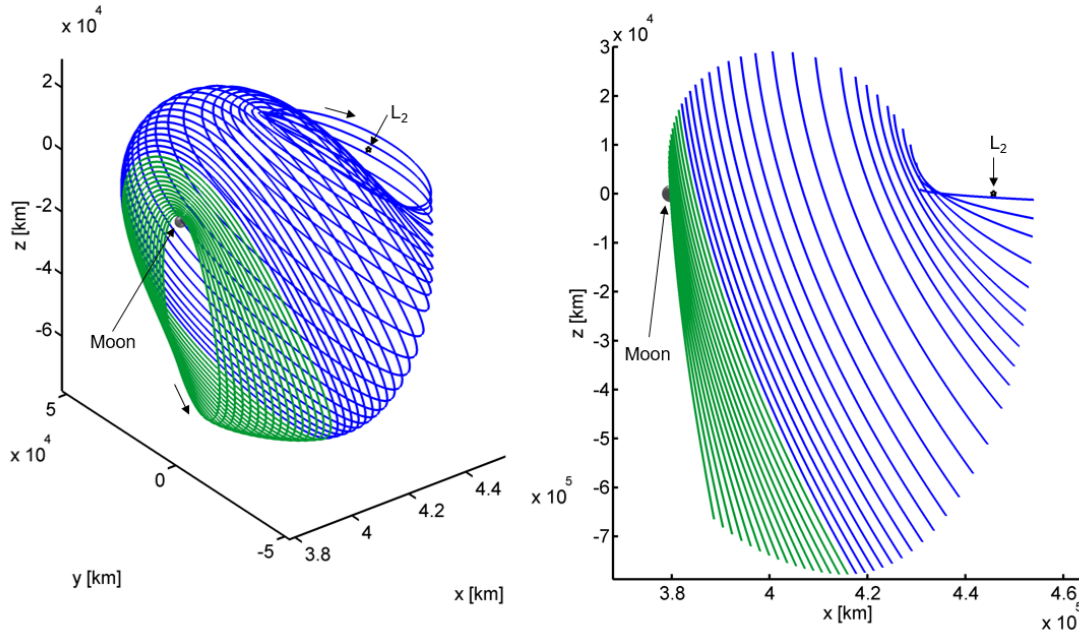
Figure 5.1. : The southern L_2 halo family in the Earth-Moon system

Characteristics of the L_2 halo family are plotted in Figure 5.2. Figure 5.2(a) depicts the Jacobi constant value versus the orbital period along the family. The NRHO subset of the family, highlighted in green, has values of Jacobi constant ranging from approximately 3.0152 to 3.0581 in the Earth-Moon system. The orbital period of the NRHOs ranges from approximately 6 days to 10.4 days. Plotted in Figure 5.2(b), halo orbits possessing perilune radii of 1832 km and 17390 km define the bounds of the L_2 NRHOs [23]. Finally, the z-amplitude of the halo family is plotted in Figure 5.2(c). The z-amplitude is computed by subtracting the minimum z-component along the orbit from the maximum z-component. The z-amplitudes along the NRHO subset of the L_2 halo family ranges from 68670 km to 95050 km.

(a)

(b)

(c)
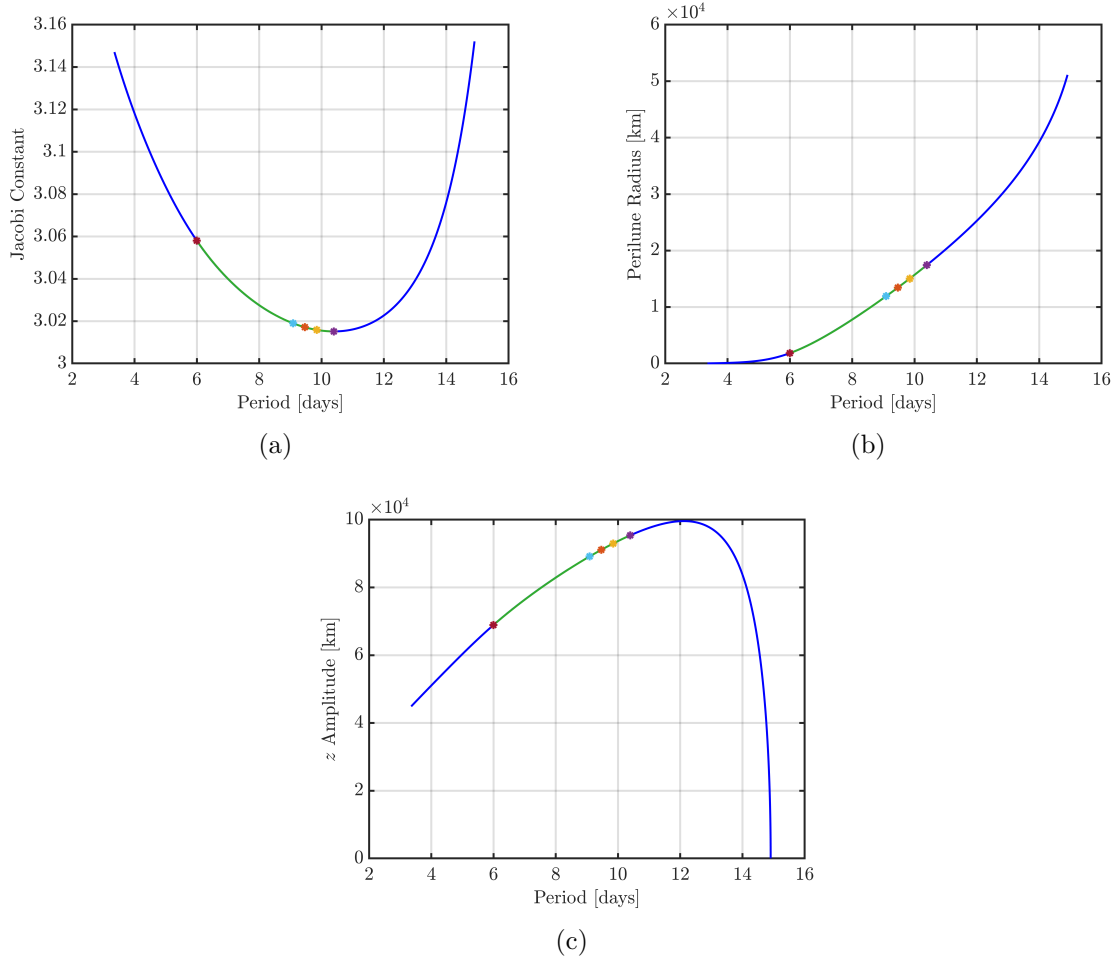
Figure 5.2. : Characteristics of the L_2 halo family; the NRHO subset is highlighted in green

5.1.1 How Big is an NRHO?

Generations of humans have been driven to look up at the night sky and wonder about the celestial objects it holds. As interest in cislunar orbits, particularly the NRHO, is piqued, this orbit's apparent size in the night sky is a natural inquiry. Figure 5.3 depicts a 4:1 synodic resonant NRHO, an NRHO with a z-amplitude of approximately 78900 km, at a size that is approximately to scale as viewed from West Lafayette, IN at 12:30 AM Eastern Time on October 16, 2019. Since the Earth is rotating and the Moon is orbiting about the Earth, the orbit would *not* appear fixed in the sky, but at an instant, if the Earth-Moon

rotating x-axis is considered to pass through the viewer's eyes, the orbit is superimposed on the Midwestern night sky.

4:1 Synodic Resonant NRHO
Approximately to scale
Viewed from West Lafayette, IN 12:30 AM
on October 16, 2019
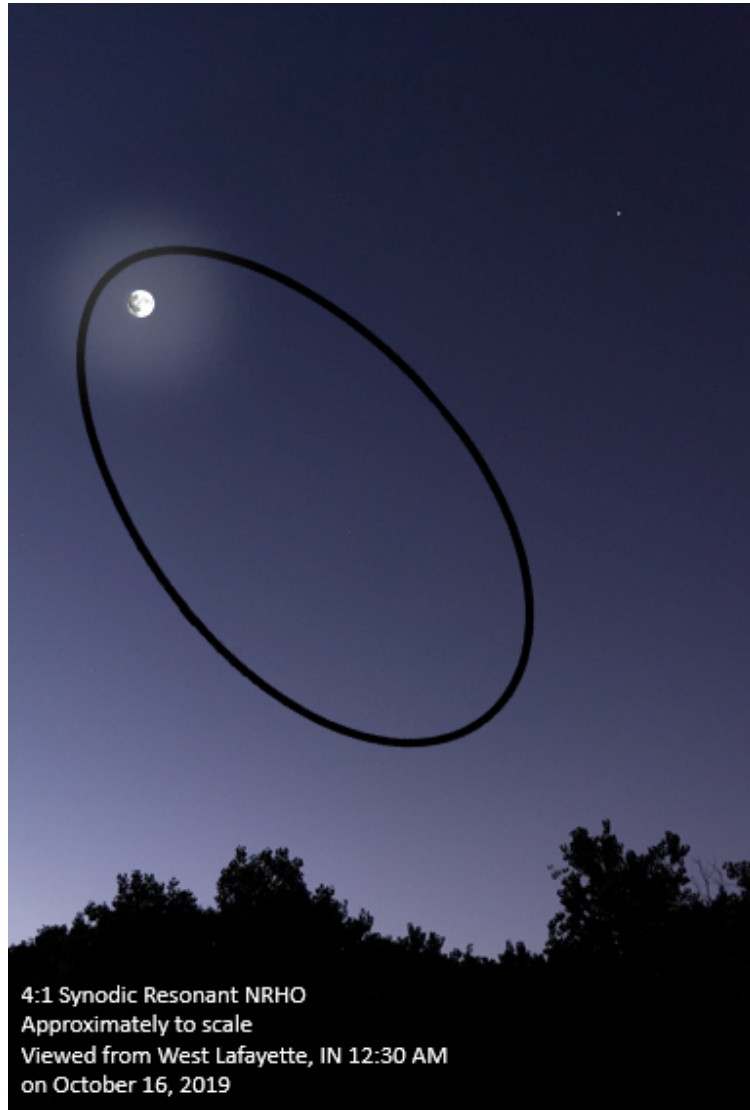
Figure 5.3. : CR3BP 4:1 NRHO as seen by an observer in West Lafayette, IN

Next, to better illustrate the size of the NRHO, it is compared to a few familiar objects. The NRHO in Figures 5.4 to 5.7 possesses a z-amplitude of 75000 km, a perilune radius of about 3930 km, and an orbital period of approximately 6.8 days. The amplitude of this particular L_2 NRHO is about 0.54 times the diameter of Jupiter or 5.89 times the diameter of Earth. This comparison is apparent in Figure 5.4. Based on the average distance
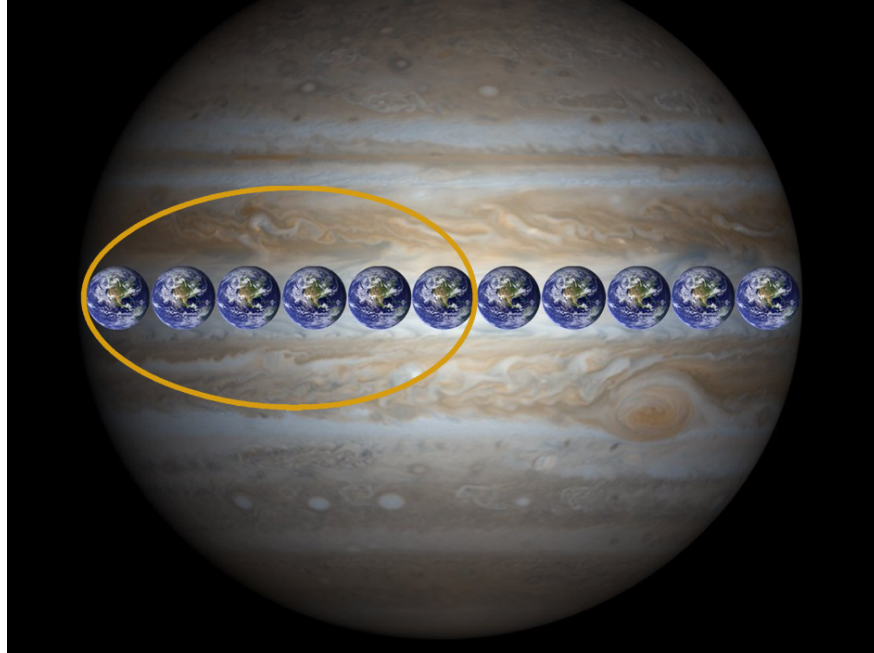
Figure 5.4. : 75000 km z-amplitude NRHO as compared to the scale of Jupiter and Earth

between the Earth and the Moon, approximately 5.1 NRHOs could fit between the Earth and the Moon if the orbits were aligned along their z-axes, as depicted in Figure 5.5. As a
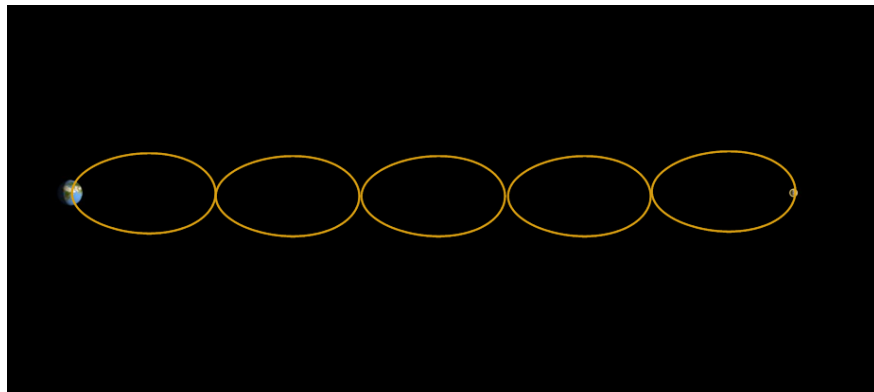
Figure 5.5. : 75000 km z-amplitude NRHO as compared to the scale of the Earth-Moon distance

different point of comparison, the longest line across the contiguous United States of America (that does not intersect the Atlantic Ocean, Pacific Ocean, or the Gulf of Mexico) is 2802 miles long [65]. Based on the spherical straight-line distance of this "ultralineamentum," the United States could fit along the z-amplitude of the NRHO approximately 16.6 times. A

depiction of the ultralineamentum in gnomonic coordinates and the NRHO with maps of the United States superimposed on it is depicted in Figure 5.6. Finally, in a more intuitive and
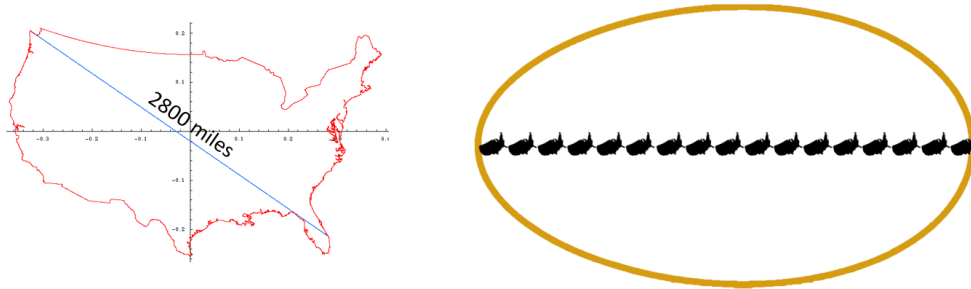
Figure 5.6. : 75000 km z-amplitude NRHO as compared to the scale of the longest straight line drawn across the contiguous United States of America [65]

tangible exercise, assuming the length of a large Mallard duck is 26 inches, approximately 113,567,534 Mallard ducks could fit along the z-axis of an NRHO [66]. This number is more than 12.2 times the number of Mallard ducks in all of North America in 2018 [67]. This concept is illustrated in Figure 5.7.
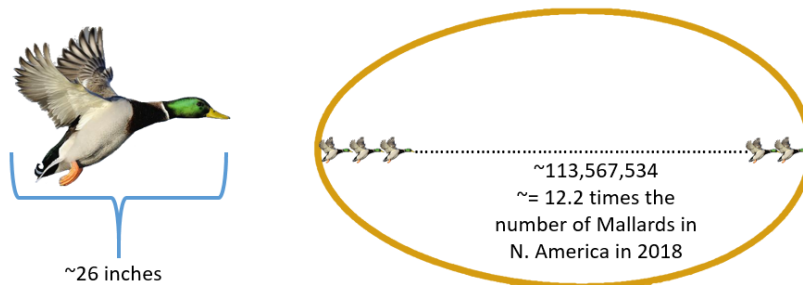
Figure 5.7. : 75000 km z-amplitude NRHO as compared to the scale of a large Mallard duck [66], [67]

5.1.2 How Fast is an NRHO?

Two particular NRHOs of interest to the NASA Gateway mission, the 4:1 and 9:2 lunar synodic resonant NRHOs, are used to illustrate the orbital speed along this subsection of the L_2 halo family. Lunar synodic resonance is described in detail in Section 5.3.2; these

particular orbits are simply sample NRHOs selected for illustration purposes here. Figure 5.8 depicts these sample CR3BP orbits in the Earth-Moon rotating frame; the 4:1 NRHO is plotted in blue and the 9:2 NRHO is plotted in green. The orbital periods of the 4:1 and 9:2 synodic resonant NRHOs are 7.375 and 6.556 days, respectively. The region along the orbits highlighted in red in Figure 5.8 depicts the portion of the orbit that possesses lunar north pole visibility, or an Earth-Moon rotating frame z-coordinate greater than the radius of the Moon. The Moon-centered inertial frame velocity and Earth-Moon rotating
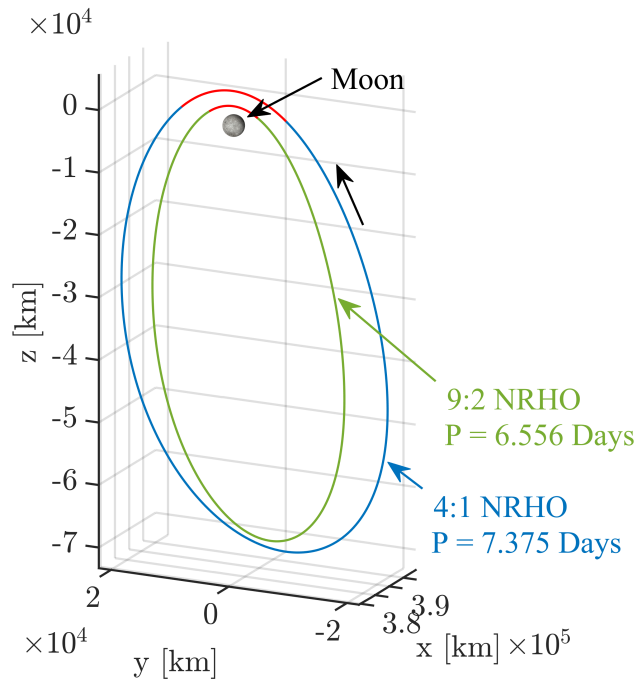
Figure 5.8. : CR3BP 4:1 and 9:2 NRHOs in the Earth-Moon rotating frame

frame velocity of a spacecraft moving along the 4:1 and 9:2 NRHOs is plotted in Figure 5.9. The colors of the curves correspond to the colors of the orbits in Figure 5.8. The portion of the plot that corresponds to the locations along the trajectories with lunar north pole visibility are plotted in red. The largest magnitude velocity along the orbits (at perilune passage) is labeled on each plot. The 9:2 NRHO reaches a maximum speed of 1.73486 km/s in the rotating reference frame and 1.73440 km/s in the Moon-centered inertial frame. The 4:1 NRHO, on the other hand, achieves a maximum velocity magnitude of 1.28658 km/s in the Moon-centered inertial frame, or equivalently, 1.28735 km/s in the Earth-Moon rotating

frame. Since the perilunes along these southern orbits coincide with lunar north pole passage,
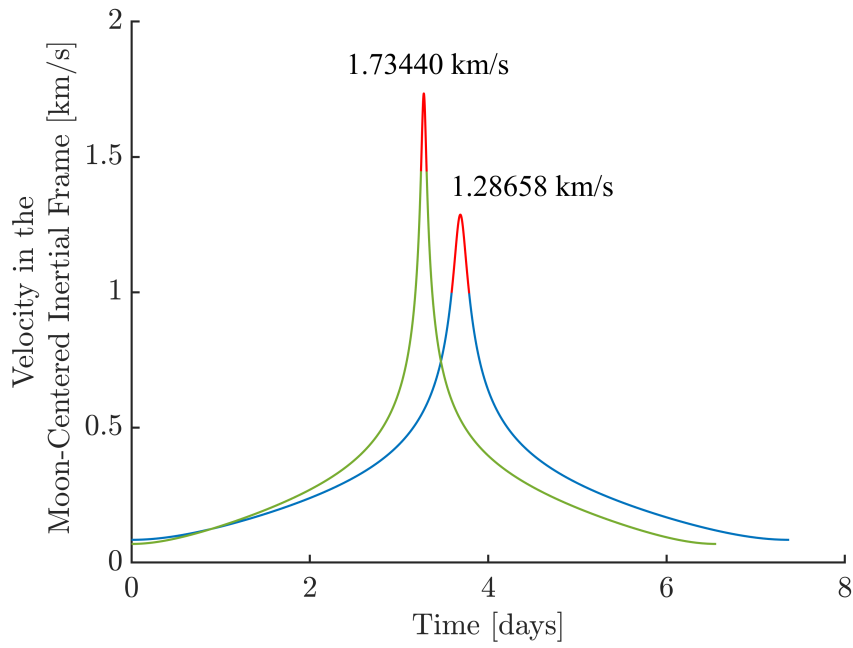
(a) Moon-centered inertial velocity
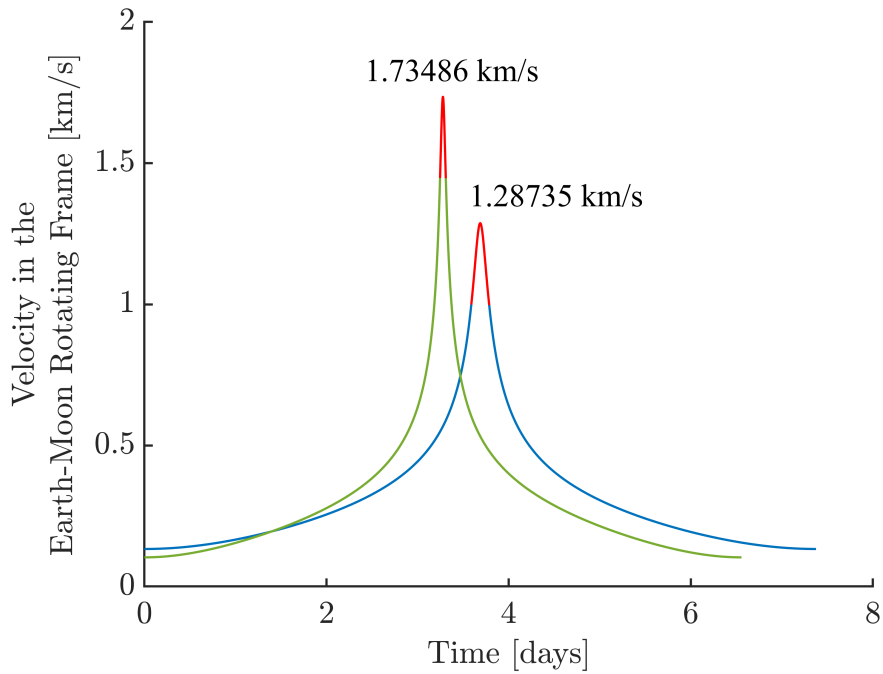
(b) Earth-Moon rotating frame velocity

Figure 5.9. : Velocity along the CR3BP 4:1 and 9:2 NRHOs

a spacecraft in an NRHO is moving quite rapidly along this portion of the trajectory. A spacecraft in a 4:1 NRHO spends 4.72 hrs or 2.67% of the orbit with north pole visibility while the a spacecraft in a 9:2 NRHO spends only 1.52 hrs or 0.96% of the orbit with north pole visibility.

It is interesting to approximate the circular orbit speed at the perilune altitude along the 9:2 and 4:1 NRHOs. This speed is then be used to subsequently estimate the required Δv required to circularize the NRHO about the Moon using a tangential maneuver when the spacecraft is at perilune. Using the Keplerian expression for circular orbit velocity for a given semi-major axis, $v_{circular} = \sqrt{\tilde{G}m_{Moon}/r_p}$, the necessary orbit velocity is computed. In this expression, $\tilde{G}$ is the dimensional gravitational constant, m_{Moon} is the dimensional mass of the Moon, and r_p is the semi-major axis of the desired circular orbit (equivalent to the perilune radius along the NRHO of interest), the Keplerian circular orbit velocity can be computed. A circular orbit that possesses a semi-major axis equal to the perilune radius along the 9:2 NRHO (approximately 3150 km) has an orbital velocity of approximately 1.25 km/s. The circular orbit corresponding to the 4:1 NRHO perilune radius (approximately 5600 km) has a lower orbital velocity at approximately 0.935 km/s. To circularize the 9:2 and 4:1 NRHOs, assuming a tangential maneuver in the anti-velocity direction, the circular orbit velocity is subtracted from the inertial velocity at the NRHO perilune. Thus, to circularize the 9:2 NRHO, approximately 0.484 km/s of Δv is required; circularizing the 4:1 NRHO requires approximately 0.353 km/s of Δv.

5.2 Identification of Nearby Dynamical Structures

As an alternative to the use of stable and unstable manifolds for trajectory design into and out of stable (or nearly stable) periodic orbits, unstable structures that exist nearby the original orbit, in terms of both energy and geometry, may be available for departing from and arriving to the vicinity. These unstable structures may themselves possess manifolds that offer application to trajectory design. To identify nearby periodic orbit families that may offer useful flows through the region, an examination of structures that exist in the

vicinity of the orbit of interest is a logical next step; the framework for this investigation is based on the identification and exploration of bifurcations in the region.

In Figure 5.10, a black curve is plotted on a Broucke stability diagram that corresponds to the L_2 halo family (specifically, the NRHO region). An arrow indicates the direction of increasing perilune radius. In this figure, colored asterisks (*) reflect the family members that correspond to bifurcations. Additionally, asterisks of the same color mark these family members in Figures 4.2(b) and 5.2 and the orbits are also traced in the corresponding colors in Figure 4.2(a). To easily recognize these bifurcating orbits and the
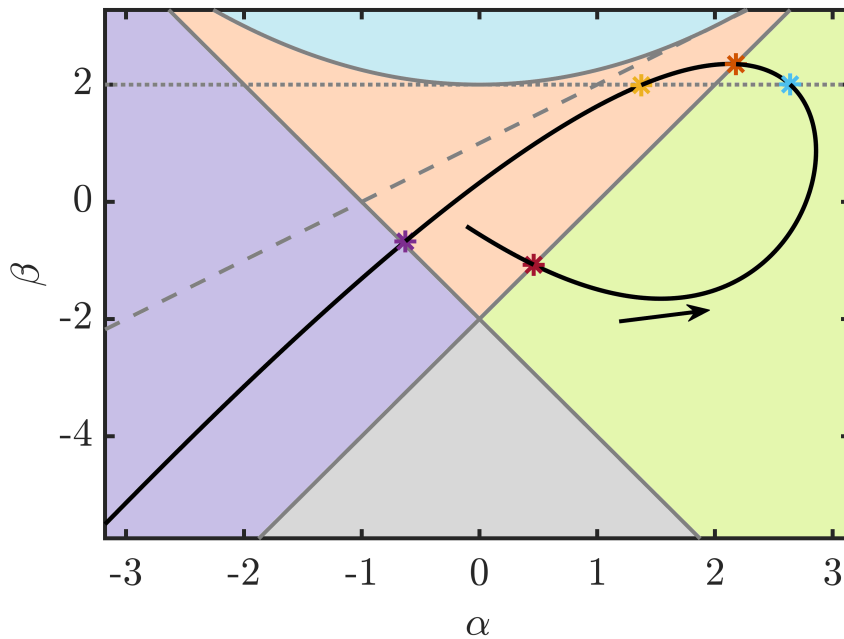
Figure 5.10. : L_2 NRHO Broucke stability diagram

corresponding families to which they belong, a naming convention for these new families is necessary. For period-multiplying bifurcations (and the resulting higher-period families) the naming format is defined: 'Pm[originating family]$_n$', where 'Pm' refers to the order of the period-multiplication (e.g., period-doubling is reflected as m = 2), '[originating family]' refers to the family from which the bifurcating family has evolved (e.g., 'HO' refers to halo orbits), and 'n' denotes a sub-family identifier (i.e., for multiple bifurcations of the same type, the first family, in order of increasing perilune radius, is labeled n = 1, the second

family is labeled n = 2, and so on). New families that originate from tangent bifurcations or Hopf bifurcations are named in accordance with a unique characteristic of the family and the 'n' sub-family identifier is maintained if necessary. The bifurcations (and the bifurcating families) across the NRHO region, in order of increasing perilune radius, are delineated in Table 5.1.

Table 5.1. : Bifurcations across the NRHO region in the halo family and the corresponding new orbit families in order of increasing perilune radius

Color	Bifurcation Type	Name of New Family	Other Useful Information
Maroon	Period-Doubling	$P2HO_1$	Also denoted the butterfly family
Blue	Period-Quadrupling	$P4HO_1$	
Orange	Period-Doubling	$P2HO_2$	
Gold	Period-Quadrupling	$P4HO_2$	
Purple	Tangent (Cyclic Fold)	N/A	No new family originates at a cyclic fold bifurcation

Employing a multiple-shooting, pseudo-arclength continuation scheme, the new families of periodic orbits originating at each of these bifurcations are computed. In Figures 5.11 through 5.15, the families originating from the NRHO bifurcations are plotted (and colored by Jacobi constant) along with the stability index values versus orbital period along the families. A black arrow indicates the direction of motion along each member of the family. One orbit within each family is highlighted in green to aid in illustrating the geometry of each unique family. Initial conditions for these families of periodic orbits, as well as initial conditions corresponding the the L_2 halo family, are available in the Appendix in Tables A.1 to A.5. In Figure 5.17, a member from each of these new families is computed in the CR3BP and plotted in orange in the Earth-Moon rotating frame to illustrate their complex multi-revolution geometries along with their unique and distinct characteristics. In each plot in Figure 5.17, an NRHO with an identical Jacobi constant value is plotted in blue, the Moon appears as a grey sphere, and the direction of motion along the trajectories is indicated by a colored arrow. Along each trajectory, the closest point to the Moon is marked with an asterisk. Note that, in each example, the southern orbits (or the segment of the

family/family member that possesses motion primarily below the xy-plane) are plotted. In each case, a northern analog also exists.

A range of orbits in the P2HO$_1$ family is plotted in Figure 5.11. This family, often termed the butterfly family, is characterized by two lobes in a "figure-8" shape, one on the L_1 side of the Moon and one on the L_2 side [17], [38]. A distinct advantage for periodic orbits in this family is the ability to access both the L_1 and L_2 sides of the Moon using natural ballistic motion. Note that the loop structures that appear in the plot of stability index versus orbital period in Figure 5.11(a) represent Hopf bifurcations. In Figure 5.17(a), an individual P2HO$_1$ orbit is plotted in orange along with an NRHO of the same Jacobi constant value ($JC = 3.047087$) in the Earth-Moon rotating frame. Similar orbital motion in the vicinity of the smaller primary in the Sun-Jupiter CR3BP is documented as early as 1980 by Robin and Markellos [68]; the butterfly family is investigated by Grebow et al. in 2006 for applications to lunar south pole coverage [69].

The P4HO$_1$ family appears in Figure 5.12. Note that, at the furthest extent of the family in Figure 5.12(b), the members with the lowest Jacobi constant values and the longest orbital periods possess multiple passes inside the lunar radius. This property could prove useful in lunar lander or impactor missions. Orbits in this family additionally offer the ability to adjust the orbital plane using natural motion; along certain family members, some portions of the orbit exist in the vertical yz-plane while other segments along the same orbit approach a more horizontal motion. A member of the P4HO$_1$ family is plotted in Figure 5.17(b) along with an NRHO at the same Jacobi constant value in the Earth-Moon rotating frame. In the P2HO$_1$ orbit plotted in Figure 5.17(b), there are two lunar passages that both possess the same minimum altitude–both passages are marked.

The characteristics of orbits in the P2HO$_2$ family are illustrated in Figure 5.13. In contrast to the other higher-period families that bifurcate from the NRHO region, this family continues smoothly into its northern counterpart passing through the xy-plane (similar to the northern and southern portions of the halo orbit families that continue through planar Lyapunov orbits). The portion of the family plotted here reaches a fully planar member.

(a)

(b)

(c)
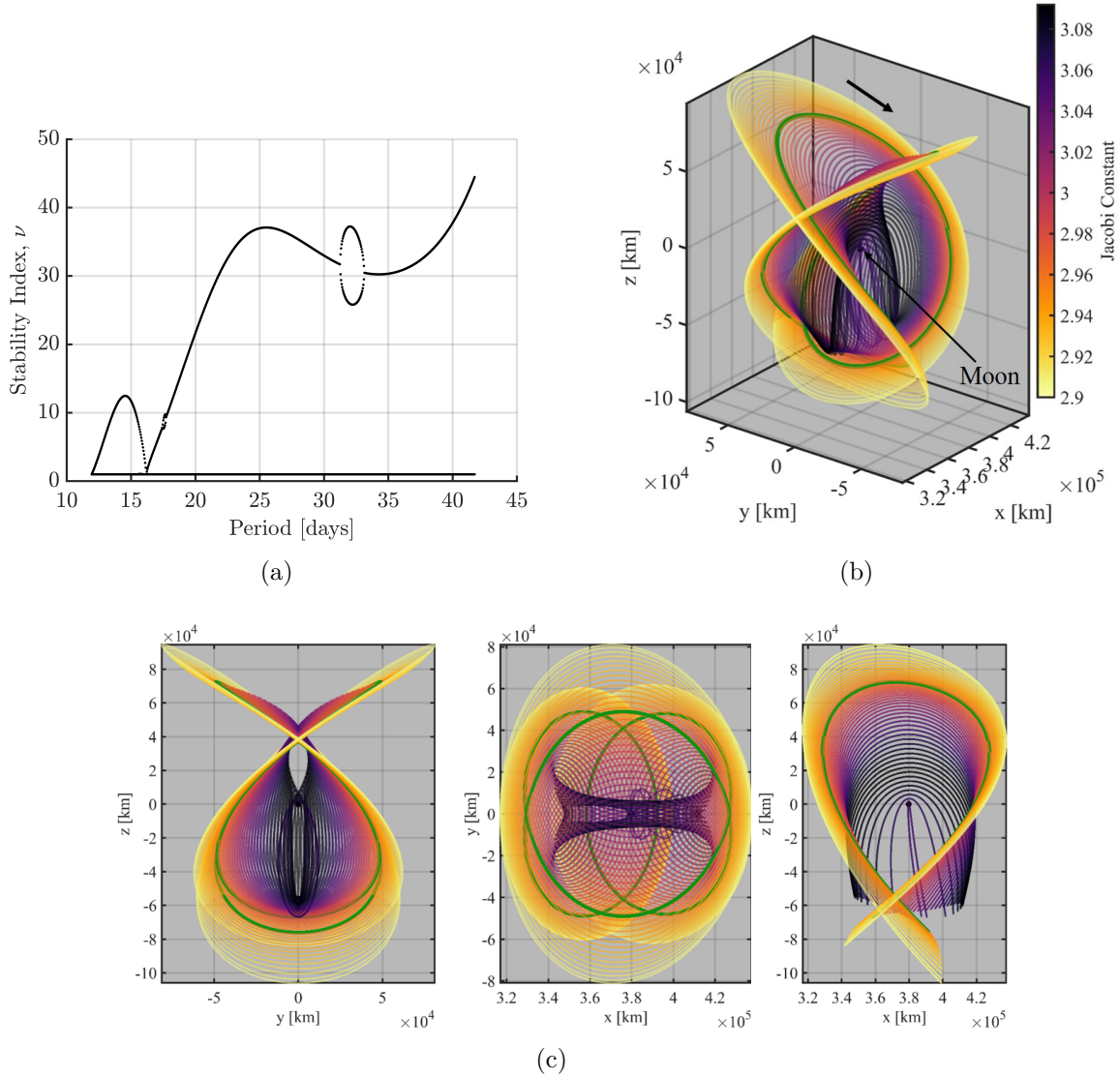
Figure 5.11. : P2HO$_1$ (butterfly) orbit family

Although the P2HO$_2$ orbits possess periods approximately double the period of the NRHOs, the P2HO$_2$ family does not offer access to both the L_1 and L_2 sides of the Moon, as do members of the P2HO$_1$ family, rather, the P2HO$_2$ orbits offer access in an "East-West" type motion–which may offer utility in certain scenarios. This motion is demonstrated in Figure 5.17(c) where an individual P2HO$_2$ is plotted along with an NRHO that shares the same Jacobi constant value.
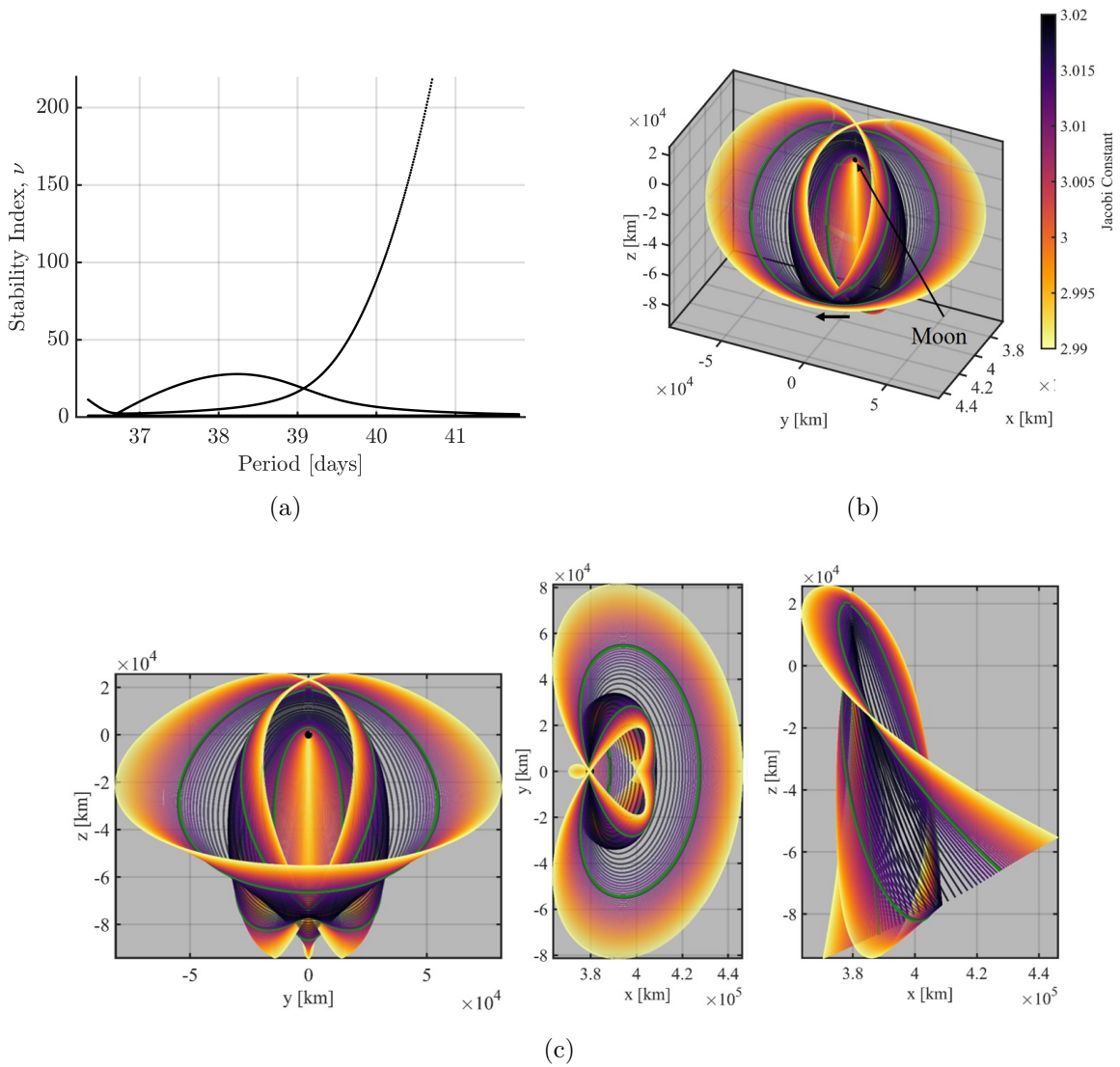
Figure 5.12. : P4HO$_1$ orbit family

Motion that appears to share characteristics with the P2HO$_2$ orbits has been demonstrated by other authors indicating that these orbits may offer a fundamental pathway nearby the NRHOs; two examples are plotted in Figure 5.14. In Figure 5.14(a), lunar impact trajectories are computed in the CR3BP. In Figure 5.14(b), a disposal trajectory from a 9:2 synodic resonant L_2 NRHO is plotted in the Earth-Moon rotating frame. Although not confirmed, it appears as though these trajectories utilize dynamical structures associated with the P2HO$_2$ orbit family.
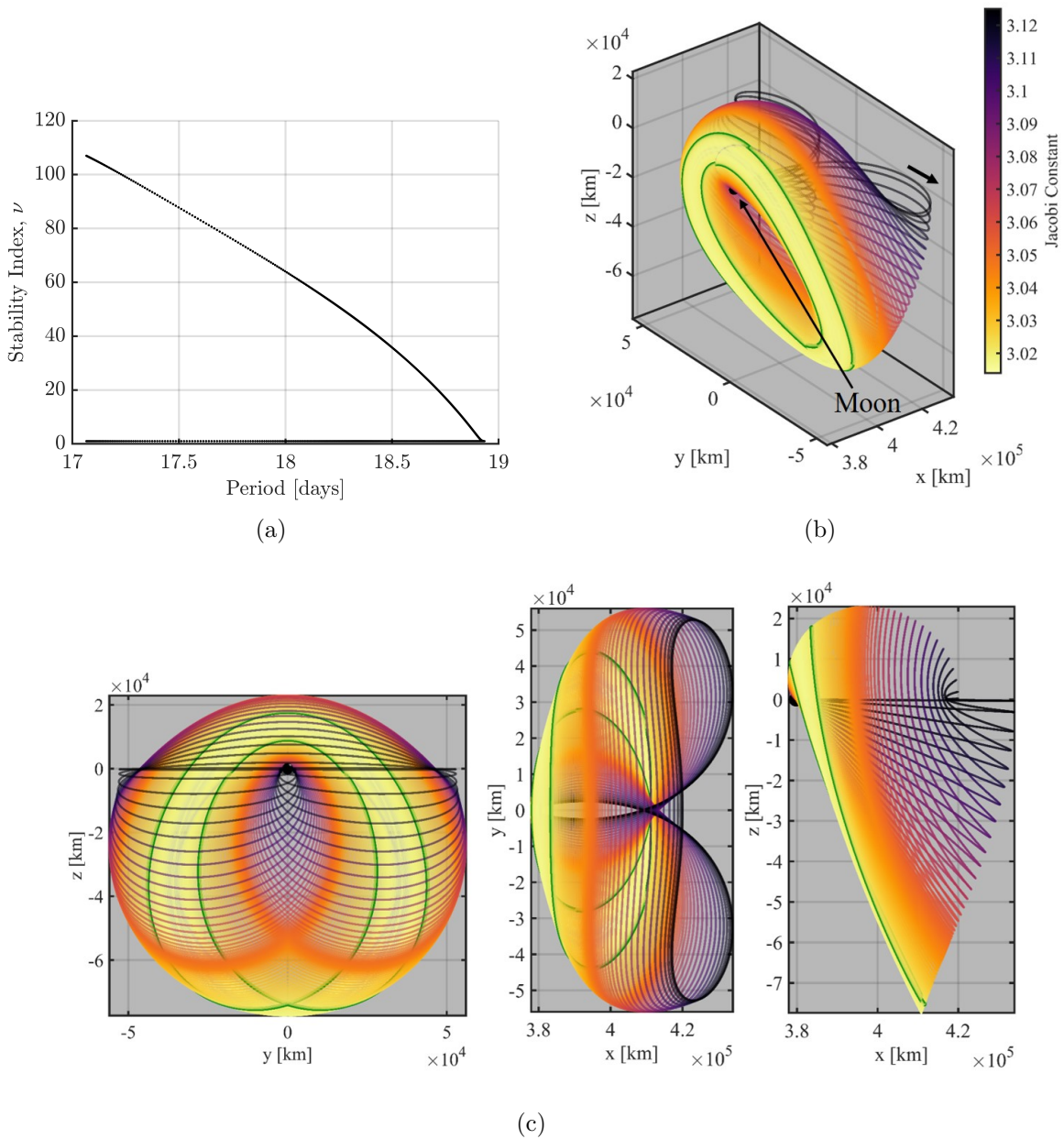
Figure 5.13. : P2HO$_2$ orbit family

Finally, a portion of the P4HO$_2$ family of orbits is plotted in Figure 5.15. The extent of this family is quite large and extends well beyond the range in Figure 5.15(b). While some of the larger members of this family offer exotic motion that evolves both perpendicular to and within the orbital plane (not pictured here), smaller members more closely approximate NRHO-like motion, albeit, with four lunar passes per period instead of one. In 2019, man-

(a) Lunar impactor trajectories from Reference [70]

(b) NRHO disposal trajectory from Reference [37]
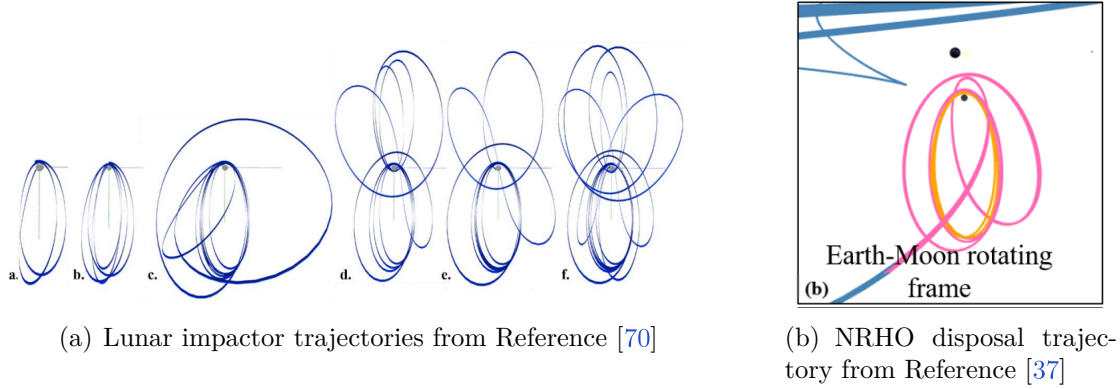
Figure 5.14. : Sample geometries found in literature that relate to the P2HO$_2$ orbit family

ifolds from the P4HO$_2$ orbits were observed to offer lunar access [71]. A member of the P4HO$_2$ family with a Jacobi constant value of 3.0168 is plotted in Figure 5.17(d) along with an NRHO at the same energy level.

Smaller members of the P4HO$_1$ and P4HO$_2$ families appear similar when plotted in configuration space and difficulties identifying to which family an orbit belongs can arise. As a note of comparison, when viewed in an xz-projection, the P4HO$_1$ orbit (plotted in light blue in Figure 5.16) appears to enclose the Moon twice, while the P4HO$_2$ orbit (plotted in orange in Figure 5.16) does not appear to enclose the Moon at all.

The larger magnitude of the stability index across each of these higher-period halo orbit families indicates that departure/arrival along an unstable/stable manifold is more rapid than the equivalent departure/arrival along an NRHO manifold. Since it is likely that an asset will remain in an NRHO, a departure that requires fewer revolutions to depart is desirable as it lessens the chances for recontact. Leveraging any structures (or orbits) that may exist in the lunar vicinity with smaller time constants can be beneficial. Additionally, since there are likely to be time-of-flight limitations for upcoming missions, short transfer times are also desirable.

A bifurcation diagram illustrating the connections between the NRHO region of the L_2 halo family and the nearby higher-period orbits is plotted in Figure 5.18. Changes in
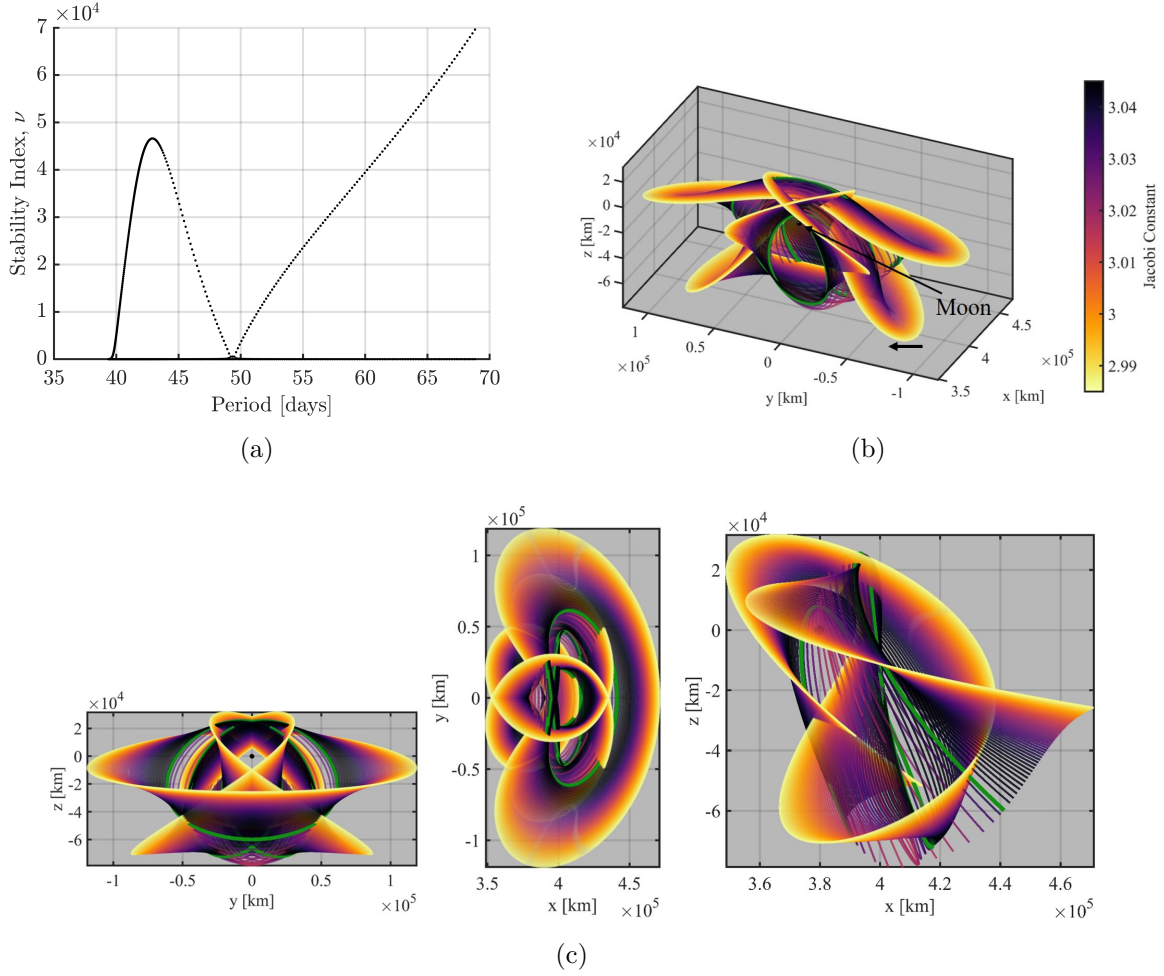
Figure 5.15. : P4HO$_2$ orbit family

the order of instability are marked by black triangles. The color of the curve corresponds to the number of unstable modes, i.e., a teal-colored curve corresponds to a solution with zero unstable modes (a stable orbit), a blue-colored curve corresponds to a solution that possesses one unstable mode, while a magenta-colored curve corresponds to a solution that has two unstable modes. The plot on the right that is framed in orange corresponds to a zoomed-in portion of the bifurcation diagram which is also marked on the left-hand plot. A solid curve corresponds to the hodograph of the L_2 halo family while the dashed curves correspond to the labeled higher-period orbit families. Note that the bifurcations to the period-quadrupled families (the P4HO$_1$ and P4HO$_2$ families) are not marked by triangles along the halo orbit family hodograph due to the fact that there is not a stability change at these bifurcations.
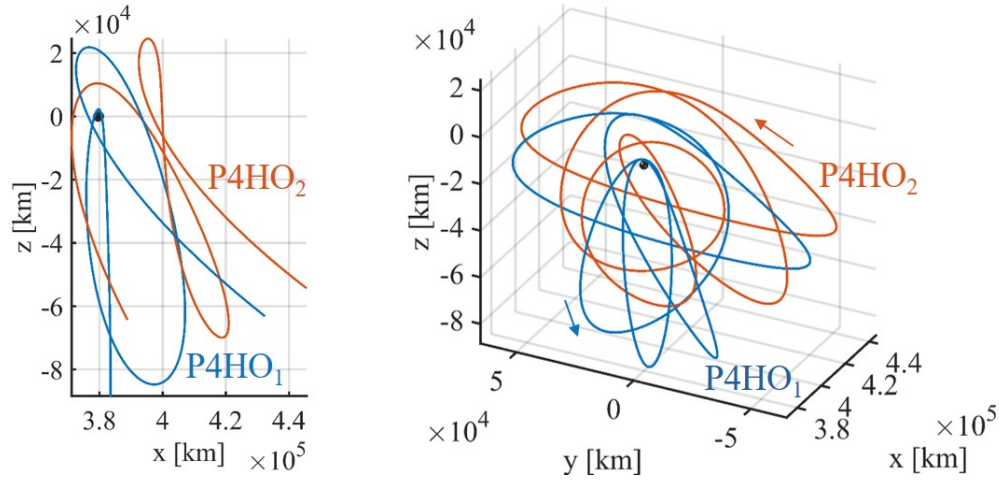
Figure 5.16. : Illustration of geometry difference between smaller members of the P4HO$_1$ and P4HO$_2$ orbit families

There is also a stability change (and tangent bifurcation) along the halo family corresponding to a minimum in Jacobi constant value–there is no new family that originates here since it is a cyclic fold type bifurcation. There are many order of instability changes (and therefore, bifurcations) along each of the hodographs corresponding to the higher-period orbit families.

The bifurcations along the higher-period families are also visible in the Broucke stability diagrams plotted in Figure 5.19. Black curves in these diagrams represent (α, β) pairs that evolve with the members of each of the orbit families. Also plotted in each subfigure are a series of colored curves that divide the stability diagram into regions that each possess particular orientations of the eigenvalues of the monodromy matrix. As the black curve intersects and evolves through the separate regions on the Broucke stability diagram, bifurcations occur. The blue parabola is the curve $\beta = \frac{\alpha^2}{4} + 2$; values of α and β that satisfy this equation correspond to secondary Hopf bifurcations. The yellow line represents $\beta + 2 = -2\alpha$ and passage through this boundary corresponds to the occurrence of a tangent bifurcation. Next, the orange line represents $\beta + 2 = 2\alpha$ which corresponds to period-doubling bifurcations. The green line corresponds to the equation $\beta = \alpha + 1$ and the horizontal purple line corresponds to $\beta = 2$; these curves correspond to eigenvalue orientations that yield period-tripling and period-quadrupling bifurcations, respectively. The bifurcations and the resulting periodic
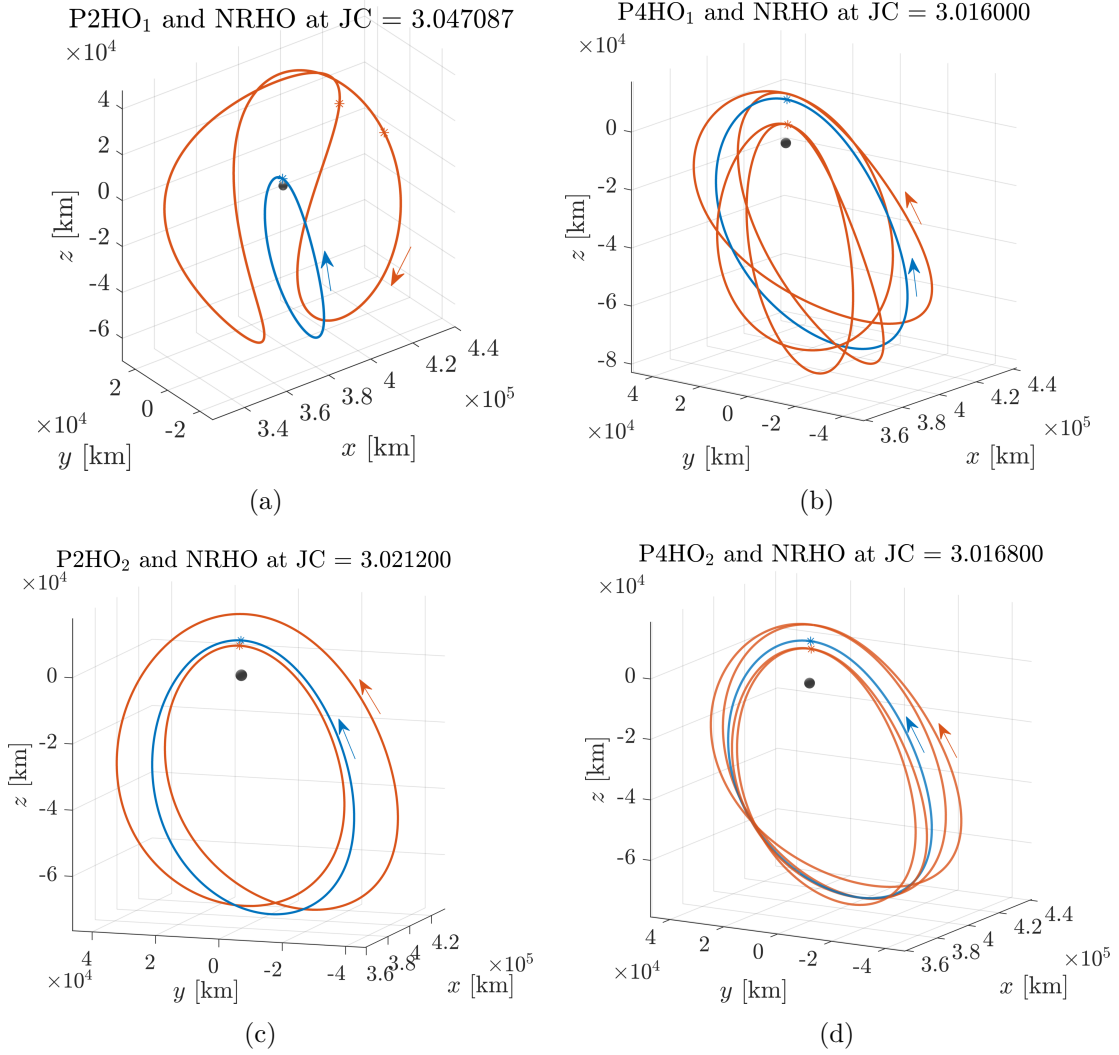
Figure 5.17. : Select members from each of the higher-period families that bifurcate from the NRHOs computed in the CR3BP and plotted in the Earth-Moon rotating frame
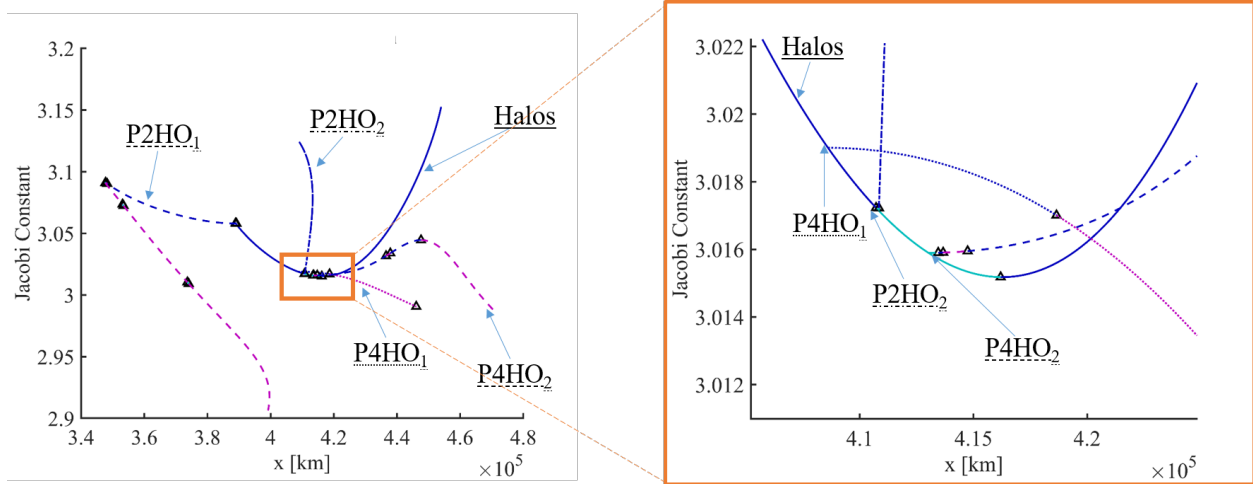
Figure 5.18. : NRHO bifurcation diagram

orbit families that evolve from these bifurcations may offer utility to transfer design in the cislunar regime, however, solving for these families is beyond the scope of this investigation.

5.3   Eclipse Avoidance Using Resonance Properties

Mission constraints due to limitations on the spacecraft thermal environment and direct line-of-sight to Earth dictate allowable eclipse durations and frequencies [72], [73]. Additionally, power requirements constrain the maximum time span for eclipsing events. Spacecraft in and nearby NRHOs are subject to both Earth eclipse and lunar eclipse conditions due to their proximity to both of these primary bodies. The NRHOs offer favorable eclipse avoidance properties due to their primarily out-of-plane orientation; the majority of the orbital motion is not coincident with the shadows of the Earth or Moon. However, duration of any passage through shadows must still be managed carefully.

5.3.1   Resonance Properties

Orbital resonance is an important consideration for meeting eclipse constraints. NRHOs and nearby orbits that are in resonance with the synodic period of the Moon are most often

(a) P2HO$_1$ Family

(b) P4HO$_1$ Family

(c) P2HO$_2$ Family

(d) P4HO$_1$ Family
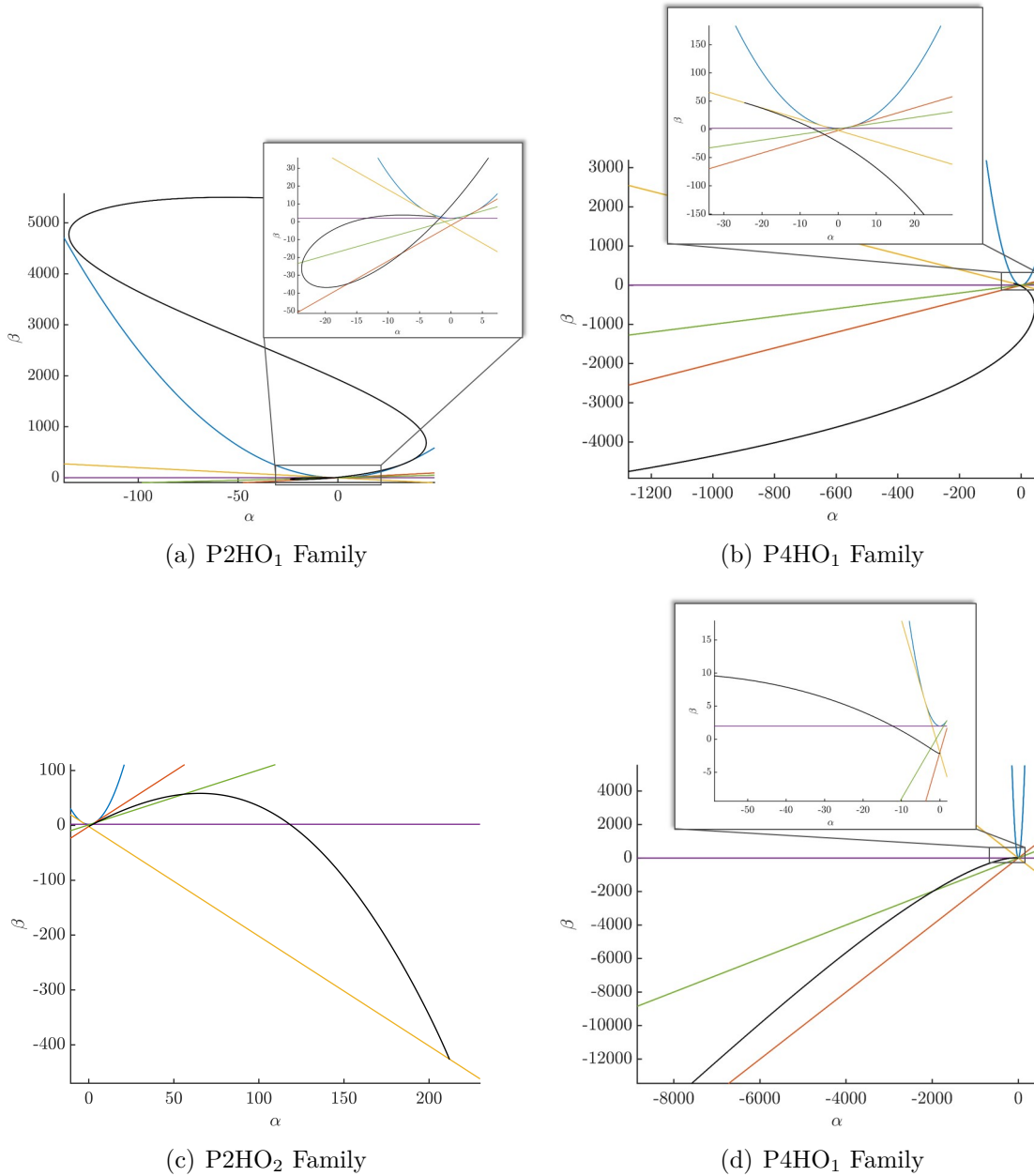
Figure 5.19. : Broucke stability diagrams for each of the higher-period orbit families nearby the NRHOs

selected for applications due to the fact that avoiding and/or predicting eclipses is important to future missions. Resonance in terms of the synodic period is defined as the time between successive conjunctions of a celestial body with the Sun, i.e., the time required for the Earth-Moon-Sun orientation to repeat. In this case, a viewer fixed at the center of the

Earth would see the Moon return to the same location with respect to the Sun after one synodic period of the Moon, however, the Moon would *not* appear in the same location to an observer in an inertial frame fixed at the center of the Earth. The Moon's synodic period is approximately 29.5 days, slightly longer than its sidereal period (approximately 27.3 days). The synodic period is also denoted as a lunar month since the full lunar cycle (i.e., time between successive full Moon phases) requires one synodic period to complete. A diagram illustrating the synodic and sidereal periods of the Moon is included in Figure 5.20.

Time = +29.5 days (Lunar Synodic Period)
Earth-Moon-Sun orientation has repeated

Time = +27.3 days (Lunar Sidereal Period)
Earth-Moon orientation has repeated

Time = 0: Start Orientation
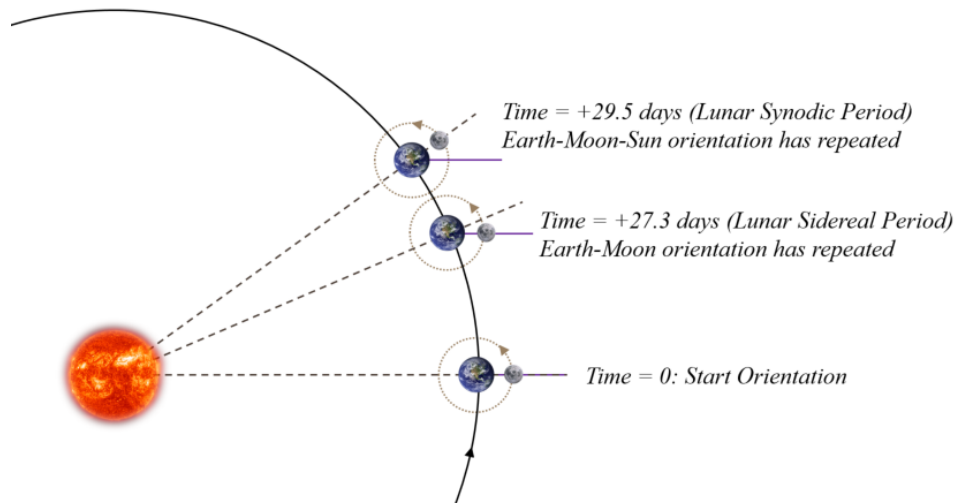
Figure 5.20. : Sidereal and synodic periods of the Moon

Orbital resonance is defined in terms of a p:q ratio, where p indicates the number of completed revolutions of a given periodic orbit over q periods of the Moon. The value of p divided by q must be positive and rational, i.e., both p and q can be written as positive integers. As an example of orbital resonance, a 4:1 synodic resonant NRHO possesses a period of approximately 7.375 days such that four revolutions of the spacecraft in this orbit can be completed over the duration of one synodic period of the Moon ($7.375 * 4 = 29.5$). A 9:2 synodic resonant NRHO possesses a period of approximately 6.556 days such that nine revolutions along this orbit are completed over two synodic periods of the Moon. Figure 5.21 illustrates the 9:2 synodic resonant NRHO (plotted in orange) and the 4:1 synodic resonant NRHO (plotted in blue) computed in the CR3BP and plotted in the Earth-Moon rotating

frame, the Moon-centered inertial frame, the Sun-Moon rotating frame, and the Sun-Earth rotating frame. In the inertial frame, these orbits do *not* appear as conics and are not periodic; note the shifting of the ascending node over each revolution. In the Sun-Moon and Sun-Earth rotating frames, gaps in the trajectory appear between the lobes of the orbit; in these frames, the geometry of p:q synodic resonant orbits repeats after q synodic periods. In Figure 5.22, the p:1 and p:2 synodic resonances for various L_2 halo orbits, as computed in the CR3BP, are plotted as a function of perilune radius.

5.3.2   Synodic Resonance and Eclipse Avoidance in the NRHOs

Some noteworthy NRHOs include the 9:2 and 4:1 synodic resonant orbits [72]. The 9:2 synodic resonant NRHO, which possesses a perilune radius of approximately 3150 km and a period of about 6.556 days in the CR3BP, is currently selected as the baseline for NASA's Gateway architecture [74]. The 4:1 synodic resonant NRHO possesses a slightly higher perilune radius of 5600 km in the CR3BP. Due to the resonance properties of these orbits, epochs are available that avoid both Moon and Earth eclipses over long durations. The geometry of synodic resonant orbits in the Sun-Moon and Sun-Earth rotating frames helps illustrate the eclipse avoidance properties of resonant orbits. In each of these rotating frames, the shadow of the smaller body (i.e., the Moon or Earth) remains fixed along the respective positive x-axis. In these frames, the yz-projection of the trajectory is equivalent to a view looking along the shadow of the smaller primary. Note that additional plots and data regarding the 4:1 and 9:2 lunar synodic resonant L_2 southern NRHOs are available in Appendix C.

Transitioning a periodic orbit to an ephemeris model from the CR3BP presents challenges in maintaining favorable geometry, especially for eclipse avoidance purposes. In particular, NRHOs are sensitive to this transition process [36], [75]. A minimum norm targeting scheme is used to maintain geometry as close to the CR3BP counterpart as possible [23]. The initial epoch along the trajectory is selected such that gaps in the trajectory align with the Earth and lunar shadows, providing ballistic eclipse avoidance. With careful epoch selec-

(a) Earth-Moon rotating frame

(b) Moon-centered inertial frame

(c) Moon-centered Inertial Frame

(d) Sun-Moon Rotating Frame

(e) Sun-Moon Rotating Frame

(f) Sun-Moon Rotating Frame

(g) Sun-Earth Rotating Frame

(h) Sun-Earth Rotating Frame
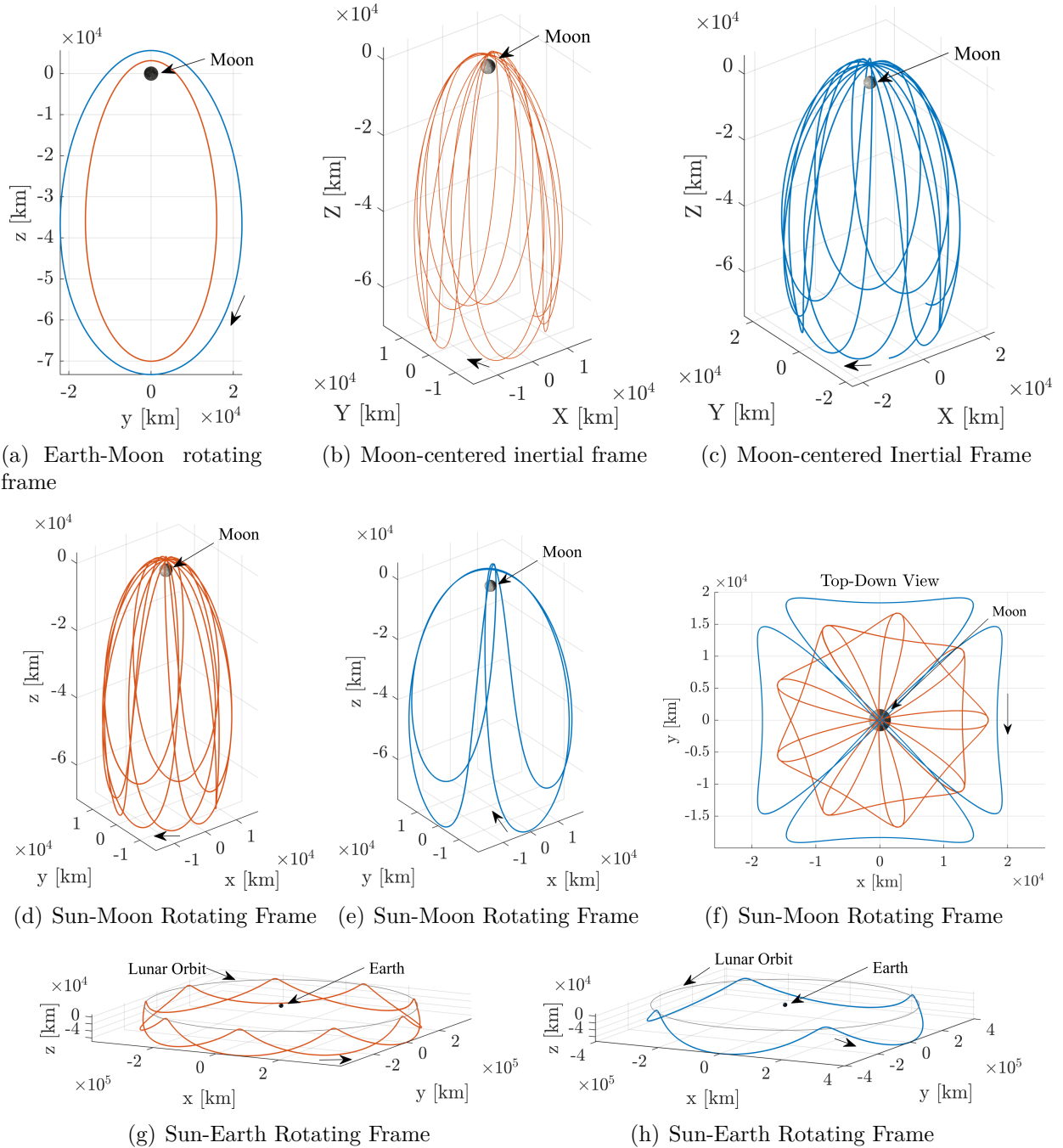
Figure 5.21. : The 9:2 synodic resonant NRHO (orange) and the 4:1 synodic resonant NRHO (blue) computed in the CR3BP

tion, the transition of a trajectory to the ephemeris model does *not* solely rely on the eclipse avoidance constraint to avoid shadow encounters, but instead relies on a favorable geometry (produced through resonance with the lunar synodic period) maintained using continuity

(a) p:1 synodic resonance (b) p:2 synodic resonance
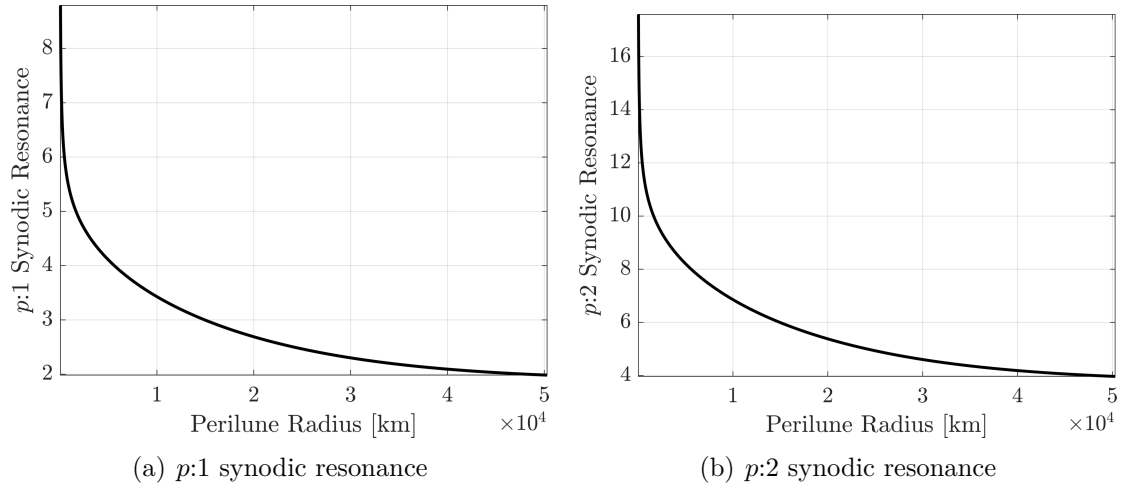
Figure 5.22. : Synodic resonances within the L_2 halo family

constraints and a minimum norm targeting scheme alone. An eclipse avoidance constraint, however, can be added to the transition process to successfully guide the generation of longer eclipse-free ephemeris solutions. The ephemeris trajectories in Figures 5.23 through 5.25 are generated without using an eclipse avoidance constraint.

The 9:2 synodic resonant NRHO, computed in the ephemeris model for 27 revolutions (approximately 6 months), is plotted in Figure 5.23 in the classical Earth-Moon rotating frame, Sun-Moon rotating frame, and Sun-Earth rotating frame. A similar pseudo-continuous fifteen year result is produced by Lee in work from 2019 [74]. Figure 5.23(a) illustrates the 9:2 synodic resonant NRHO in the Earth-Moon rotating frame; the red trajectory is the CR3BP orbit, while the blue trajectory is computed in a higher-fidelity NAIF SPICE-based ephemeris model. Figures 5.23(b) through 5.23(d) illustrate the trajectory in the Sun-Moon rotating frame; in this frame there are nine lobes corresponding to the nine revolutions of the NRHO per two synodic periods of the Moon. The Moon's shadow passes primarily through a gap in the lobes, based on careful epoch selection, thereby nearly avoiding all lunar eclipse events. The shadow passage through the lobes is apparent in the planar projections of the trajectory in Figures 5.23(c) and 5.23(d). Due to high velocity near the perilune along the NRHO, spacecraft transits through the lunar shadow are less than 90 minutes in duration; eclipse events less than 90 minutes are allowable for the Gateway space-

craft [74]. In this trajectory, an epoch of January 9, 2020 is selected for the initial apoapsis. In Figure 5.23(e), in the Sun-Earth rotating frame, there are 9 peaks corresponding to the 9 perilune passes along the revolutions of the orbit; the Earth's shadow passes cleanly through a gap between these peaks and, therefore, all Earth eclipse events are avoided, as observed in the yz-projection of the trajectory in Figure 5.23(f). The lobes and peaks are approximately repeated after 9 revolutions due to the resonant period of the orbit with the lunar month.

The 4:1 synodic resonant NRHO is plotted in Figure 5.24 in a variety of rotating frames. In Figure 5.24(a), the red periodic orbit demonstrates the 4:1 synodic resonant NRHO as computed in the CR3BP; the blue trajectory in this case corresponds to the higher-fidelity ephemeris trajectory, computed for 24 revolutions and plotted in the Earth-Moon rotating frame. The resonant geometry of this particular orbit is clearly apparent in Figures 5.24(b) through 5.24(f). In Figures 5.24(b) through 5.24(d), when the ephemeris trajectory is plotted in the Sun-Moon rotating frame, four distinct lobes are observed that correspond to the four revolutions of the trajectory over each lunar month. Figures 5.24(e) and 5.24(f) illustrate the trajectory in the Sun-Earth rotating frame; these figures highlight four peaks and troughs corresponding to the perilune passes and apolune passes, respectively. Relatively wide gaps are observed within the lobes in the trajectory in the Sun-Moon rotating frame and the peaks along the trajectory in the Sun-Earth rotating frame allow for margin in eclipse avoidance and flexibility in the insertion epoch selection. The planar projections of the trajectory in the Sun-Moon rotating frame (Figures 5.24(c) and 5.24(d)) and in the Sun-Earth rotating frame (Figure 5.24(f)) illustrate the passage of the shadows of the Moon and Earth, respectively, through gaps in the trajectory. A 19 year pseudo-continuous eclipse-free solution, as constructed by Williams et al. in 2017, is available [72].

To illustrate the efficacy of synodic resonance in an eclipse avoidance scheme, an NRHO that does *not* possess a resonance with the synodic period of the Moon is illustrated in Figure 5.25. The period of this particular NRHO in the CR3BP is 7.52 days and the perilune radius is approximately 4571.7 km. This orbit is nearby geometrically to both the 9:2 and 4:1 synodic resonant NRHOs, however, it does not have the same predictable

(a) Earth-Moon rotating frame

(b) Sun-Moon rotating frame

(c) Sun-Moon rotating frame

(d) Sun-Moon rotating frame

(e) Sun-Earth rotating frame

(f) Sun-Earth rotating frame
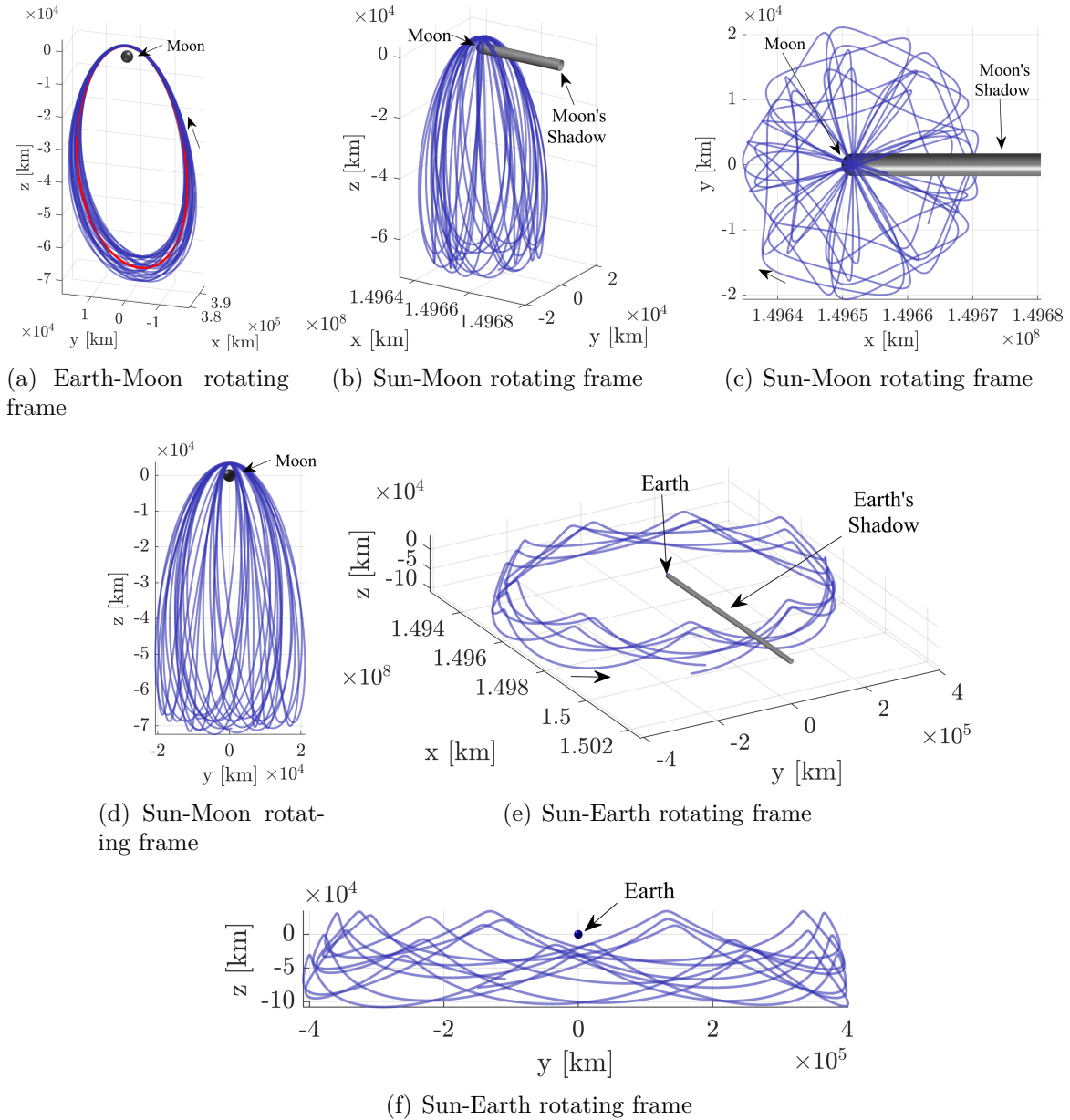
Figure 5.23. : 9:2 synodic resonant NRHO in various rotating frames, converged without eclipse avoidance constraint enforced; long eclipses avoided via careful epoch selection

repeating behavior in the Sun-Earth and Sun-Moon rotating frames, as is evidenced by the trajectory plotted in Figures 5.25(b) through 5.25(f). Figure 5.25(d) illustrates the yz-projection of the trajectory included in the box in Figures 5.25(b) and 5.25(c) to clearly illustrate the trajectory crossing through the shadow of the Moon (note the depth of the projection as illustrated by the box). The yz-projection of the trajectory included in the box

(a) Earth-Moon rotating frame

(b) Sun-Moon rotating frame

(c) Sun-Moon rotating frame

(d) Sun-Moon rotating frame

(e) Sun-Earth rotating frame

(f) Sun-Earth rotating frame
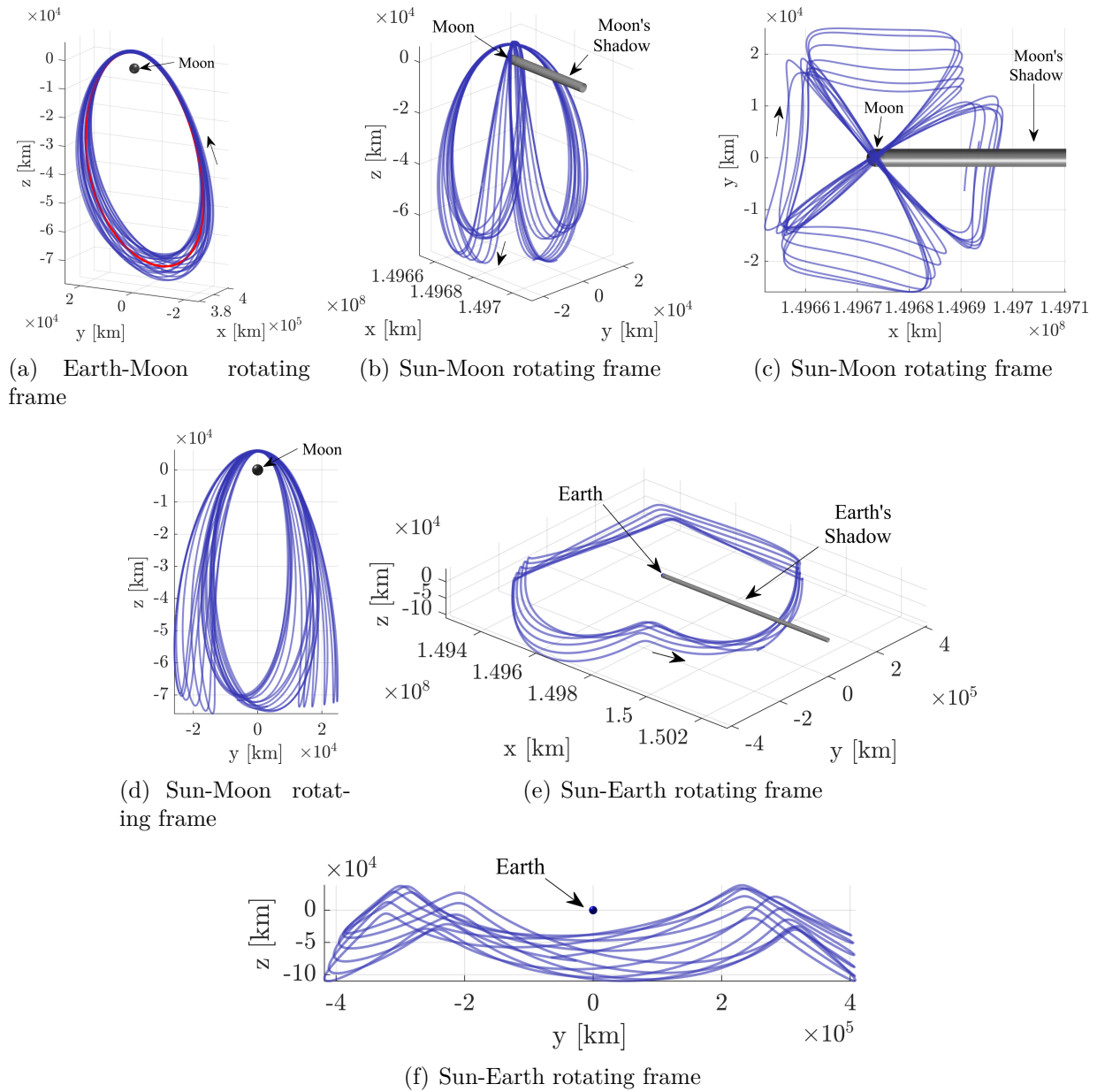
Figure 5.24. : 4:1 synodic resonant NRHO in various rotating frames, converged without eclipse avoidance constraint enforced; long eclipses avoided via careful epoch selection

in Figure 5.25(e) is plotted in Figure 5.25(f) to visibly illustrate the passage of the trajectory through the Earth's shadow.

(a) Earth-Moon rotating frame   (b) Sun-Moon rotating frame   (c) Sun-Moon rotating frame

(d) Sun-Moon rotating frame   (e) Sun-Earth rotating frame

(f) Sun-Earth rotating frame
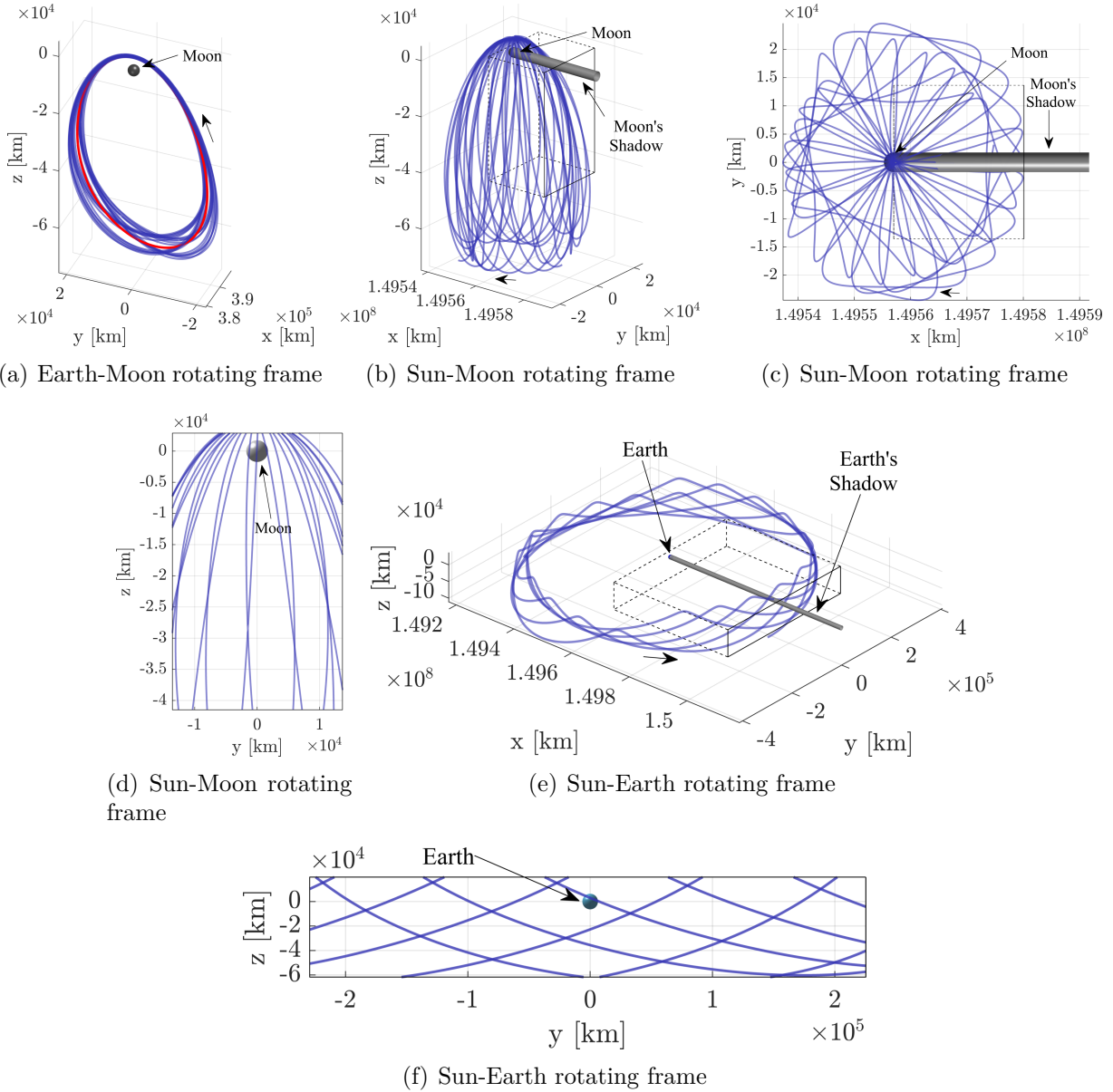
Figure 5.25. : A non-synodic resonant NRHO in various rotating frames, converged without eclipse avoidance constraint

Additional Considerations for Eclipse Avoidance in the 9:2 NRHO

Due to the complex geometry of the 9:2 lunar synodic resonant NRHO in the Sun-Moon rotating frame, careful epoch selection combined with a minimum norm targeting scheme is not necessarily enough to produce a lunar eclipse-free orbit. The 'gaps' in the

trajectory depicted in Figures 5.21(g) and 5.21(f) shift such that short lunar eclipses are encountered if the trajectory is not carefully constrained. Enforcing the eclipse avoidance constraint described in Section 3.1.5 allows for the production of an entirely eclipse-free ephemeris reference trajectory. Note that this constraint must be enforced along the entire trajectory. If the eclipse avoidance constraint is only enforced along certain segments of the trajectory, eclipse-free segments may shift into shadow as constrained segments move out of the shadow during the differential corrections process. Enforcing the eclipse avoidance constraint along the entire trajectory avoids this challenge but does add to the required computation time.

The 9:2 synodic resonant NRHO is computed in the ephemeris model for 30 revolutions (approximately 6.5 months) and is plotted in Figure 5.26 in the classical Earth-Moon rotating frame, Sun-Moon rotating frame, and Sun-Earth rotating frame. Contrary to the trajectory plotted in Figure 5.23, the eclipse avoidance constraint **is** enforced during the corrections process of this 30 revolution baseline. Because the eclipse avoidance constraint is enforced, the trajectory has zero passages through the Earth and Moon shadows. The trajectory is ballistic and no maneuvers are required to produce 6.5 months of eclipse-free motion. Similar to Figure 5.23, in this trajectory, an epoch of January 9, 2020 is selected for the initial apoapsis. Note that the geometry of the trajectory, including perilune and apolune passage altitude is slightly shifted from the solution converged without the eclipse avoidance constraint; this shift in geometry is guided by the additional constraint since in both cases, a CR3BP initial guess was used to generate the ephemeris solution. The solution plotted in Figure 5.26 required approximately 9.9 hours of wall-clock time to converge; this is significantly longer than the required time to produce the trajectory in Figure 5.23.

Longer duration eclipse-free baselines are of interest for long-term missions, e.g., the Gateway. As demonstrated by the solution in Figure 5.26, converging fully-continuous (maneuver-free) 9:2 NRHO baseline trajectories that fully avoid both the Earth and Moon shadows is a time-intensive process within a highly sensitive dynamical regime. Attempts to converge a second 6 month completely eclipse-free NRHO trajectory with an initial position

109

(a) Earth-Moon rotating frame

(b) Sun-Moon rotating frame

(c) Sun-Moon rotating frame

(d) Sun-Moon rotating frame

(e) Sun-Earth rotating frame

(f) Sun-Earth rotating frame
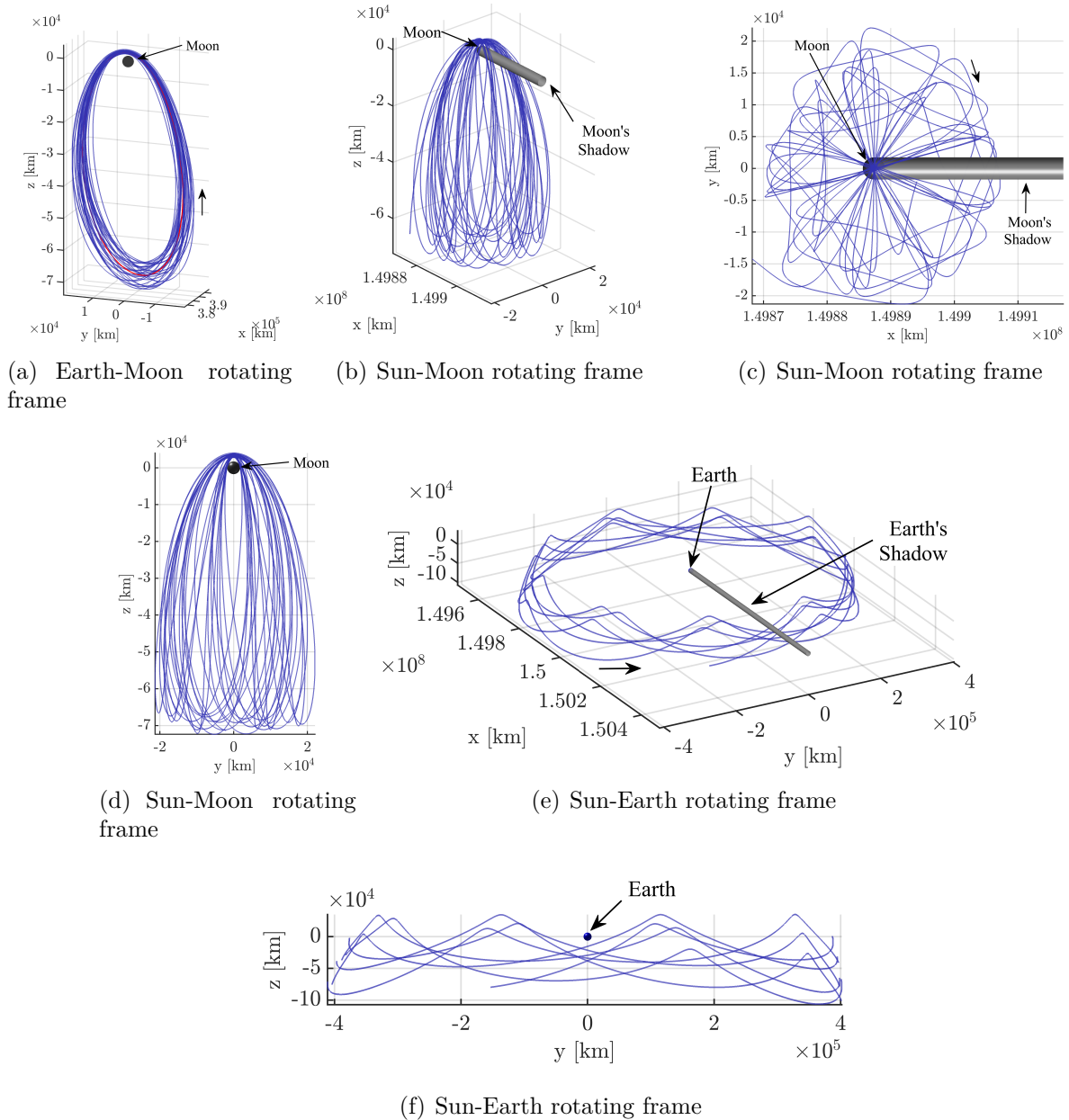
Figure 5.26. : 9:2 synodic resonant NRHO in various rotating frames, converged **with** eclipse avoidance constraint enforced, initial epoch January 9, 2020

and epoch constrained to be equal to a position and epoch combination along the solution plotted in Figure 5.26 were unsuccessful. With an initial epoch of July 3, 2020 at apolune, the geometry of the NRHO in the Sun-Moon rotating frame is shifted such that there are direct passages through the lunar shadow, as is plotted in the Sun-Moon rotating frame in

Figure 5.27. Views in the Earth-Moon and Sun-Earth rotating frame are also included. The red star corresponds to the location of the position and epoch constraint along the trajectory. Portions of the trajectory highlighted in magenta correspond to passages through the lunar umbra while a cyan color corresponds to passage through the penumbra. The trajectory in Figure 5.27 is produced starting from a CR3BP initial guess that is transitioned to the ephemeris model without an initial position constraint. This intermediate solution is then used as an initial guess for a convergence process where an initial position constraint *is* enforced. When the eclipse avoidance constraint is enforced on this constrained trajectory, however, convergence is unable to be reached to within tolerance. The differential corrections algorithm is unable to shift the geometry of the trajectory enough (sans maneuvers) to accommodate the natural motion that passes through the lunar shadow. Thus, careful initial guess generation based on favorable geometry is necessary to produce long duration eclipse-free, ephemeris reference orbits. Note that although lunar eclipses are unable to be avoided using the eclipse avoidance constraint, each lunar shadow transit lasts less than 90 minutes in duration and no Earth eclipse conditions exist along this trajectory. The simpler geometry of the 9:2 NRHO in the Sun-Earth rotating frame (with large 'gaps' between peaks and troughs along the orbit) provides an Earth eclipse-free solution, even without eclipse avoidance constraints enforced. If the eclipse avoidance constraint *is* enforced and maneuvers are allowed at each apolune to accommodate modifications in orbital geometry required to avoid the lunar shadow, a 30 revolution eclipse-free solution with an identical initial epoch of July 3, 2020 can be computed–this solution is plotted on the right in Figure 5.28 in the Sun-Moon rotating frame. Red asterisks mark the locations of maneuvers along this trajectory. The solution on the left in Figure 5.28 illustrates the ballistic NRHO from Figure 5.27 that does encounter lunar eclipses.

It is apparent that there is a correlation between successful lunar eclipse avoidance in the 9:2 NRHO and the epoch of the initial apolune. The Earth-Moon-Sun orientation is approximately identical at the initial epochs studied; the angle between the Earth-Moon line and the Earth-Moon barycenter-Sun line is approximately 160 degrees on both January 9, 2020 and July 3, 2020. A key difference, however, is that on January 9, 2020, the Earth is

(a) Earth-Moon rotating frame


(b) Sun-Moon rotating frame

(c) Sun-Earth rotating frame
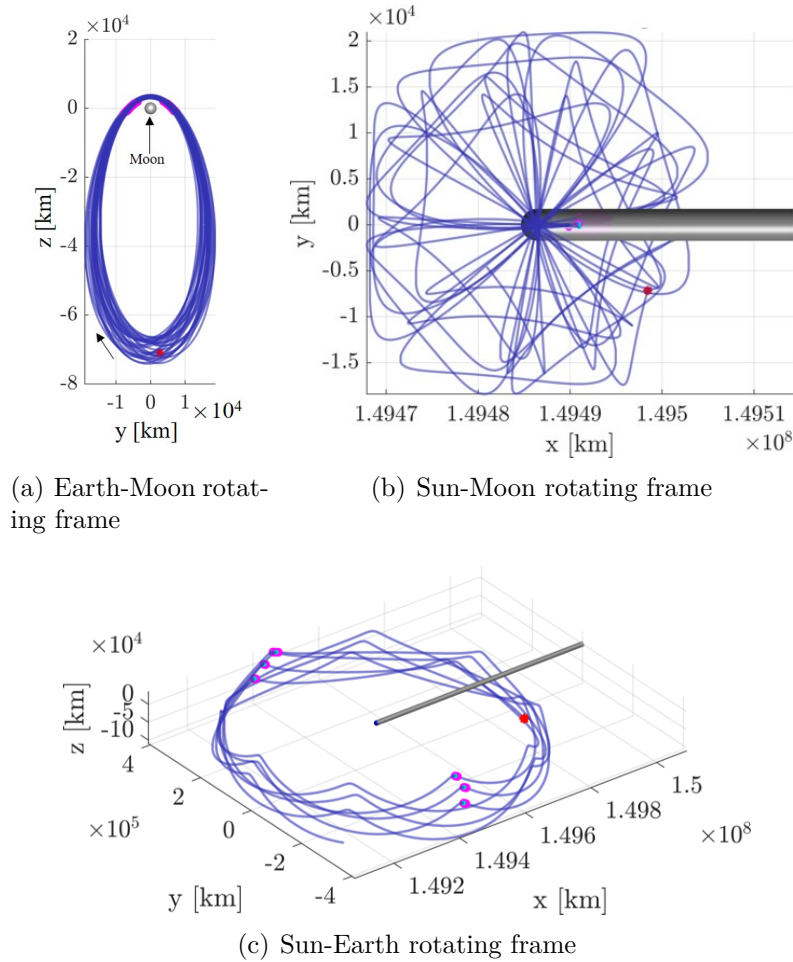
Figure 5.27. : 9:2 synodic resonant NRHO in various rotating frames, converged **without** eclipse avoidance constraint enforced, initial epoch July 3, 2020

near perihelion; approximately 6 months later on July 3, 2020, the Earth is near aphelion. Therefore, although the forces acting on the spacecraft are in similar directions, they are different in magnitude. This difference results in a slight orbital geometry shift that prevents a ballistic lunar eclipse-free solution from being generated using the described techniques.

A 60 revolution 9:2 NRHO (approximately 390 days) is computed and plotted in Figure 5.29. Along this trajectory, cyan and magenta colored segments correspond to passages through the lunar penumbra and umbra, respectively. The trajectory is plotted in the Earth-Moon rotating frame in Figure 5.29(a). Note that the blue colored ephemeris-computed trajectory remains close to the red curve that corresponds to the CR3BP 9:2 NRHO. Ad-
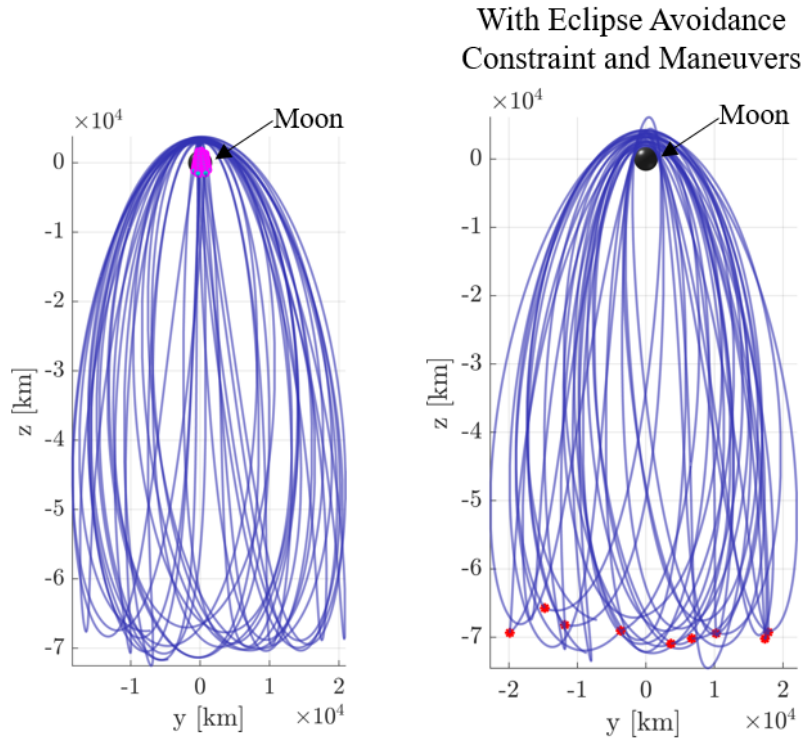
Figure 5.28. : 9:2 NRHO (initial epoch July 3, 2020) in Sun-Moon rotating frame converged without eclipse avoidance constraint enforced (left) and with eclipse avoidance constraint enforced and maneuvers allowed at apolune (right)

ditionally, even without an eclipse avoidance constraint enforced, this ballistic trajectory is Earth eclipse-free due to favorable resonant geometry. The nine distinct peaks and troughs along the trajectory in the Sun-Earth rotating frame, plotted in Figures 5.29(e) and 5.29(c), allow for Earth eclipses to be easily avoided. The gaps in the trajectory, distinctly visible in Figures 5.26(b) through 5.26(d) are no longer apparent in Figures 5.29(b) through 5.29(d). Although all lunar eclipses along the 60 revolution solution are less than 90 minutes, lunar eclipses are encountered due to a 'smearing' of the gaps in the Sun-Moon rotating frame geometry of the 9:2 NRHO if full state continuity is enforced along the trajectory.

(a) Earth-Moon rotating frame

(b) Sun-Moon rotating frame

(c) Sun-Moon rotating frame

(d) Sun-Moon rotating frame

(e) Sun-Earth rotating frame

(f) Sun-Earth rotating frame
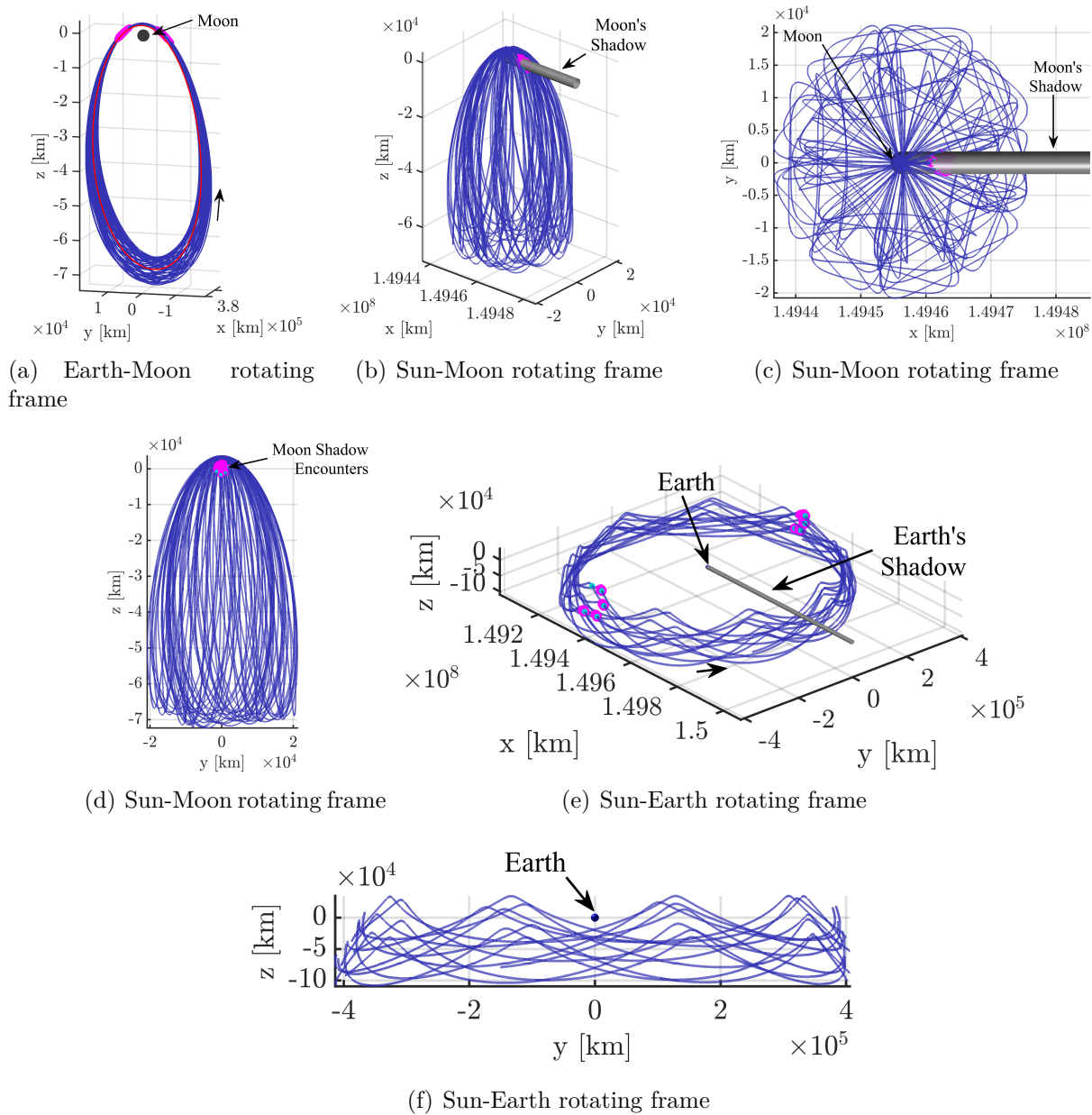
Figure 5.29. : 60 revolutions along the 9:2 synodic resonant NRHO in various rotating frames, converged **without** eclipse avoidance constraint enforced

5.3.3   Synodic Resonance and Eclipse Avoidance in Nearby Related Orbits

Since transfers into nearby higher-period orbits are likely to involve similar eclipsing constraints as those enforced for missions in NRHOs, it is useful to investigate the resonance

properties of the nearby orbits as well. Like the resonant NRHOs, with careful epoch selection, the transition of a higher-period halo orbit into the ephemeris model does not rely on the eclipse avoidance constraint to avoid shadow encounters; instead, favorable eclipse-free geometry, produced through resonance with the lunar synodic period, is maintainable using continuity constraints and a minimum norm targeting scheme alone. Transitioning resonant structures to the ephemeris model also serves to validate the persistence of these orbits under the influence of higher-fidelity perturbations. Of course, the eclipse avoidance constraint *can* be enforced during the transition from the CR3BP to an ephemeris model, however, it is not strictly necessary to produce eclipse-free solutions due to the existence of favorable resonances. In Figure 5.30, the p:1 resonance is represented for each of the higher-period orbit families from Figures 5.11 through 5.15. Specific resonant solutions from
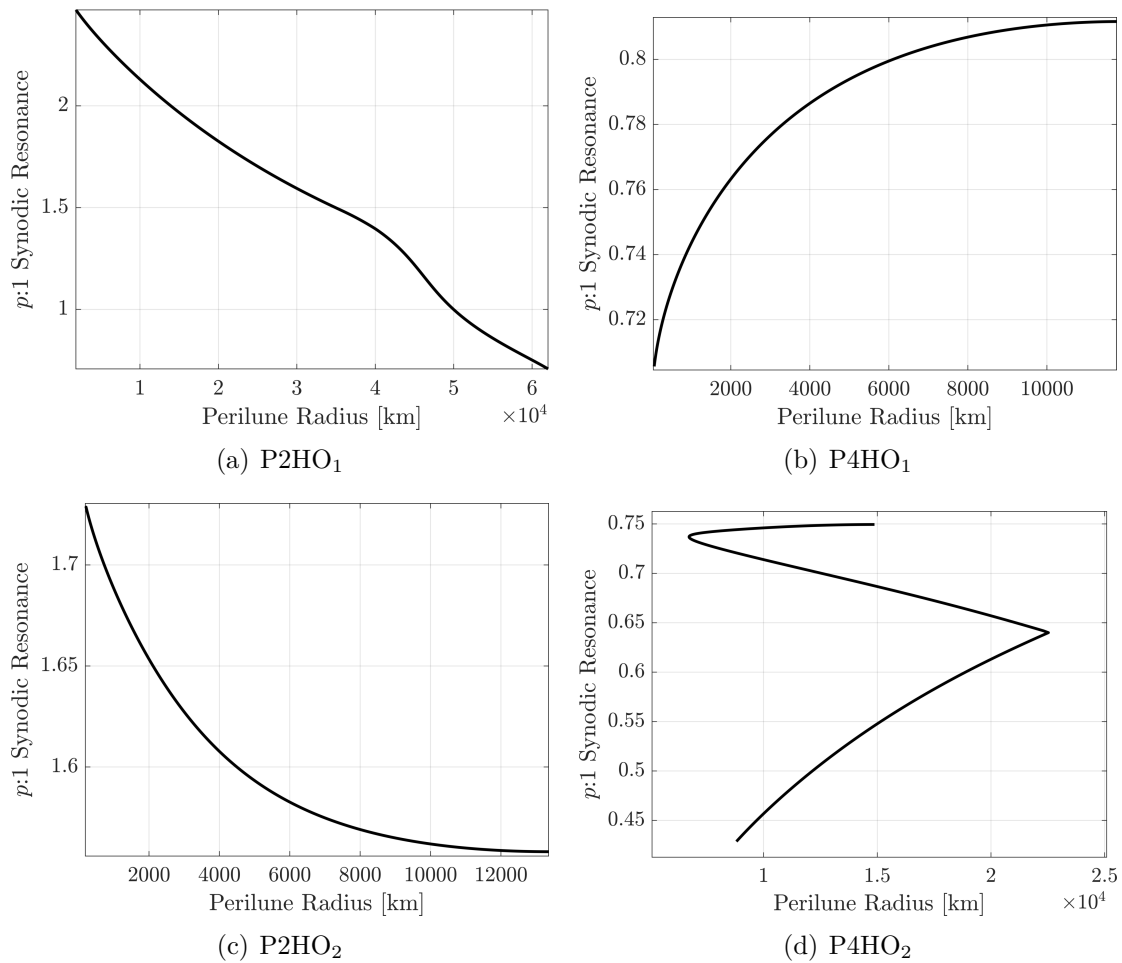
Figure 5.30. : p:1 synodic resonance in nearby related orbits

115

the P2HO$_1$ and P4HO$_2$ families are investigated further due to their favorable long-duration eclipse avoidance properties; the resonant orbits investigated include the 2:1, 1:1, and 3:2 P2HO$_1$ and the 1:2 P4HO$_2$. These sample resonant orbits are computed in the CR3BP and are plotted in the nondimensionalized Earth-Moon rotating frame in Figure 5.31. Depending on the mission application and length of stay in a higher-period orbit, many other members of these families could be useful, however, they may not possess long-term eclipse avoidance geometries. The P4HO$_1$ and P2HO$_2$ families do not possess any simple p:q resonances that
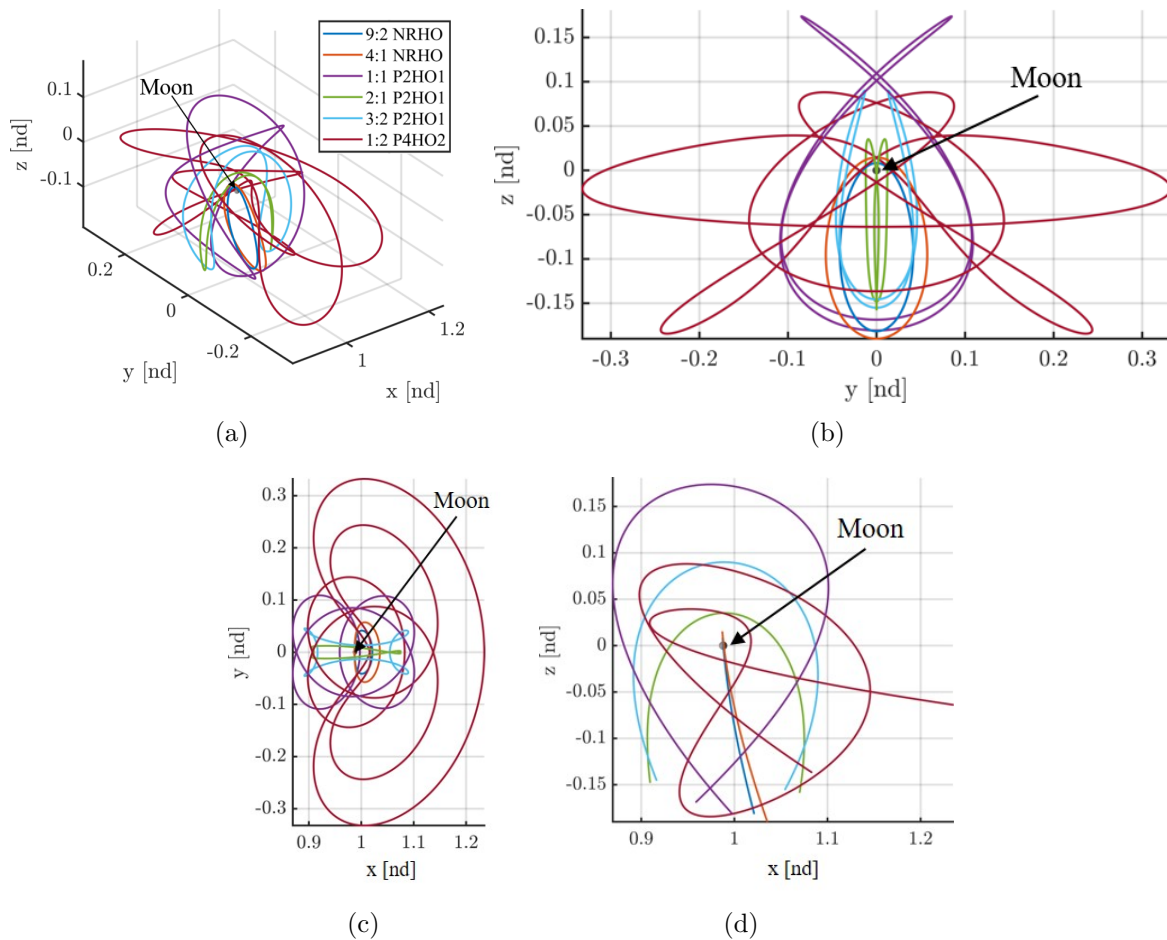
Figure 5.31. : Sample resonant orbits of interest for eclipse avoidance

are defined in terms of $q = 1$ or $q = 2$. For higher-period orbits, such as those nearby the NRHOs, requiring multiple lunar months (i.e., $q > 2$) for resonance with the appropriate orbital period (i.e., an integer ratio between p and q) results in exceedingly complex geometries

in the Sun-Moon and Sun-Earth rotating frames that, while relatively predictable, do not successfully avoid eclipses over a long time period in an ephemeris model. Hence, periodic orbits in nearby families with p:1 and p:2 ratios that avoid eclipses for multiple revolutions are examined further.

To offer a comparison to the spacecraft speed along the 4:1 and 9:2 lunar synodic resonant NRHOs (plotted in Figure 5.9), the Earth-Moon rotating frame velocity magnitude and Moon centered inertial frame velocity magnitude along each of the higher-period orbits is plotted in Figure 5.32. The perilune speed along the NRHOs in the inertial frame is significantly larger than any velocity magnitude reached along the resonant higher-period halo orbits investigated here. As is observed in Figure 5.32(b), a velocity magnitude of nearly 0 km/s, as measured in the Earth-Moon rotating frame, along the 2:1 P2HO$_1$ orbit is encountered. Plotting this particular CR3BP orbit along with a Zero-Velocity Surface (ZVS) corresponding to the appropriate Jacobi constant value highlights that the trajectory nearly encounters the ZVS, as expected [23]. The periodic orbit, Earth, Moon, and ZVS are all plotted in Figure 5.33. In this figure, the near encounter with the ZVS is indicated by a magenta arrow.

Based on Figure 5.30(a), it is apparent that 2:1, 1:1, and 3:2 (equivalently, ³/₂:1) synodic resonant orbits exist across the region of the P2HO$_1$ family nearby the NRHOs. It is inferred that the 2:1 synodic resonant P2HO$_1$ orbit possesses similar eclipse avoidance properties to that of the 4:1 synodic resonant NRHO. The full cycle of the P2HO$_1$ orbit includes two revolutions about the Moon while the full cycle for an NRHO includes one revolution about the Moon; therefore, the time required for one revolution about the Moon is commensurate between the 2:1 synodic resonant P2HO$_1$ orbit and the 4:1 synodic resonant NRHO. The 2:1 synodic resonant P2HO$_1$ orbit is illustrated in Figure 5.34 in three rotating frames. In the CR3BP, this butterfly orbit is defined with a perilune radius of 13967 km and an orbital period of 14.76 days. In Figure 5.34(a), the red orbit corresponds to the solution in the CR3BP, while the blue trajectory corresponds to 15 revolutions (221.3 days) of the orbit computed in the higher-fidelity ephemeris model. The familiar four lobes and

117
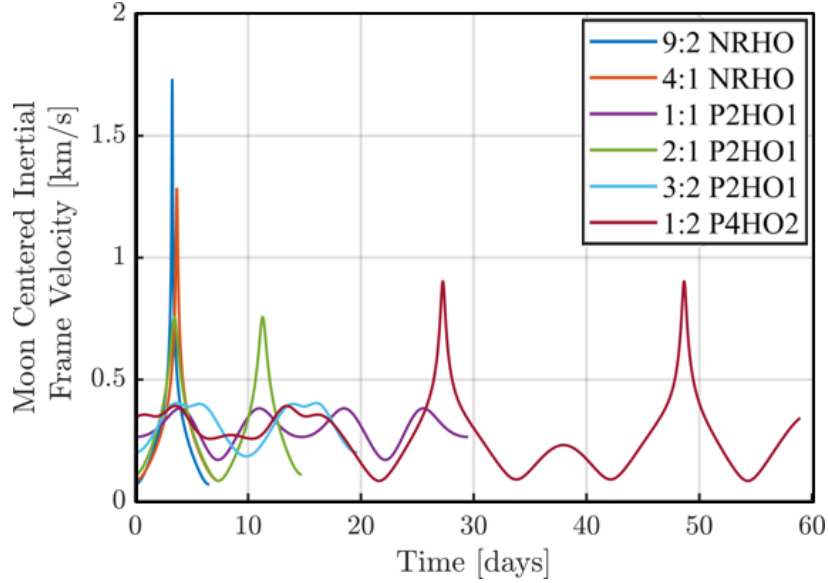
(a) Moon-centered inertial velocity
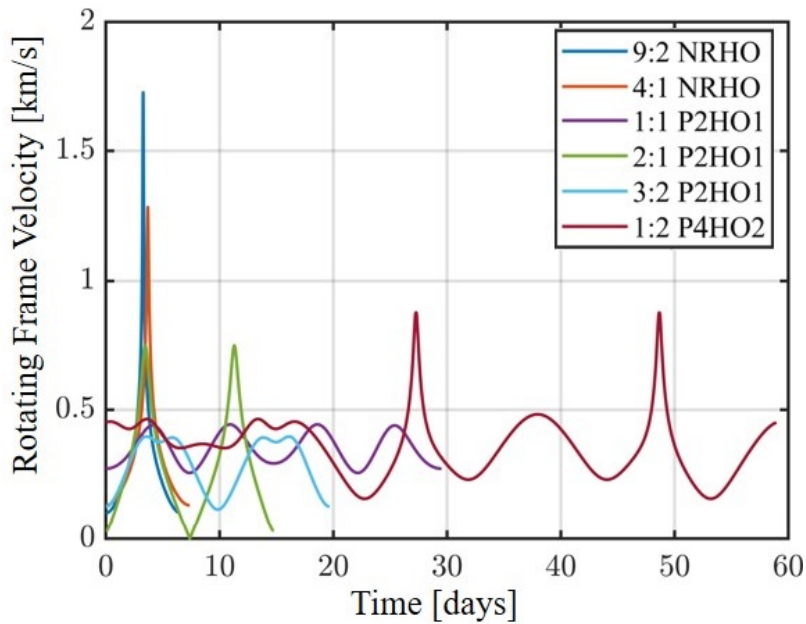
(b) Earth-Moon rotating frame velocity

Figure 5.32. : Velocity along sample resonant orbits of interest for eclipse avoidance

four peaks (similar to those of the 4:1 synodic resonant NRHO) appear in Figures 5.34(b) through 5.34(f). Note that while the geometry is slightly different from the 4:1 synodic resonant NRHO, the general structure and eclipse avoidance properties are retained. The 2:1 synodic resonant P2HO$_1$ orbit is unstable but with a maximum stability index of 12.31
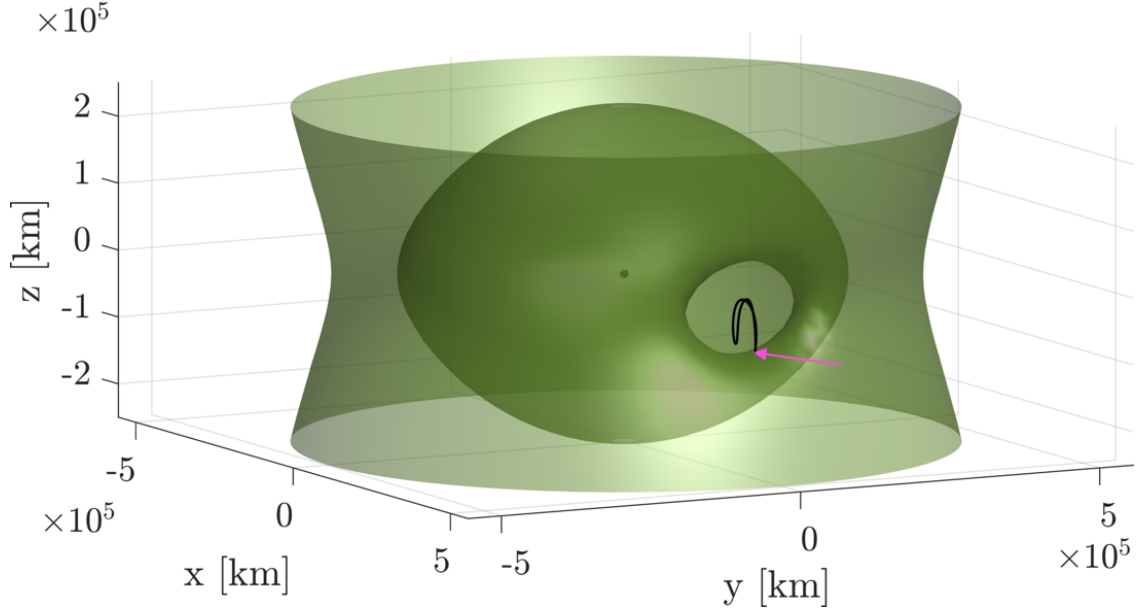
Figure 5.33. : CR3BP 2:1 P2HO$_1$ orbit and corresponding zero velocity surface

(corresponding to a time constant of $\Upsilon = 0.0919$ revolutions); unstable orbits potentially possess useful manifold structures for transfer design.

In Figure 5.35, the 1:1 synodic resonant P2HO$_1$ is plotted in the Earth-Moon, Sun-Moon, and Sun-Earth rotating frames. The perilune radius of this orbit is 49986 km and the period of the orbit in the CR3BP (plotted in red in Figure 5.35(a)) is equal to the synodic period of the Moon, i.e., 29.5 days. Although the geometry of this orbit appears complex in the Earth-Moon rotating frame, the trajectory possesses a constant line of sight to Earth. Additionally, the 1:1 synodic resonant P2HO$_1$ ephemeris trajectory (plotted in blue) maintains geometry similar to the CR3BP solution over many revolutions. This particular trajectory also possesses a very simple geometry in the Sun-Moon frame and Sun-Earth frame that leads to a simple eclipse avoidance scheme. In the Sun-Moon rotating frame, with the proper epoch selection, the shadow of the Moon passes directly through the large opening in the trajectory, as observed in Figures 5.35(b) and 5.35(c). Illustrated in Figure 5.35(d) and 5.35(e) in the Sun-Earth rotating frame, the Earth's shadow passes above a dip in the trajectory (corresponding to an apolune pass) and is successfully avoided along each revolution. The 1:1 synodic resonant P2HO$_1$ is unstable, as well, with a maximum stability

(a) Earth-Moon rotating frame

(b) Sun-Moon rotating frame

(c) Sun-Moon rotating frame

(d) Sun-Moon rotating frame

(e) Sun-Earth rotating frame

(f) Sun-Earth rotating frame
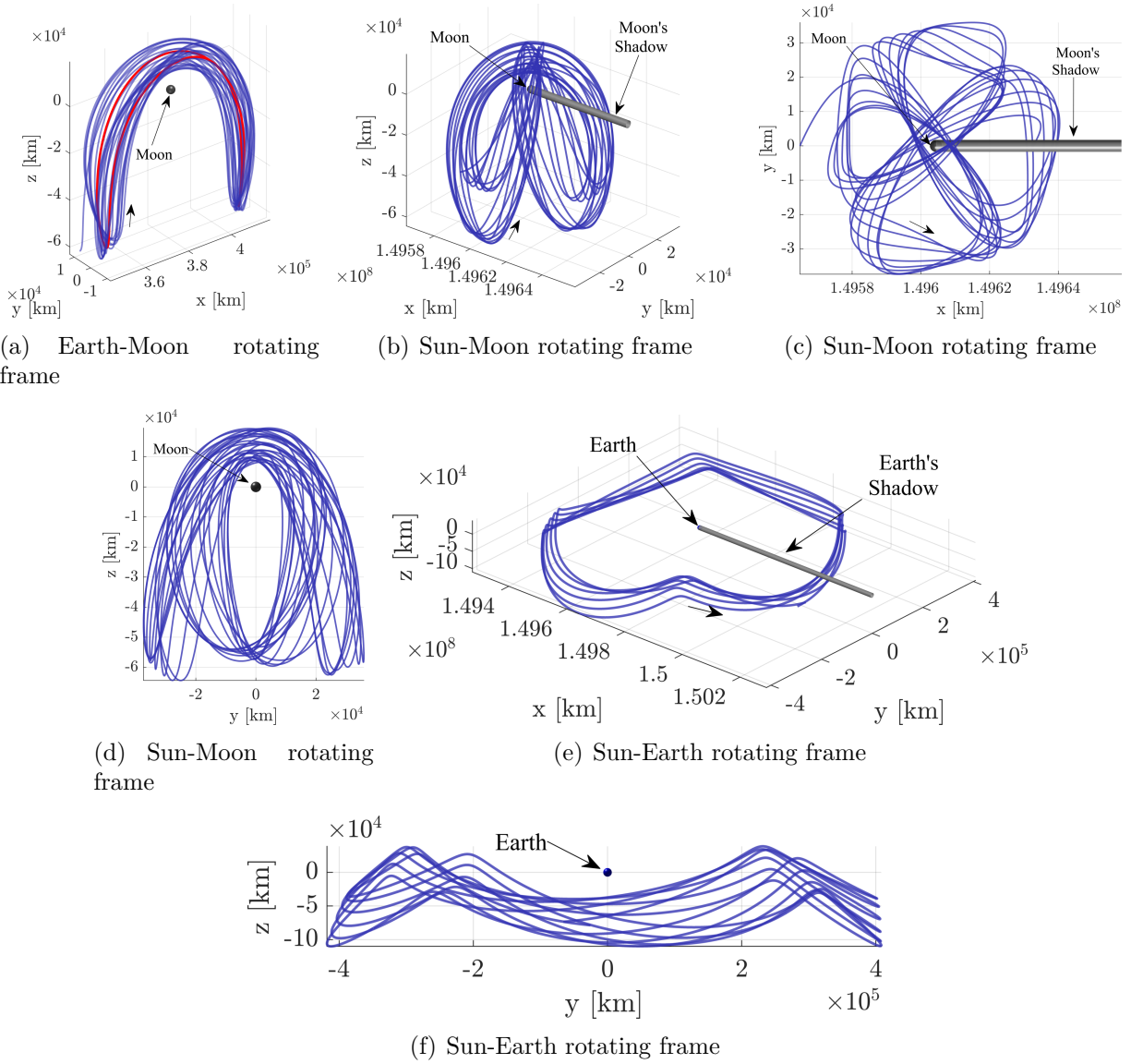
Figure 5.34. : 2:1 synodic resonant P2HO$_1$ orbit in various rotating frames

index of 33.55 or time constant of $\Upsilon = 0.03499$ revolutions; this orbit possesses unstable and stable spiral manifold structures that could offer utility in transfer design in the region. Spiral manifold structures arise when an orbit possesses complex eigenvalues with magnitudes greater than one; the dynamic flow spirals around the orbit while arriving/departing the vicinity [43], [57].

(a) Earth-Moon rotating frame

(b) Sun-Moon rotating frame

(c) Sun-Moon rotating frame

(d) Sun-Earth rotating frame

(e) Sun-Earth rotating frame
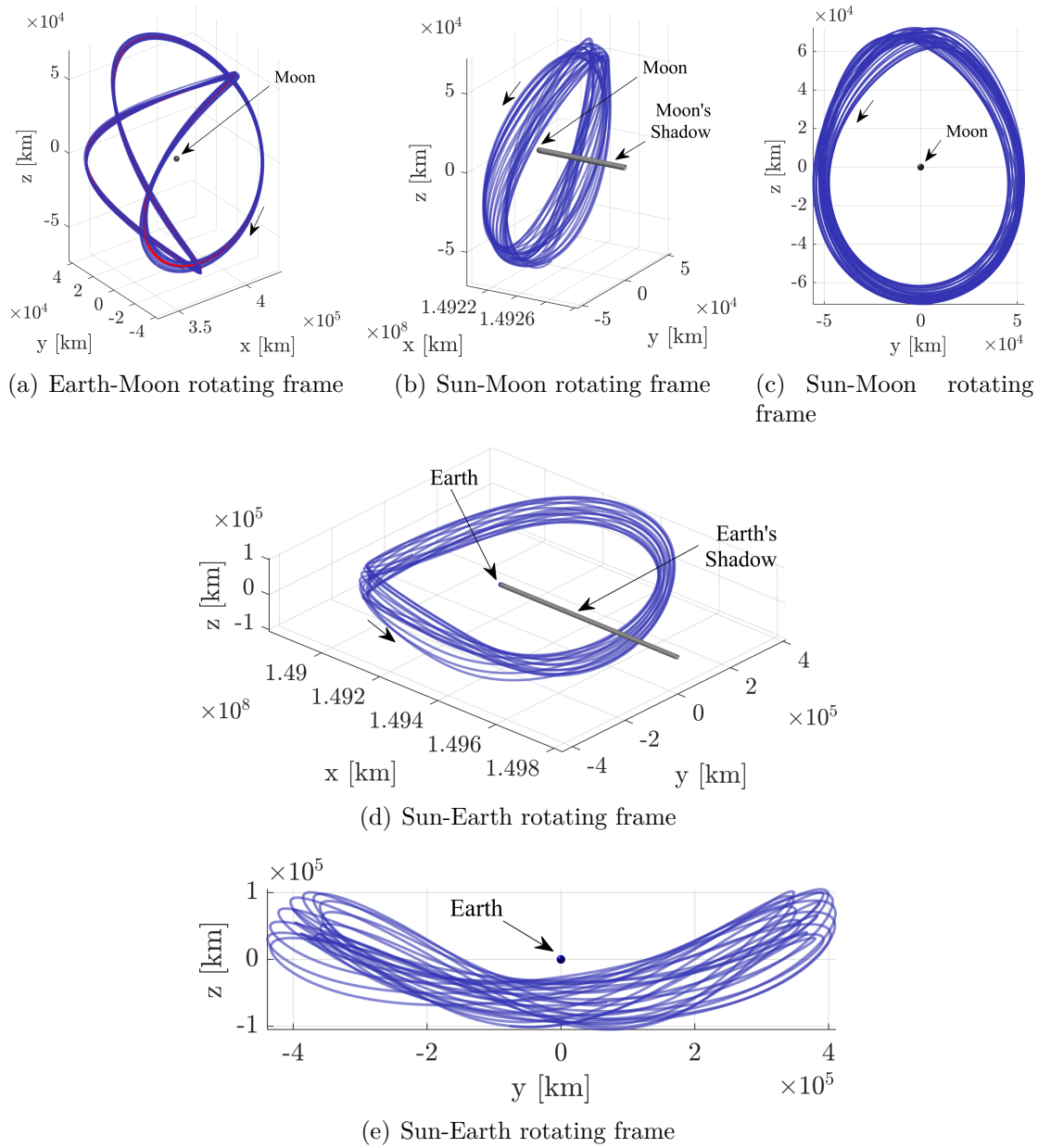
Figure 5.35. : 1:1 synodic resonant P2HO$_1$ orbit in various rotating frames

The 3:2 synodic resonant P2HO$_1$ is plotted in Figure 5.36. In the CR3BP, this periodic solution possesses a perilune radius of 34970 km and a period of 19.67 days. In this case, an ephemeris solution corresponding to 295 days successfully avoids all lunar and Earth eclipses. The orbit is illustrated in the Earth-Moon rotating frame in Figure 5.36(a); note that the ephemeris solution (colored blue) does not vary greatly from the CR3BP counterpart

121

(colored red). Similar to the 9:2 synodic resonant NRHO, the geometry of this solution in the Sun-Moon and Sun-Earth rotating frames is complex due to the fact that two lunar months are required to achieve an integer ratio with the period of the orbit, i.e., resonance, however, eclipses are still successfully avoided. Figures 5.36(b) through 5.36(d) illustrate the trajectory in the Earth-Moon rotating frame. The box plotted in Figures 5.36(b) and 5.36(c) illustrates the portion of the trajectory included in Figure 5.36(d); the depth of the projection in Figure 5.36(d) is consistent with the side length of the box in the x-direction in Figures 5.36(b) and 5.36(c). Similarly, the box included in Figure 5.36(e) illustrates the projection of the trajectory in the Sun-Earth frame included in Figure 5.36(f). The maximum stability index for this orbit is 19.94 or equivalently, the time constant associated with this orbit is $\Upsilon = 0.05988$ revolutions. This particular P2HO$_1$ possesses stable and unstable spiral manifolds that could be useful in transfer design into or out of the vicinity, for example, leveraging such flow to arrive at or depart from the NRHO.

Finally, in the P4HO$_2$ family, there is an orbit that possesses 1:2 resonance with the synodic period of the Moon. For each single period along this orbit, the Earth-Moon-Sun orientation repeats twice. In Figure 5.37, three revolutions (approximately half of a year) along the ephemeris trajectory are plotted in blue in various rotating frames. The CR3BP periodic solution appears in Figure 5.37(a) in red. A northern family member is plotted here since it more successfully avoids lunar eclipses than its southern counterpart for this particular initial epoch and duration. The complex geometry of this trajectory does introduce some additional challenges in epoch selection as the margin in available epochs for eclipse avoidance is not as wide as in trajectories with simpler geometries due to narrower gaps in the trajectory for the Earth and Moon shadows; this phenomenon is illustrated in Figures 5.37(b) through 5.37(e). Note that the box included in Figure 5.37(b) illustrates the depth of the yz-projection of the trajectory in Figure 5.37(c) that is used to clearly illustrate that the trajectory is not passing through the lunar shadow over the span of the trajectory plotted. The 1:2 synodic resonant P4HO$_2$ orbit possesses two unstable nodes corresponding to invariant manifolds that approach/depart from this periodic orbit; this orbit does not possess a center subspace. The maximum stability index of this orbit is a notably large

122

(a) Earth-Moon rotating frame

(b) Sun-Moon rotating frame

(c) Sun-Moon rotating frame

(d) Sun-Moon rotating frame

(e) Sun-Earth rotating frame

(f) Sun-Earth rotating frame
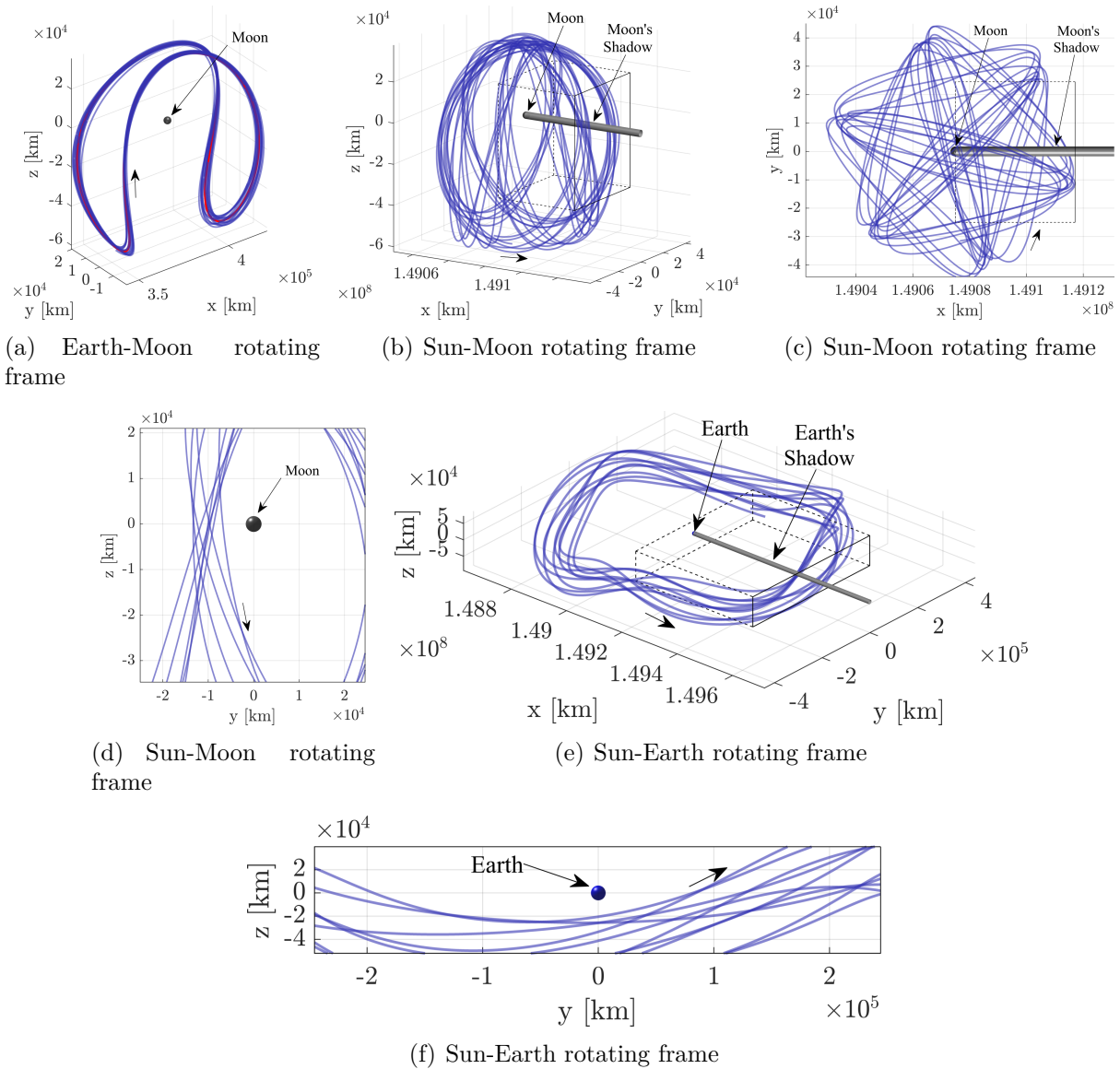
Figure 5.36. : 3:2 synodic resonant P2HO$_1$ orbit in various rotating frames

value at 36189.68. Manifolds approach/depart from the vicinity of this trajectory rapidly, potentially offering utility for time of flight restricted transfer design into and out of the lunar region. The time constant associated with this larger unstable node is defined as $\Upsilon = 0.006616$ revolutions.

(a) Earth-Moon rotating frame

(b) Sun-Moon rotating frame

(c) Sun-Moon rotating frame

(d) Sun-Earth rotating frame

(e) Sun-Earth rotating frame
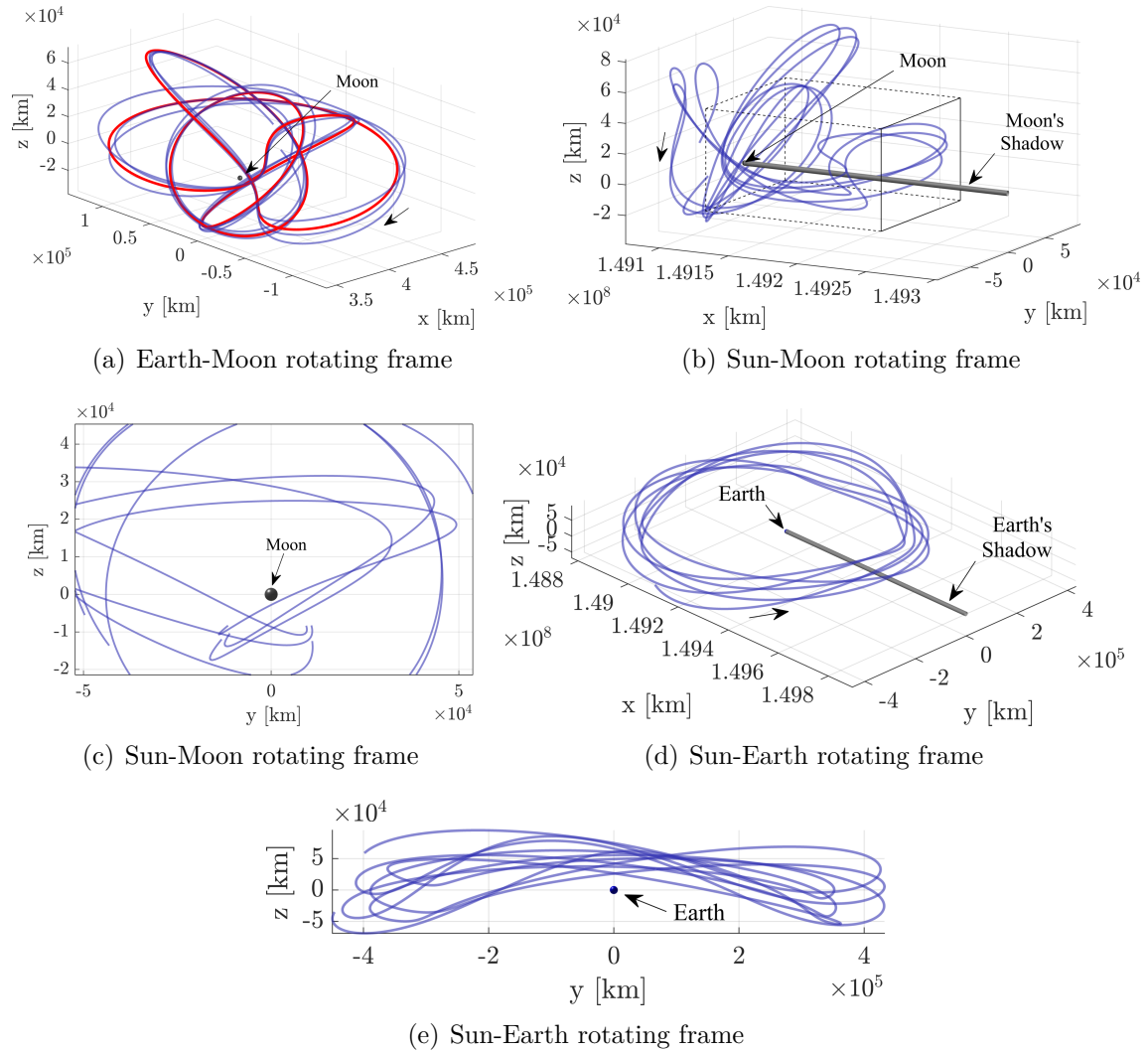
Figure 5.37. : 1:2 synodic resonant northern P4HO$_2$ orbit in various rotating frames

5.4 Distant Retrograde Orbits and Nearby Dynamical Structures

The Distant Retrograde Orbits (DROs) are planar orbits that originate from motion centered about the smaller primary (e.g., the Moon in the Earth-Moon system). This (primarily) stable family of orbits is of interest to cislunar exploration. In fact, the Artemis I mission aims to send a human-rated spacecraft to a DRO in the early 2020s [76], [77]. Since the DROs are stable or nearly-stable, alternative methods beyond manifold trajectories are necessary to initiate transfer design into and out of these orbits.

5.4.1 Distant Retrograde Orbit Characteristics

Like the near rectilinear halo orbits, distant retrograde orbits are a viable option for long-duration operations in the vicinity of the Moon. The DRO family is computed in the CR3BP and plotted in the Earth-Moon rotating frame in Figure 5.38. Characteristics of
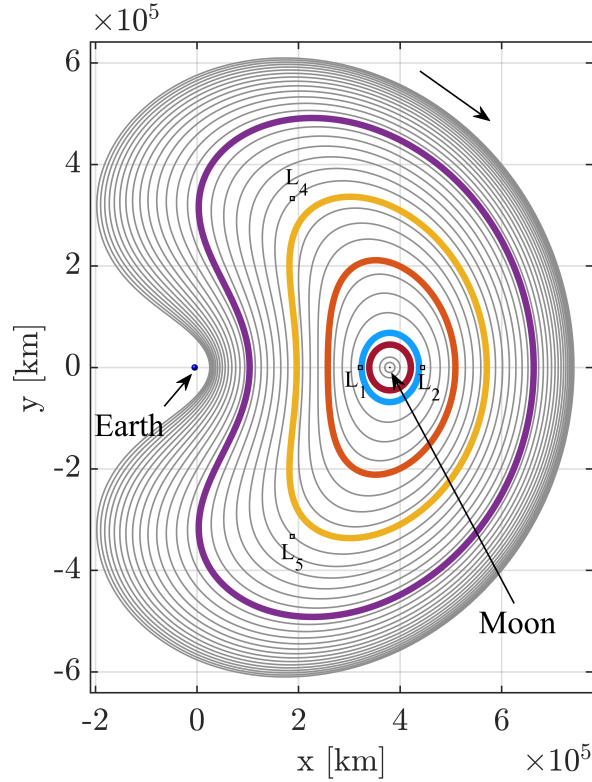
Figure 5.38. : DRO family

the DRO family are plotted in Figure 5.39. Figure 5.39(a) depicts the Jacobi constant value versus the orbital period along the family. The stability index is computed for each member of the family and is plotted in Figure 5.39(b).

5.4.2 Identification of Nearby Dynamical Structures

The DROs are attractive for long-duration missions due to their inherent stability and potential for low orbit maintenance costs. Due to the lack of an unstable subspace however,
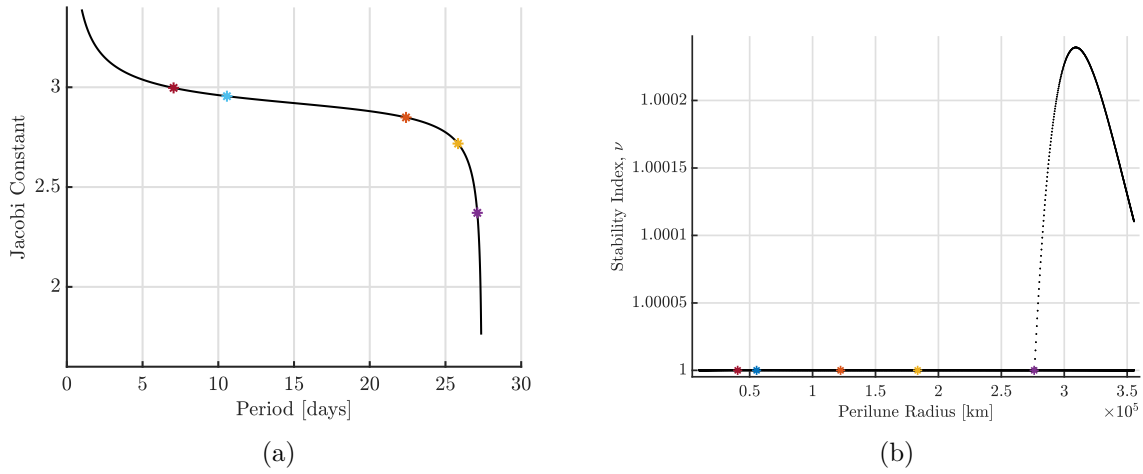
Figure 5.39. : Characteristics of the DRO family

arriving to/departing from orbits in this family poses challenges. In Figure 5.40, a black curve is plotted on the Broucke stability diagram that corresponds to the DRO family of orbits. An arrow indicates the direction of increasing perilune radius. In this figure, colored asterisks (*) reflect the family members that correspond to bifurcations. Additionally, asterisks of the same color mark these family members in Figure 5.39 and the orbits are also traced in the corresponding colors in Figure 5.38. Following the naming convention described in Section 5.2, Table 5.2 delineates the bifurcations and bifurcating families across the DRO family in order of increasing perilune radius.

Table 5.2. : Bifurcations across the DRO family and the corresponding new orbit families in order of increasing perilune radius

Color	Type	Name of New Family	Other Useful Information
Maroon	Period-Quadrupling	P4DRO$_1$	
Blue	Period-Tripling	P3DRO$_1$	Only one period-three DRO family exists
Orange	Period-Tripling	P3DRO$_2$	(denoted the P3DRO family).
Gold	Period-Quadrupling	P4DRO$_2$	
Purple	Tangent	3D-DRO	A three-dimensional family of DROs.

126
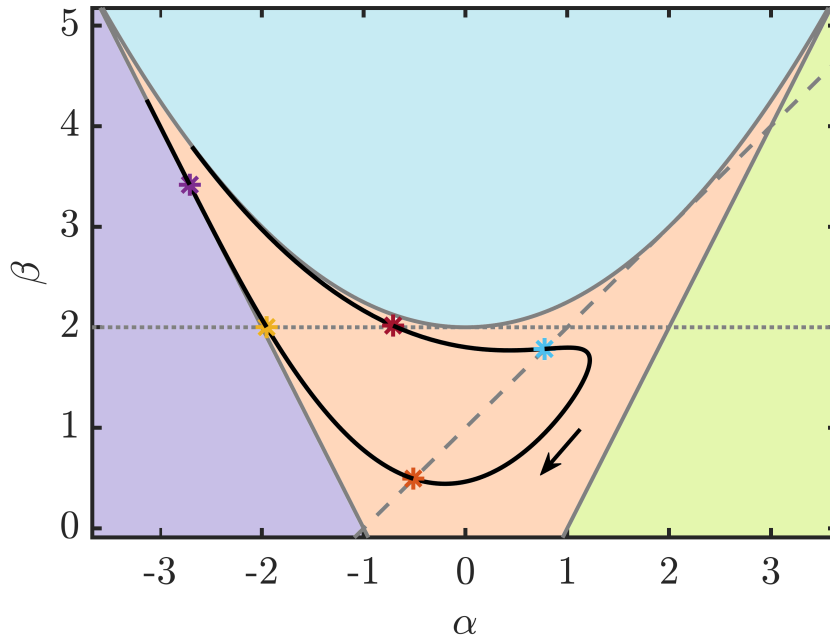
Figure 5.40. : DRO Broucke stability diagram

The families that originate from the DRO bifurcations, colored by Jacobi constant, are plotted in Figures 5.41 to 5.44 along with plots of stability index versus orbital period. Initial conditions for these families of periodic orbits, along with the initial conditions for the DRO family, are available in the Appendix in Tables A.6 to A.10. Both the P4DRO$_1$ family and the 3D-DRO family (plotted in Figures 5.41(b) and 5.44(b), respectively) are stable or nearly-stable, similar to the foundational DRO family. Thus, these orbits may not offer useful initial guesses for transfer options, however, they may offer long-term, low stationkeeping cost destinations for future Gateway mission scenarios. In contrast, the P3DRO and the P4DRO$_2$ families each possess members with manifold structures that can be accessed for initial guesses in transfer design. In fact, manifolds originating from a P3DRO are employed for initial guess generation to produce transfers into a DRO from an NRHO by Zimovan et al. in 2017 [38]. As noted in Table 5.2, only one P3DRO family exists despite the fact that there are two period-tripling bifurcations along the DRO family (colored in blue and orange in Figure 5.38), i.e., two periodic orbits belong to both the DRO family and the P3DRO family.
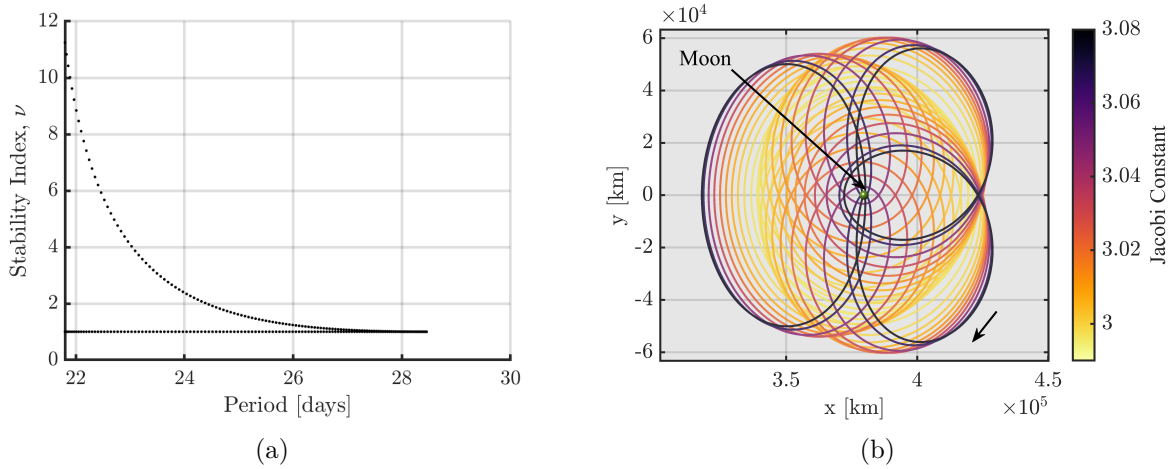
Figure 5.41. : P4DRO₁ orbit family
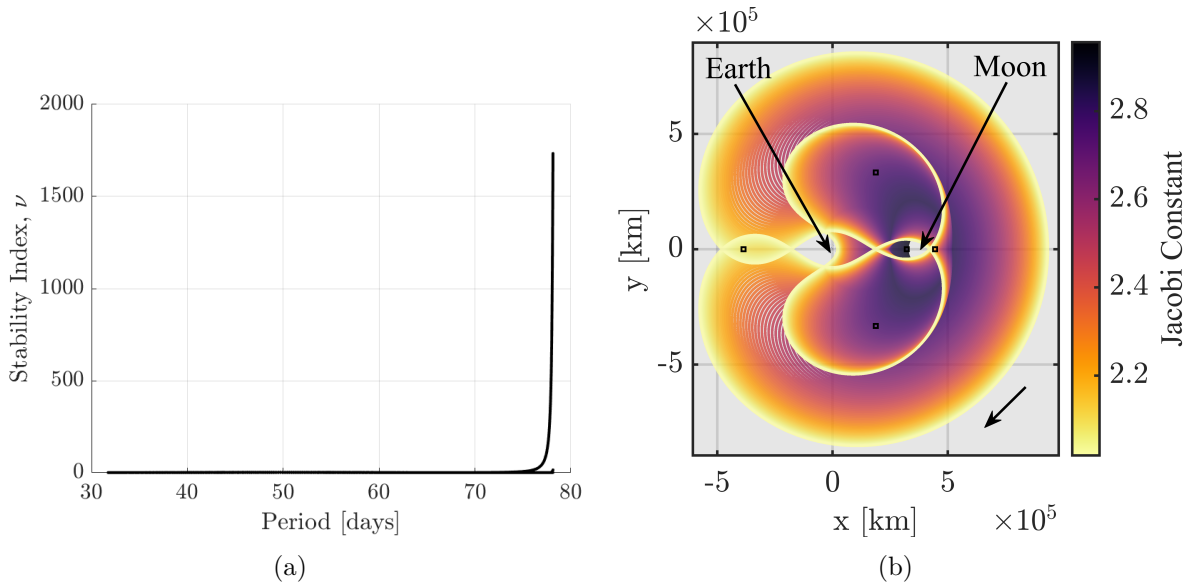
Figure 5.42. : P3DRO orbit family

Excursions throughout the Earth-Moon neighborhood, even to the vicinity of Lagrange points L_3, L_4, and L_5, are available via some of the larger members of the P3DRO and P4DRO₂ families. Although not the focus of this investigation, moving from a DRO to other destinations in these vicinities may be an option through these higher-period orbits and their manifolds. As a final note, the 3D-DROs offer potential eclipse avoidance properties due to their out-of-plane characteristics. Given the stable nature of these 3D trajectories,
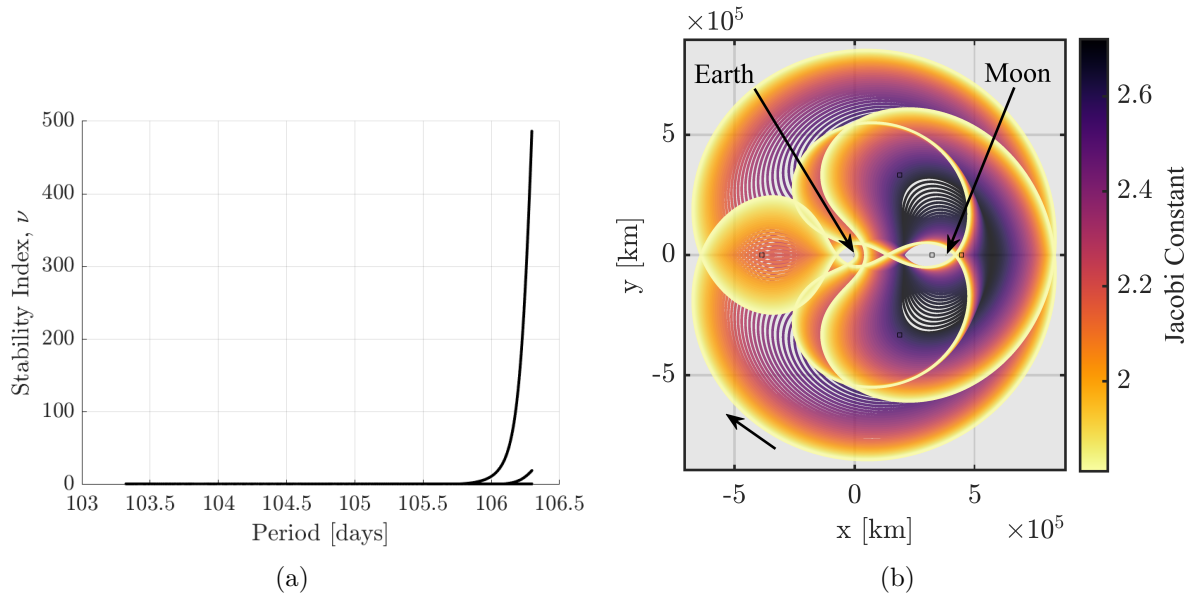
Figure 5.43. : P4DRO$_2$ orbit family
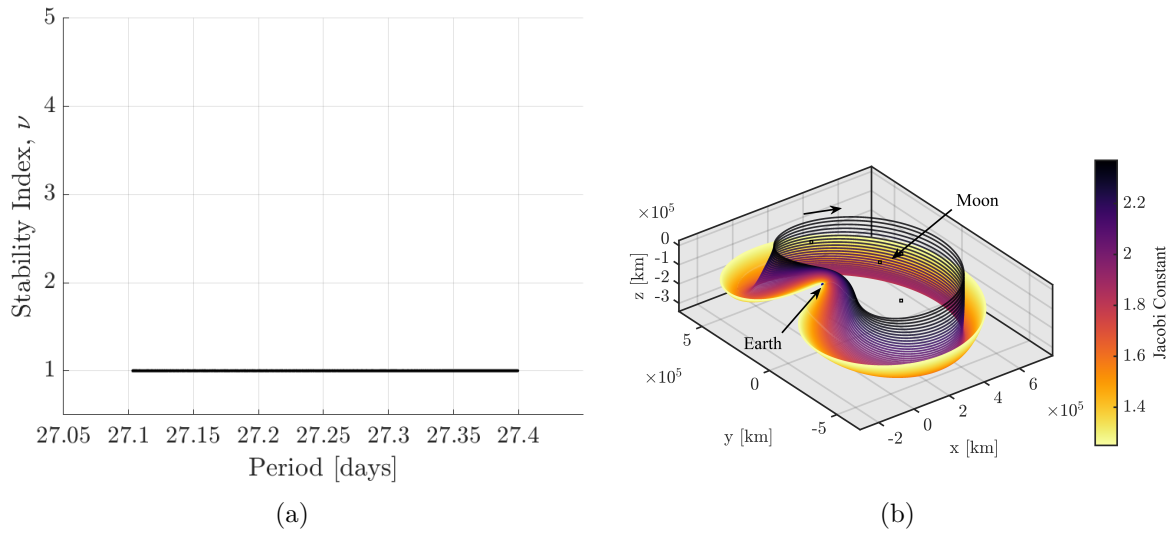
Figure 5.44. : Southern portion of 3D-DRO orbit family

it is likely that stationkeeping costs in this vicinity are minimal. Figure 5.45 illustrates a member from each of the bifurcating families that originate from the DROs. Note that the primary direction of motion is retrograde.

Some of the structures exemplified by the nearby bifurcating families are apparent in plots of transfer trajectories from NRHOs to DROs and other destinations that have been
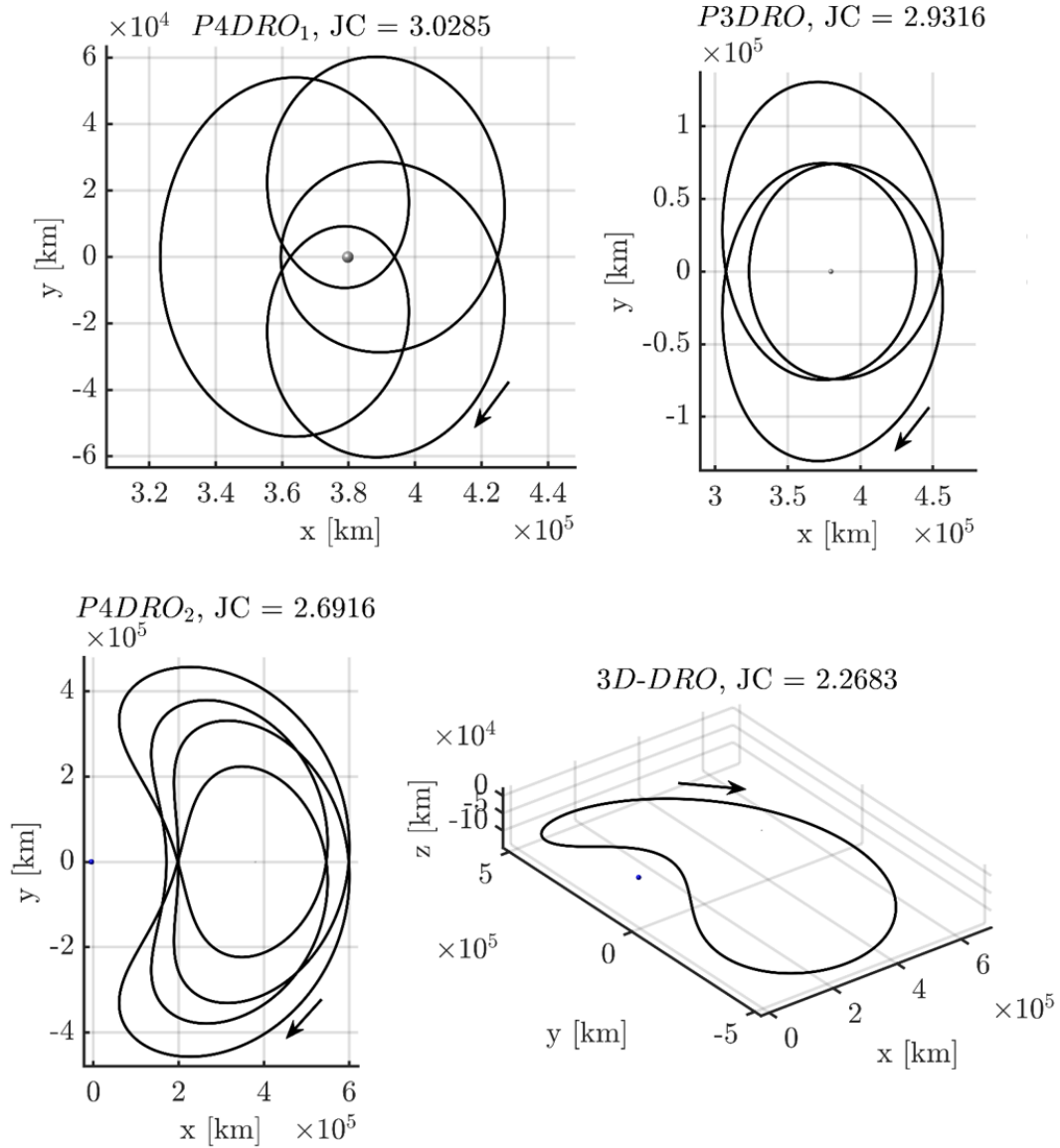
Figure 5.45. : Select members from each of the families that bifurcate from the DROs

generated by other authors. In McCarty et al., a 9:2 NRHO to DRO transfer features a post-NRHO departure geometry that shares characteristics with a P2HO$_2$ orbit [29]. This particular transfer also features motion consistent with either a P3DRO or P4DRO$_2$ near the arrival into the DRO.

A bifurcation diagram illustrating the connections between the DRO family of orbits and the nearby bifurcating families of orbits is plotted in Figure 5.46. Changes in the order

of instability are marked by black triangles. The color of the curve corresponds to the number of unstable modes as before, i.e., a teal-colored curve corresponds to a solution with zero unstable modes (a stable orbit), a blue-colored curve corresponds to a solution that possesses one unstable mode, while a magenta-colored curve corresponds to a solution that has two unstable modes. The plot on the right, framed in orange, corresponds to a zoomed-in portion of the bifurcation diagram which is also marked on the left-hand plot. A solid curve corresponds to the hodograph of the DRO family while the dashed curves correspond to the labeled bifurcating families. Note that the hodograph corresponding to the P3DRO family intersects with the DRO family hodograph twice. In this unique case, there are two separate bifurcations between the P3DRO family and the DRO family.
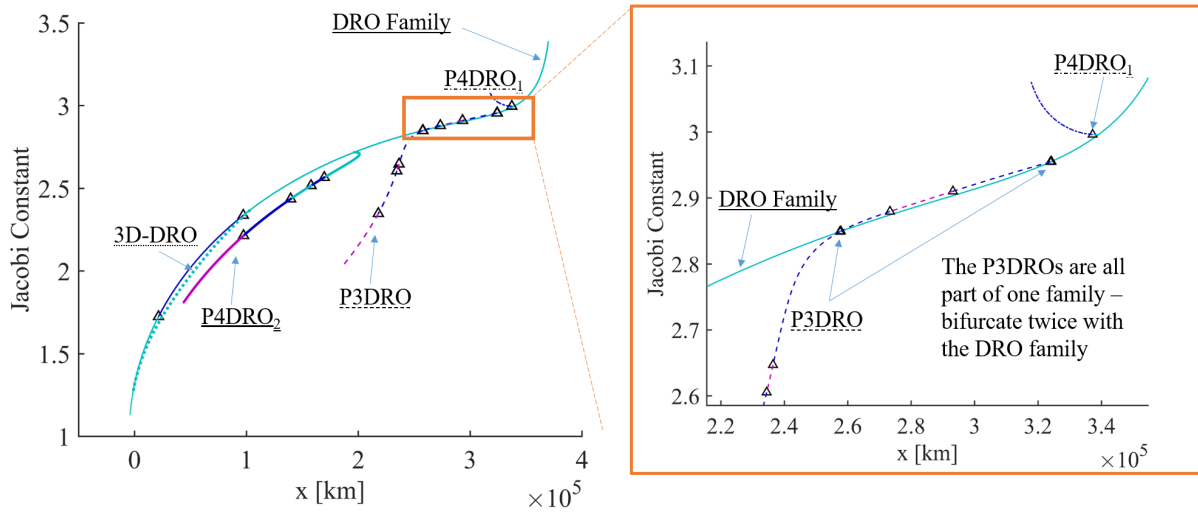
Figure 5.46. : DRO bifurcation diagram

6. TRANSFER DESIGN METHODOLOGY AND APPLICATIONS

An increased understanding of dynamical flow in the vicinity of stable and nearly-stable orbits, e.g., the NRHOs and DROs, is offered by a bifurcation analysis of these families of interest. A subsequent computation of structures in the vicinity of these orbits produces options for alternatively initiating transfer design. A next step after the identification of nearby structures, is the use of these structures to design transfer trajectories that are directly applicable to the exploration program.

6.1 Transfers Linking a Near Rectilinear Halo Orbit and a Distant Retrograde Orbit

The design of transfers between NRHOs and DROs is a topic of recent interest, and thus, trajectories that link the 9:2 synodic resonant NRHO (the current Gateway baseline orbit) and a DRO at the same value of Jacobi constant are explored. The perilune radius of this DRO is approximately 29800 km.

6.1.1 Initial Design in the CR3BP

Transfers between orbits at the same energy level allow maneuvers to be used for geometry changes rather than for changing the Jacobi constant value. Therefore, in this investigation, the NRHO, DRO, and all intermediate orbits employed for initial guesses are characterized by a Jacobi constant equal to that of the 9:2 NRHO ($JC \approx 3.04719$). Figure 6.1 illustrates the higher-period orbits that exist at this energy level. These particular periodic orbits are obtained from the families that are apparent in Figures 5.11 through 5.15.

To generate an initial guess for transfers in this vicinity, segments from cislunar trajectories in a design database are "stitched" together. The design methodology is divided
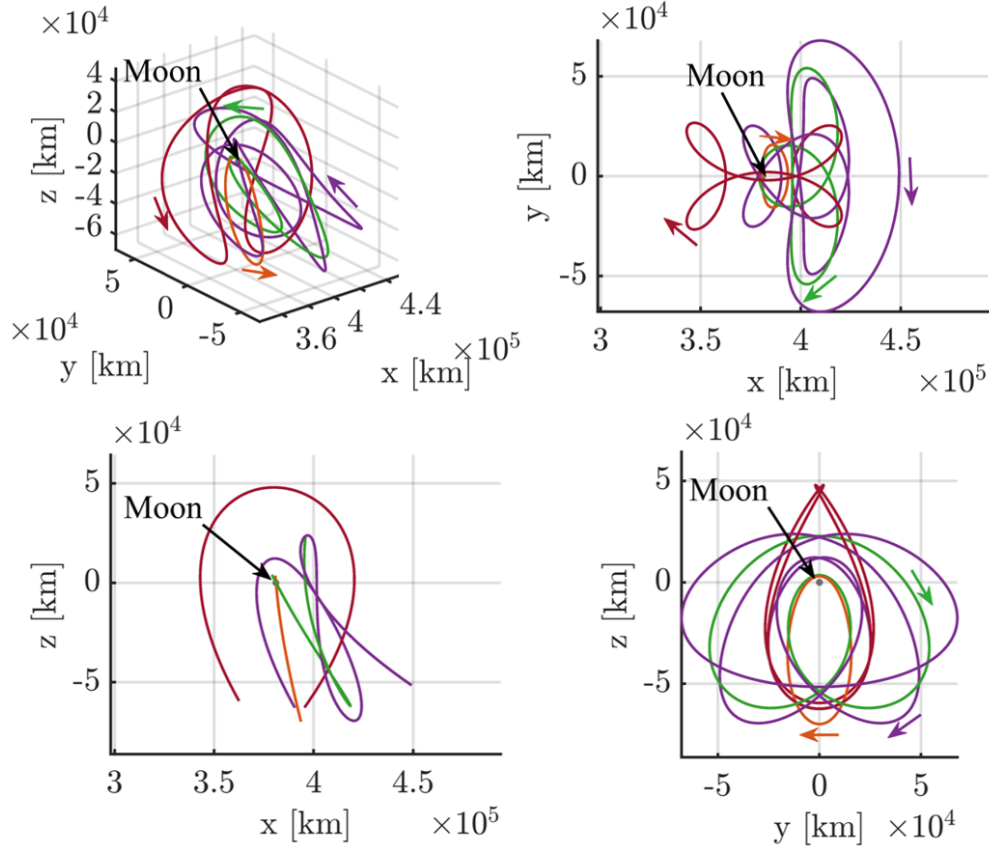
Figure 6.1. : A 9:2 synodic resonant NRHO with higher-period orbits that occur at the same Jacobi constant ($JC \approx 3.04719$) where orange: 9:2 NRHO, red: P2HO$_1$, green: P2HO$_2$, purple: P4HO$_2$

into two segments: one segment linking the NRHO to a higher-period orbit and a second segment connecting the higher-period orbit to the final destination orbit, a DRO. For each segment, a Poincaré map is used to locate paths that offer potential connections between the considered orbits. The design database for the Poincaré map includes higher-period families that bifurcate from the NRHOs, the manifolds that correspond to these orbits, and a variety of well-known resonant and libration point orbits. The resonant and libration point orbits are extracted from the Adaptive Trajectory Design (ATD) catalog, designed as a part of a collaborative effort between Purdue University and NASA Goddard Space Flight Center [78]–[81]. Each segment is separately corrected for continuity using a multiple-shooting algorithm. Because the CR3BP is autonomous, time continuity is not of concern in this model.

Thus, with an appropriate number of revolutions along the intermediate higher-period orbit included in the design, an end-to-end transfer connecting the NRHO and DRO is produced.

Direct Transfers Between the NRHO and Intermediate Higher-Period Orbits

A multiple-shooting scheme that incorporates a stable manifold arc from the higher-period orbit as an initial guess is leveraged to generate direct impulsive transfer options from the NRHO to the intermediate orbit. Due to both close proximity and a corresponding direction of motion along the orbits, transfers from the NRHO into the $P4HO_2$ and $P2HO_2$ orbits at the same energy level are easily accomplished. The $P2HO_1$ orbit is located relatively far from the 9:2 NRHO. Despite the larger distance, transfers from the NRHO into the $P2HO_1$ orbit are successfully accomplished. Near apolune, however, where the the positions align more closely, the directions of motion within the two orbits are opposing and this discrepancy must be accommodated.

A sample Poincaré map displaying the stable manifold crossings of the $P2HO_2$ orbit appears in Figure 6.2(a). The stable manifolds of the $P2HO_2$ orbit are denoted as blue circles with green colored centers. For this particular Poincaré map, a hyperplane at $\{\Sigma : y = 0\}$ is selected. The crossings of the NRHO at this hyperplane are denoted as orange triangles with black outlines in Figure 6.2(a). Crossings in close proximity to the NRHO are investigated as possible transfer options linking the NRHO and the higher-period orbit. As a sample initial guess generated via the Poincaré map, the green arrow in Figure 6.2(a) identifies a $P2HO_2$ stable manifold crossing on the map that is in close proximity to the NRHO crossing on the map. The trajectory arc associated with this crossing is plotted in Figure 6.2(b), in blue, along with the departure NRHO and arrival $P2HO_2$ (in orange and green, respectively); this manifold arc forms the basis for an initial guess to produce a transfer linking the NRHO and the $P2HO_2$. This initial guess can then be corrected into a multi-impulse continuous transfer using a minimum norm differential corrections scheme.
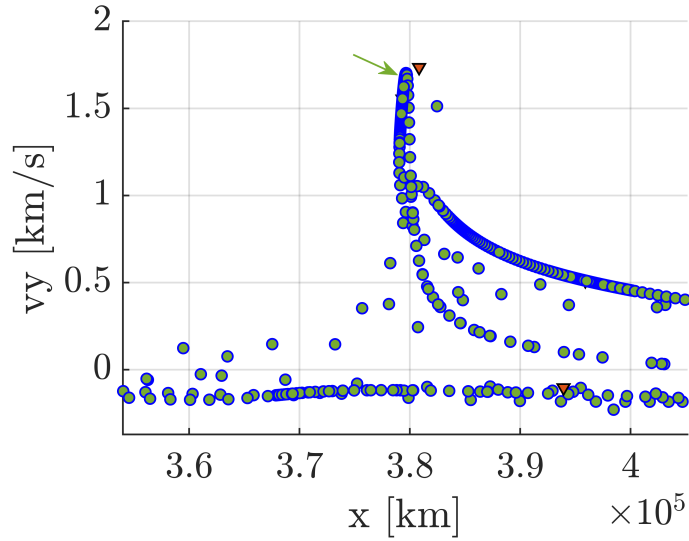
(a) Poincaré map that includes stable manifold crossings from the P2HO$_2$ (green-centered blue circles) and NRHO crossings (orange-centered black triangles)
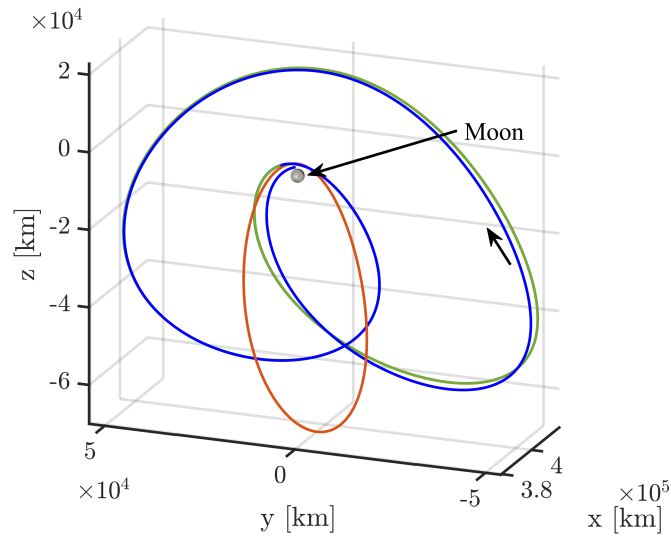
(b) Manifold associated with the selected Poincaré map crossing in Figure 6.2(a)

Figure 6.2. : A Poincaré map is used to select trajectory segments that serve as an initial guess in a targeting scheme.

Following a similar process, low-cost, low time-of-flight motion between the NRHO and P2HO$_1$, P4HO$_2$ and P2HO$_2$ orbits at $JC = 3.04719$ is computed and appears in Figure 6.3. Since a demonstration of the utility of these higher-period orbits in designing transfers

that originate at the NRHO is the main goal, rather than an optimal solution, feasible transfers that include two impulsive maneuvers are delivered initially. A transfer between the NRHO and the P4HO$_1$ is not included since a P4HO$_1$ orbit does not exist at this energy level. In Figure 6.3, the numbered red circles indicate the impulsive maneuver locations along the transfer arc. In each sample transfer, a Δv is employed to both depart the NRHO and to enter into the higher-period orbit. The time-of-flight for each transfer depicted in Figure 6.3 is approximately 20 days and the total cost for the maneuvers is on the order of 200 m/s. The transfer in Figure 6.3(b) is corrected from the initial guess displayed in Figure 6.2(b).

Design of Transfers Linking an Intermediate P2HO$_2$ Orbit and a Destination DRO

As a next step, Poincaré maps are constructed to link manifold arcs from these intermediate higher-period orbits directly to a DRO or to other useful structures *en route* to a DRO. Two structures of particular interest are a planar 3:4 resonant orbit and a 4:3 resonant orbit from the ATD Orbit Reference Catalog [78]–[81]. These two secondary intermediate orbits not only share similar characteristics with manifolds from each of the higher-period halo orbits, but the resonant orbits also each possess retrograde loops around the Moon nearby the DRO of interest, as apparent in Figure 6.4.

Selecting a hyperplane at $\{\Sigma : y = 0\}$, an x-v_y Poincaré map is generated that reflects a combination of the stable and unstable manifold crossings of the higher-period halo orbits, plane crossings from the periodic 3:4 and 4:3 resonant orbits and their respective manifolds, as well as the DRO plane crossings. A sample Poincaré map for creating a transfer from a P2HO$_2$ to a DRO via an arc originating from a 3:4 resonant orbit appears in Figure 6.5(a). In this map, triangles indicate periodic orbit crossings and circles highlight manifold crossings; red circles indicate unstable manifold crossings, while blue circles indicate stable manifold crossings. The center of each marker is colored according to the orbit from which it was generated; a green-centered marker indicates origination at the P2HO$_2$ and a black centered
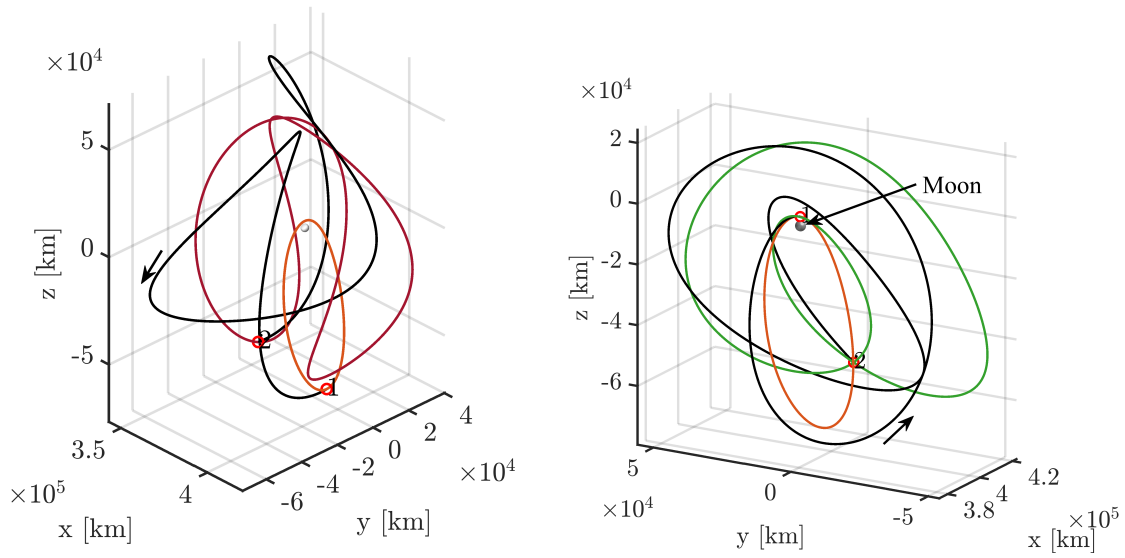
(a) NRHO to P2HO$_1$; $\Delta v = 0.2130\,km/s$; $TOF = 21.48\,days$

(b) NRHO to P2HO$_2$; $\Delta v = 0.2466\,km/s$; $TOF = 21.25\,days$
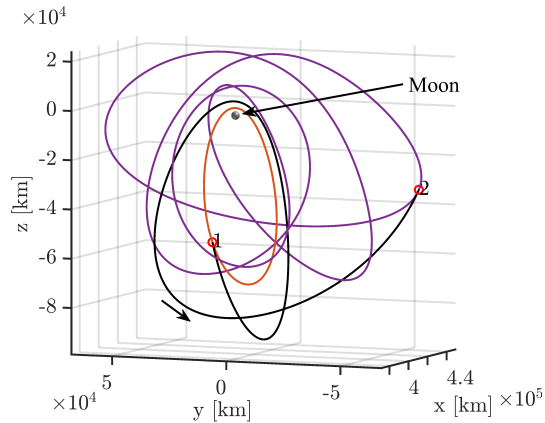
(c) NRHO to P4HO$_2$; $\Delta v = 0.2565\,km/s$; $TOF = 16.36\,days$

Figure 6.3. : Transfers between a 9:2 NRHO and higher-period orbits plotted in the Earth-Moon rotating frame

marker denotes origination at the 3:4 resonant orbit. As a sample initial guess generated via the Poincaré map, the green arrow in Figure 6.5(a) is directed at a P2HO$_2$ unstable manifold crossing on the map, while the black arrow indicates a stable manifold crossing of the 3:4 resonant orbit. Note that close proximity on a Poincaré map alone does not guarantee a good initial guess for a transfer design; since only three of six states are defined by the map ($y = 0$ at the hyperplane crossing and x-$\dot{y}$ (where $\dot{y} = v_y$) coordinates are indicated by the
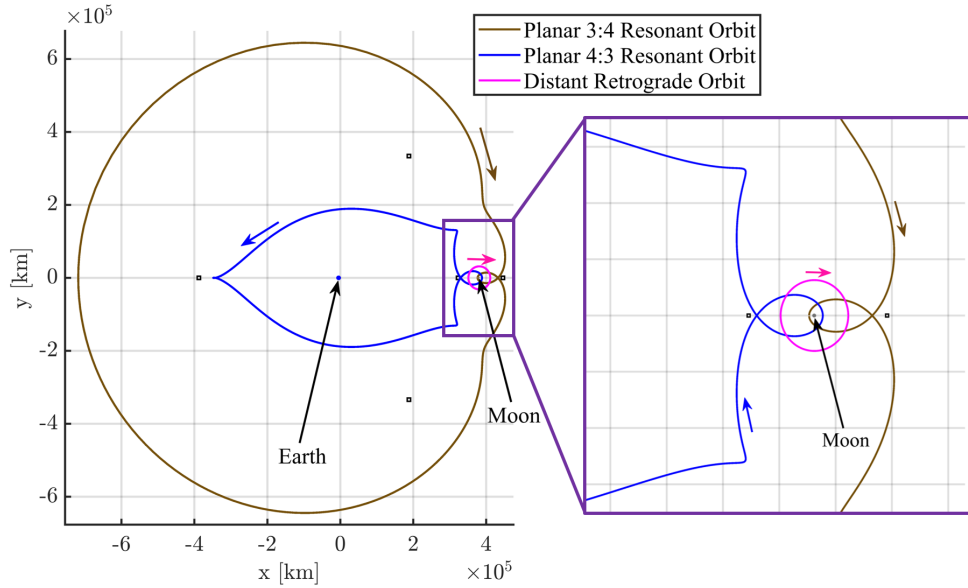
Figure 6.4. : Useful resonant orbits and a DRO at a Jacobi constant value of approximately 3.04719

plotted markers), other considerations are necessary. The trajectory arcs associated with the indicated crossings are plotted in Figure 6.5(b), in red and blue, respectively, along with the periodic orbits from which they are generated. These manifold arcs form the basis of an initial guess to produce a transfer linking the $P2HO_2$ and the DRO.

A variety of transfer geometries that exist between the intermediate higher-period halo orbits and a DRO are illustrated in Figures 6.6 through 6.8. In each transfer, the strategy illustrated in Figure 6.5 is employed to generate the initial guess for the corrections scheme. To maintain the characteristics and geometry of an initial guess for a transfer path constructed through an intentional selection of orbit segments, a minimum norm multiple-shooting scheme enforces constraints and yields a converged solution. Continuity constraints and position constraints on the departure and arrival locations along the intermediate orbit and the DRO, respectively, are included in the corrections process. The converged transfer solution for the initial guess illustrated in Figure 6.5(b) (accessing a manifold from the 3:4 resonant orbit) is plotted in Figure 6.6(a). The final solution includes three maneuvers: one to depart the $P2HO_2$, one on the L_3 side of Earth to accomplish the majority of the plane
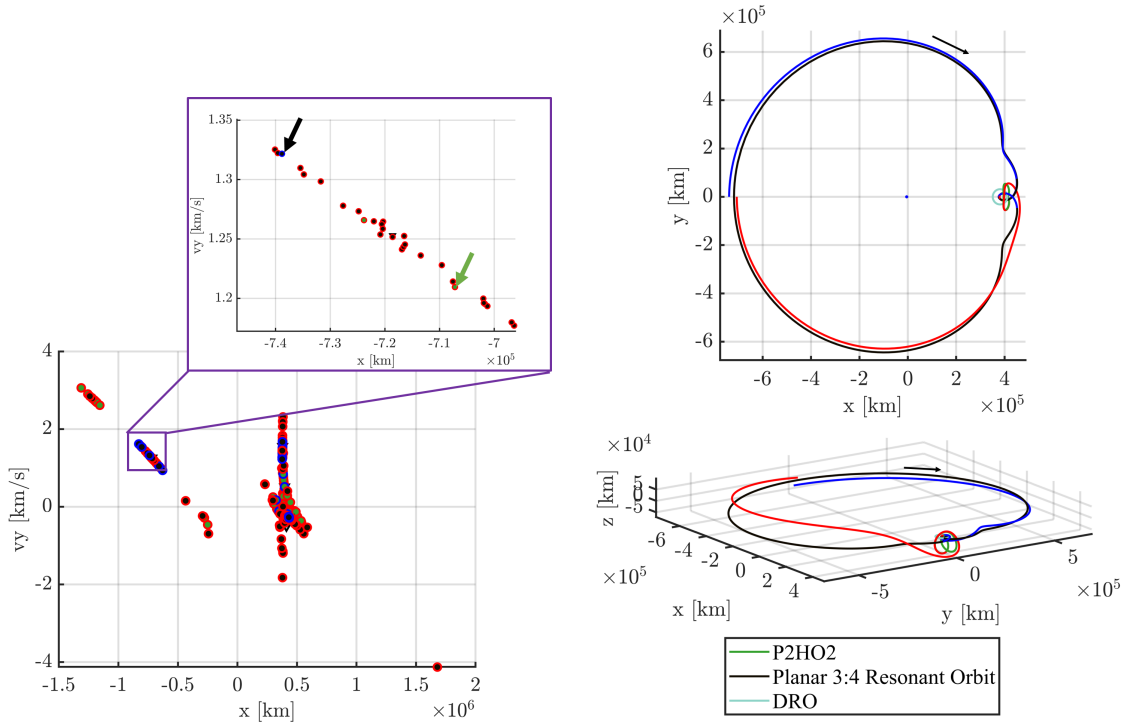
(a) Poincaré map that includes manifold crossings from the P2HO$_2$ (green-centered circles) and 3:4 resonant orbit (black-centered circles); red and blue outlines correspond to unstable and stable manifold trajectories, respectively

(b) Manifolds associated with the selected Poincaré map crossings in Figure 6.5(a)

Figure 6.5. : A Poincaré map is used to select trajectory segments that serve as an initial guess in a targeting scheme.

change, and one to enter the DRO. The total time of flight (TOF) is 89.16 days and the total Δv is 0.5969 km/s (non-optimized). The transfer plotted in Figure 6.6(b) requires a similar total propellant cost (requiring a total Δv of 0.5595 km/s across three maneuvers) with a total TOF of 80.67 days. In this second sample transfer in Figure 6.6(b), a manifold from the P2HO$_2$ is combined with a manifold from a planar 4:3 resonant orbit. The corrections process shifts the arc from the 4:3 resonant orbit out of plane, however, the resonant geometry is still apparent.
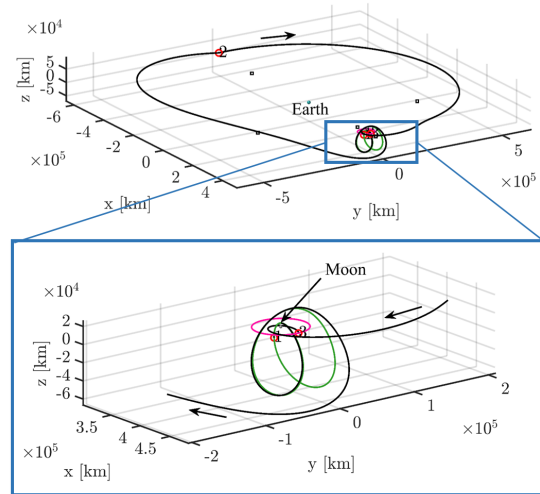
(a) P2HO$_2$ to DRO (via a 3:4 resonant orbit); $\Delta v = 0.5969\ km/s$; $TOF = 89.16\ days$
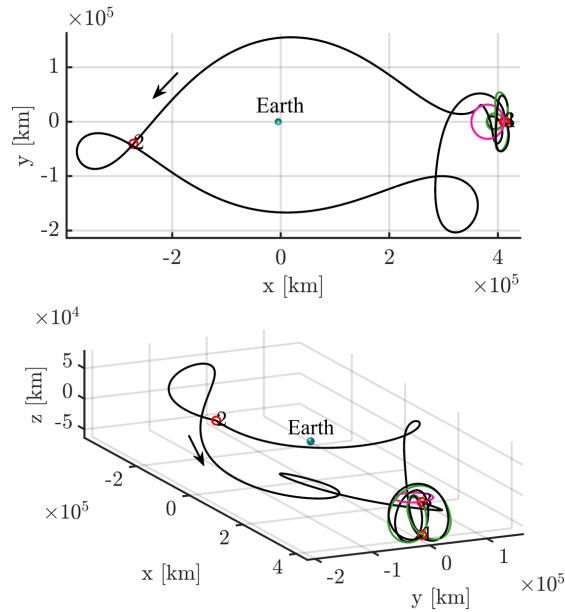
(b) P2HO$_2$ to DRO (via a 4:3 resonant orbit); $\Delta v = 0.5595\ km/s$; $TOF = 80.67\ days$

Figure 6.6. : Transfers between a P2HO$_2$ and a DRO plotted in the Earth-Moon rotating frame

Design of Transfers Linking an Intermediate P4HO$_2$ Orbit and a Destination DRO

Manifolds originating from an intermediate P4HO$_2$ orbit also offer multiple geometries for transfers into the DRO. Three sample converged transfers appear in Figure 6.7; one is

direct and two illustrate geometries that employ secondary intermediate orbits. In Figure 6.7(a), a manifold from the P4HO$_2$ orbit supplies an initial guess for a direct connection into the DRO. The solution requires two maneuvers and a total cost of $\Delta v = 0.4859\,km/s$ over a TOF of 40.69 days. Figure 6.7(b) includes a transfer from the P4HO$_2$ to the DRO using a secondary intermediate arc from a 3:4 resonant orbit for the initial guess. This transfer requires $\Delta v = 0.6341\,km/s$ with three maneuvers over 81.67 days. Note that the majority of the plane change is accomplished via a ballistic arc departing from the vicinity of the P4HO$_2$ after the first maneuver–the unstable manifold supplied in the initial guess delivers much of the required plane change to move from the NRHO to the DRO. The geometry of the transfer in Figure 6.7(b) closely resembles that in Figure 6.6(a) which originates at a P2HO$_2$ orbit indicating that this geometry may utilize a fundamental structure in the lunar vicinity. An alternative geometry appears in Figure 6.7(c). In this transfer, a 4:3 resonant secondary intermediate orbital arc provides the initial guess. Similar to the transfer in Figure 6.6(b), the final solution moves the planar initial guess out of the Earth-Moon plane, however, the general geometry is maintained. The converged transfer incurs a 75.05 day TOF with a total cost of $\Delta v = 0.7613\,km/s$. This transfer path and the associated maneuver cost is non-optimized. The three P4HO$_2$ transfers depicted in Figure 6.7 illustrate significantly different geometries that depend on the respective initial guesses; two transfer options depart the lunar vicinity entirely while one remains near the Moon.

Design of a Transfer Linking an Intermediate P2HO$_1$ Orbit and a Destination DRO

A number of transfers from an NRHO to a DRO are illustrated using a P2HO$_2$ orbit as an intermediate orbit in the design process. Adding secondary intermediate orbits, e.g., resonant orbits, offers a larger range of geometries. But, as previously investigated by Pritchett, Zimovan, and Howell, the P2HO$_1$ orbits, also denoted as butterfly orbits, also offer segments that can be leveraged to deliver initial guesses that represent transfers between the NRHO and a DRO [47]. Significant, however, is the fact that the manifolds

(a) P4HO$_2$ to DRO; $\Delta v = 0.4859\ km/s$; $TOF = 40.69\ days$

(b) P4HO$_2$ to DRO (via a 3:4 resonant orbit; $\Delta v = 0.6341\ km/s$; $TOF = 81.67\ days$

(c) P4HO$_2$ to DRO (via a 4:3 resonant orbit); $\Delta v = 0.7613\ km/s$; $TOF = 75.05\ days$
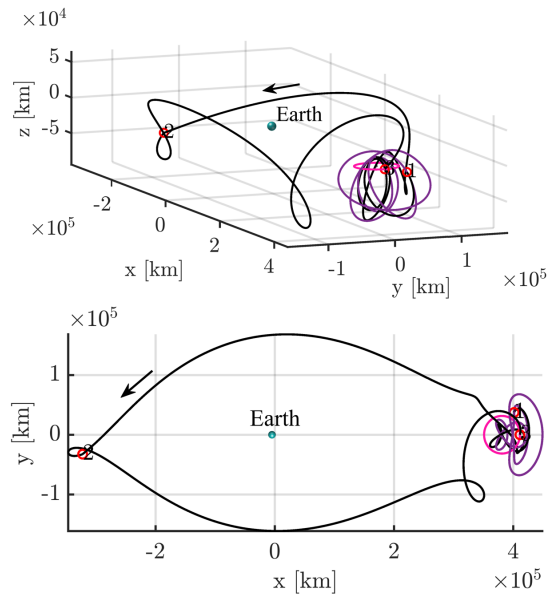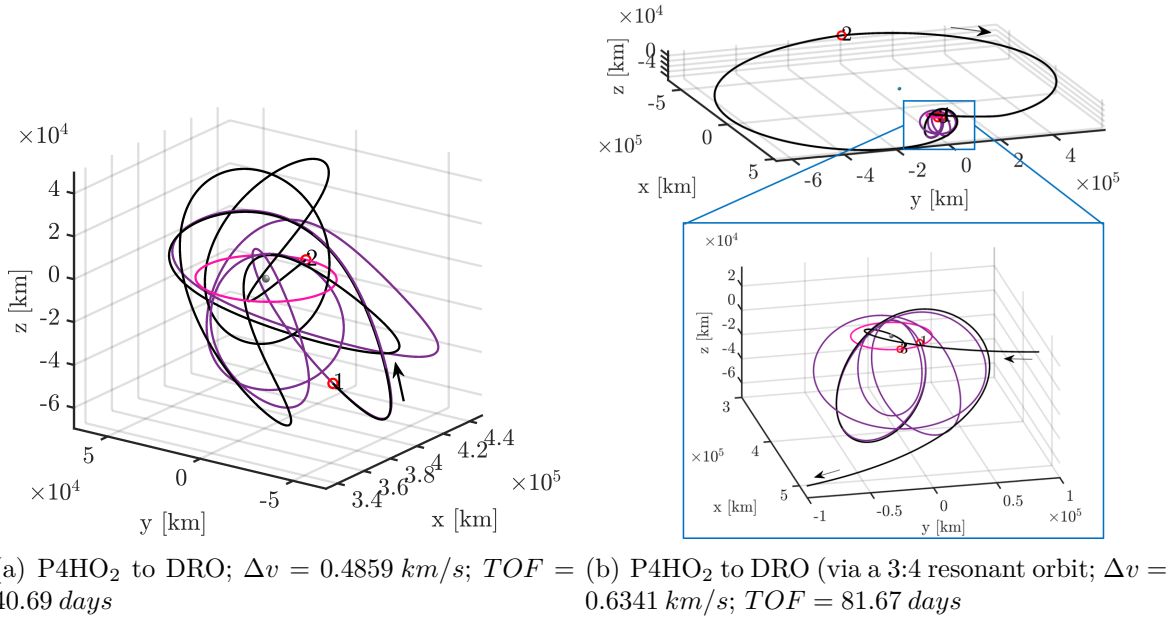
Figure 6.7. : Transfers between a P4HO$_2$ and a DRO plotted in the Earth-Moon rotating frame

originating from certain P2HO$_1$ orbits are *spiral* modes, that is, the path spirals around the orbit while departing/arriving [43], [57]. These orbits possess complex eigenvalues with magnitudes greater than one. Figure 6.8 illustrates a sample case where an unstable manifold

originating from a P2HO$_1$ is linked to a segment from a 4:3 resonant orbit to form a transfer initial guess. The solution possesses three maneuvers with a total Δv of 0.4961 km/s. The transfer TOF is 97.41 days.
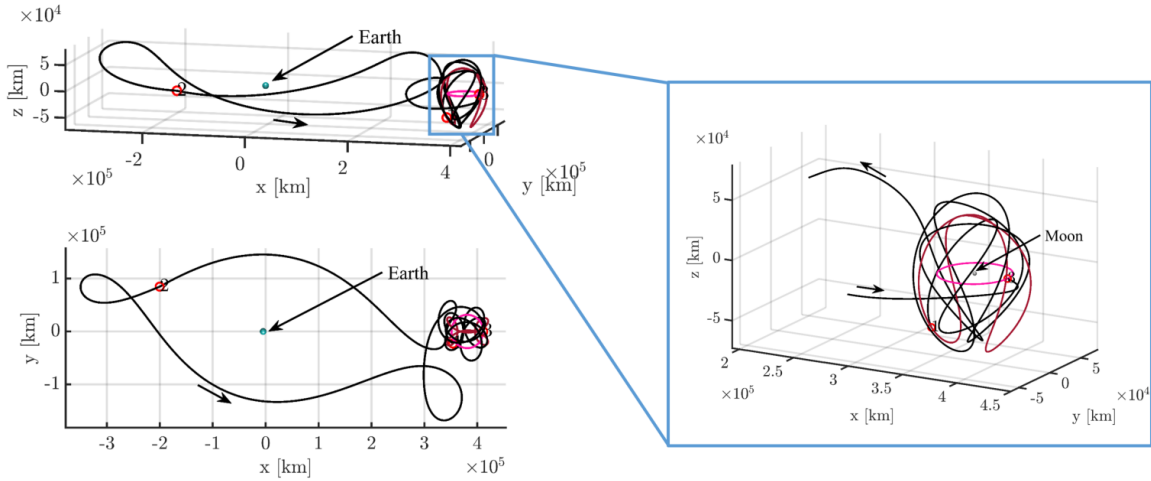
Figure 6.8. : Transfer between a P2HO$_1$ and a DRO (via a 4:3 resonant orbit); $\Delta v = 0.4961\ km/s$; $TOF = 97.41\ days$

Optimization of Transfer Trajectories in the CR3BP

The transfers in Figures 6.6 - 6.8 serve as a representative sub-sample of available transfer geometries that exist between various higher-period halo orbits and the selected DRO. Additionally, incorporating higher-period DRO manifolds from families illustrated in Section 5.4 may offer significant insight into arrival geometries that naturally flow into the region. Without any optimization, reasonable times of flight and propellant costs for predictable solution geometries emerge that maintain the characteristics of the initial guess. Combining a transfer from an NRHO to a higher-period orbit (e.g., one from Figure 6.3) with a transfer from the higher-period orbit to a DRO (e.g., those in Figures 6.6 - 6.8) supplies a converged solution linking an NRHO and a DRO; such solutions serve as starting points for optimization. Since it may not be necessary to transit through the higher-period orbit *en route* to the DRO, transfer times may decrease and geometries may shift slightly within

143

an optimization scheme. Alternatively, transit through the intermediate higher-period orbit may be used for spacecraft phasing or for check-out procedures prior to departure along a second transfer arc. This second arc may leave the vicinity of the NRHO and travel around the Earth-Moon system, or it may remain near the Moon.

As an example of an optimized trajectory in the CR3BP, the transfer arc linking the NRHO and the P2HO$_2$ orbit, plotted in Figure 6.3(b), is optimized using Matlab's `fmincon` procedure [63]. The feasible solution from Figure 6.3(b) is optimized using a sequential quadratic programming (SQP) optimization scheme with a cost function given as min $J = \Delta v_{departure} + \Delta v_{arrival}$. The departure and arrival positions along the initial periodic orbit (the NRHO) and the intermediate periodic orbit (the P2HO$_2$), respectively, are fixed to be equivalent to the locations given in the feasible solution; maneuvers are permitted only at these locations. The TOF along the transfer is allowed to vary and is *not* held to be equivalent to the TOF of the feasible solution. Through the implementation of an SQP optimization scheme, the total required propellant cost for the transfer between the NRHO and P2HO$_2$ is 140.6 m/s with a TOF of 21.34 days. This is equivalent to a cost reduction of 106.03 m/s or a 43% decrease from the original design. For the optimized result, the TOF is approximately 2.25 hours longer than that of the feasible design. The optimized transfer geometry is plotted in Figure 6.9.

In Figure 6.9, the light grey curve corresponds to the feasible design, also plotted in Figure 6.3(b). The optimal trajectory solution is plotted in purple. The orange curve in Figure 6.9 corresponds to the initial orbit, the 9:2 NRHO, while the green curve corresponds to the P2HO$_2$. Red asterisks correspond to locations of maneuvers (and the location of the departure/arrival position constraints). Although the maneuvers occur at the same position values as in the feasible solution, their components and magnitudes are different from those in the feasible solution, thus yielding a lower cost for the transfer design. Characteristics of the initial guess (plotted in Figure 6.2(b)) and the feasible solution (illustrated in Figure 6.3(b)) are maintained in this reduced-cost configuration.
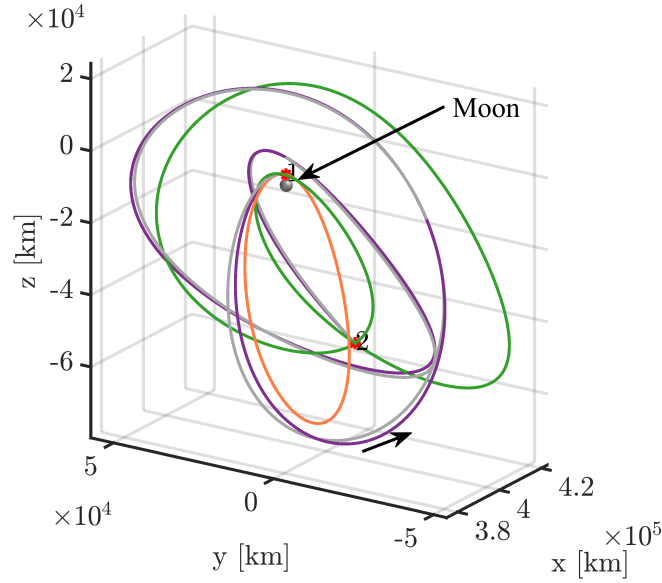
Figure 6.9. : Optimized transfer linking an NRHO and a P2HO$_2$; $\Delta v = 0.1406 \ km/s$; $TOF = 21.34 \ days$

An alternative formulation, one where TOF is constrained to be equal to that in the initial CR3BP feasible solution and the cost function is slightly modified, is provided by Zimovan-Spreen, Howell, and Davis in 2019 [46]. The transfer trajectory linking the NRHO and a P2HO$_2$, in Figure 6.3(b), and the transfer arc from that particular P2HO$_2$ to the DRO, in Figure 6.6(a), are optimized using Matlab's `fmincon` procedure [63]. This optimization scheme uses a combination of cost functions and built-in algorithms to produce alternative time-fixed, reduced-cost transfers. First, the feasible solution is optimized using an interior-point method with an objective of min $\bar{J} = \sum_i (\Delta v_i)^2$. In this cost function, Δv_i represents the maneuver magnitude at each patch point, including the departure and arrival maneuvers. This objective function is selected due to its favorable conditioning and the existence of relatively simple partial derivatives. As a second step, the optimal result seeds an SQP optimization scheme with a cost function given as min $\widetilde{J} = \sum_i \Delta v_i$. This second phase provides some additional reduction in cost and the objective function, $\widetilde{J}$, by minimizing the total transfer cost. Note that minimizing $\bar{J}$ does not always equate to minimizing $\widetilde{J}$, however, a two-step optimization scheme is used due to numerical challenges within the formulation in $\widetilde{J}$. For each of the two optimization steps, the departure and arrival positions along the

initial periodic orbit and the final periodic orbit, respectively, are fixed to be equivalent to the locations given in the initial feasible solution. Additionally, the TOF along the transfer arcs is constrained to be equivalent to the TOF of the corresponding feasible solution. In this alternative formulation, maneuvers are allowed at any patch point along the trajectory; the total number of maneuvers may increase from that in the feasible solution. The resulting optimized transfer geometries for both phases of the transfer between the NRHO and the DRO are plotted in Figure 6.10.
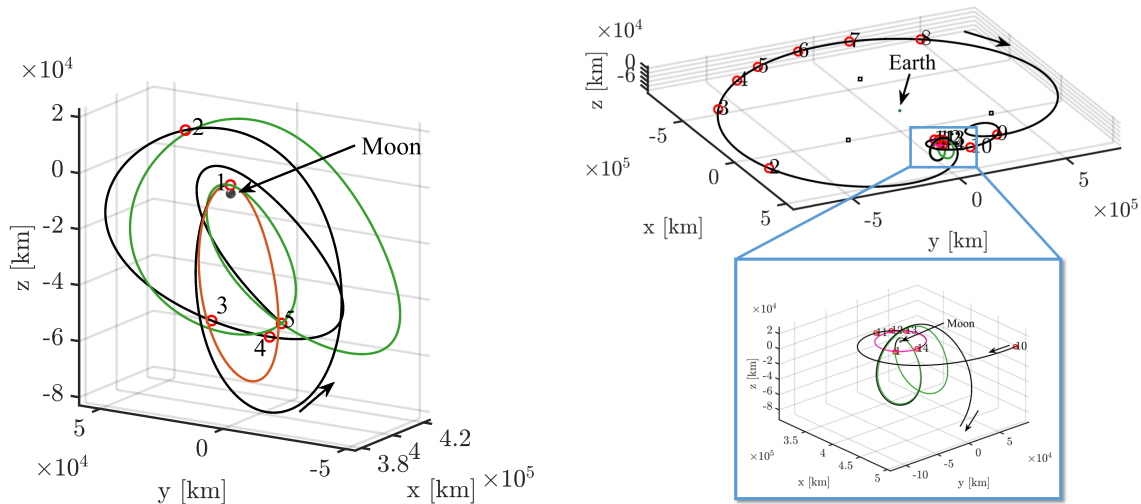
(a) Phase 1: NRHO to P2HO$_2$; $\Delta v = 0.0899 km/s$; $TOF = 21.25\,days$

(b) Phase 2: P2HO$_2$ to DRO; $\Delta v = 0.2156\,km/s$; $TOF = 89.16\,days$

Figure 6.10. : Optimized transfer from an NRHO to a DRO via a P2HO$_2$, maneuvers are numbered and marked as red circles

With this formulation, phase one of the transfer, a segment connecting the NRHO to the P2HO$_2$, requires a total cost of 89.9 m/s over four maneuvers. The geometry of the feasible solution (plotted in Figure 6.3(b)) is readily apparent in the reduced-cost result in Figure 6.10(a) and the TOF-variable optimized result in Figure 6.9. The second phase of the transfer, plotted in Figure 6.10(b), links the P2HO$_2$ to a DRO. The total cost over fourteen maneuvers is 0.2156 km/s. Characteristics of the initial guess (plotted in Figure 6.5(b)) and the feasible solution (illustrated in Figure 6.6(a)) are maintained in this reduced-cost config-uration. Notice that differing cost functions and constraints on the trajectory yield different results from the optimizer, even though both cases are considered local minima. It is critical

146

to carefully define constraints (e.g., TOF-fixed or free and number of allowable maneuvers along a trajectory) and optimization goals in order to produce the desired optimized result.

6.1.2   Transition to a Higher-Fidelity Ephemeris Model

As an example of a two-phase transfer in which an intermediate higher-period orbit is included along the path, the transfer trajectories linking the NRHO to the P2HO$_2$, appearing in Figure 6.3(b), and the transfer arc from that particular P2HO$_2$ to the DRO, plotted in Figure 6.6(a), are concatenated and transitioned to the higher-fidelity ephemeris model. If optimization is the final goal, it is *not* necessary to optimize the CR3BP solution prior to transitioning and optimizing in the ephemeris model. Doing so may provide an alternative optimized ephemeris solution, but it will not necessarily be lower-cost. The initial epoch along the NRHO is selected such that the geometry along the synodic resonant NRHO successfully avoids Earth and lunar eclipses [45]. Three ballistic revolutions along the intermediate P2HO$_2$ are incorporated in the NRHO to DRO transfer trajectory. This segment offers flexibility to the corrections algorithm to eventually meet additional constraints along the transfer path. Initially, no eclipse avoidance constraint is included in the multiple-shooting scheme used to transition the trajectories into the higher-fidelity model, thus, each phase along the transfer trajectory is free to encounter eclipse conditions. The unoptimized, continuous ephemeris transfer trajectories are plotted in the classical Earth-Moon rotating frame in Figure 6.11. Note that the ephemeris solution geometry closely resembles the CR3BP solution for both phases of the transfer. The initial phase along the transfer between the NRHO and the P2HO$_2$ orbit, plotted in Figure 6.11(a), possesses eclipsing events that occur along portions of the trajectory beyond the revolutions in the NRHO. This segment possesses a 0.5 hour lunar eclipse followed approximately 38.2 days later by a 4 hour Earth eclipse; both of these events are highlighted in the figure. Figure 6.11(b) illustrates the second phase of the transfer. The initial Julian date along the P2HO$_2$ orbit is consistent with the end date of the NRHO to P2HO$_2$ ephemeris trajectory plotted in Figure 6.11(a) to ensure these trajectories represent an end-to-end NRHO to DRO transfer when combined.

In this transfer, there are four lunar eclipsing events and one Earth eclipsing event, each lasting an average 1.8 hours; the passages through shadow are highlighted in Figure 6.11(b). Recall, the initial guess for the transfer (produced in the CR3BP) did not include any eclipse avoidance constraints. The total Δv for the end-to-end transfer is 1.035 km/s.
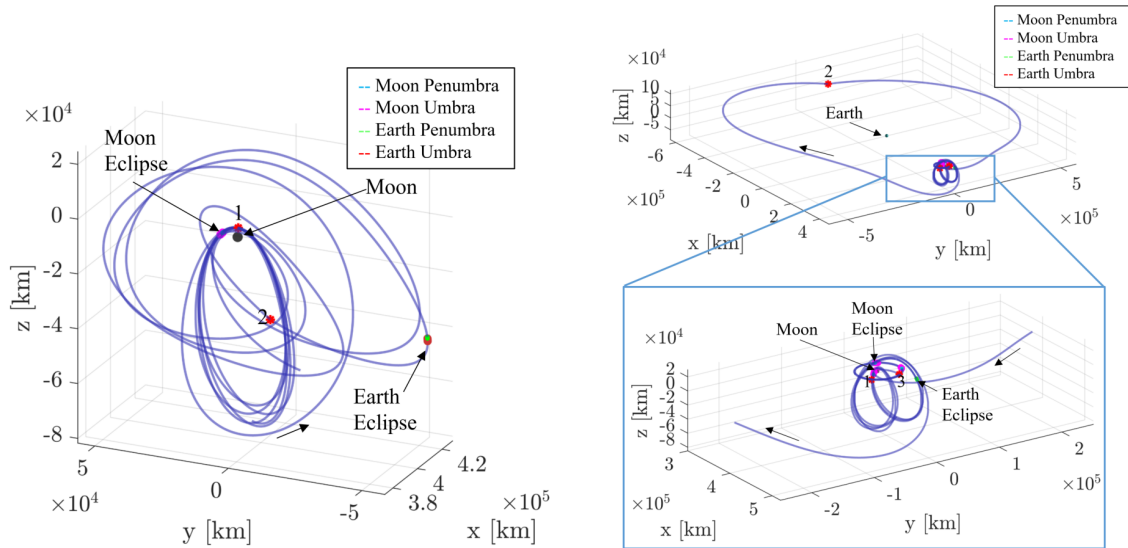
(a) Transfer between the 9:2 synodic resonant NRHO and a P2HO$_2$ orbit; $\Delta v = 0.3425\ km/s$; $TOF = 21.57\ days$

(b) Transfer between a P2HO$_2$ and a DRO; $\Delta v = 0.6921\ km/s$; $TOF = 89.34\ days$

Figure 6.11. : Transfer trajectories computed in a higher-fidelity ephemeris model

The views of the transfers in the Sun-Earth and Sun-Moon rotating frames illustrate the passages of the trajectory through the shadows of the Earth and Moon, respectively. In each of these rotating frame views, the shadow of the smaller body (i.e., the Earth or Moon) remains fixed along the respective positive x-axis. Additionally, when viewing the transfer trajectory in these frames, the yz-projection is equivalent to a view looking down the shadow cone of the respective primary. Figures 6.12 and 6.13 illustrate the transfers from Figures 6.11(a) and 6.11(b), respectively, in the Sun-Moon and Sun-Earth rotating frames.

To satisfy potential mission requirements, the transfer trajectories connecting the NRHO to the DRO must be eclipse-free. Re-converging the transfers from the CR3BP to the ephemeris model while enforcing the eclipse avoidance path constraint from Section 3.1.5 yields the results displayed in Figure 6.14 in the Earth-Moon rotating frame. In this

(a) Sun-Moon rotating frame

(b) Sun-Earth rotating frame
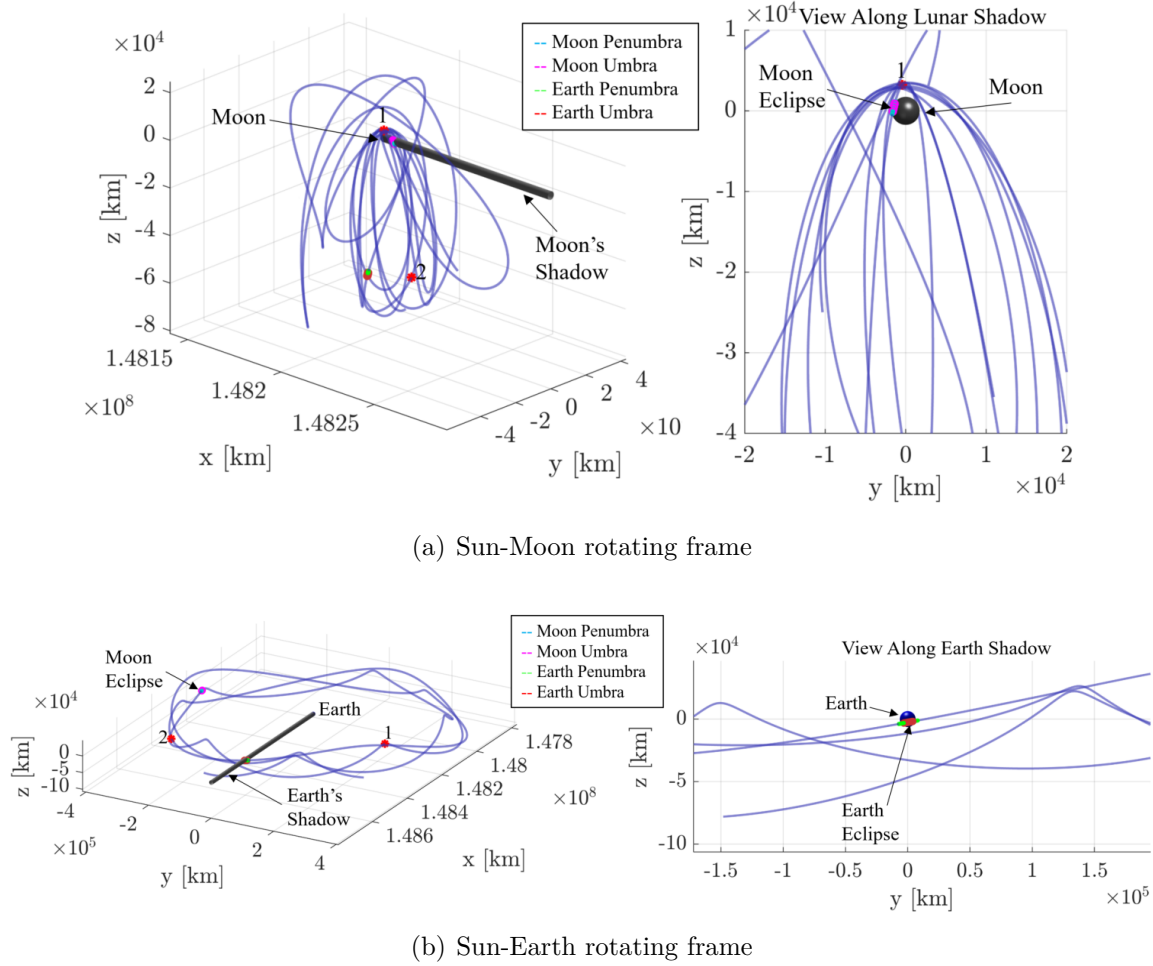
Figure 6.12. : Transfer between the 9:2 synodic resonant NRHO and a P2HO$_2$ in the higher-fidelity ephemeris model without eclipse avoidance constraint enforced

case, both transfer solutions approximately maintain the CR3BP geometry, however, all Earth and lunar eclipses are avoided. The TOF along each phase of the transfer does not significantly change when the eclipse avoidance constraint is enforced, increasing from 21.57 days to 21.81 days for the NRHO to P2HO$_2$ portion of the transfer and increasing from 89.34 days to 89.46 days for the P2HO$_2$ to DRO phase of the transfer. Phase one of the transfer has a cost relatively similar with and without the eclipse avoidance path constraint; the cost decreases by about 14.2 m/s when the eclipse avoidance constraint is enforced. The cost for the second phase of the transfer increases slightly once the eclipse avoidance constraint is enforced due to the fact that the lunar flyby prior to arrival along the DRO
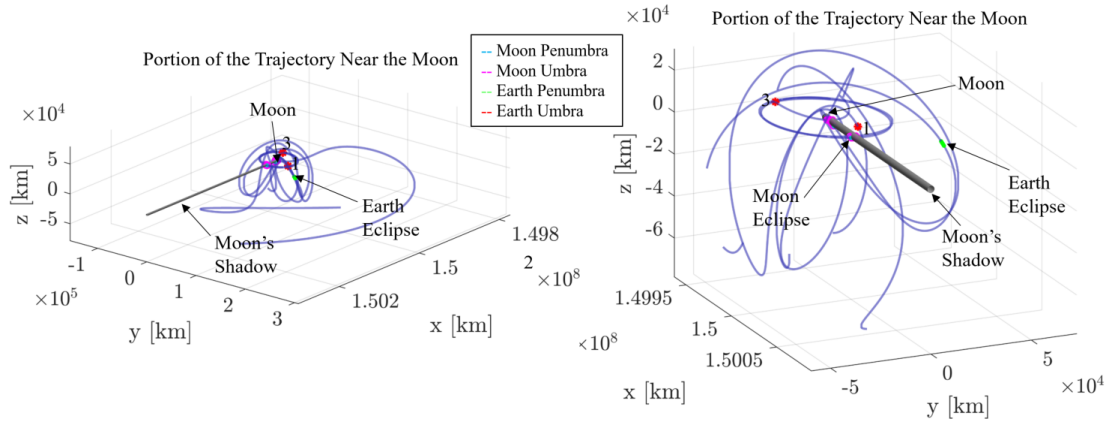
(a) Sun-Moon rotating frame
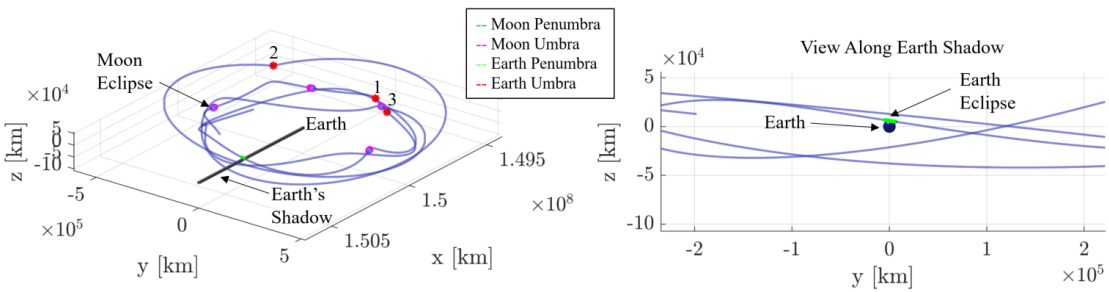
(b) Sun-Earth rotating frame

Figure 6.13. : Transfer between a P2HO$_2$ and a DRO in the higher-fidelity ephemeris model without eclipse avoidance constraint enforced

(apparent in Figure 6.11(b)) is no longer incorporated once lunar eclipses are prohibited, thus, the cost of the transfer increases by 0.3887 km/s. Modifying the epoch of arrival by remaining in the intermediate P2HO$_2$ orbit for additional/fewer revolutions could avoid the lunar eclipse while still allowing for a flyby to yield lower transfer costs. Figure 6.15 illustrates the NRHO to P2HO$_2$ transfer in the Sun-Moon and Sun-Earth rotating frames; the eclipse avoidance constraint is enforced for these transfer trajectories. Note that the trajectory does *not* pass through either the Moon or Earth shadows. Similarly, Figure 6.16 illustrates the P2HO$_2$ to DRO transfer in the Sun-Moon and Sun-Earth rotating frames, and all shadows are successfully avoided in an ephemeris solution. Reduction of the transfer cost in the ephemeris model is possible through an optimization scheme; the non-optimized, eclipse-free solutions serve as a starting point for that optimization process.
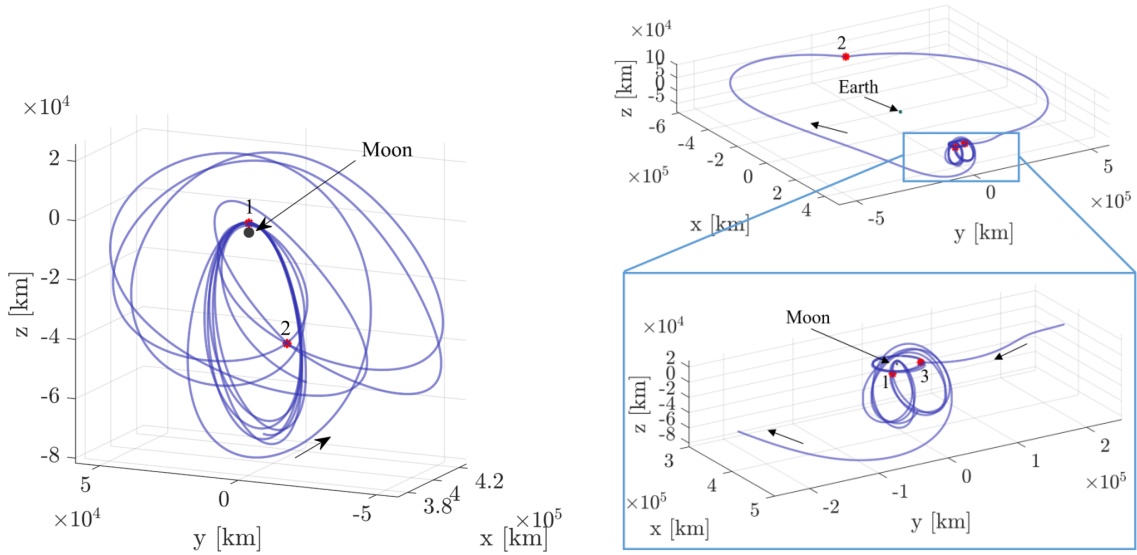
(a) $\Delta v = 0.3283 km/s$; $TOF = 21.81 days$ between maneuvers

(b) $\Delta v = 1.0808 km/s$; $TOF = 89.46 days$ between maneuvers one and three

Figure 6.14. : Eclipse-free transfer between the 9:2 NRHO and a P2HO$_2$ (a) and a P2HO$_2$ and DRO (b) in a higher-fidelity ephemeris model

6.2 Recovery of Inadvertent Departures from an NRHO Using Nearby Structures

The current baseline trajectory for the Gateway is a 9:2 lunar synodic resonant southern L_2 Near Rectilinear Halo Orbit (NRHO) [74]. The NRHO is a nearly-stable orbit, thus, orbit maintenance (OM) costs are typically low. Regular OM, however, is required for a spacecraft to remain in the NRHO over the long-term [48], [73], [75]. If scheduled orbit maintenance maneuvers (OMMs) are repeatedly missed, or in the case of accidental thrust, ballistic trajectories tend to depart naturally from the NRHO either toward heliocentric space, toward the vicinity of the Earth, or to lunar impact [36], [71].

Previous investigations have characterized intentional departures from the NRHO baseline orbit for heliocentric disposal options and lunar impactor missions. Davis et al. determine that a small departure burn is sufficient to predictably initiate departure from the NRHO baseline orbit into heliocentric space. However, uncontrolled perturbations can
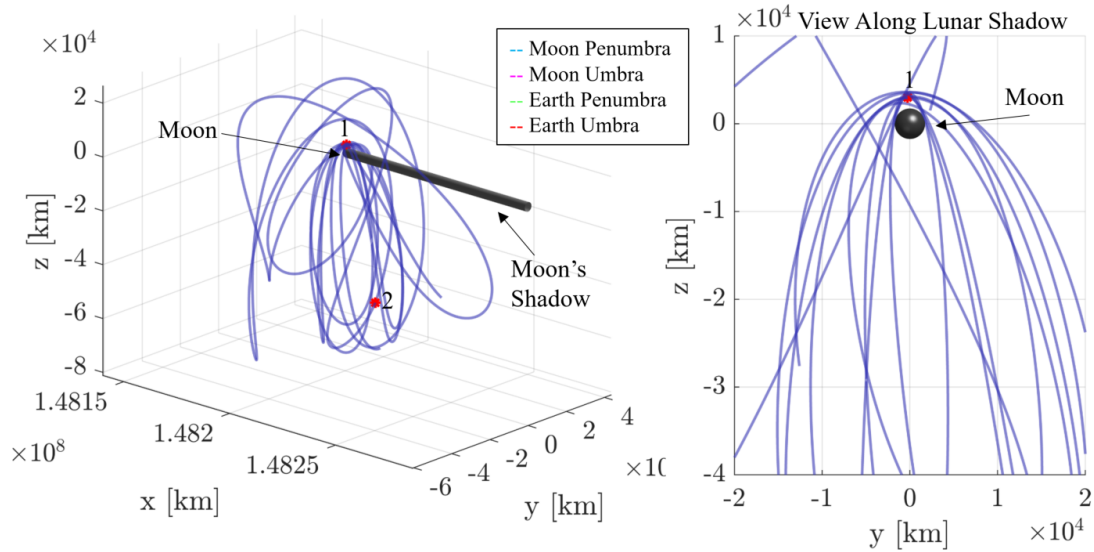
(a) Sun-Moon rotating frame
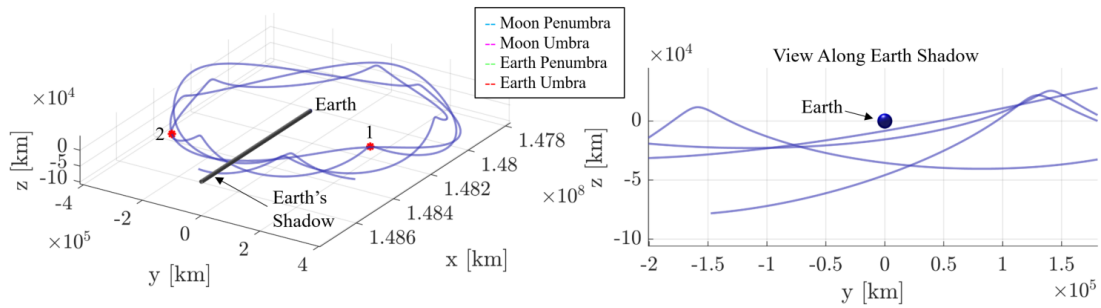
(b) Sun-Earth rotating frame

Figure 6.15. : Eclipse-free transfer between the 9:2 synodic resonant NRHO and a P2HO$_2$ in the higher-fidelity ephemeris model

also lead to departures from the NRHO when OM is not active. The departure then evolves within an expected timeframe [36], [37]. Davis et al. also investigate low Δv magnitude lunar impactor trajectories originating from the NRHO in the CR3BP [36]. Unintentional departures of the spacecraft from an NRHO suggest a small potential for lunar impact, as well. Thus, while previous authors have investigated strategies to depart intentionally from the NRHO for various mission applications, there has not yet been significant work investigating recovery of departing trajectories for return to the baseline NRHO. Analysis of NRHO departure/recovery trajectories is relevant in the case of a 'runaway' spacecraft and
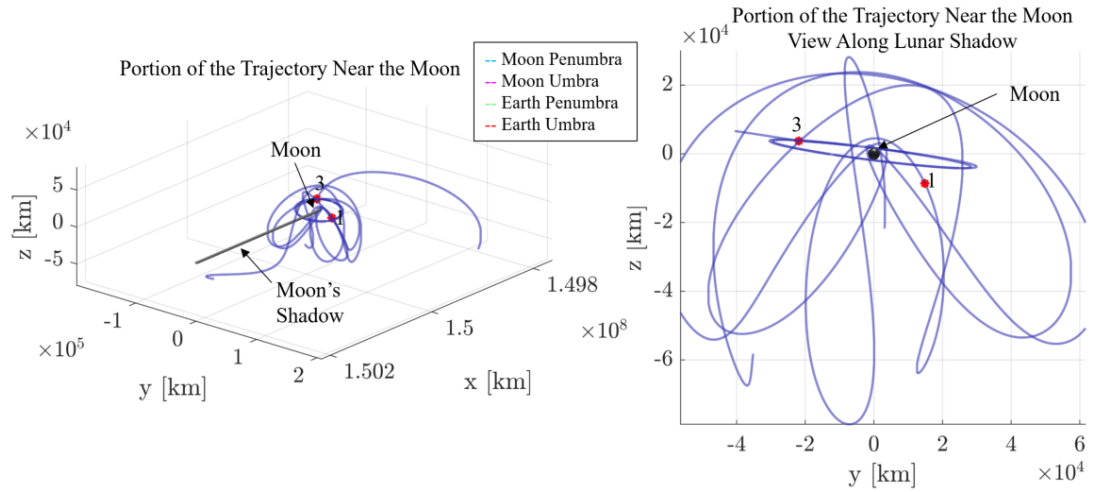
(a) Sun-Moon rotating frame
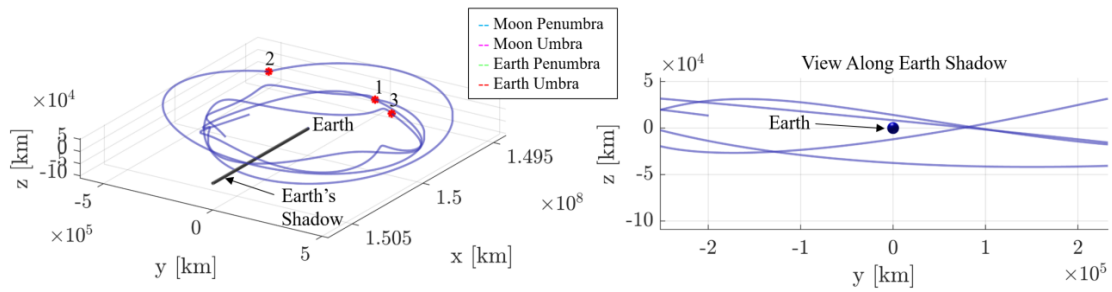
(b) Sun-Earth rotating frame

Figure 6.16. : Eclipse-free transfer between a P2HO$_2$ and a DRO in the higher-fidelity ephemeris model

unintentional departures, as well as for mission scenarios designed to depart, and then later return, to the same baseline NRHO, e.g., a CubeSat.

As described in Reference [44], strategies for the recovery of trajectories departing from the NRHO are categorized in terms of three regimes. Regime 1 encompasses departing flow that can be reliably recovered by a standard OM approach. Departing trajectories that remain in the lunar vicinity, but are not recoverable by OM maneuvers, are deemed to be in recovery regime 2. Finally, recovery regime 3 includes trajectories that have departed from the lunar vicinity toward heliocentric space or toward the Earth; such departures may then be more difficult and expensive to recover. It is expected that Earthbound departures

may be recoverable using cislunar structures similar to those used for regime 2 recovery. Examples of departures in each regime appear in Figure 6.17.
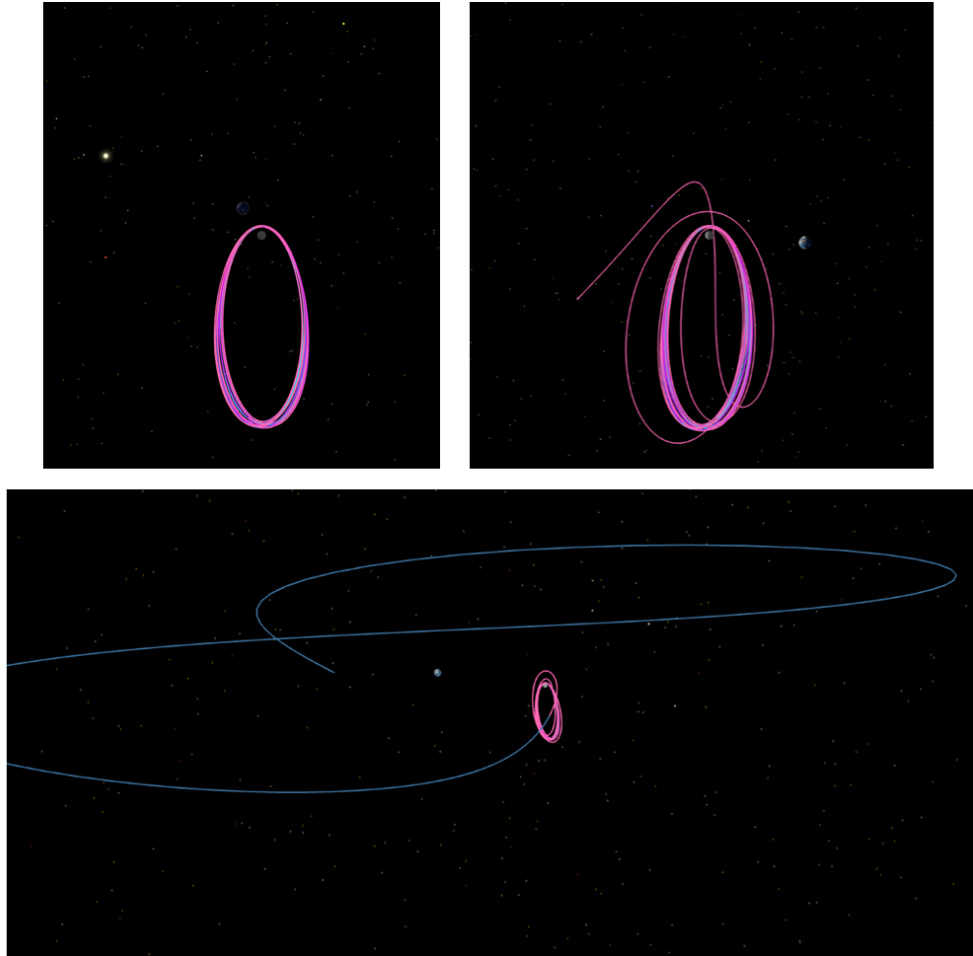
Figure 6.17. : Departure trajectory in recovery regime 1 (upper left), regime 2 (upper right), and regime 3 (bottom center) [44]

Regime 2 denotes the portion of a departing trajectory when OM targeting is no longer effective to return the spacecraft to the baseline NRHO due to a failure of the OM algorithm to converge. Depending on the errors present in the spacecraft trajectory, regime 2 is entered after 7-11 revolutions without orbit maintenance. The spacecraft remains in regime 2 for about six revolutions, though the precise duration depends on the specific departing trajectory and is dependent on epoch and perturbations on the spacecraft. In this regime, the spacecraft is further from the baseline NRHO than in regime 1, but still remains within

the lunar vicinity. Because a standard OM recovery approach, generally successful for regime 1, no longer reliably converges on a recovery trajectory solution an alternative approach is necessary. Therefore, in regime 2, the spacecraft is first shifted into an intermediate orbit, where phasing or spacecraft check-out is performed. Once the spacecraft is safely in the intermediate orbit, a second transfer arc, from the intermediate orbit back to the baseline NRHO, is implemented.

To demonstrate the recovery methodology for regime 2, a sample departure trajectory is generated in an ephemeris model. A spacecraft state along the departure trajectory, termed the "recovery state," is assigned as the initial point along the recovery trajectory. The recovery state is defined in the Earth-Moon rotating frame and is identified as a fixed point in the corrections process. The initial design for the recovery is completed in the CR3BP. Next, the CR3BP recovery trajectory is transitioned to an ephemeris model and the total Δv is minimized. When transitioning to the ephemeris model, the recovery state (and its associated epoch time) is assumed fixed within the corrections process. Further refinements and/or optimization schemes can then be accommodated.

6.2.1   Generation of Sample Departures for Recovery

To demonstrate the recovery process, sample departing trajectories are first generated in an Earth-Moon-Sun ephemeris model [43]. States along the NRHO reference trajectory between 08:09:36 UT on 2 January 2024 and 08:09:36 UT on 2 January 2025 are randomly selected and a perturbation of 2 m/s in the velocity direction is incorporated. The NRHO reference trajectory is available in a SPK-type kernel compatible with the SPICE ephemeris system and is available on the JPL website [82]. A variety of true anomaly values are considered, not only those that correspond to perilune or apolune states along the NRHO. The perturbation does not significantly modify the departure trajectory geometry from ballistic departing motion, but rather reduces the number of revolutions that the spacecraft remains in the immediate NRHO vicinity; the maneuver simply speeds up analysis time and reduces numerical error introduced through extended numerical integration time. The perturbed

155

state is propagated for 100 days or until the propagated trajectory crosses a hyperplane defined as a specified value of the x-coordinate, i.e., the value at the L_1 or L_2 Lagrange points. A selection of trajectories departing from the baseline NRHO are plotted in the Earth-Moon rotating frame in Figure 6.18. The blue trajectory represents the baseline NRHO while each of the other colored curves represents a different ephemeris departure trajectory.

6.2.2 NRHO Manifold Trajectories

The ephemeris departures from the NRHO, plotted in Figure 6.18, closely follow CR3BP unstable manifold trajectories, indicating that the lower-fidelity model provides a reasonably accurate representation of the dynamics in the lunar vicinity. Insight into alternative departing geometries from the NRHO, beyond the computed sample ephemeris departures, is offered through propagation of unstable manifold trajectories in the CR3BP. Additionally, CR3BP trajectories that ballistically approach the NRHO from the lunar vicinity, those that aid in the design of the second phase of regime 2 transfers from an intermediate orbit back to the NRHO, are offered through CR3BP NRHO stable manifolds.

In 2019, Davis et al. produced a subset of the manifolds departing from the CR3BP 9:2 NRHO (those near apolune) and observed that the angle between the stable and unstable eigenvectors along the 9:2 NRHO near perilune is near zero [36]. Davis et al. state that the stable and unstable eigenvectors (and thus, the manifold structures) are not well defined near perilune due to the small angle between the eigenvectors in addition to strong nonlinear effects and numerical challenges associated with the close proximity to the Moon. In this research, a range of step-off distances, $5\ km \leq \epsilon \leq 50\ km$ are taken along the eigenvectors defined near apolune and used to compute manifold trajectories. This strategy, discussed in Section 4.3, offers an alternative method to find a more complete representation of the unstable and stable manifold structures departing/approaching the 9:2 NRHO. By including a range of step-off distances, different portions of the manifold tube are accessed, including portions that may originate near the more challenging perilune region. In fact, a single step-off distance taken along eigenvectors around the *entire* NRHO (including near perilune) offers

156
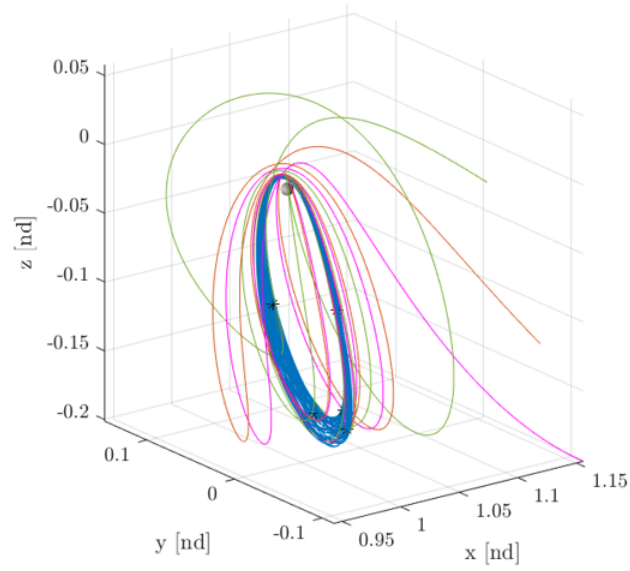
(a)
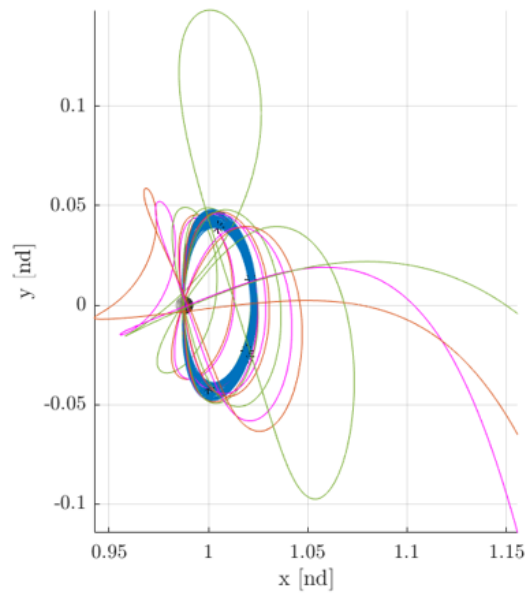
(b)

Figure 6.18. : Sample trajectories that depart from the 9:2 NRHO baseline orbit computed in an ephemeris model and plotted in a nondimensional Earth-Moon rotating frame

an identical result indicating that the manifold tubes can actually be accurately computed along the entire NRHO.

The 9:2 lunar synodic resonant NRHO manifolds are plotted in Figure 6.19. Maroon and orange colored trajectories correspond to unstable manifold trajectories that depart from the NRHO; a maroon color indicates a step in the positive unstable eigenvector direction, while trajectories colored orange indicate a step taken in the negative unstable eigenvector direction. On the other hand, blue colored trajectories correspond to stable manifold trajectories that approach the NRHO in forward time; light blue corresponds to a step in the negative eigenvector direction while dark blue corresponds to a step taken in the positive eigenvector direction to generate the stable manifold trajectories. The manifold trajectories originate from 100 points along the NRHO that are equally spaced in time. Each manifold arc is propagated for 100 days TOF. A position-normalized step of 15 km along the eigenvector directions along the orbit is used to propagate the trajectories.

To simplify the visualization of the trajectories arriving/departing from the NRHO via manifolds, an x-v_x Poincaré map is computed. To generate the map, the NRHO manifolds are propagated for a slightly longer duration TOF than that depicted in Figure 6.19. In Figure 6.20, a 300 day TOF is used for the propagation of each manifold along with a 15 km step-off distance along the eigenvector direction. The propagation is terminated if a manifold trajectory intersects the surface of the Earth or Moon, or if an x-coordinate that is 15 nondimensional units from the barycenter of the Earth-Moon system is reached. In Figure 6.20, blue dots correspond to stable manifold trajectory intersections with the hyperplane, defined at $y = 0$ in the rotating frame, while maroon dots correspond to unstable manifold trajectory intersections with the $y = 0$ rotating frame. The x-coordinates of the collinear Lagrange points are indicated by black lines and are labeled on the map, as well.

Additional investigation of trajectories on the unstable manifold of the NRHO is relevant to understanding ballistic (or low-Δv) departure scenarios from the NRHO. Limiting the Poincaré map in Figure 6.20 to hyperplane crossings of trajectories that occur within the bounds defined by the x-coordinates of the L_1 and L_2 Lagrange points within 100 days TOF of departure from the NRHO provides a subset of the unstable manifolds for further analysis. Figure 6.21(a) depicts the map colored by time since departure from the NRHO,
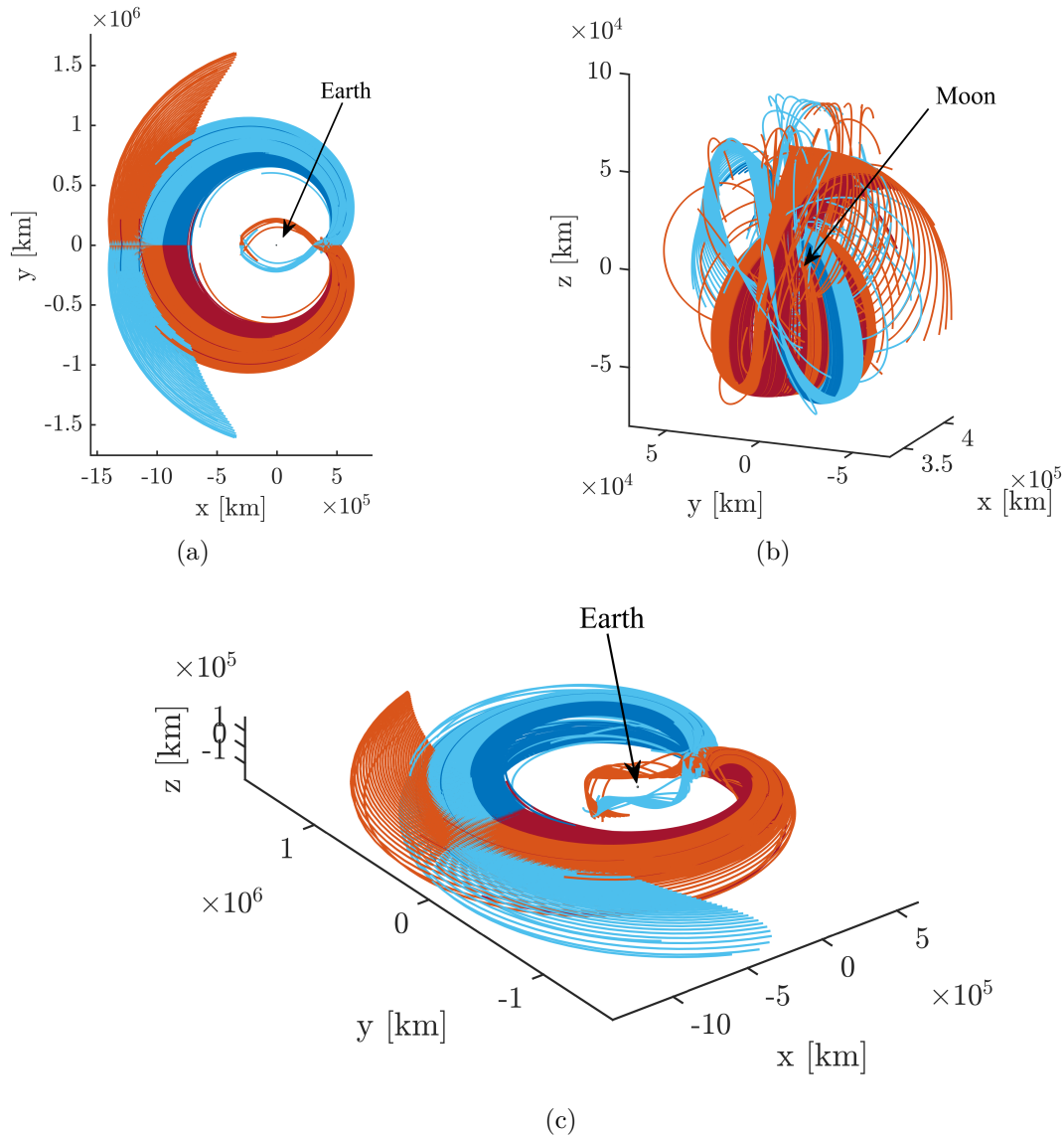
Figure 6.19. : Stable and unstable manifolds of the 9:2 lunar synodic resonant NRHO in the Earth-Moon rotating frame

or equivalently, the propagation time (TOF) from the initial condition along the manifold trajectory to the corresponding intersection with the $y = 0$ plane. Arrows indicate that the darker colored markers are centered around the crossings of the periodic orbit on the map; the manifolds remain quite close to the periodic orbit initially. Figure 6.21(b) depicts the same map as that in Figure 6.21(a), however, Figure 6.21(b) is colored by the osculating Keplerian true anomaly of the departure location along the NRHO. Note, the Keplerian true
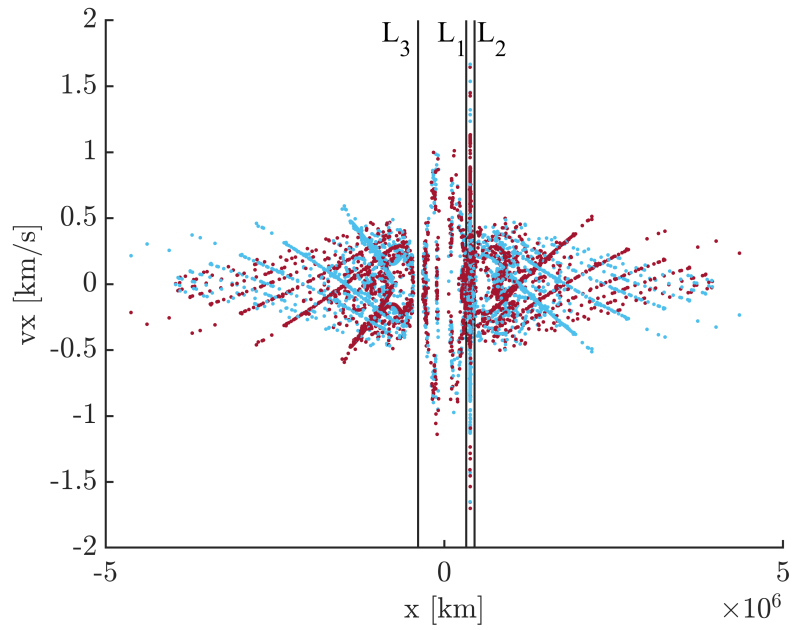
(a) Poincaré map
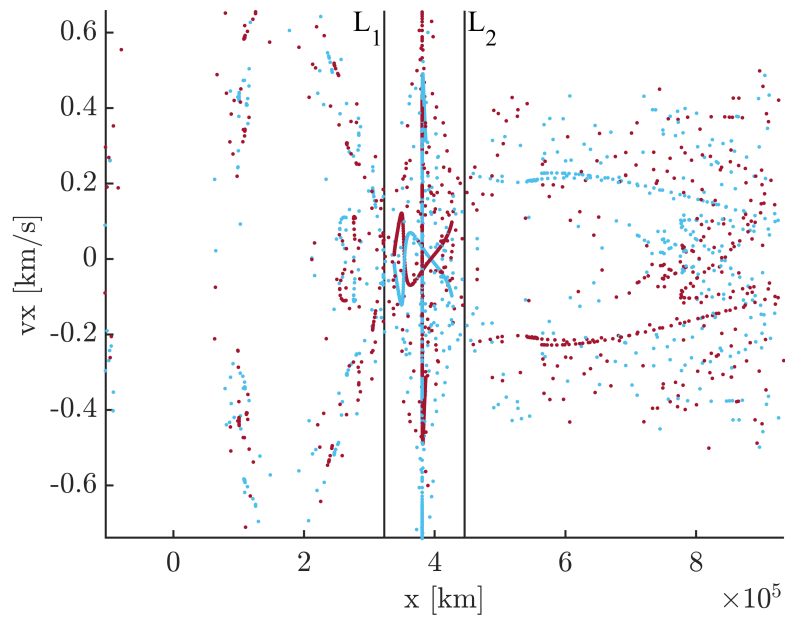
(b) Portion of Poincaré map from (a) near the Moon

Figure 6.20. : An x-v_x Poincaré map ($\Sigma : y = 0$) of the stable and unstable manifolds of the 9:2 lunar synodic resonant NRHO in the Earth-Moon rotating frame

anomaly is computed by first transitioning the NRHO from the Earth-Moon rotating frame to an arbitrary Moon-centered inertial frame. Then, the instantaneous inertial position and velocity values in that frame are used to compute true anomaly. The arbitrary inertial frame is defined such that the rotating frame x-axis and inertial frame X-axis are aligned when the spacecraft is at apolune. Additionally, the rotating z-axis and inertial Z-axis are aligned for all time. Caution should be used when correlating a manifold departure location to a true anomaly along an orbit. The value of true anomaly reported assumes a step off of 15 km along an eigenvector direction normalized by position components, as discussed in Section 4.3. Generating the map in Figure 6.21(b) using an alternative step-off distance or normalization scheme for the unstable eigenvector will produce different results since a different portion of the invariant unstable manifold tube may be accessed from what appears to be the same true anomaly. A value of true anomaly is, however, still useful to classify types of departures, but assumptions are important to the interpretation of the map. The 9:2 lunar synodic resonant NRHO appears in Figure 6.22 in the Earth-Moon rotating frame and is colored by true anomaly value. Note that the true anomaly angle changes very rapidly near perilune and changes slowly near apolune along the NRHO [83].

Departure location on an unstable manifold trajectory originating along the NRHO can be linked to eventual trajectory destination. Recall, this analysis assumes a 15 km step-off distance along unstable eigenvector directions normalized by the position components. In Figures 6.23(a) and 6.23(b), the 9:2 NRHO is colored by eventual destination of the unstable manifold trajectory. Figure 6.23(a) corresponds to departures along the half-manifold surface associated with negative eigenvector directions, while Figure 6.23(b) corresponds to departures along the half-manifold associated with positive eigenvector directions. The 'direction' of the eigenvector as positive or negative is defined at apolune; the positive eigenvector direction is defined by a positive y-component while the negative eigenvector direction has a negative y-component at the apolune fixed point. The STM is used to translate the eigenvectors along the NRHO to compute trajectories originating from alternative fixed points along the NRHO; the definition of eigenvector 'direction' remains as is defined at apolune. In Figure 6.23(a), blue-colored dots correspond to unstable manifold
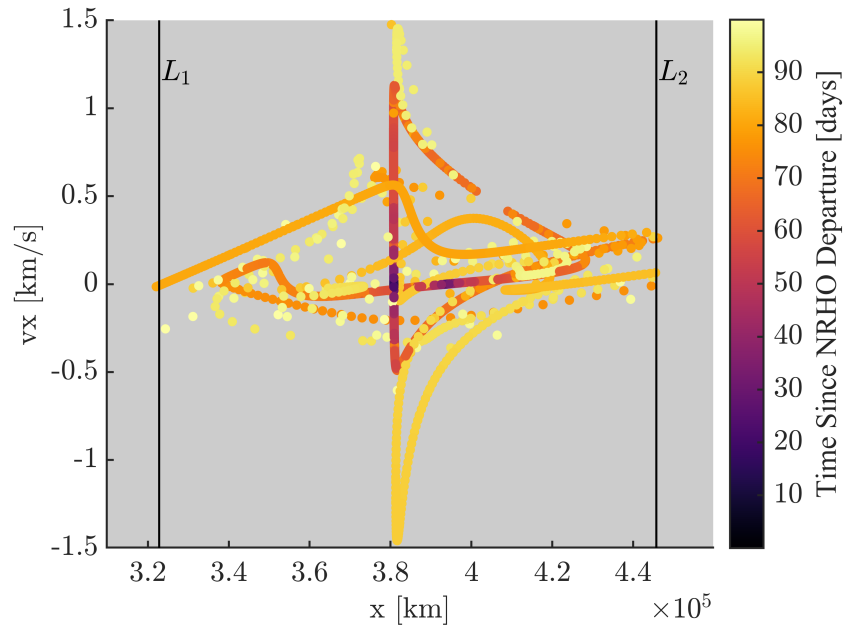
(a) Time since departure from NRHO
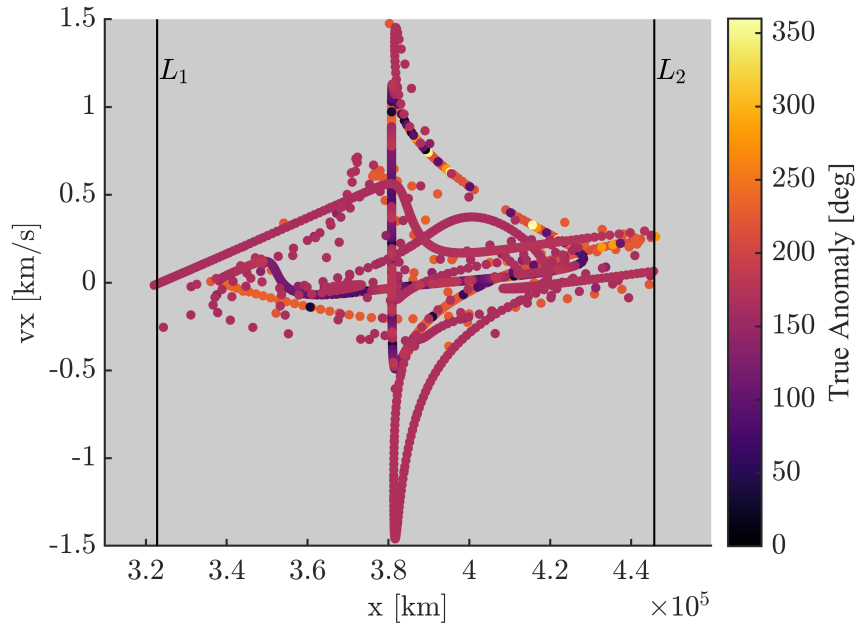
(b) True anomaly of departure from NRHO

Figure 6.21. : x-v_x Poincaré maps $(\Sigma : y = 0)$ colored by crossing event condition

trajectories that eventually depart through the L_2 portal, green-colored dots correspond to trajectories that depart through the L_1 portal, and black-colored dots remain in the lunar
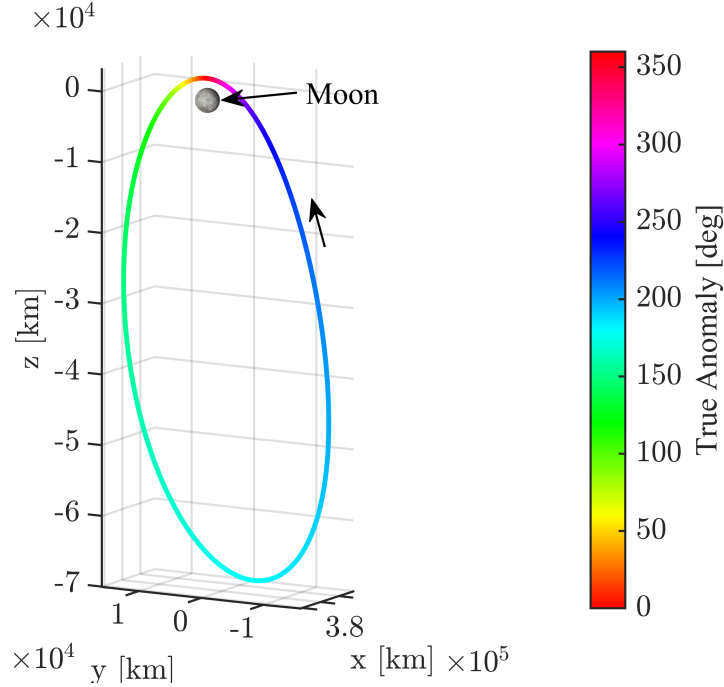
Figure 6.22. : True anomaly along the southern L_2 9:2 lunar synodic resonant NRHO [83]

vicinity (do not depart through a portal or impact the Moon) for 100 days. The black $\times$ corresponds to a lunar impact trajectory–the corresponding trajectory is plotted in Figure 6.24 and closely resembles a low Δv impactor trajectory identified by Davis et al. [84]. Other impact trajectories may be associated with manifolds departing the NRHO. Departures associated with the positive eigenvector direction, plotted in Figure 6.23(b), all depart through the L_2 portal and are thus all colored as magenta dots. A Poincaré map (with hyperplane $\Sigma : y = 0$) depicting the crossings of unstable manifold trajectories in the lunar vicinity is colored by the eventual trajectory destination in Figure 6.23(c). In Figure 6.23(c), blue dots correspond to an eventual departure through the L_2 portal and green dots corresponds to an eventual departure from the L_1 portal. Additionally, black dots indicate that the trajectory associated with the map crossing will remain in the lunar vicinity for at least 100 days without departing or impacting the Moon and, finally, a black-colored '$\times$' indicates a trajectory that leads to lunar impact.

Based on Figure 6.23, it is observed that trajectories that depart from the L_2 NRHO are more likely to progress toward the vicinity of L_2 rather than toward L_1. A Keplerian
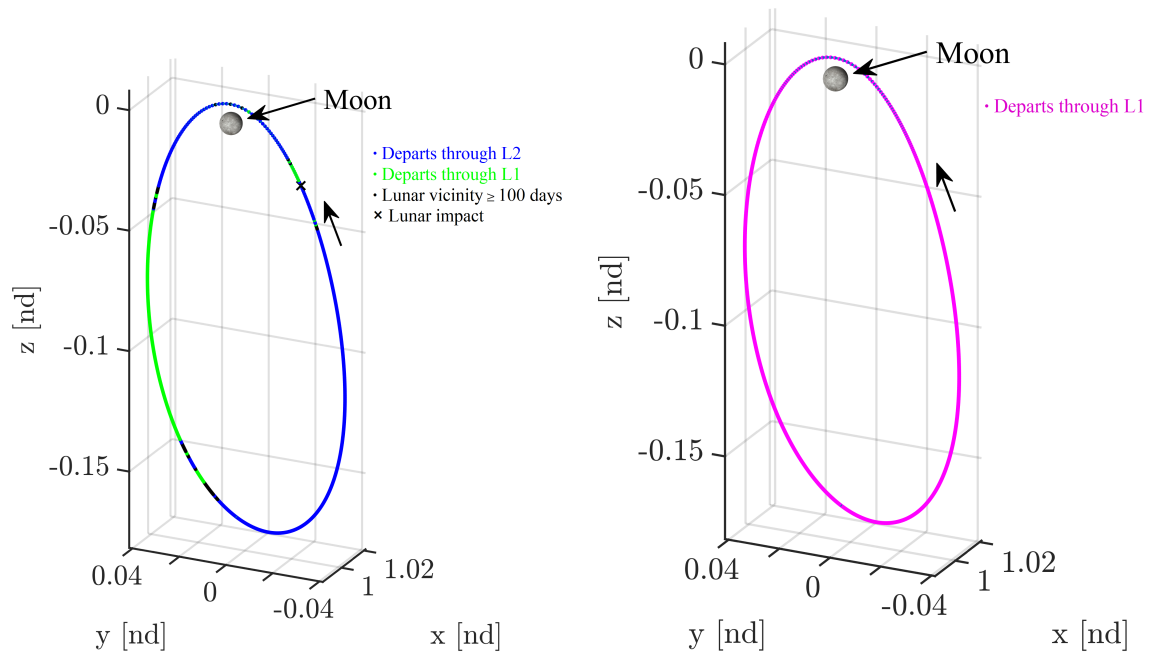
(a) Destinations corresponding to departure along negative eigenvector direction

(b) Destinations corresponding to departure along positive eigenvector direction
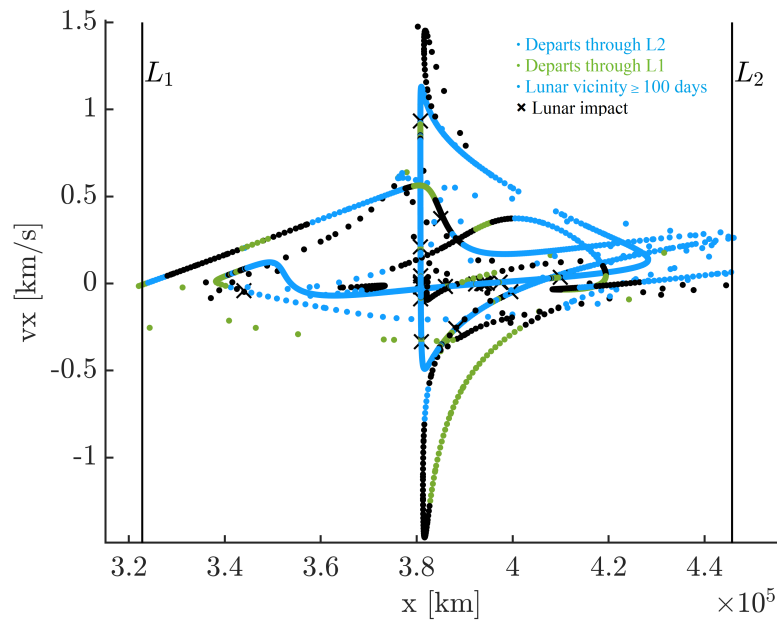
(c) Poincaré map colored by eventual destination of corresponding trajectory

Figure 6.23. : Eventual destination of 9:2 NRHO unstable manifold trajectories
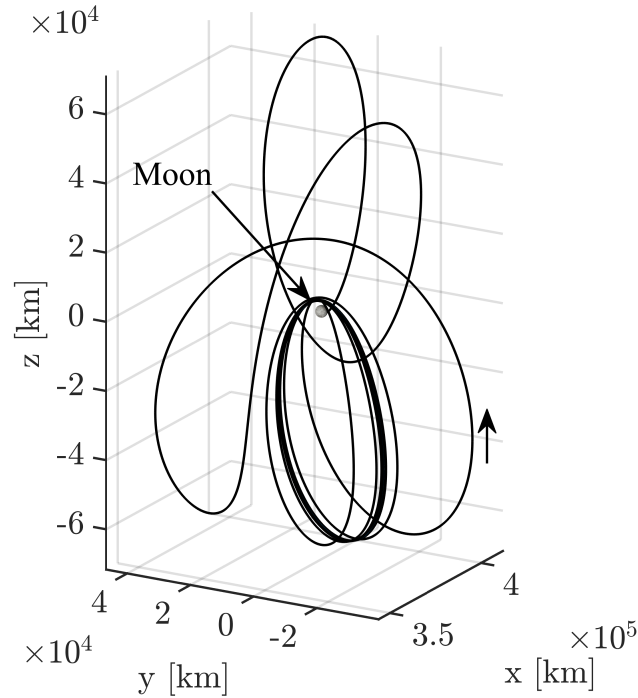
Figure 6.24. : Sample unstable manifold trajectory leading to lunar impact

analysis of motion around the Earth offers a simple explanation. By definition, when the force of gravity acting on a spacecraft $(F_{grav} = \frac{GM_E m_{sc}}{r_{E/sc}^2})$ balances with the centrifugal force $(F_{cent} = m\omega^2 r_{E/sc})$, a circular orbit results in the inertial frame. Note that $r_{E/sc}$ is the distance from the Earth to the point of interest and $\omega \approx 2.6638 * 10^{-6}$ rad/sec for the Earth-Moon rotating frame. The point at which gravity force and centrifugal force balance corresponds to a stationary point in the Earth-Moon rotating frame. The balance point occurs at the approximate location of the Moon's orbit about the Earth, as expected, since the Moon's orbit about Earth is nearly circular in the Earth-centered inertial frame. At distances further from the Earth than the balance point, e.g., at the L_2 point, centrifugal force is greater than the force of gravity thus trajectories tend to depart away from the Earth. At distances closer than the balance point, e.g., at L_1, trajectories tend to move toward the Earth as the gravitational force is larger than the centrifugal force. The NRHO has a small Earth-Moon rotating frame velocity along the majority of the trajectory, thus the approximation of a spacecraft in an NRHO as a stationary point in this frame is reasonable.

165

Since trajectories that depart from the L_2 NRHO originate at a distance where $F_{grav} < F_{cent}$, these departure arcs tend to favor L_2. The plot in Figure 6.25 illustrates the trends in gravitational and centrifugal acceleration as a function of radial distance from the Earth. The intersection between the centrifugal and gravitational acceleration curves occurs at approximately the radius of the Moon's orbit about the Earth.
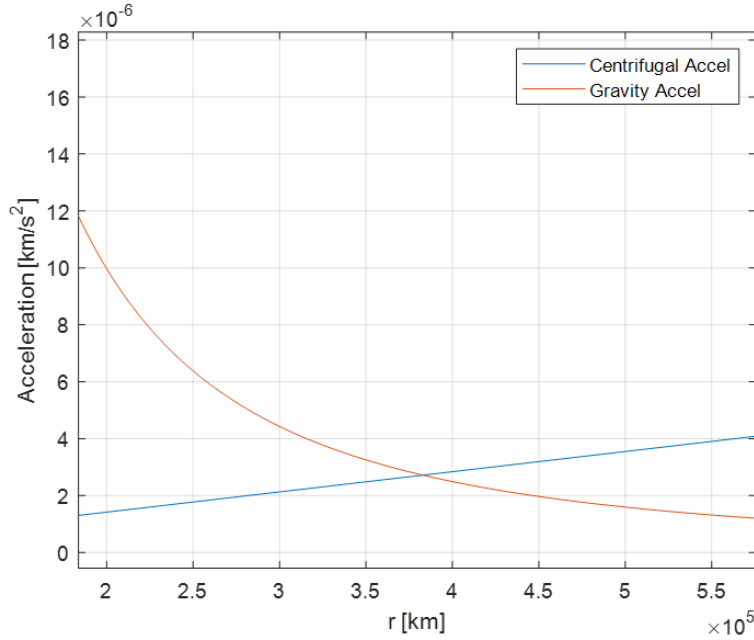
Figure 6.25. : Gravitational and centrifugal acceleration as a function of radial distance from the Earth

The manifolds of three different halo orbits are compared to further illustrate the departure tendencies of L_1 and L_2 orbits. Figures 6.26(a) and 6.26(b) illustrate an L_1 NRHO with Jacobi constant value equal to 3.004, a "flatter" L_1 halo orbit, and the L_2 9:2 lunar synodic resonant NRHO. The "flatter" L_1 halo orbit and the L_2 9:2 NRHO both share a Jacobi constant value equal to approximately 3.04719. The black Zero Velocity Curve (ZVC) in Figure 6.26(b) corresponds to a Jacobi constant of 3.04719 while the red ZVC corresponds to a Jacobi constant value of 3.004. The magnitude of the largest stability index for the L_1 NRHO is 2.331, for the "flatter" L_1 halo the largest stability index is 67.04, and for the L_2 9:2 NRHO, the largest magnitude stability index equals 1.304. Trajectories along the unstable

manifolds departing from each of these orbits are propagated for 100 days TOF and are plotted in Figure 6.26(c) along with the corresponding ZVCs. Trajectories departing from the sample L_1 orbits, despite having varying Jacobi constant values, favor motion toward L_1 while departures from the L_2 NRHO favor motion toward the L_2 side.

(a) Sample halo orbits

(b) Sample halo orbits and ZVCs

(c) Unstable manifold trajectories departing from sample halo orbits
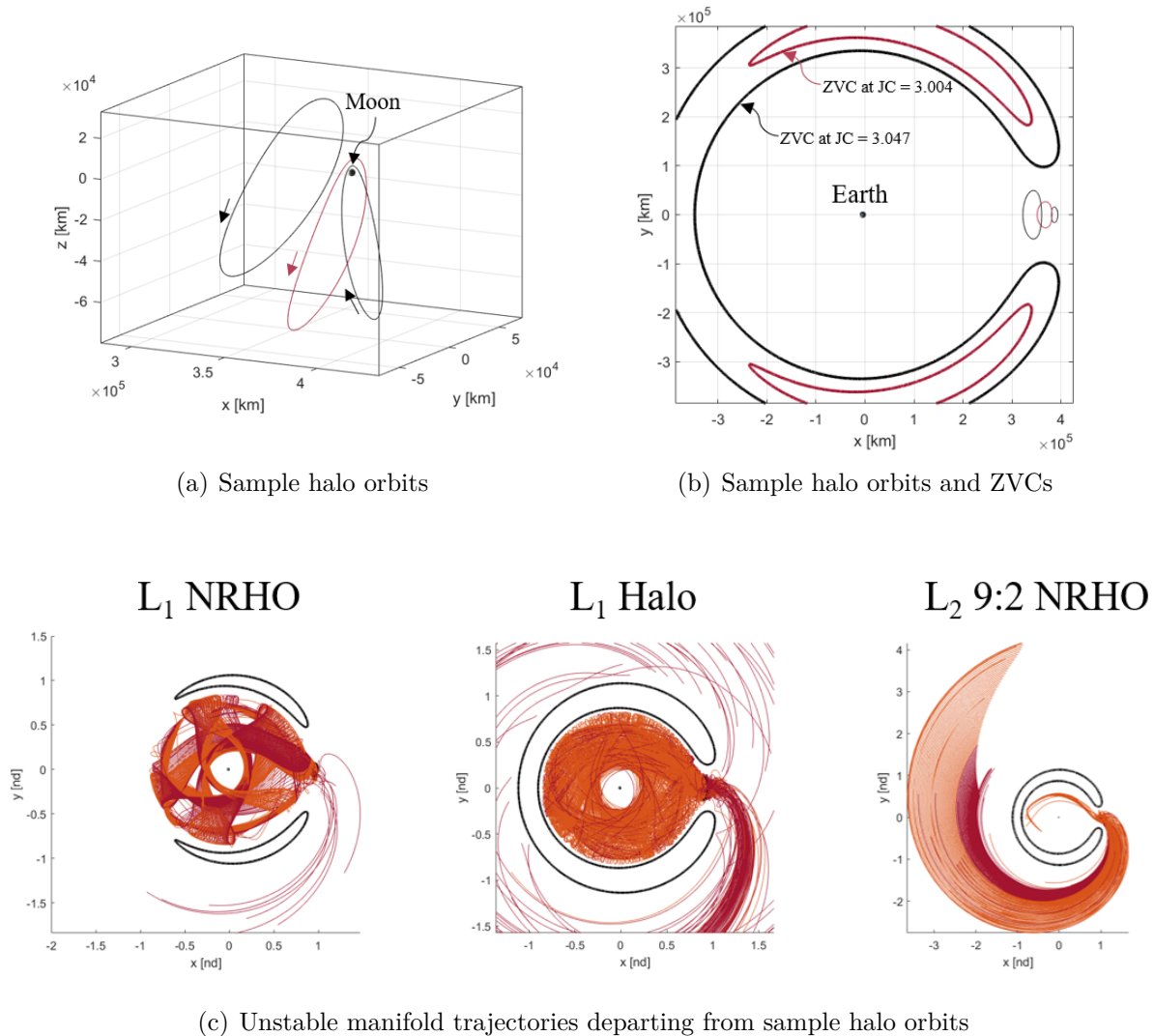
Figure 6.26. : Comparison of unstable manifold trajectories departing from sample L_1 and L_2 halo orbits

6.2.3 Recovery Design Method

To produce an initial guess for a recovery trajectory, segments from cislunar trajectories are stitched together by overlaying Poincaré maps. This design methodology is comprised of two steps: (1) a first trajectory arc that transitions the spacecraft from a departing trajectory into an intermediate orbit, then (2) a second arc that connects the intermediate orbit back to the 9:2 NRHO. To return to the original baseline NRHO, one that was designed to satisfy all mission constraints, timing and phasing must be incorporated in a higher-fidelity model. For the initial design, both steps of the recovery trajectory are considered in the CR3BP for rapid analysis of the underlying flow, thus, step 2 leverages a CR3BP NRHO and intermediate orbit. Phasing considerations at the end of step 2 are ignored in the initial design. Generation of a new baseline orbit after inadvertent spacecraft departure and subsequent recovery may offer a lower-cost alternative than returning to the original baseline NRHO, however this option is beyond the scope of this work.

Some candidate periodic orbits examined for the intermediate staging orbit are plotted in the Earth-Moon rotating frame in the CR3BP in Figure 6.27. The candidate orbits considered are: a northern L_2 9:2 NRHO (orange), a southern L_2 9:2 NRHO (light blue), an L_1 halo orbit (yellow), L_1 and L_2 vertical orbits (purple and green, respectively), a P2HO$_2$ orbit (grey), and a P2HO$_1$ or butterfly orbit (dark blue) [43]. The higher-period halo orbits considered originate from the families plotted in Figures 5.11 through 5.15. Each orbit possesses a Jacobi constant value equal to that of the 9:2 NRHO in the CR3BP ($JC = $ 3.04719). Additionally, each of these orbits is unstable at this energy level and, therefore, possesses stable and unstable manifolds that serve as useful initial guesses for transfer design [46].

A Poincaré map offers insight into potential connections between a departing trajectory and candidate intermediate orbits. A sample departure from the NRHO is plotted in Figure 6.28(a) in the Earth-Moon rotating frame. This trajectory, propagated in the ephemeris model, departs from the Gateway baseline orbit with a Δv of 2 m/s in the ve-
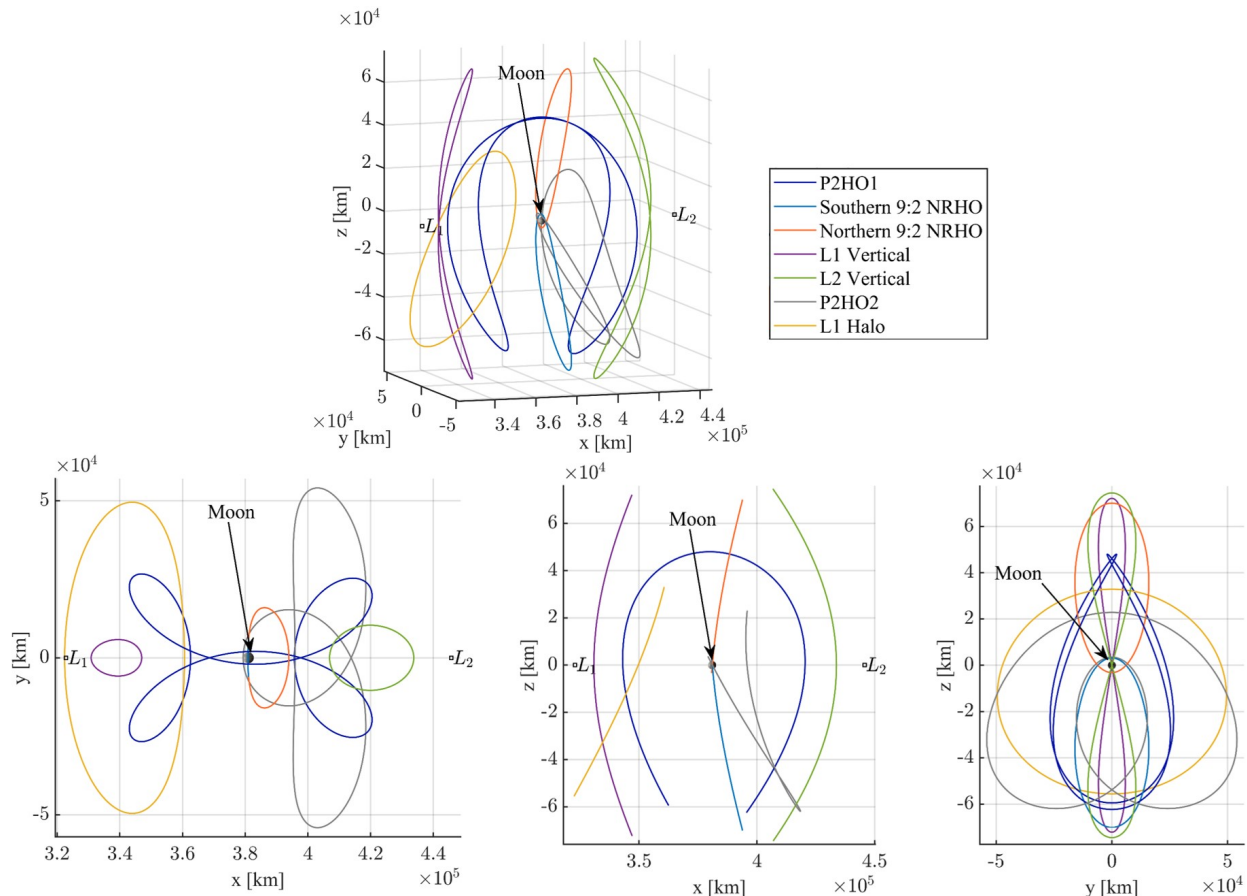
Figure 6.27. : Sample periodic orbits that exist nearby the L_2 southern 9:2 NRHO computed in the CR3BP and plotted in the Earth-Moon rotating frame

locity direction on 04:43:53 UT on 04 January 2024 and serves as the sample departure from the baseline orbit. In a real-world application, this path is not necessarily known *a priori*, however, the departure conditions in this analysis demonstrate the methodology. A hyperplane at $y = 0$ in the Earth-Moon rotating frame is selected to generate the Poincaré map. Figure 6.28(b) depicts the geometric hyperplane in grey where trajectory intersections with the hyperplane, denoted as 'events,' are highlighted as green stars. At each event, the full spacecraft state (position and velocity) is recorded. In Figure 6.28(c), the Earth-Moon rotating x and v_x coordinates for the events are plotted as green stars. Each star is numbered to indicate the order of the event, i.e., event 1 is the first intersection of the departing trajectory with the hyperplane, event 2 is the second intersection, and so on. The events are considered as snapshots along the departure trajectory.
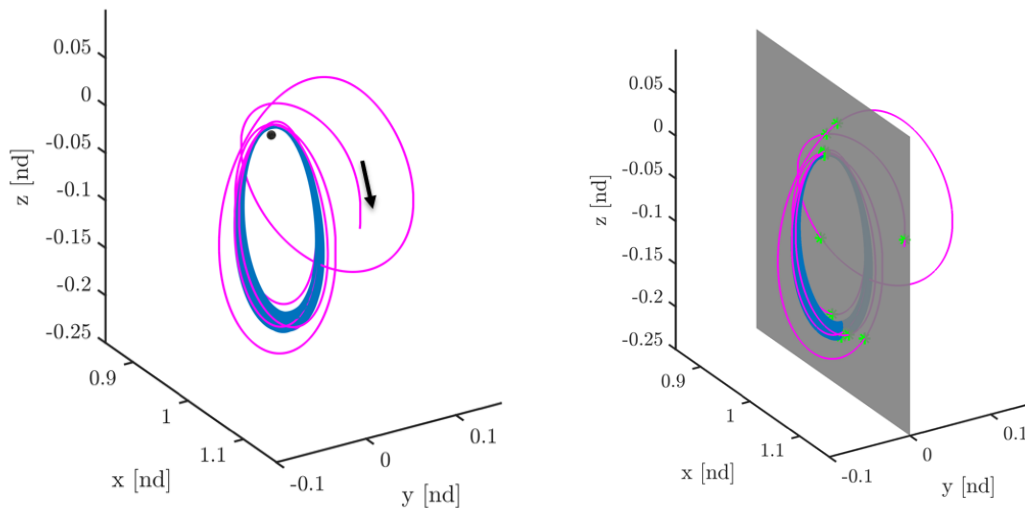
(a) Sample ephemeris trajectory (magenta) departing from baseline 9:2 NRHO (blue) plotted in the Earth-Moon rotating frame

(b) Hyperplane at the Earth-Moon rotating $y = 0$ plane (grey) and crossings of the hyperplane (green)
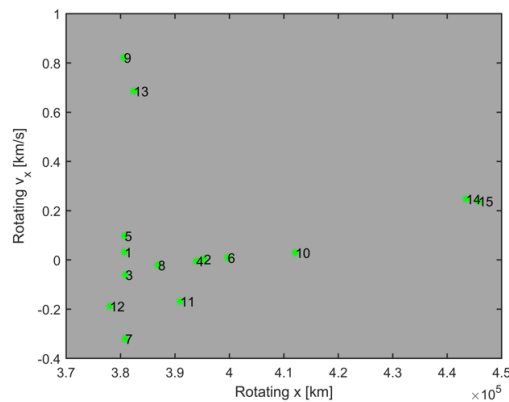
(c) An x-v_x Poincaré map depicting hyperplane crossings of the departing flow from (a) marked with green stars

Figure 6.28. : Departing trajectory in the Earth-Moon rotating frame (a) and an associated Poincaré map used to identify candidate recovery options (b)

A similar process for generating the Poincaré map is repeated for the stable manifolds associated with each of the candidate intermediate orbits. These periodic orbits and their respective manifolds are computed in the CR3BP [23]. Stable manifolds reflect flow *toward* the intermediate orbit for the first step of the recovery trajectory. The Poincaré map appearing in Figure 6.29 illustrates the stable manifold intersections with the rotating $y = 0$

hyperplane for each of the candidate intermediate orbits. The events are depicted as blue circles with colored centers. The center color of each marker corresponds to the periodic orbit from which the manifold trajectory originated, as specified in Figure 6.27. The map associated with the departure trajectory, depicted in Figure 6.28(c), is overlaid on the map associated with the manifolds in Figure 6.29. Although the departure trajectory is computed in the ephemeris model and the manifolds of the intermediate orbits are computed in the CR3BP, the maps can be overlaid with one another since they both possess states plotted in the Earth-Moon rotating frame. Map crossings of the unstable manifolds associated with the CR3BP southern 9:2 NRHO are plotted as red circles with blue colored centers. The departure trajectory, computed in the ephemeris model and marked in green stars in Figure 6.29, closely follows an unstable CR3BP manifold arc, as is expected for ballistic departing flow.

To demonstrate the recovery design process, a sample recovery state along the ephemeris departure trajectory is described. The recovery state is defined as a state along the departing flow at which the spacecraft is assumed to be controllable (i.e., maneuvers are allowed) with a known position and velocity in the Earth-Moon rotating frame. The departure trajectory prior to the recovery state is not relevant to the design process for the recovery trajectory, as it may not be known to designers in the case of an inadvertent departure. In this example, the recovery state is denoted "event 11" along the departure trajectory depicted in Figure 6.28. Recall, "event 11" corresponds to the 11th intersection of the ephemeris departure trajectory with the Earth-Moon rotating $y = 0$ plane. The recovery state is also marked in the zoomed-in view of the Poincaré map depicted in Figure 6.29(b). By identifying crossings on the Poincaré map associated with the stable manifolds of intermediate orbits nearby the recovery state, initial guesses for recovery trajectories are designed. Two examples are examined here; the first employs a P2HO$_2$ as an intermediate orbit and the second example considers a northern L_2 9:2 NRHO as an intermediate orbit. The orange arrow in Figure 6.29(b) corresponds to the initial guess for the first step of a recovery trajectory into a period-2 halo orbit (P2HO$_2$) [43]. This initial guess is plotted in Figure 6.30(a). The green arrow in Figure 6.29(b) corresponds to a stable manifold crossing of a northern L_2
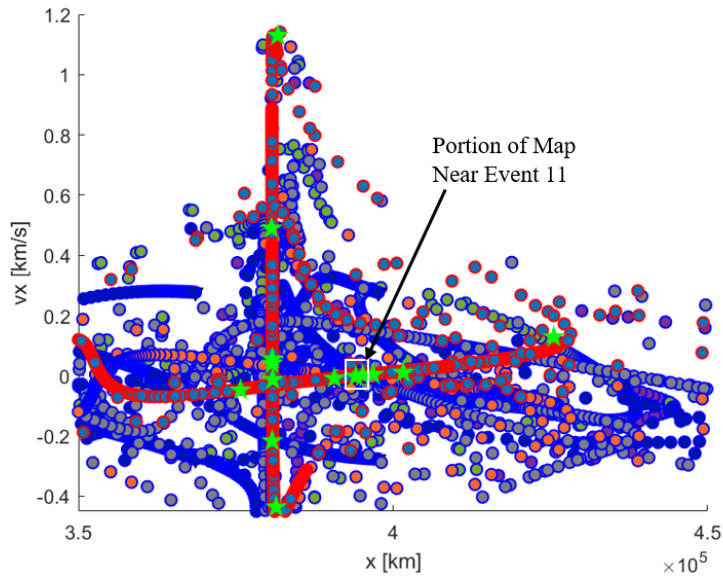
(a) Poincaré map displaying the Earth-Moon rotating frame x-v_x crossings of the hyperplane (Earth-Moon rotating $y = 0$)
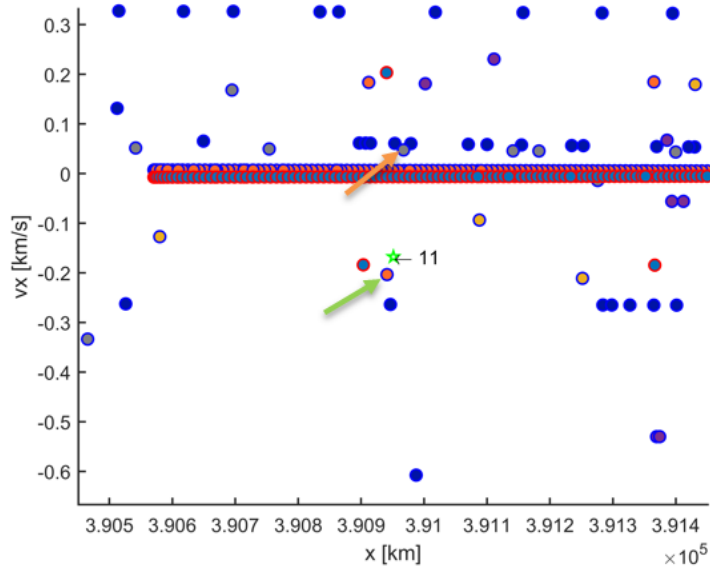
(b) Zoom into portion of Poincaré map from (a)

Figure 6.29. : Poincaré map for design of first segment of recovery trajectory; blue circles indicate stable manifold trajectories of candidate intermediate orbits, red circles indicate unstable manifolds departing from the CR3BP 9:2 NRHO, and green stars indicate the ephemeris departure events

9:2 NRHO and the trajectory corresponding to this map crossing is plotted in configuration space in Figure 6.30(b). In Figure 6.30, the magenta curve corresponds to the ephemeris departure trajectory; the magenta curve terminates at the recovery state, i.e., event 11. The blue curves in Figure 6.30 are computed in the CR3BP and correspond to stable manifolds toward candidate intermediate orbits, here, a P2HO$_2$ and a northern 9:2 NRHO. Note the small discontinuities visible where the blue and magenta curves meet. Although the initial guesses selected from the Poincaré maps do not yield perfectly continuous solutions, the discontinuities are small.

(a) Initial guess for recovery option from event 11 to a P2HO$_2$

(b) Initial guess for recovery option from event 11 to a northern L_2 NRHO
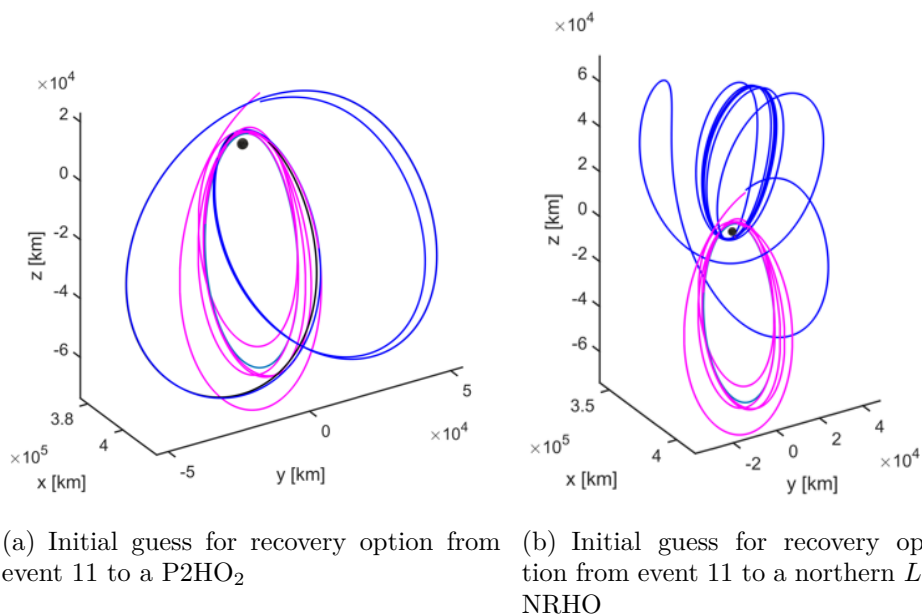
Figure 6.30. : Initial guesses for recovery options from a ballistic NRHO departure plotted in the Earth-Moon rotating frame

Once an intermediate orbit is selected and the initial step of the recovery is designed (connecting the recovery state along the departure trajectory in the ephemeris model to an intermediate orbit), a second step of the transfer (transitioning the spacecraft from the intermediate orbit back to the NRHO) is required. The design process is repeated in reverse, i.e., a Poincaré map offers potential transfer options from the intermediate orbit to the NRHO by employing unstable manifolds associated with the selected intermediate orbit and stable manifolds associated with the NRHO. Stable manifolds from the CR3BP southern 9:2

173

NRHO are connected with the unstable manifolds of the intermediate orbit to generate an initial guess for the second segment of the recovery; there may be multiple step 2 options associated with each step 1 option.

Once again, the initial guesses for step 2 of the recovery yield transfers with small discontinuities. Thus, the step 1 and step 2 transfers are corrected for continuity in the CR3BP using a multiple-shooting algorithm. The recovery state is assumed to be a fixed state within the corrections process. Because the CR3BP is autonomous, time continuity is not of concern in this model; thus, with an appropriate number of revolutions along the intermediate higher-period orbit included in the design, an end-to-end transfer connecting the recovery state back to the NRHO using two trajectory steps is generated. Figure 6.31 depicts end-to-end transfers that link the recovery state (event 11 from Figure 6.28) back to an NRHO in the CR3BP. The solution depicted in Figure 6.31(a) uses approximately 337 m/s of Δv over six impulsive maneuvers with a TOF of approximately 119 days, not including any ballistic revolutions along the intermediate P2HO$_2$. The recovery option in Figure 6.31(b) requires 92 m/s over six impulsive maneuvers and a TOF of approximately 241.3 days. The cost for the second step of the recovery depicted in Figure 6.31(b) is near zero since it utilizes a heteroclinic (maneuver-free) transfer option between the northern and southern 9:2 NRHO that exists in the CR3BP. Not all periodic orbits that exist at the same energy level will possess heteroclinic connections, however, they can contribute to low-cost solutions if utilized when available. Both of these CR3BP solutions are feasible solutions but are not optimized.

6.2.4 Transition to an Ephemeris Model and Optimization

Once both step 1 and step 2 of the transfer are designed in a lower-fidelity model, the end-to-end recovery trajectory is transitioned to a higher-fidelity ephemeris model and optimized. Copernicus, a trajectory optimization software package developed under a project at NASA JSC, yields both a feasible result in the ephemeris model as well as a recovery option that minimizes the total Δv for an optimized ephemeris solution [85]. Additional revolutions
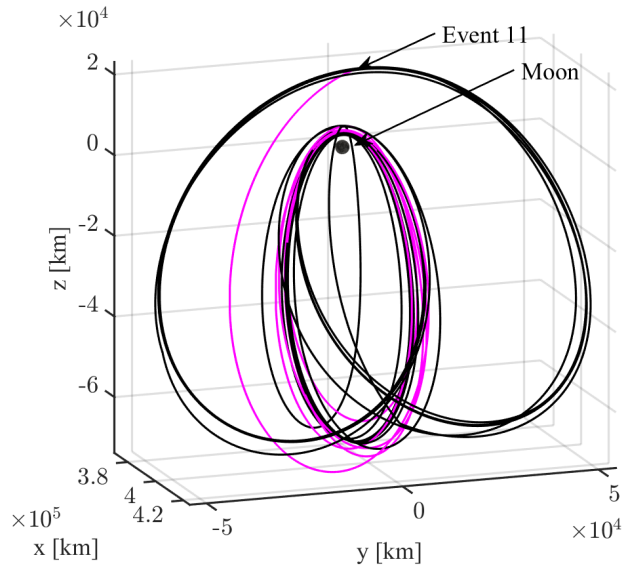
(a) CR3BP recovery option from event 11 using a P2HO$_2$ as an intermediate orbit
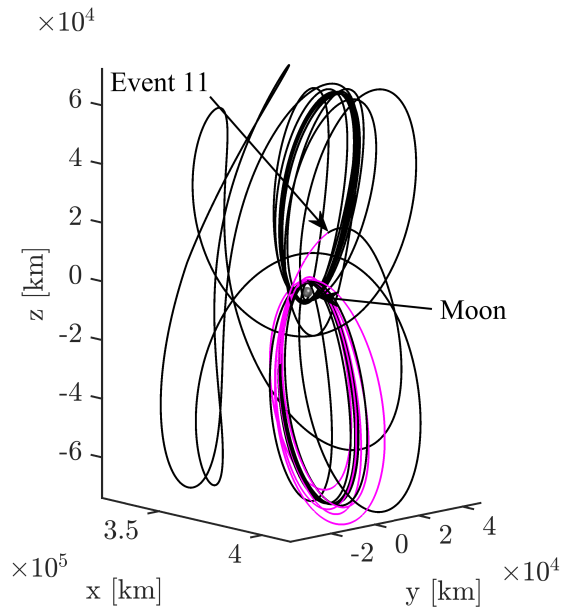
(b) CR3BP recovery option from event 11 using a northern L_2 NRHO as an intermediate orbit

Figure 6.31. : Recovery options computed in the CR3BP

along the intermediate orbit are inserted along the end-to-end trajectory in the ephemeris model, therefore, time of flight along the recovery may appear to increase as compared to the CR3BP solution.

One example of a feasible, continuous, but unoptimized recovery trajectory propagated in the ephemeris model appears in Figure 6.32(a) in the Earth-Moon rotating frame. This sample path utilizes the CR3BP end-to-end solution from 6.31(a) as an initial guess. Approximately five revolutions, or 91 days, of ballistic motion along the intermediate P2HO$_2$ are included in the design. The total time of flight, including time spent in the intermediate orbit, is approximately 163 days, and the solution requires a Δv of 311 m/s. Similarly, the solution in Figure 6.31(b) is transitioned to the ephemeris model and plotted in Figure 6.32(b). Approximately 108 days, or 15 revolutions, in the northern L_2 NRHO are included in the design, thus, the total recovery lasts 253 days and uses 146 m/s of Δv. In both cases, the feasible ephemeris solution closely maintains the geometry of the CR3BP initial guess. This persistence indicates that the structures in the CR3BP supply geometries that remain present in higher-fidelity modeling.
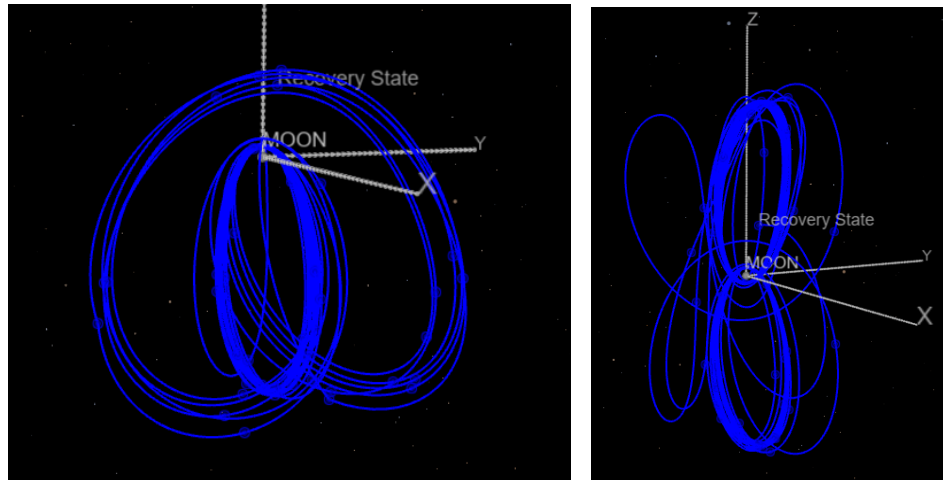
(a) Non-optimized ephemeris recovery option from event 11 using a P2HO$_2$ as an intermediate orbit

(b) Non-optimized ephemeris recovery option from event 11 using a northern L_2 NRHO as an intermediate orbit

Figure 6.32. : Non-optimized (feasible) recovery options computed in the ephemeris model

Next, using SNOPT within Copernicus, the feasible ephemeris solutions are optimized to determine locally minimum Δv solutions. The cost function is defined as $J = \sum ||\Delta v_\mathrm{i}||$. Constraints to maintain a sufficient altitude above the surface of the Moon are necessarily introduced to prevent sub-surface passages of the trajectory. Optimization without these

constraints often reduces the altitude of close passes near the primaries that dramatically reduces the total cost, however, practical limitations must be maintained. In both cases, a basin hopping scheme delivers progressively lower cost locally-optimal solutions [86]. The total cost for the strategy that utilizes a P2HO$_2$ orbit within the initial guess is reduced to 35 m/s with a time of flight of approximately 170 days (including approximately 5 ballistic revolutions in the P2HO$_2$ orbit). The optimized result is plotted in the Earth-Moon rotating frame in Figure 6.33(a). Note the decrease in Δv of 276 m/s achieved by optimization. The optimized cost for the recovery option that uses a northern NRHO as the intermediate orbit is 119 m/s. The optimized result, which has a time of flight of approximately 254 days, including the intermediate revolutions along the northern NRHO, appears in Figure 6.33(b).
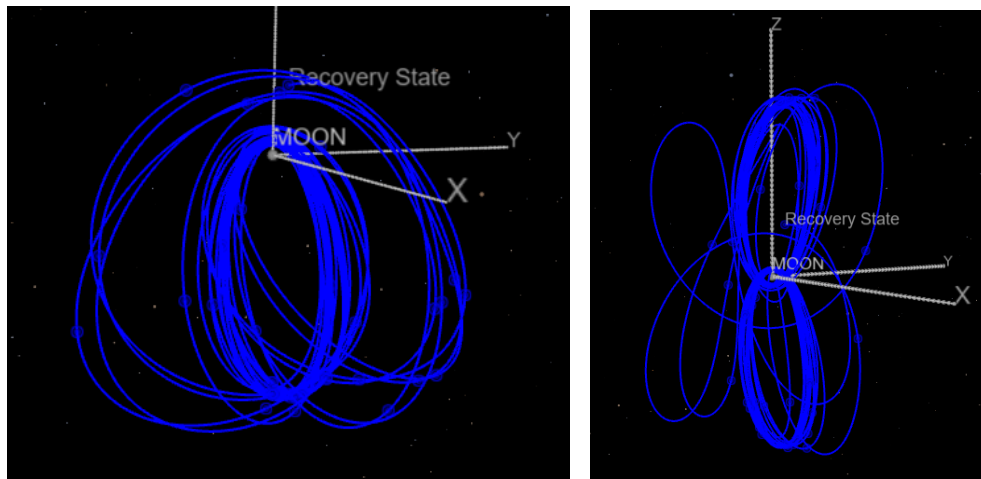
(a) Optimized ephemeris recovery option from event 11 using a P2HO$_2$ as an intermediate orbit

(b) Optimized ephemeris recovery option from event 11 using a northern L_2 NRHO as an intermediate orbit

Figure 6.33. : Optimized recovery options computed in the ephemeris model

In both of the optimized solutions plotted in Figure 6.33, the geometry is slightly modified from that of the feasible ephemeris solutions presented in Figure 6.32. However, even though a basin-hopping optimization scheme reduces the total cost, the underlying CR3BP structures are still apparent. The initial guess, produced using structures in the CR3BP is, therefore, nearby a locally optimal ephemeris solution. The optimized trajectories

in Figure 6.33 represent a subset of the available recovery options for this particular combined departure scenario and recovery event. In both of these cases, a maneuver is implemented as soon as the spacecraft is controllable. However, in some cases, it is advisable to allow the spacecraft to continue to progress along the departing trajectory prior to executing the first maneuver, i.e., it may produce a lower cost or lower total time of flight recovery option if the first maneuver is delayed. Figure 6.34 displays three sample step 1 recovery options that begin with a maneuver at event 13 along the departing trajectory displayed in Figure 6.28. These are viable options for the end-to-end recovery even if the spacecraft is controllable at an earlier time. The step 2 portions of the recoveries and the end-to-end optimized ephemeris solutions for these alternate step 1 trajectories are produced using a similar process as described for the optimized trajectories in Figure 6.33.

6.2.5 Additional Regime 2 Recovery Example

An alternative escape trajectory geometry, one that departs the Gateway baseline orbit at 02:53:44 UT on 22 July 2024 with a 2 m/s maneuver in the velocity direction, is subsequently investigated for an additional demonstration of the regime 2 recovery methodology. This additional example supports the fact that the success of the methodology does not rely on a particular departure geometry. The alternate ephemeris departure is plotted in Figure 6.35(a) in the Earth-Moon rotating frame. The blue curve represents the Gateway baseline orbit, the magenta curve represents the departure trajectory, and the green stars once again correspond to crossings of the rotating $y = 0$ plane. Arbitrarily selecting the fourteenth crossing of the $y = 0$ plane (i.e., event 14 marked in Figure 6.35(a)) as the recovery state, the trajectory design process proceeds. As previously illustrated, the first step in the recovery process is to generate a Poincaré map that features the recovery state as well as the stable manifold crossings of candidate periodic orbits in the nearby vicinity. The portion of the Poincaré map associated with the region nearby event 14 is illustrated in Figure 6.35(b). Event 14 is marked as a green star, the stable manifold crossings of candidate orbits are marked as blue circles with colored centers corresponding to the color of
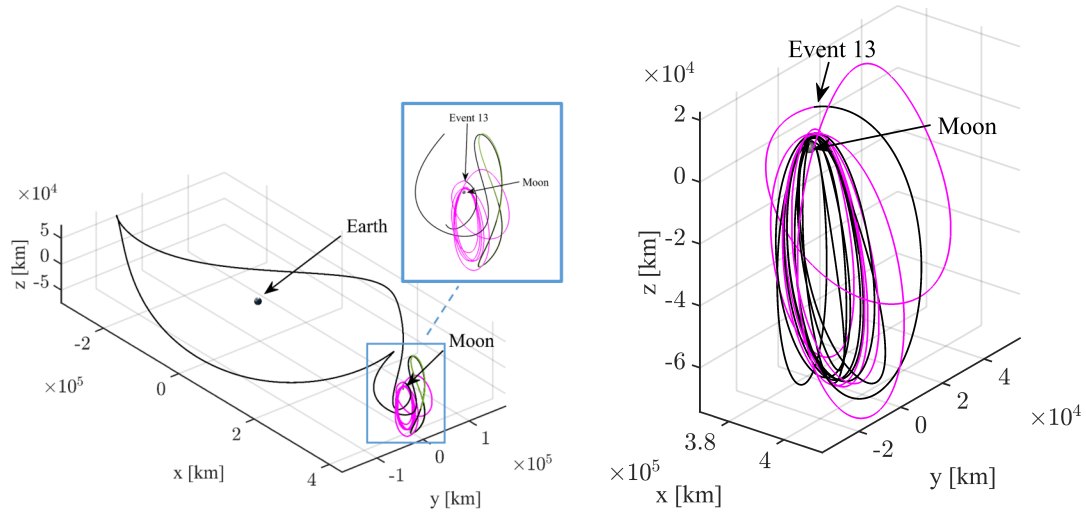
(a) Step 1 recovery option from event 13 using an intermediate L_2 vertical orbit (green)

(b) Step 1 recovery option from event 13 that returns directly to the southern 9:2 NRHO
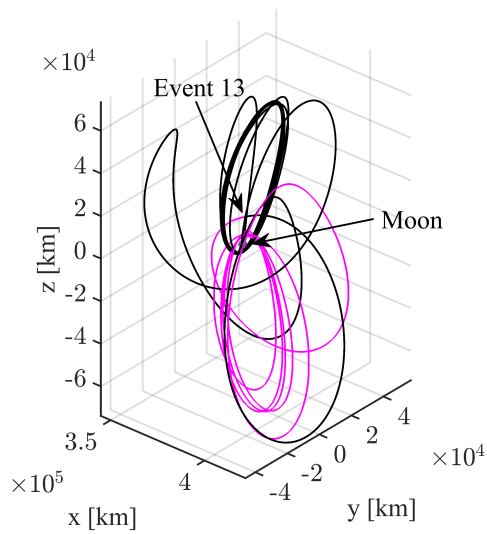
(c) Step 1 recovery option from event 13 using an intermediate northern 9:2 NRHO

Figure 6.34. : Sample step 1 recovery options from event 13 of the departure trajectory plotted in Figure 6.28

the orbit from which they originated (these colors are denoted in Figure 6.27). Red circles with blue centers correspond to the unstable manifolds of the CR3BP 9:2 NRHO and are again included to illustrate the similarity between the ephemeris departure and the NRHO unstable manifold trajectories.
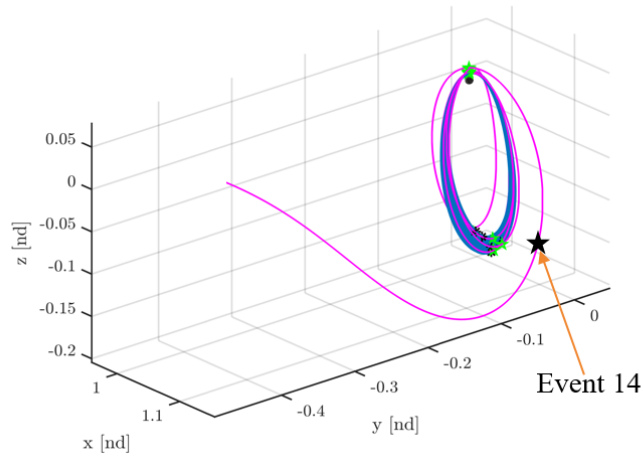
(a) Alternative sample ephemeris trajectory (magenta) departing from baseline 9:2 NRHO (blue)
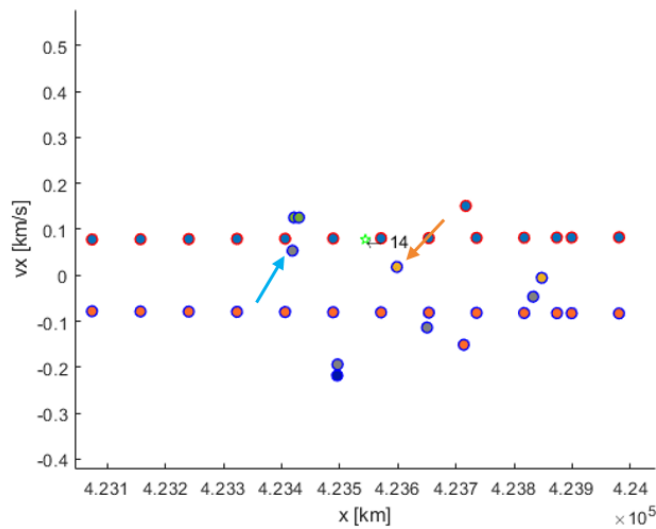
(b) Poincaré map illustrating the x-v_x crossings of the rotating $y = 0$ plane

Figure 6.35. : Alternative sample ephemeris departure trajectory and portion of Poincaré map displaying rotating $y = 0$ plane crossings near event 14

Candidate intermediate orbits for use in the spacecraft recovery from this particular ephemeris departure and specific recovery state combination are selected based on their proximity to the recovery state on the map. Two options are indicated by arrows in Figure 6.35(b); the orange arrow in Figure 6.35(b) corresponds to a stable manifold crossing of

an L_1 halo orbit, while the aqua-colored arrow corresponds to a stable manifold crossing of a P2HO$_2$ orbit. The stable manifolds associated with these crossings (computed in the CR3BP) are plotted in blue in Figure 6.36. The magenta curve corresponds to the ephemeris departure from Figure 6.35(a) and terminates at the recovery state, i.e., event 14. The L_1 halo orbit is plotted in yellow in Figure 6.36(a) and the P2HO$_2$ is plotted in grey in Figure 6.36(b). The stable manifolds offer two separate initial guesses for step 1 recovery in the CR3BP.

Next, the step 1 options from Figure 6.36 are combined with a transfer trajectory that links the intermediate orbit back to a CR3BP 9:2 NRHO. Here, the candidate orbit is selected as the L_1 halo orbit, thus, the initial guess for step 1 of the recovery appears in Figure 6.36(a). The initial guess for step 2 of the recovery trajectory is constructed by linking an unstable manifold from the L_1 halo orbit with a stable manifold of the CR3BP 9:2 NRHO using a Poincaré map. Both step 1 and step 2 of the transfer are then separately corrected for continuity in the CR3BP; the corrected step 1 transfer trajectory appears in Figure 6.37(a). Together the CR3BP step 1 and step 2 trajectories supply an end-to-end recovery option that is then transitioned into the ephemeris model and optimized.

The end-to-end optimized ephemeris recovery trajectory, linking the recovery state at event 14 along the departure from Figure 6.35(a) back to the 9:2 NRHO, is plotted in Figure 6.37(b). The trajectory is first transitioned to the ephemeris model and corrected as a feasible (continuous) solution using Copernicus. Next, a basin-hopping approach is employed to reduce the total recovery cost to 110 m/s with a time of flight of approximately 248 days, including about 6 revolutions or 72 days in the intermediate L_1 halo orbit. The revolutions in the L_1 halo orbit are apparent on the left of Figure 6.37(b), while the final revolutions of the spacecraft after it is returned to the 9:2 NRHO are apparent in the center of the image. The recovery state is labeled as well.
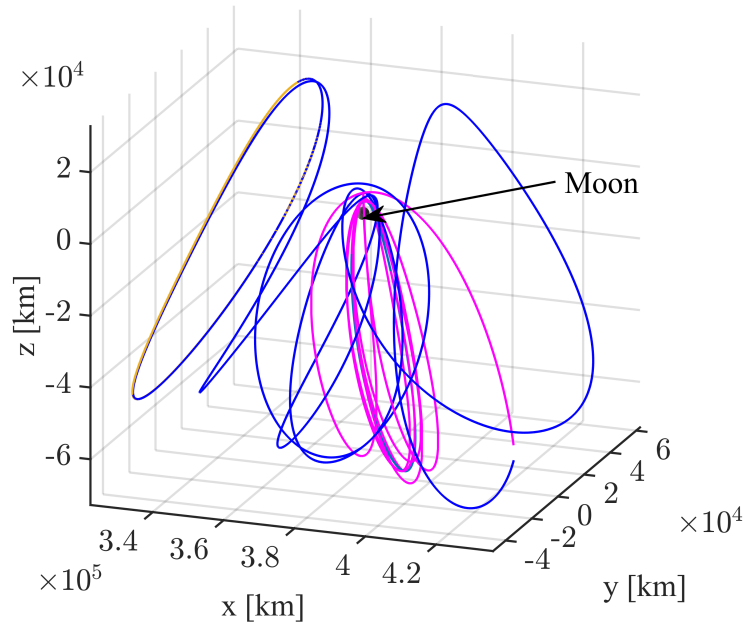
(a) Initial guess for recovery option from event 14 to an L_1 halo orbit
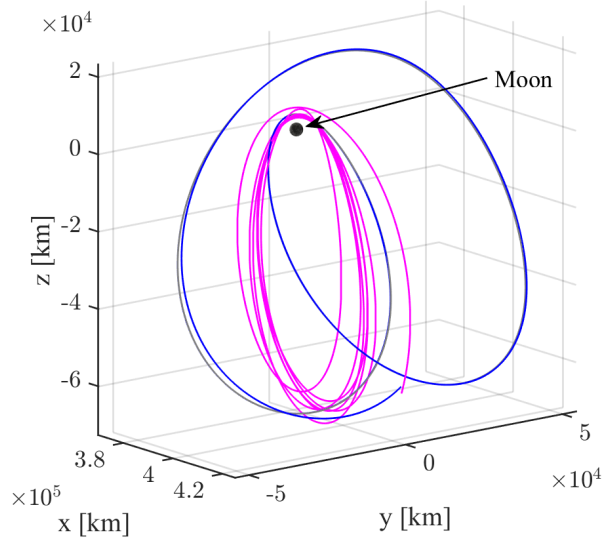
(b) Initial guess for recovery option from event 11 to a P2HO$_2$

Figure 6.36. : Initial guesses for recovery options from a ballistic NRHO departure
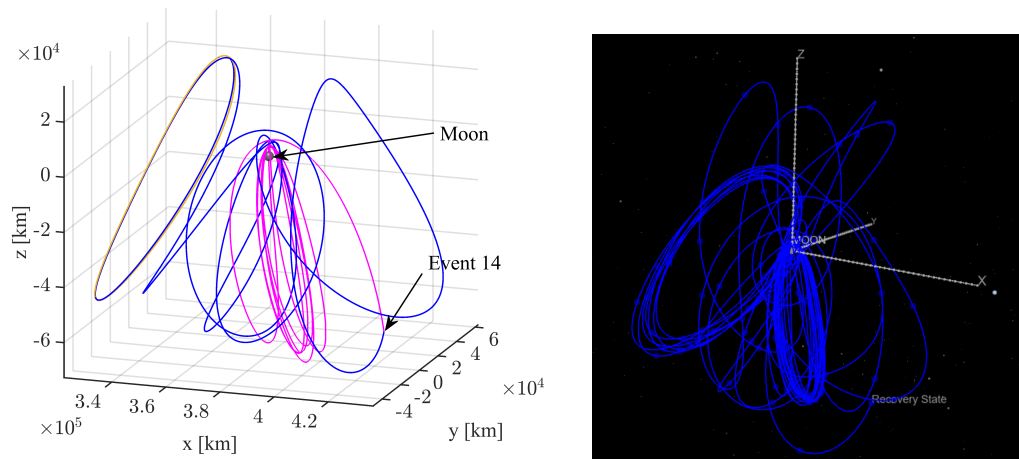
(a) CR3BP recovery option from event 14 to an L_1 halo orbit

(b) Optimized ephemeris recovery option from event 14 using an L_1 halo orbit as an intermediate orbit

Figure 6.37. : Recovery from event 14 utilizing an L_1 halo orbit as the intermediate orbit

6.3 Identification of a Fundamental Structure that is Applicable to Long-Duration Transfer Trajectories Between Unstable Cislunar Orbits

Future missions within cislunar space and beyond are planned to originate from a long-term hub (e.g., NASA's Gateway) in an Earth-Moon NRHO, thus strategies for transfer design between NRHOs and multiple types of cislunar orbits are relevant to upcoming needs. In Section 6.1, a method is discussed to develop transfer trajectories between NRHOs and DROs. The DROs are stable and therefore do not possess manifold structures that ballistically arrive at or depart from them, prompting the development of an alternative strategy to formulate initial guesses for transfer trajectories. Other periodic orbits in cislunar space do, however, possess manifold structures that can be useful for initial guess generation. A strategy to design trajectories that utilizes manifolds to link the L_2 southern 9:2 lunar synodic resonant NRHO (the current Gateway baseline orbit) and sample unstable cislunar orbits at the same value of Jacobi constant is therefore explored. This investigation focuses on the identification of transfer geometries that are external to, or outside of, the immediate Earth-Moon vicinity. Equivalently, the trajectories are primarily in the region *outside* the Zero-Velocity Curve (ZVC) that exists at this Jacobi constant value; this 'external' region

183

is plotted in light blue in Figure 6.38. The white region is the region denoted as 'internal' to the ZVC and the area shaded in grey is the forbidden region that is inaccessible at this energy level.
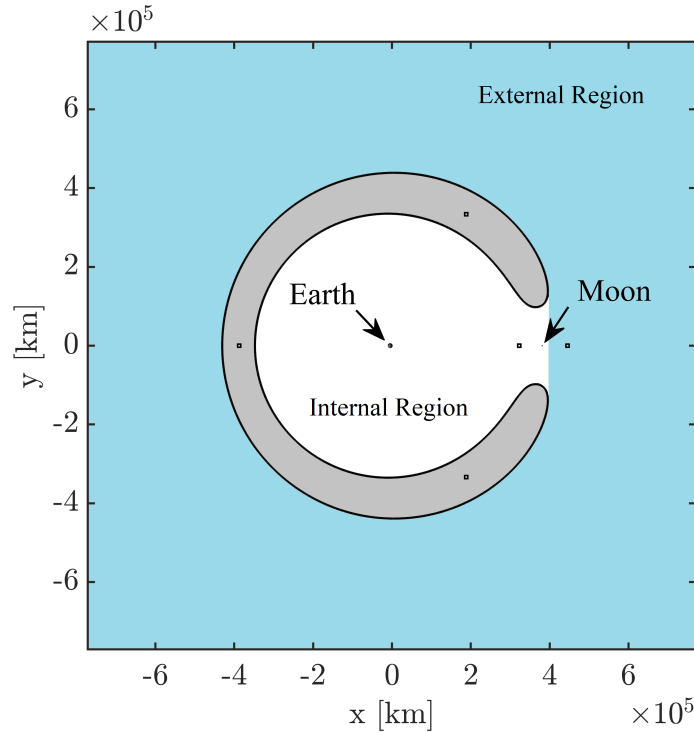
Figure 6.38. : Zero velocity curve at a Jacobi constant value of approximately 3.04719

Plotted in Figure 6.39 in the Earth-Moon rotating frame are sample CR3BP orbits of interest in cislunar space that exist at a Jacobi constant equal to that of the Gateway baseline NRHO. The orange curve corresponds to the southern L_2 9:2 lunar synodic resonant NRHO, a P2HO$_2$ orbit is plotted in blue, the yellow trajectory corresponds to a southern L_1 halo orbit, the green curve is a member of the 4:3 resonant orbit family, and a member of the 3:4 resonant orbit family is plotted in purple. Note, the 3:4 resonant orbit and the 4:3 resonant orbit plotted in Figure 6.39 also appear in Figure 6.4. These resonant orbits are used for transfer design between an NRHO and DRO. Each of the periodic orbits in Figure 6.39 is unstable and therefore possesses stable and unstable invariant manifold structures. Trajectories that lie on these surfaces form the basis for initial guesses for transfer trajectories linking these periodic orbits. In order to simplify the visualization of these structures that
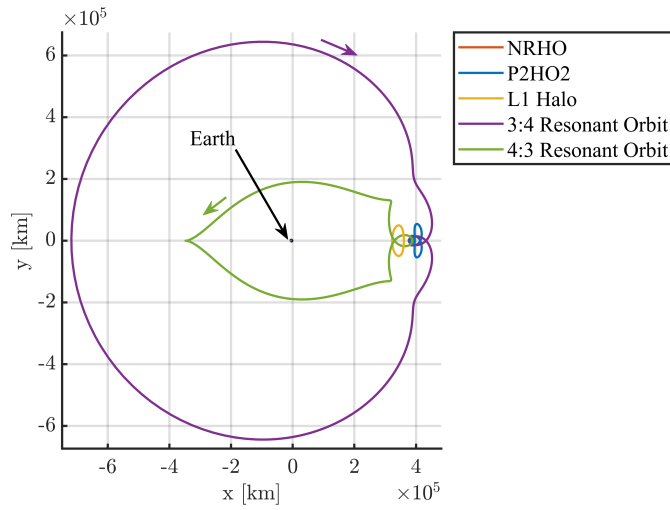
(a)
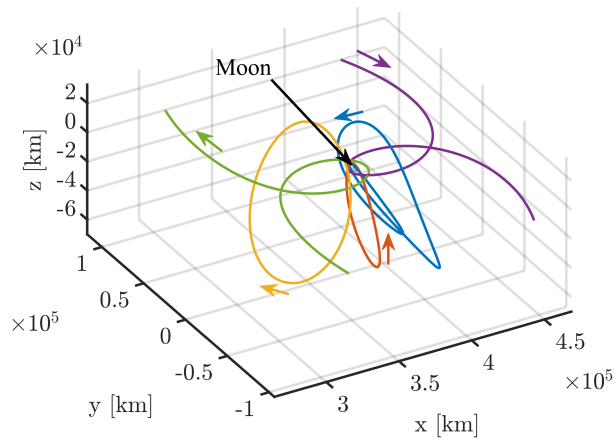
(b)

Figure 6.39. : CR3BP sample orbits of interest in the nondimensional Earth-Moon rotating frame

exist in both position and velocity space, a Poincaré mapping technique is used. Figure 6.40 illustrates the intersection of stable and unstable manifold trajectories originating at each of the periodic orbits plotted in Figure 6.39 with the rotating $y = 0$ plane. The colors of the dots on the map correspond to the color of the periodic orbits in Figure 6.39, e.g., orange colored dots in Figure 6.40 correspond to unstable and stable manifold crossings of

185

the NRHO that is plotted in orange in Figure 6.39. Stable manifold crossings are plotted in a darker shade of the orbit color and unstable manifold intersections with the map are plotted in a lighter shade of the same color. Figure 6.40(a) displays a 'global' portrait of the manifolds within cislunar space and beyond. The region near the Earth is detailed more closely in the portion of the map plotted in Figure 6.40(b). Similarly, the lunar vicinity of the Map is detailed in Figure 6.40(c). The portion of the map plotted in Figure 6.40(d) details a 'diamond-like' structure that appears on the map in the region external to the ZVC.
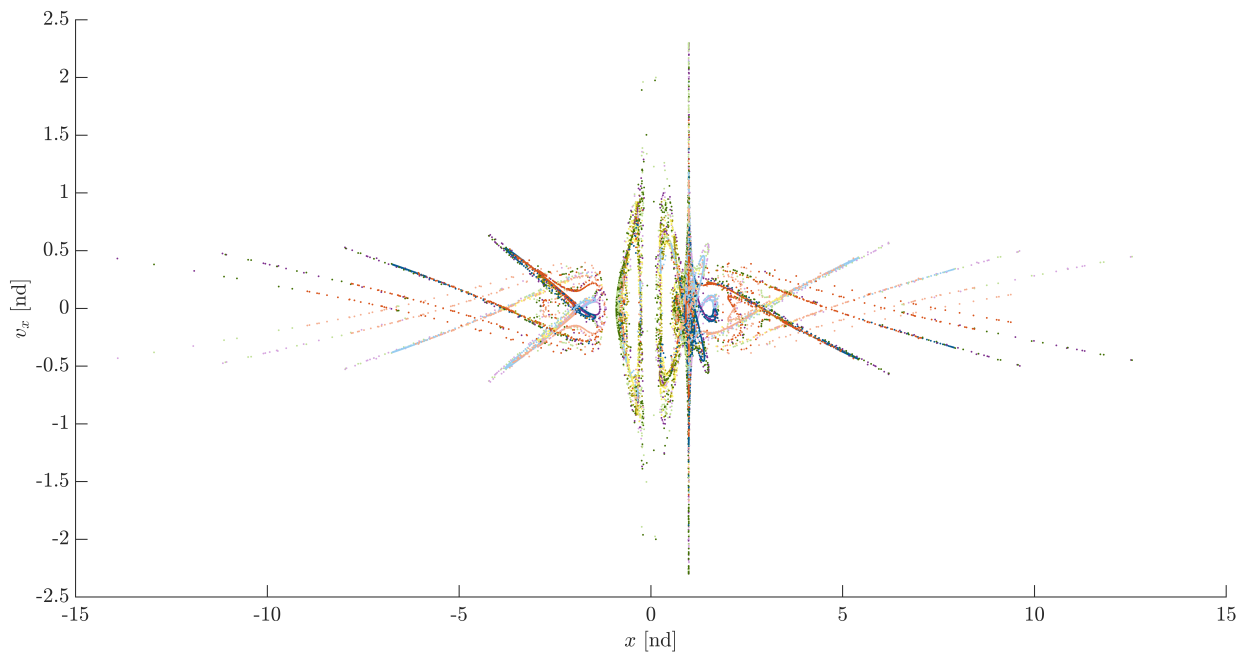
(a) Global portrait
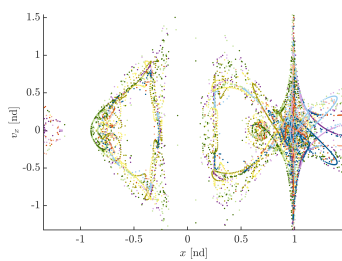
(b) Region near Earth
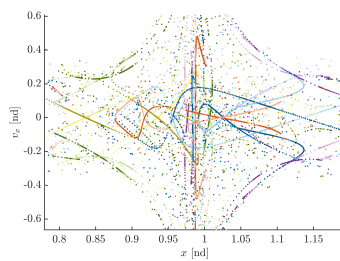
(c) Region near Moon
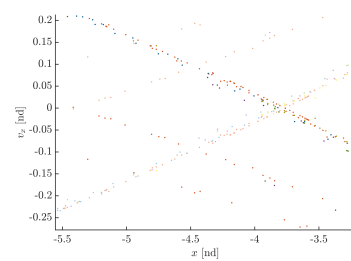
(d) Region external to ZVC

Figure 6.40. : Poincaré map corresponding to the CR3BP sample orbits from Figure 6.39; light colors: unstable manifolds, dark colors: stable manifolds

Although the portions of the Poincaré map nearby the Earth and Moon, plotted in Figures 6.40(b) and 6.40(c), are useful to design transfer trajectories that may remain in the vicinity of the Earth or Moon ('internal' type transfers), transfers that primarily remain outside this vicinity (denoted 'external') are of interest. Various authors have identified low-cost external-type transfer trajectories linking cislunar orbits using optimization schemes. For example, McCarty et al. design low thrust transfers between an L_2 southern NRHO, a 'flat' L_2 southern halo orbit, and an L_1 northern halo orbit using a monotonic basin-hopping approach [87]. Additionally, McGuire et al. investigate transfer trajectories between an NRHO and two different L_2 halo orbits using a similar optimization scheme [28]. While monotonic basin hopping or other optimization strategies do produce low-cost results, a strategy based on fundamental dynamical structures may lead to more predictable results that are produced more quickly. Designs based on fundamental structures offer a starting point for optimization that may be closer to a local minimum than may be otherwise available.

Figures 6.41 to 6.44 demonstrate an exploration of various geometries formed by manifold trajectories originating at the sample orbits of interest and selected from various regions on the Poincaré map. Stable and unstable manifold trajectory arcs are plotted in inset figures around the perimeter of the map. Arrows indicate the location of the map crossings corresponding to the stable and unstable manifold trajectories that are plotted in each inset plot. Stable manifold trajectories are plotted in blue in configuration space while unstable manifold trajectories are colored red. Both Figures 6.41 and 6.42 correspond to manifold trajectories that originate at the L_2 9:2 lunar synodic resonant NRHO. Although the inset plots display an x-y projection of the trajectories, the arcs that originate at three-dimensional orbits are non-planar. Plotted in Figure 6.43 are a variety of manifold structures that originate at an L_1 halo orbit. Finally, an exploration of trajectories originating at the P2HO$_2$ is offered in Figure 6.44. An investigation of manifold trajectories corresponding to the 4:3 and 3:4 resonant orbits produces results that remain within the x-y plane.
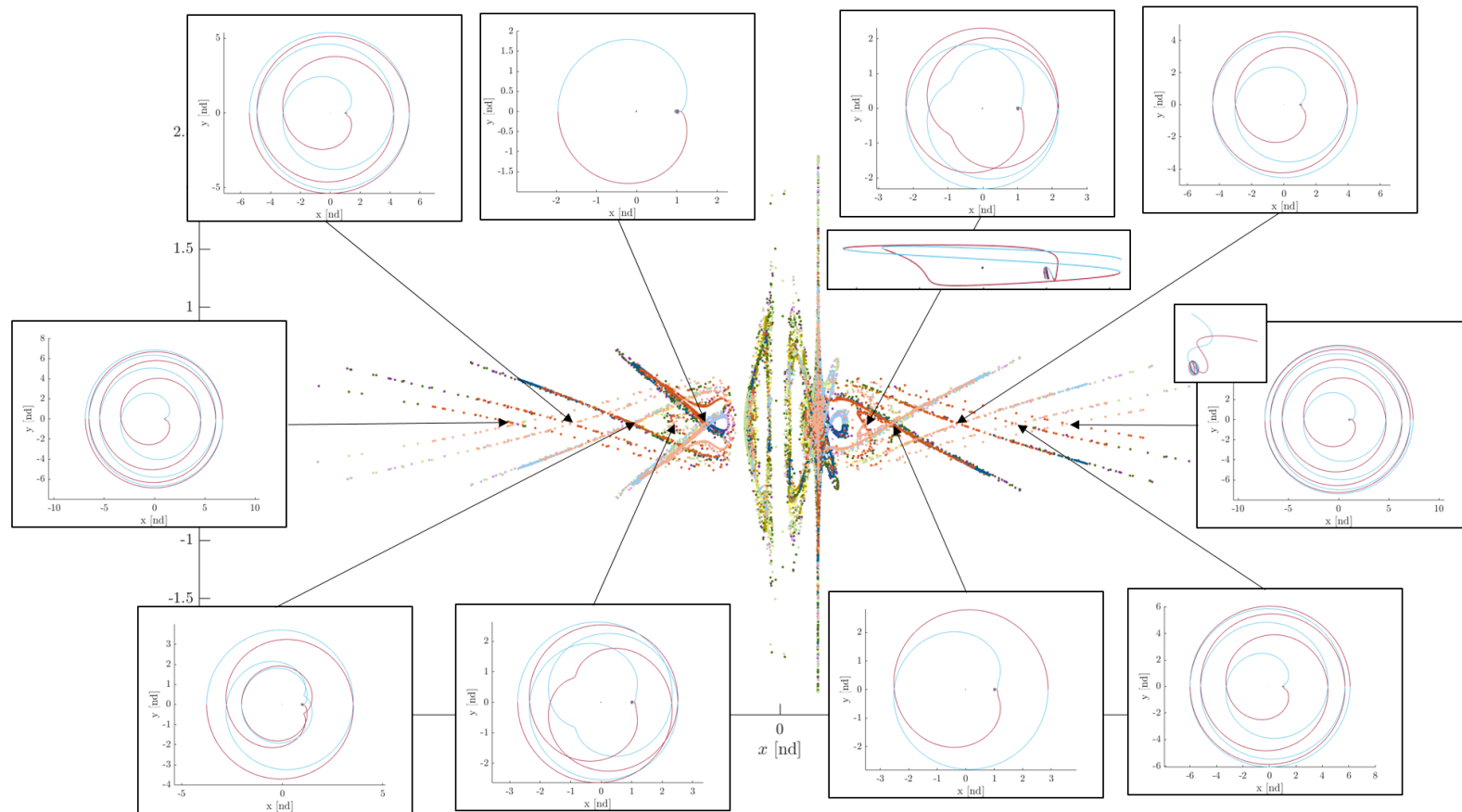
Figure 6.41. : Exploration of 9:2 lunar synodic resonant NRHO manifolds
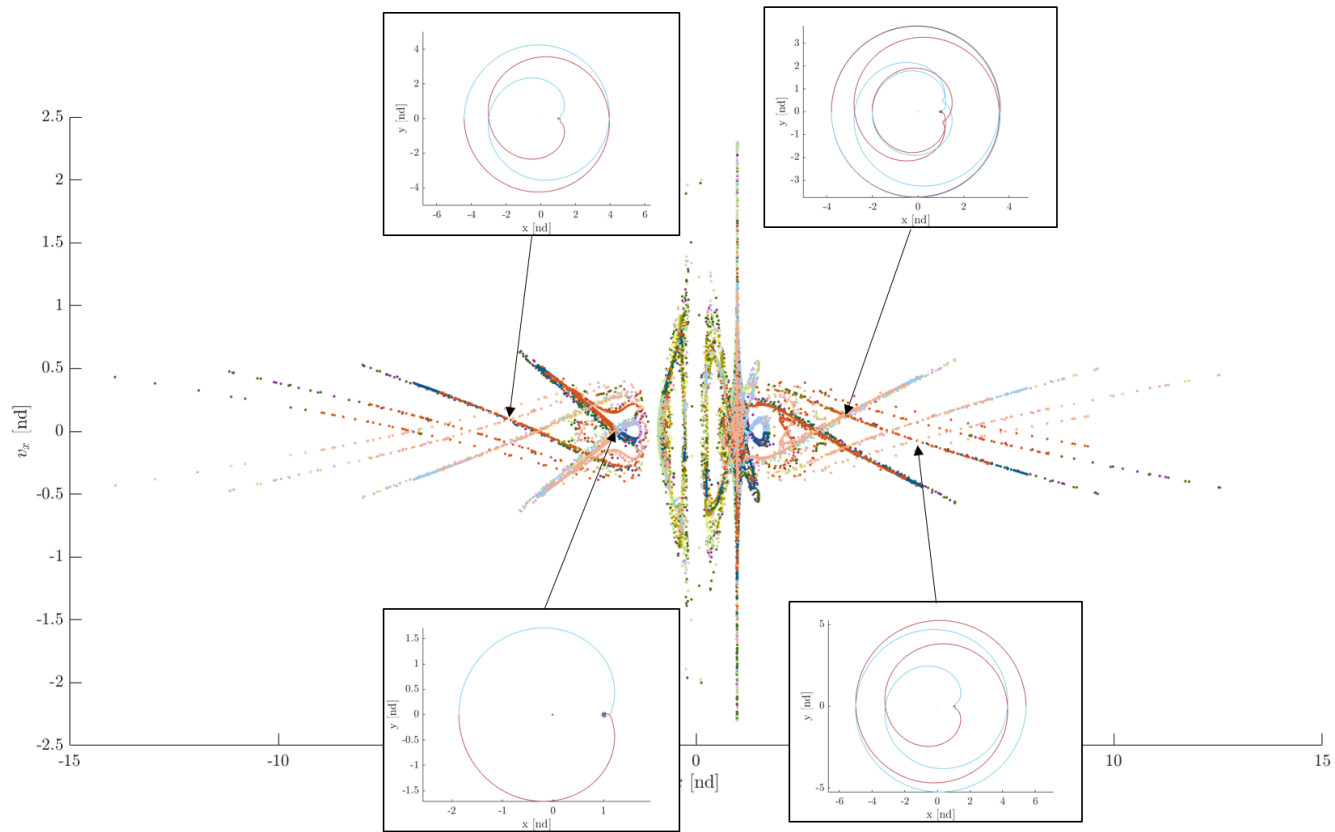
Figure 6.42. : Exploration of 9:2 lunar synodic resonant NRHO manifolds
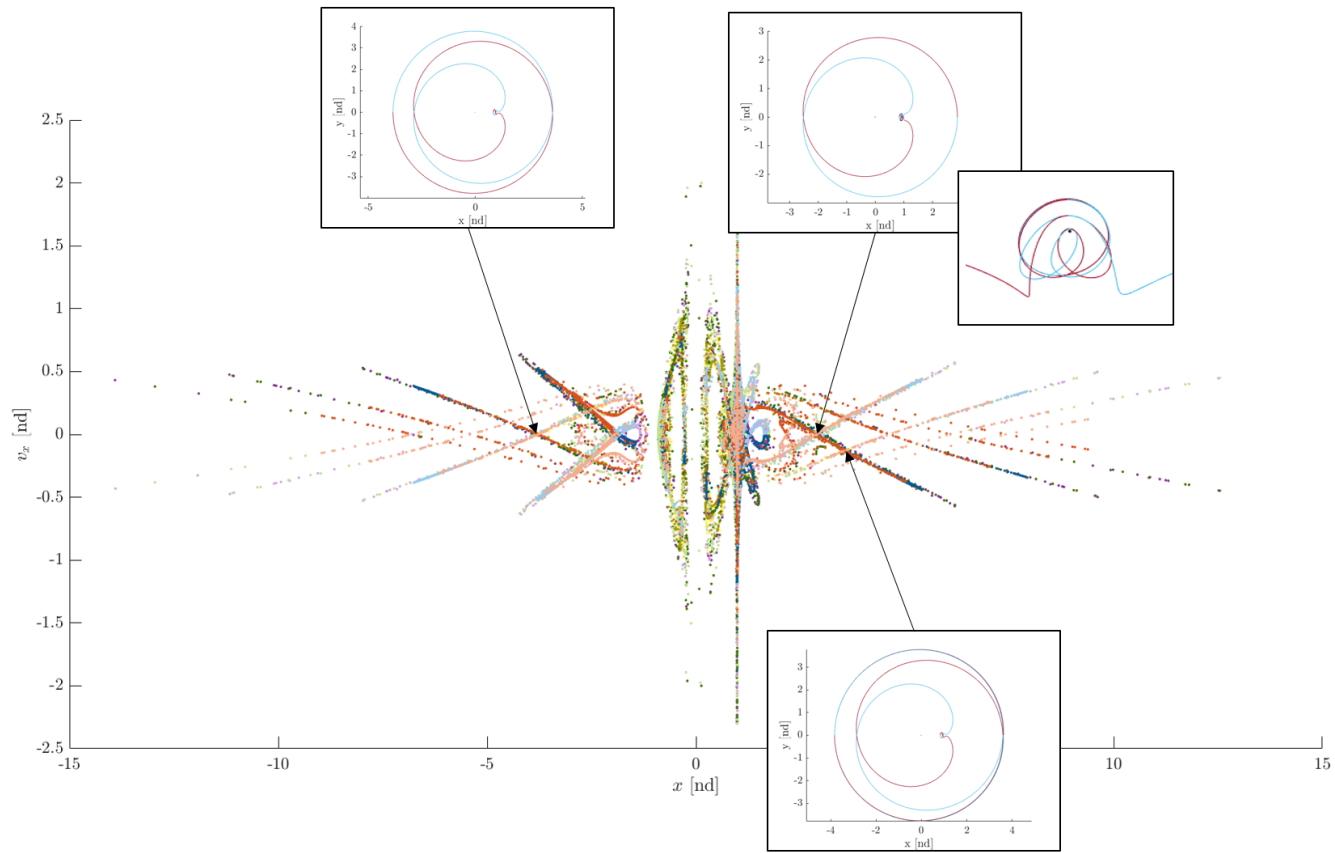
Figure 6.43. : Exploration of L_1 halo orbit manifolds
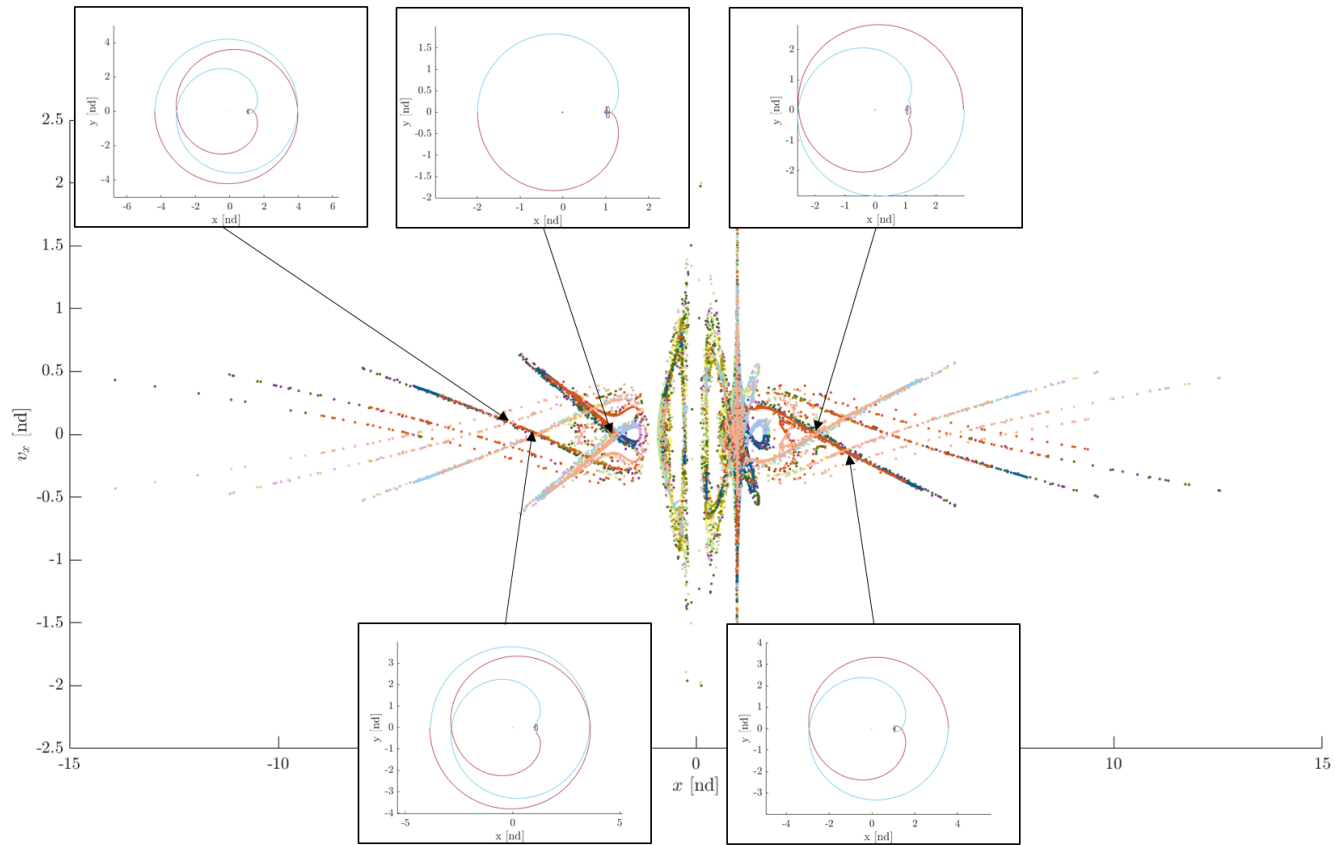
Figure 6.44. : Exploration of P2HO$_2$ manifolds

Similarities between the dynamical structures that correspond to each of the periodic orbits investigated are apparent in both configuration space and the x-v_x Poincaré map, particularly in the regions of interest external to the ZVC. In Figure 6.40(a), a diamond pattern that is made up of manifold crossings originating at the various sample periodic orbits is observable. Points along these 'diamonds' correspond to the configuration space plots inset within Figures 6.41 through 6.44. In fact, a particular geometry that is common to the stable/unstable manifolds originating at each of the sample periodic orbits is also observed in optimized low thrust transfer trajectories computed by McCarty et al. and McGuire et al. [28], [87]. This geometry, that corresponds to the region of the Poincaré map plotted in Figure 6.40(d), possesses three revolutions about the Earth-Moon system. Each of the sample periodic orbits possess manifolds that share this geometry, as is evidenced in Figure 6.45. Unstable and stable manifolds from each of the sample periodic orbits are plotted in the nondimensionalized Earth-Moon rotating frame in Figure 6.45; the colors of the curves in the figure correspond to the periodic orbit that the manifold surface originates at. The orange box corresponds to a three-dimensional zoomed-in view near the Moon that is indicated in the left-hand figure.
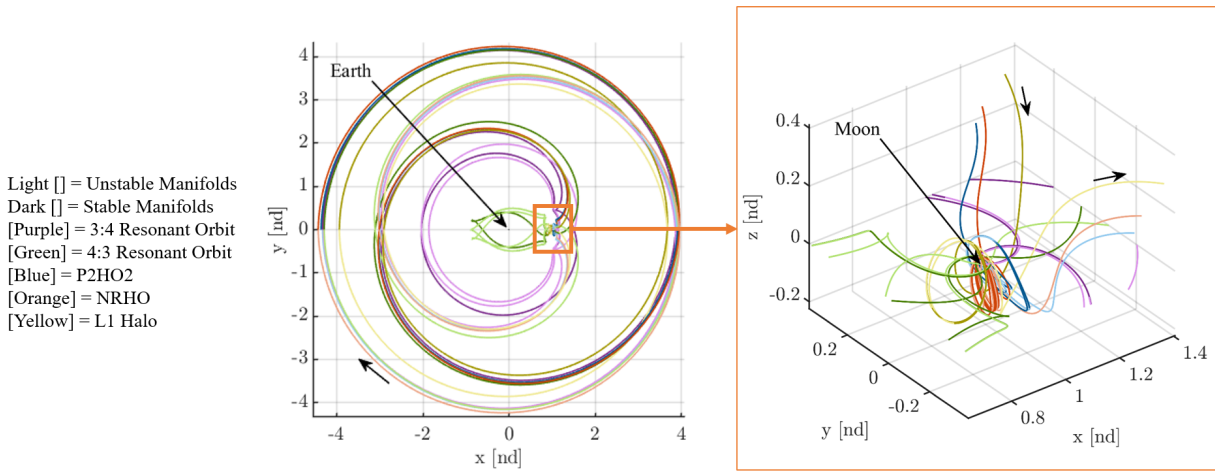
Figure 6.45. : Common three-revolution manifold geometry

It is useful to identify the fundamental 'three revolution' dynamical structure that appears to drive the geometry of external transfers between cislunar orbits and the evolution

of their manifolds outside of the ZVC. Once identified, the dynamical structure, or segments along it, are available as building blocks for transfer design between orbits in the region. Utilization of fundamental dynamical structures for transfer design between periodic orbits yields a strategy that does not require extensive manifold trajectory computation, a process that requires significant amounts of time. Instead, dynamical structures that are *similar to*, or representative of, manifold trajectories form portions of the transfer arc initial guess used within a differential corrections process. A similar process in which fundamental dynamical structures are utilized for transfer design is described in Section 6.1.1. In Section 6.1.1, resonant orbits are used to aid in the design of links between higher-period halo orbits and a DRO. To identify the 'three revolution' structure, segments along the unstable and stable manifold trajectories of the 3:4 resonant orbit corresponding to the geometry of interest are used as an initial guess in a differential corrections algorithm; these segments are plotted in red and blue, respectively, in Figure 6.46(a). Patchpoints are marked as asterisks in the figure. Within the corrections algorithm, the objective is the generation of a symmetric peri-

(a) Initial guess

(b) Converged solution
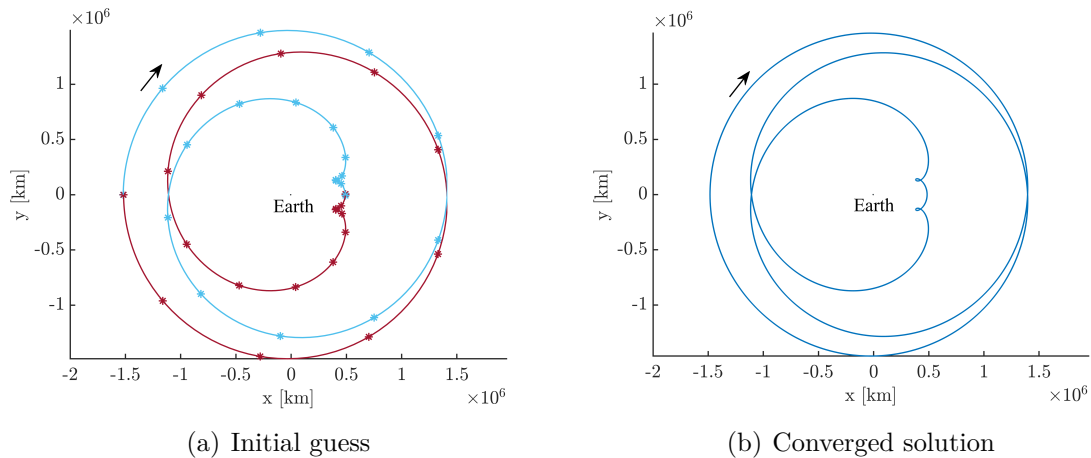
Figure 6.46. : Periodic orbit corresponding to 'three revolution' geometry, identified using arcs from manifold trajectories

odic orbit that maintains the geometry of interest. The converged periodic solution, plotted in the Earth-Moon rotating frame in Figure 6.46(b), has an orbital period of approximately 127.4 days and closely maintains the geometry of the initial guess.

A pseudo-arclength continuation scheme is used to produce additional members of the periodic orbit family that the individual orbit in Figure 6.46(b) belongs to. This orbit family is defined as the 1:4 resonant orbit family and initial conditions for this family are available in Table A.11; Gupta and Vaquero identified a smaller subset of the family in 2020 and 2017, respectively [88], [89]. Both Gupta and Vaquero observe that resonant orbits are often important to understanding fundamental motion in the solar system and incorporating them into transfer designs can yield low-cost, novel scenarios. Including members of the 1:4 family in designs used to link cislunar orbits is expected to produce low-cost feasible solutions as well as yield improvements in the optimization process. A range of members of the 1:4 resonant periodic orbit family with Jacobi constant values ranging between approximately 1.74 and 3.57 are plotted in Figure 6.47(a). Plotted in Figures 6.47(b) through 6.47(d) is a 1:4 resonant orbit at a Jacobi constant value equal to the Jacobi constant value of the 9:2 NRHO ($JC = 3.04719$). In these figures, the 1:4 resonant orbit is depicted as a black curve in the Earth-Moon rotating frame. Unstable and stable manifold trajectories corresponding to the L_2 9:2 lunar synodic resonant NRHO are plotted in red and blue, respectively. In Figure 6.47(b), the ZVC at this energy level is included in the plot in grey. The 1:4 resonant orbit appears to 'bounce' off of the ZVC near the Moon. In the region external to the ZVC, illustrated in Figures 6.47(b) and 6.47(c), the manifold trajectories corresponding to the NRHO align closely with the 1:4 resonant orbit. However, Figure 6.47(c) illustrates that the 1:4 resonant orbit is planar, while the NRHO manifold trajectories are three-dimensional; despite this difference, the 1:4 resonant orbit still provides a close approximation for the manifold trajectories external to the ZVC. Nearby the Moon, the manifold trajectories, plotted in blue and red in Figure 6.47(d), and the 1:4 resonant orbit are different–in this region, the resonant orbit does not provide as close of an approximation for the geometry of the manifolds as in the region external to the ZVC.

Since many orbits of interest are not constrained to the plane, identification of a three-dimensional 1:4 resonant family offers additional options. A tangent bifurcation along the 1:4 resonant family, located via a Broucke stability diagram, leads to such a family. A portion of the southern half of the three-dimensional 1:4 resonant family is plotted in the
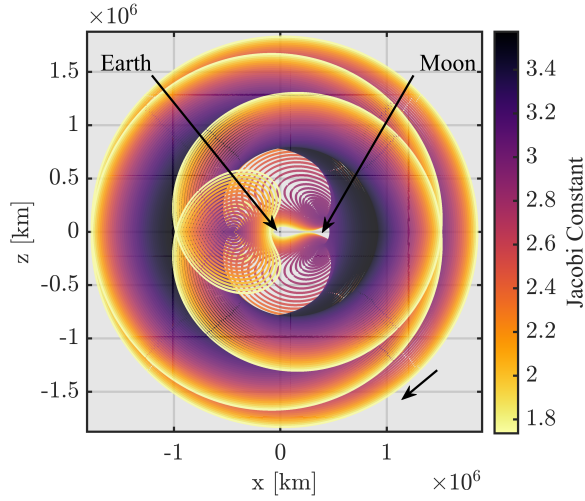
(a) 1:4 resonant orbit family
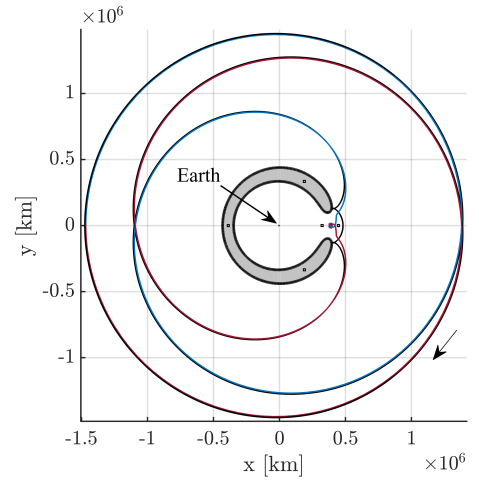
(b) x-y projection of 1:4 resonant orbit and NRHO manifolds
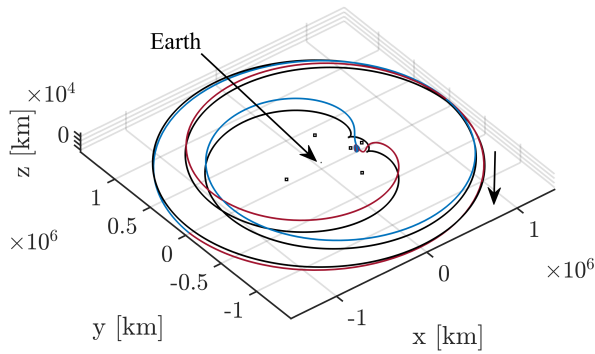
(c) Spatial view of 1:4 resonant orbit and NRHO manifolds
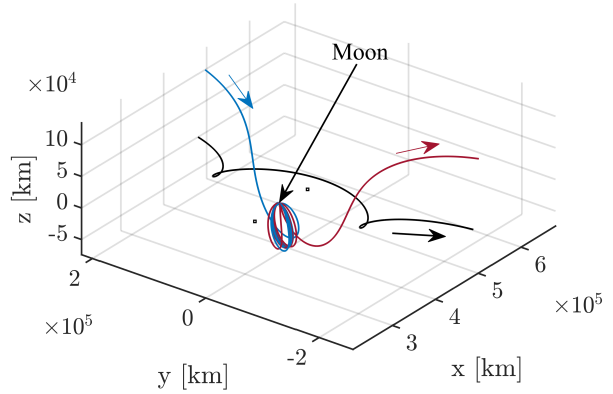
(d) 1:4 resonant orbit and NRHO manifolds in lunar vicinity

Figure 6.47. : 1:4 resonant orbit family (a) and comparison of a 1:4 resonant orbit at $JC = 3.04719$ to L_2 9:2 NRHO manifold trajectories in (b)-(d)

Earth-Moon rotating frame in Figure 6.48(a). The Jacobi constant value along the portion of the family plotted ranges from approximately 2.87 to 2.98; the energy level does not significantly change as the geometry changes along the family. Although the portion of the family computed does not reach the same energy level as the 9:2 lunar synodic resonant

NRHO, it may be useful for transfers between orbits at higher energies. Initial conditions for this periodic orbit family are available in Table A.12.

(a) 3D 1:4 resonant orbit family

(b) Jacobi constant vs period
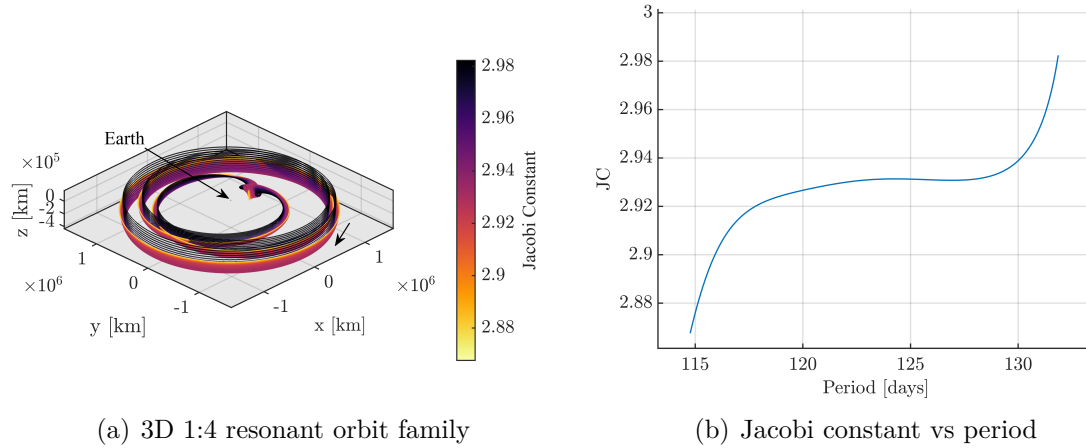
Figure 6.48. : 3D 1:4 resonant orbit family

6.4   NRHO Heteroclinic/Homoclinic Connections

Connections between the southern 9:2 lunar synodic resonant L_2 NRHO (the Gateway baseline orbit) and its northern counterpart are identified using a Poincaré mapping technique. By locating states in close proximity to one another on a Poincaré map, trajectories linking the southern and northern NRHOs are identified. States on the map used to link the southern NRHO to the northern NRHO correspond to unstable manifolds departing from a southern NRHO and stable manifolds approaching toward a northern NRHO. Since the 9:2 NRHO is unstable in a linear sense, its manifold trajectories are able to be computed. A heteroclinic connection is a ballistic (Δv-free) transfer trajectory that links two periodic orbits and can be identified by overlapping crossings on the Poincaré map. Such connections between the southern and northern 9:2 NRHOs exist; sample geometries are computed in the CR3BP and are plotted in the Earth-Moon rotating frame in Figure 6.49.

Heteroclinic transfer trajectories can also be computed in the reverse direction, that is, a transfer connecting the northern NRHO to its southern counterpart. When a 'southern
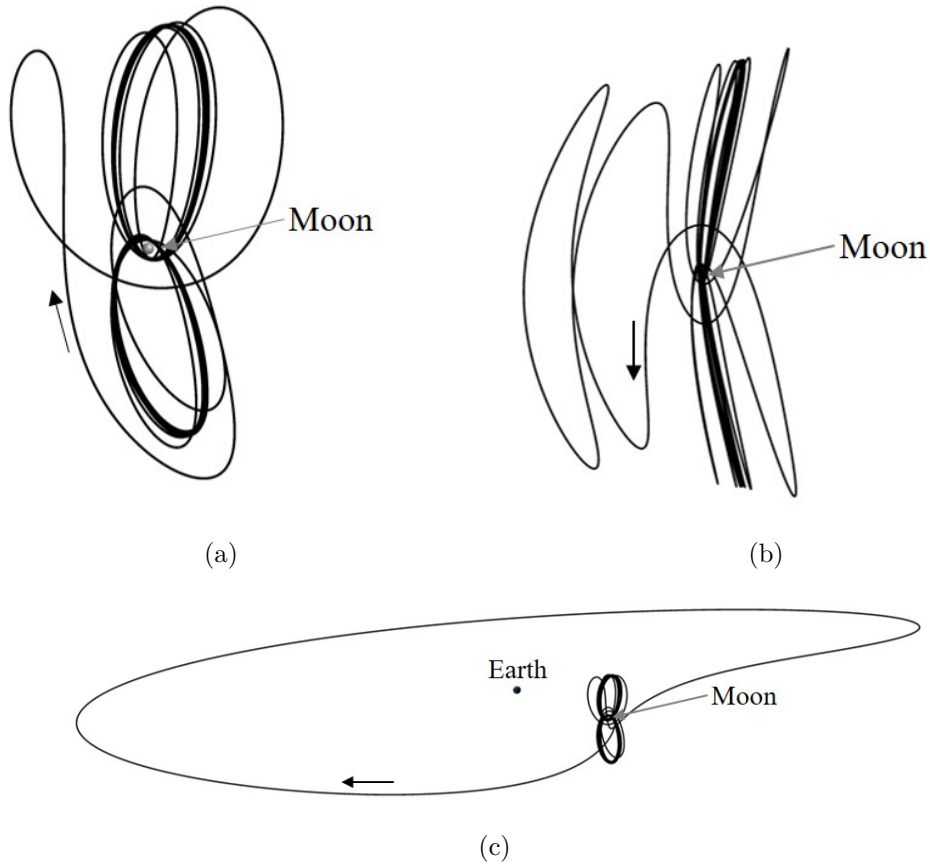
Figure 6.49. : Three sample southern to northern 9:2 NRHO heteroclinic connections

to northern' NRHO heteroclinic connection is combined with a 'northern to southern' NRHO heteroclinic connection, a transfer that departs the southern NRHO and subsequently returns to that same southern NRHO is generated. Ballistic trajectories that depart from and later return to the same periodic orbit are defined as homoclinic connections. Other homoclinic connections are available that do *not* utilize revolutions in the northern 9:2 NRHO. One example is plotted in the Earth-Moon rotating frame in Figure 6.50.

The heteroclinic transfer trajectories linking the southern and northern 9:2 NRHO also persist in a higher-fidelity model. The transfer trajectories displayed in Figures 6.49(a) and 6.49(b) are transitioned to the Earth-Moon-Sun ephemeris model and are plotted in the Earth-Moon rotating frame in Figure 6.51. Note, the white segment in Figure 6.51(a) possesses a TOF of 56 days, while the white segment in Figure 6.51(b) has a TOF of 82 days.
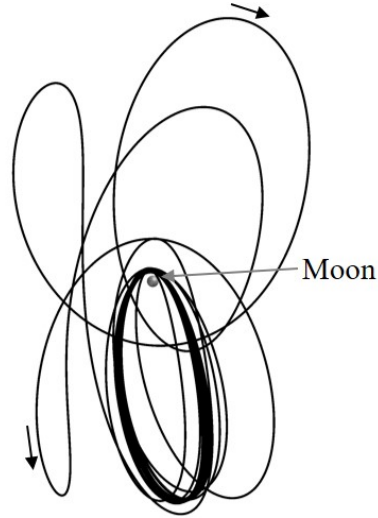
Figure 6.50. : Homoclinic transfer trajectory linking the southern 9:2 NRHO with itself

The total cost of these transfers in an ephemeris model is dependent on epoch, however, the total required Δv is typically near zero.

(a)

(b)
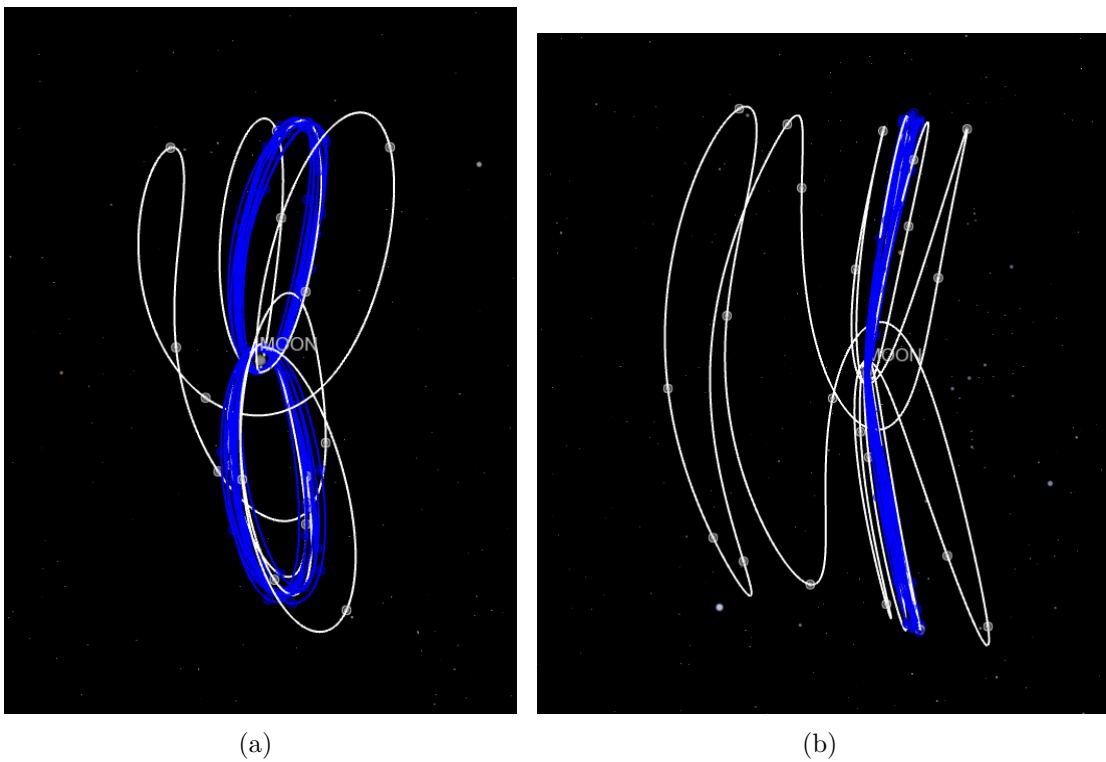
Figure 6.51. : Sample southern to northern 9:2 NRHO transfers in a higher-fidelity model plotted in the Earth-Moon rotating frame

7. CONCLUDING REMARKS

To enable the expansion of a human presence beyond low-Earth orbit and into deep space, understanding the complex multi-body dynamical regime of cislunar space within the context of trajectory planning and targeting is critical. This investigation contributes to the development of a methodology to move through cislunar space between destinations of interest, including stable and nearly-stable orbits, while implementing innovative strategies to incorporate realistic mission constraints. The development of this trajectory design approach allows for an understanding of fundamental motion in cislunar space that applies across many missions (including future hub/Gateway missions) enabling a more informed design approach, rather than focusing solely on point solutions. Additionally, just as the prescribed mission dictates the necessary trajectory, knowledge of accessible paths within the cislunar trajectory 'road-map' suggests available concepts, thereby allowing the emergence of previously unknown alternatives to be explored. This research effort aims to allow for the implementation of advanced trajectory concepts and to enable adaptability in complex designs. A simultaneous approach for designing the path, incorporating constraints, and understanding options in response to contingencies or requirement changes allows for a streamlined mission design flow from concept to implementation.

7.1 Response to Fundamental Questions and Investigation Summary

To review the impact of this research, it is beneficial to return to the fundamental questions posed in the introduction. Responses to the fundamental questions are discussed within the context of a summary of the investigation.

1. *Are there structures nearby stable or nearly-stable orbits (candidates for a long-duration cislunar hub) that have favorable stability characteristics for transfer design (i.e., possess unstable/stable manifolds into/out of the vicinity)?*

Nearby the L_2 NRHOs and the DROs, periodic orbit families that contain unstable members (and therefore have stable and unstable manifold structures) are identified using a bifurcation analysis. Since the periodic families of orbits identified in the analysis originate from bifurcations along the families of interest, the unstable structures are nearby both geometrically and in terms of energy/Jacobi constant value.

To answer this question, a dynamical model for analysis, the circular restricted three-body problem, is defined. The model is described in the context of the Earth-Moon system. Coordinate frames, e.g., the Earth-Moon rotating frame, and numerical techniques, e.g., single- and multiple-shooting differential corrections schemes are derived. Next, stability measures based on a variational discrete-time sensitivity matrix, the state transition matrix, are defined. The eigenvalues of the monodromy matrix, equivalent to the state transition matrix evaluated over one orbital period, yield stability bounds that dictate if an orbit is linearly stable or unstable. Since the monodromy matrix is symplectic, eigenvalues can be combined–the definition of stability index is then provided. Information about bifurcations is directly available from the evolution of stability along a periodic orbit family. Various types of bifurcations that are of interest to this investigation are described including tangent bifurcations, period-doubling bifurcations, period-multiplying bifurcations (where the multiplying factor is greater than 2), secondary Hopf bifurcations, and modified secondary Hopf bifurcations. The Broucke stability diagram, a tool used to monitor for bifurcations, is derived. The Broucke stability diagram is used to identify bifurcations along the NRHO portion of the L_2 halo family and the DRO family. Another useful tool, the bifurcation diagram, is introduced. The bifurcation diagram allows for connections between periodic orbit families to be identified visually. Additional information, such as order of instability changes along a family, is also available on a bifurcation diagram. Once bifurcations along the stable/nearly-stable orbit families of interest are identified, continuation schemes are combined with a free-variable and constraint multi-variable Newton's method to compute new families of periodic orbits. Both natural parameter and pseudo-arclength continuation methods are utilized in this study. It is in these

new families of periodic orbits, identified via a bifurcation analysis, that unstable orbit members with manifolds that ballistically approach and depart the vicinity are recognized.

2. *Can invariant manifolds from these nearby structures be incorporated, along with other known periodic orbits and manifolds, into a design technique for transfers into/out of a hub orbit to other destinations of interest?*

Trajectories along the invariant manifold surfaces belonging to the structures nearby the hub orbit (in this case, the 9:2 NRHO) are incorporated into a transfer design technique successfully. In addition to these manifold trajectories, other periodic orbit families in cislunar space and their manifolds are incorporated into the transfer design process as well. Of particular interest, members of the 3:4, 4:3, and 1:4 resonant orbit families and their corresponding manifolds are demonstrated to offer design utility in the region. Within the CR3BP, transfers connecting the 9:2 NRHO to a DRO at the same energy level are delivered. Additionally, methods to design recovery trajectories from inadvertent NRHO departures are detailed. As a part of these processes, transfers between the NRHO and multiple other cislunar orbits are computed. Finally, heteroclinic and homoclinic connections involving the L_2 southern and northern 9:2 lunar synodic resonant NRHO are identified.

To address this second fundamental question, a variety of strategies are first developed. A method to compute trajectories that lie along the invariant manifold surfaces associated with unstable periodic orbits is derived. This method involves identifying the eigenvectors associated with the unstable/stable eigenvalues of the monodromy matrix associated with a fixed point of a periodic orbit. Once the eigenvectors are identified, states are numerically propagated along these eigenvector directions to produce trajectories. In order to simplify the visualization of complex dynamical flow and to find connections between structures, including manifold trajectories, a Poincaré mapping technique is used. Poincaré mapping involves defining a hyperplane and recording trajectory crossings of that hyperplane. Combinations of states at the hyperplane crossings (e.g., x and $\dot{x}$) are then plotted on a 'map.' Crossings in close proximity on the

map may correspond to trajectory arcs that approach closely in the full state vector, thus, these arcs form the basis for initial guesses for transfer trajectories. To solve for transfer trajectories that meet various constraints, including position and velocity continuity, differential corrections are used. In this investigation, a multi-variable Newton's method in the form of a free-variable and constraint method is utilized.

The manifolds associated with the nearby periodic orbits identified from the bifurcation analysis of the NRHOs deliver useful initial guesses that reduce total time of flight required to depart the NRHO vicinity. Since transfer time of flight is often constrained, especially for crewed applications, strategies to produce shorter-duration transfers are useful. As an additional part of this investigation, useful intermediate structures in the form of members of resonant orbit families are also identified. These structures aid in the construction of transfer trajectories that connect the NRHO with other cislunar orbits of interest. Using Poincaré mapping of manifolds associated with unstable cislunar orbits at the same energy level as the 9:2 NRHO, the 3:4, 4:3, and 1:4 resonant orbit families are observed to offer additional transfer design options. In fact, the 1:4 resonant orbit family in particular is similar in geometry to optimized results from other authors. Using intermediate periodic orbits, e.g., the higher-period halo orbits, is an effective strategy to design transfers into and out of the hub orbit. Applications demonstrated include transfer design between the NRHO and DRO, heteroclinic and homoclinic connections involving the southern and northern 9:2 NRHO, transfers between various other cislunar orbits and the NRHO, and recoveries from inadvertent NRHO departures that return a spacecraft back to an NRHO. The geometries obtained from the design technique, which involves using an intermediate orbit to initiate departure from the NRHO then connecting the intermediate orbit to a destination of interest, are shown to persist when optimized in the CR3BP.

3. *Do designs based on these fundamental structures (found in the CR3BP) persist in a higher-fidelity dynamical model?*

Newly identified dynamical structures, e.g., members of the higher-period halo orbit families, are demonstrated to persist in a higher-fidelity ephemeris model. Addi-

tionally, transfer trajectories initially designed in the CR3BP are able to be transitioned to the ephemeris model and geometry is predominantly maintained.

To answer this third fundamental question, the ephemeris model is first described. A strategy to transition periodic orbits and transfer trajectories from the CR3BP to the N-body ephemeris model is then derived. This transition strategy necessarily involves frame rotations between the CR3BP rotating frame and primary-centered inertial frames. Additionally, to meet constraints on ephemeris trajectories, including position, velocity, and epoch continuity, an ephemeris differential corrections process is derived. In this investigation, to demonstrate that the fundamental structures themselves do indeed persist in the higher-fidelity model, sample synodic resonant orbits from multiple orbit families are selected as sample cases. It is observed that over multiple revolutions, the ephemeris quasi-periodic orbits remain in close proximity to their corresponding CR3BP counterpart. Next, a variety of transfer trajectories based on fundamental structures in cislunar space, that are initially designed in the CR3BP, are transitioned to the ephemeris model. The geometries of the CR3BP transfer trajectories are demonstrated to persist in the higher-fidelity ephemeris model. Finally, designs in the ephemeris model are optimized for reduction in total Δv. When optimized, the fundamental structures are still prevalent indicating that they do indeed persist, even when optimized within a higher-fidelity ephemeris model.

4. *Can challenging mission constraints (e.g., eclipse avoidance) be implemented in the initial design process to yield a more cohesive transition from design to application?*

Multiple types of mission constraints are considered in this study. However, in response to a particularly challenging limitation and upcoming mission needs, a strategy to avoid eclipse conditions along multi-revolution, quasi-periodic ephemeris orbits using synodic resonance is demonstrated. Additionally, eclipse conditions are avoided through the use of a path constraint within the differential corrections process associated with transitioning trajectories from the CR3BP to the ephemeris model. The eclipse-avoidance constraint promotes the successful computation of eclipse-free, many revolution quasi-periodic orbits and transfer trajectories within the higher-fidelity

ephemeris model. The eclipse-free, quasi-periodic orbits and transfer trajectories remain consistent with designs from the CR3BP, thus strategies to produce a more cohesive transition from design (in the CR3BP) to application (demonstrated in the ephemeris model) are indeed delivered.

In this investigation, a primary focus on eclipse avoidance is placed due to upcoming mission needs, e.g., NASA's Gateway mission. Prior to developing a strategy to avoid eclipse conditions, a model for the shadows cast by the Earth and Moon is developed. This model is based on the penumbral shadow cone. It is also noted that useful visualization frames are defined; the Sun-Moon rotating frame allows for simple visualization of lunar eclipses while the Sun-Earth rotating frame allows for visualization of encounters with the Earth's shadow. The shadow cast by the smaller primary in each of these frames remains fixed along the corresponding rotating frame x-axis. Next, lunar synodic resonance within the context of the NRHOs and higher-period structures that exist in their vicinity is explored. Lunar synodic resonant orbits along the families are identified in the CR3BP and sample resonant orbits are transitioned to the ephemeris model. Not only did the geometry of these sample synodic resonant orbits persist in the higher-fidelity model, but the geometries of these orbits are such that, with careful epoch selection, Earth and Moon eclipses are successfully avoided over an extended duration. The resonant orbits are visualized in the Sun-Earth and Sun-Moon rotating frames. Next, an integral-type eclipse avoidance path constraint is derived. This constraint is enforced in the differential corrections process associated with transitioning trajectories from the CR3BP to the ephemeris model. Note that typically constraints are placed at nodes or patch points along trajectories and enforced at these locations alone. In order to successfully avoid shadow conditions however, a constraint along the path that exists between patchpoints is necessary. Using the eclipse avoidance path constraint, trajectories are transitioned from the CR3BP to the ephemeris model and complex mission constraints are enforced. The technique is demonstrated to produce many-revolution, quasi-periodic ephemeris orbits that avoid all Earth and Moon eclipses. In addition, transfer trajectories in the ephemeris model

are produced that do not encounter any shadow conditions. Since the geometry of the CR3BP initial guess in both of these cases is maintained, the strategy developed in this investigation to meet constraints does, in fact, produce a predictable final design.

7.2 Recommendations for Future Work

As is the case with many research endeavors, options for future work are numerous. A few areas of interest that could serve to enhance and continue the investigation are enumerated below:

- *Investigate how transfer designs based on ballistic fundamental structures are affected by transitioning to a low-thrust engine model.*

  Various types of spacecraft are expected to utilize both the cislunar hub and a transportation network in the Earth-Moon neighborhood. To broaden the design techniques developed in this investigation beyond spacecraft with chemical engines (that are modeled with impulsive burns), a low-thrust extension of transfer trajectories in this regime is necessary. Impulsive transfer solutions are able to be transitioned to a low-thrust model using a strategy posed by Pritchett, Zimovan, and Howell [39]. Transfer geometries transitioned between engine models using this strategy tend to persist with both engine models. Low-thrust solutions computed in the CR3BP must also be verified in a higher-fidelity low-thrust ephemeris model to demonstrate that the designs are realizable for mission scenarios.

- *Investigate bifurcations along the computed higher-period orbit families as well as period-multiplying bifurcations with multiplying factor greater than four. Investigate the utility that new families arising from these bifurcations may offer to transfer design in the region.*

  The current investigation is limited to bifurcations from the NRHO portion of the L_2 halo family and the DRO family. Additionally, in the conducted bifurcation analysis,

period-multiplying bifurcations are limited to a multiplying factor of less than or equal to four. As illustrated in the Broucke stability diagrams in Figure 5.19 and bifurcation diagrams in Figures 5.18 and 5.46, the dynamics in the vicinity of the Moon give rise to many complex dynamical structures beyond those computed here. Although a number of new families of periodic orbits are identified in this investigation, there are many more dynamical structures that may arise from bifurcations along these new families or from period-multiplying bifurcations along the NRHOs and DROs that are beyond multiplying factor four. In other words, just as the L_2 halo family originates at a bifurcation from the L_2 Lyapunov family and the P2HO$_1$ family originates from a bifurcation in the L_2 halo family, bifurcations along the P2HO$_1$ family may lead to new, useful structures. As an example, a period-tripling bifurcation exists along the P2HO$_1$ family. The family that originates at this period-tripling bifurcation, the period-3 P2HO$_1$ (or P3P2HO$_1$) family is plotted in Figure 7.1(a); an individual member of the family is plotted in Figure 7.1(b). The initial conditions for this orbit family are available in Table A.13. Members of this orbit family and other families not yet computed may offer advantages for various design scenarios. A continued analysis of bifurcations is useful to further expand understanding of the complex dynamics in the vicinity of the Moon.

- *Investigate use of higher-period structures nearby the NRHOs to design transfers between hub orbit and heliocentric space for applications to reach Mars and beyond.*

  Missions beyond the Earth-Moon neighborhood into heliocentric space are of interest in the near-term. As operations in the proposed hub orbit ramp up, low-cost disposal trajectories to heliocentric space will become increasingly necessary to rid the vicinity of spent vehicles and other debris objects. Boudad et al. investigate some disposal trajectory options from the NRHOs [37]. Beyond disposal trajectories, exploration missions departing to regions outside of cislunar space from the hub orbit, e.g. to reach Mars, must be reliably and predictably designed. The strategies developed in this investigation to design trajectories that depart from stable and nearly-stable hub orbits, such as the NRHOs, are expected to be applicable to accessing regions beyond cislunar
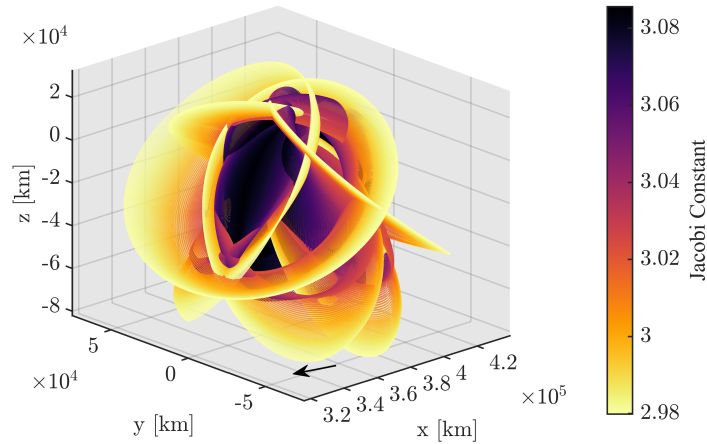
(a) Period-3 P2HO$_1$ family
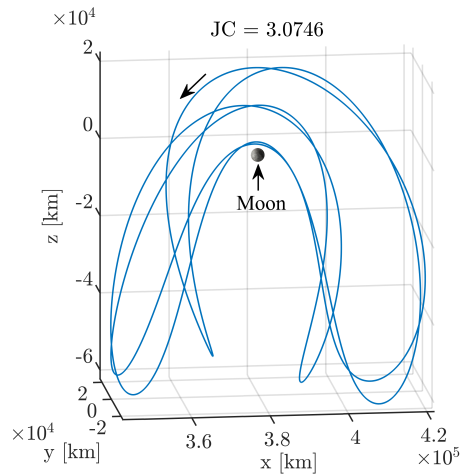
(b) Period-3 P2HO$_1$ orbit at $JC = 3.0746$

Figure 7.1. : Period-3 P2HO$_1$ family plotted in the Earth-Moon rotating frame

space as well. Connecting manifolds departing the nearby higher-period structures in the vicinity of the NRHOs to heliocentric arcs will require careful consideration of the Sun's gravitational influence and will also lead to additional phasing requirements.

- *Expand analysis of recovery trajectories for inadvertent departures from the NRHO to include 'regime 3.'*

In the present analysis, regime 2 recoveries are explored. Reference [44] details regime 1 recovery analysis conducted using a Monte Carlo approach. Recovery regime 3 includes

207

trajectories that have departed the lunar vicinity toward heliocentric space or toward the Earth. It is expected that regime 3 Earthbound departures may be recoverable using cislunar structures similar to those used for regime 2 recovery, however, this analysis has yet to be completed. Additional strategies may be necessary to design recovery trajectories for departures that have reached heliocentric space. In this regime, the bi-circular four-body model may be useful to incorporate solar gravity [40].

REFERENCES

[1] W. H. Gerstenmaier, *Progress in Defining the Deep Space Gateway and Transport Plan*, https://go.nasa.gov/312ZUOc, NASA, Mar. 2017.

[2] *Deep Space Gateway to Open Opportunities for Distant Destinations*, https://www.nasa.gov/feature/deep-space-gateway-to-open-opportunities-for-distant-destinations, Editor: Kathryn Hambleton, NASA, Aug. 2018.

[3] I. Newton, *The Principia: Mathematical Principles of Natural Philosophy*. University of California Press, 1999, Translated by I. Bernard Cohen and Anne Whitman.

[4] J. Barrow-Green, *Poincaré and the Three Body Problem, History of Mathematics Vol. 11*. American Mathematical Society, 1997.

[5] V. Szebehely, *Theory of Orbits: The Restricted Problem of Three Bodies*. New York: Academic Press, Inc., 1967.

[6] G. W. Hill, "Reasearches into the Lunar Theory," *American Journal of Mathematics*, vol. 1, no. 1, pp. 5–26, 1878.

[7] J. H. Poincaré, *Les Méthodes Nouvelles de la Mécanique Céleste, Vol. 1-3*. Gauthier-Villars et fils, 1899.

[8] R. Farquhar, D. Muhonen, and L. Church, "Trajectories and Orbital Maneuvers for the ISEE-3/ICE Comet Mission," in *Astrodynamics Conference*, 1984.

[9] M. Woodard, D. Folta, and D. Woodfork, "ARTEMIS: the First Mission to the Lunar Libration Orbits," in *21st International Symposium on Space Flight Dynamics*, Toulouse, France, 2009.

[10] M. W. Lo, B. G. Williams, W. E. Bollman, D. Han, Y. Hahn, J. L. Bell, E. A. Hirst, R. A. Corwin, P. E. Hong, K. C. Howell, B. Barden, and R. Wilson, "Genesis Mission Design," *The Journal of the Astronautical Sciences*, vol. 49, no. 1, pp. 169–184, 2001. DOI: https://doi.org/10.1007/BF03546342.

[11] H. B. Keller, *Numerical Solution of Two Point Boundary Value Problems*. SIAM, 1976.

[12] S. M. Roberts and J. S. Shipman, "Continuation in Shooting Methods for Two-Point Boundary Value Problems," *Journal of Mathematical Analysis and Applications*, vol. 18, no. 1, pp. 45–58, 1967.

[13] S. M. Roberts and J. S. Shipman, "Justification for the Continuation Method in Two-Point Boundary Value Problems," *Journal of Mathematical Analysis and Applications*, vol. 21, no. 1, pp. 23–30, 1968.

[14] M. R. Osborne, "On Shooting Methods for Boundary Value Problems," *Journal of Mathematical Analysis and Applications*, vol. 27, no. 2, pp. 417–433, 1969.

[15] T. A. Pavlak, "Trajectory Design and Orbit Maintenance Strategies in Multi-Body Dynamical Regimes," Ph.D. Dissertation, School of Aeronautics and Astronautics, Purdue University, West Lafayette, Indiana, May 2013.

[16] F. R. Moulton, *Periodic Orbits*. Carnegie Institution of Washington, 1920.

[17] D. J. Grebow, "Generating Periodic Orbits in the Circular Restricted Three-Body Problem with Applications to Lunar South Pole Coverage," M.S. Thesis, School of Aeronautics and Astronautics, Purdue University, West Lafayette, Indiana, May 2006.

[18] W. R. Schlei, "Interactive Spacecraft Trajectory Design Strategies Featuring Poincaré Map Topology," Ph.D. Dissertation, School of Aeronautics and Astronautics, Purdue University, West Lafayette, Indiana, May 2017.

[19] R. W. Farquhar, "The Control and Use of Libration-Point Satellites," Ph.D. Dissertation, Stanford University, 1968.

[20] J. V. Breakwell and J. V. Brown, "The 'Halo' Family of 3-Dimensional Periodic Orbits in the Earth-Moon Restricted 3-Body Problem," *Celestial Mechanics*, vol. 20, pp. 389–404, November 1979.

[21] K. C. Howell, "Three-Dimensional, Periodic, 'Halo' Orbits," *Celestial Mechanics*, vol. 32, pp. 53–71, January 1984.

[22] K. C. Howell and J. V. Breakwell, "Almost Rectilinear Halo Orbits," *Celestial Mechanics*, vol. 32, no. 1, pp. 29–52, 1984.

[23] E. M. Zimovan, "Characteristics and Design Strategies for Near Rectilinear Halo Orbits within the Earth-Moon System," M.S. Thesis, School of Aeronautics and Astronautics, Purdue University, West Lafayette, Indiana, Aug. 2017.

[24] L. Capdevila, "A Transfer Network Linking Earth, Moon and the Libration Point Regions in the Earth-Moon System," Ph.D. Dissertation, Purdue University, West Lafayette, Indiana, 2016, pp. 1–127.

[25]   J. S. Parker, C. Bezrouk, and K. E. Davis, "Low-Energy Transfers to Distant Ret-
        rograde Orbits," *Advances in the Astronautical Sciences Spaceflight Mechanics 2015*,
        AAS 15–311.

[26]   J. F. C. Herman, "Improved Collocation Methods to Optimize Low-Thrust, Low-
        Energy Transfers in the Earth-Moon System," Ph.D. Dissertation, University of Col-
        orado, Boulder, Colorado, 2015, pp. 1–168.

[27]   N. L. Parrish, J. S. Parker, S. P. Hughes, and J. Heiligers, "Low-Thrust Transfers From
        Distant Retrograde Orbits To L2 Halo Orbits in the Earth-Moon System," in *Inter-
        national Conference on Astrodynamics Tools and Techniques*, Darmstadt, Germany,
        2016, pp. 1–9.

[28]   M. McGuire, L. Burke, S. McCarty, K. J. Hack, R. Whitley, D. C. Davis, and C.
        Ocampo, "Low Thrust Cis-Lunar Transfers Using a 40 kW-Class Solar Electric Propul-
        sion Spacecraft," in *AAS/AIAA Astrodynamics Specialist Conference 2017*, Stevenson,
        Washington, Aug. 2017.

[29]   S. L. McCarty and M. L. McGuire, "Parallel Monotonic Basin Hopping for Low Thrust
        Trajectory Optimization," in *AIAA SciTech Forum*, Kissimmee, Florida, Jan. 2018.

[30]   G. Lantoine, "Efficient NRHO to DRO Transfers in Cislunar Space," in *AAS/AIAA
        Astrodynamics Specialist Conference*, Stevenston, Washington, Aug. 2017.

[31]   M. Loucks, K. Post, and J. Carrico, "Lunar Near Rectilinear Orbits and Cis-Lunar
        Transfer Trajectories in Support of the Deep Space Proving Ground," in *Paper No.
        AAS 16-244*, 2016.

[32]   R. W. Farquhar, "The Utilization of Halo Orbits in Advanced Lunar Operations," in
        NASA Technical Note D-6365, Goddard Space Flight Center, Greenbelt, Maryland,
        1971.

[33]   General Electric Company, "Final Report for Lunar Libration Point Flight Dynam-
        ics Study," in *Contract NAS-5-11551 with Goddard Space Flight Center*, Greenbelt,
        Maryland, April 1969.

[34]   D. C. Folta, T. A. Pavlak, A. F. Haapala, and K. C. Howell, "Preliminary Design
        Considerations for Access and Operations in Earth-Moon L1/L2 Orbits," in *Paper No.
        AAS 13-339, 23rd AAS/AIAA Spaceflight Mechanics Meeting*, Kauai, Hawaii, Feb.
        2013.

[35]   R. Whitley and R. Martinez, "Options for Staging Orbits in Cis-Lunar Space," in *2016
        IEEE Aerospace Conference*, 2016.

[36] D. C. Davis, K. K. Boudad, R. J. Power, and K. C. Howell, "Heliocentric Escape and Lunar impact from Near Rectilinear Halo Orbits," in *2019 AAS/AIAA Astrodynamics Specialist Conference*, Portland, Maine, Aug. 2019.

[37] K. K. Boudad, D. C. Davis, and K. C. Howell, "Disposal Trajectories from Near Rectilinear Halo Orbits," in *Paper No. AAS 18-289, AAS/AIAA Astrodynamics Specialist Conference, Snowbird, Utah*, Aug. 2018.

[38] E. M. Zimovan, K. C. Howell, and D. C. Davis, "Near Rectilinear Halo Orbits and Their Application in Cis-Lunar Space," in *3rd International Academy of Astronautics Conference on Dynamics and Control of Space Systems*, Moscow, Russia, May 2017.

[39] R. Pritchett, E. Zimovan, and K. C. Howell, "Impulsive and Low-Thrust Transfer Design between Stable and Nearly-Stable Periodic Orbits in the Restricted Problem," in *18th AIAA SciTech Forum*, Kissimmee, Florida, January 8–12, 2018.

[40] K. Boudad, K. Howell, and D. Davis, "Near Rectilinear Halo Orbits in Cislunar Space Within the Context of the Bicircular Four-Body Problem," in *2nd IAA/AAS SciTech Forum*, Moscow, Russia, Jun. 2019.

[41] J. A. O. Romero and K. C. Howell, "Transfers from GTO to Sun-Earth Libration Orbits," in *AAS/AIAA Astrodynamics Specialist Conference, Portland, Maine*, Portland, Maine, Aug. 2019.

[42] J. D. Aziz, "Low-Thrust Many-Revolution Trajectory Optimization," Ph.D. Dissertation, University of Colorado, Boulder, Colorado, 2018.

[43] E. M. Zimovan-Spreen, K. C. Howell, and D. C. Davis, "Near Rectilinear Halo Orbits and Nearby Higher-Period Dynamical Structures: Orbital Stability and Resonant Properties," *Celestial Mechanics and Dynamical Astronomy*, vol. 132, no. 28, Jun. 2020. DOI: https://doi.org/10.1007/s10569-020-09968-2.

[44] E. M. Zimovan-Spreen, D. C. Davis, and K. C. Howell, "Recovery Trajectories for Inadvertent Departures from an NRHO," in *31st AAS/AIAA Space Flight Mechanics Meeting*, Virtual, Feb. 2021.

[45] E. M. Zimovan-Spreen, K. C. Howell, and D. C. Davis, "Eclipse Avoidance in Dynamical Structures Nearby NRHOs in a Higher-Fidelity Model," in *2020 AAS/AIAA Astrodynamics Specialist Virtual Conference*, Lake Tahoe, California, Aug. 2020.

[46] E. M. Zimovan-Spreen and K. C. Howell, "Dynamical Structures Nearby NRHOs with Applications in Cislunar Space," in *2019 AAS/AIAA Astrodynamics Specialist Conference*, Portland, Maine, Aug. 2019.

[47] R. Pritchett, E. Zimovan, and K. C. Howell, "Impulsive and Low-Thrust Transfer Design between Stable and Nearly Stable Periodic Orbits in the Restricted Problem," in *18th AIAA SciTech Forum*, Kissimmee, Florida, Jan. 2018.

[48] D. Guzetti, E. M. Zimovan, K. C. Howell, and D. C. Davis, "Stationkeeping Analysis for Spacecraft in Lunar Near Rectilinear Halo Orbits," in *Paper No. AAS-2017-395, AAS/AIAA Spaceflight Mechanics Meeting*, San Antonio, Texas, Feb. 2017.

[49] D. C. Davis, S. A. Bhatt, K. Howell, J. Jang, R. Whitley, F. Clark, D. Guzzetti, E. Zimovan, and G. Barton, "Orbit Maintenance and Navigation of Human Spacecraft at Cislunar Near Rectilinear Halo Orbits," in *Paper No. AAS 17-269, AAS/AIAA Spaceflight Mechanics Meeting*, San Antonio, Texas, Feb. 2017.

[50] C. H. Acton Jr., *Ancillary Data Services of NASA's Navigation and Ancillary Information Facility*, https://naif.jpl.nasa.gov/naif/, Jan. 1996.

[51] R. V. Robertson, "Highly Physical Solar Radiation Pressure Modeling During Penumbra Transitions," Ph.D. Dissertation, Virginia Polytechnic Institude and State University, 2015.

[52] E. Doedel and V. Romanov, "Elemental Periodic Orbits Associated with the Libration Points in the Circular Restricted 3-Body Problem," *International Journal of Bifurcation and Chaos*, vol. 17, no. 8, pp. 2625–2677, 2007.

[53] H. B. Keller, "Numerical Solutions of Bifurcations and Nonlinear Eigenvalue Problems," *Applications of Bifurcation Theory*, pp. 359–384, 1977, Editor: Paul Rabinowitz, Academic Press.

[54] L. Perko, *Differential Equations and Dynamical Systems*. New York, 3rd Edition: Springer-Verlag, 2001.

[55] N. Bosanac, "Leveraging Natural Dynamical Structures to Explore Multi-Body Systems," Ph.D. Dissertation, Purdue University, West Lafayette, Indiana, 2016.

[56] W. S. Koon, M. W. Lo, J. E. Marsden, and S. D. Ross, *Three Body Problem and Space Mission Design*. Springer-Verlag, 2006.

[57] E. Campbell, "Bifurcations from Families of Periodic Solutions in the Circular Restricted Problem with Application to Trajectory Design," Ph.D. Dissertation, Purdue University, West Lafayette, Indiana, 1999.

[58] D. C. Heggie, "Bifurcation at Complex Instability," *Celestial Mechanics*, vol. 35, pp. 357–382, 1985.

[59] J. K. Hale and H. Koçak, *Dynamics and Bifurcations*, 1st Edition, ser. Texts in Applied Mathematics. Springer-Verlag, 1991.

[60] R. Broucke, "Stability of Periodic Orbits in the Elliptic, Restricted Three-Body Problem," *AIAA Journal*, vol. 7, no. 6, pp. 1003–1009, 1969.

[61] D. Grebow, "Trajectory Design in the Earth-Moon System and Lunar South Pole Coverage," Ph.D. Dissertation, Purdue University, West Lafayette, Indiana, 2010.

[62] B. P. McCarthy, "Characterization of Quasi-periodic Orbits for Applications in the Sun-Earth and Earth-Moon Systems," M.S. Thesis, School of Aeronautics and Astronautics, Purdue University, West Lafayette, Indiana, Dec. 2018.

[63] MATLAB, *Version 9.6.0.1135713 (R2019a)*. Natick, Massachusetts: The MathWorks, Inc., 2019.

[64] K. K. Boudad, K. C. Howell, and D. C. Davis, "Dynamics of Synodic Resonant Near Rectilinear Halo Orbits in the Bicircular Four-Body Problem," *Advances in Space Research*, vol. 66, no. 9, pp. 2194–2214, 2020. DOI: https://doi.org/10.1016/j.asr.2020.07.044.

[65] C. Pickover, *The longest line in america!* http://sprott.physics.wisc.edu/pickover/pc/american-line.html, Physics Department at University of Wisconsin, Madison.

[66] The Cornell Lab of Ornithology, *All About Birds: Mallard Identification*, https://www.allaboutbirds.org/guide/Mallard, Cornell University, 2019.

[67] U.S. Fish and Wildlife Service, "Waterfowl Population Status, 2018," U.S. Department of the Interior, Washington, D.C., USA, Tech. Rep., 2018.

[68] I. Robin and V. Markellos, "Numerical determinations of three-dimensional orbits generated from vertical self-resonant satellite orbits," *Celestial Mechanics*, vol. 21, pp. 395–434, 1980.

[69] D. Grebow, M. Ozimek, K. Howell, and D. Folta, "Multi-Body Orbit Architectures for Lunar South Pole Coverage," *Journal of Spacecraft and Rockets*, vol. 45, no. 2, pp. 344–358, 2008.

[70] D. C. Davis, K. K. Boudad, S. M. Phillips, and K. C. Howell, "Disposal, Deployment, and Debris in Near Rectilinear Halo Orbits," in *Paper No. AAS 19-466, 29th AAS/AIAA Space Flight Mechanics Meeting, Ka'anapali, Maui, Hawaii*, Jan. 2019.

[71] R. J. Power, "Characterization of Lunar Access Relative to Cislunar Orbits," M.S. Thesis, School of Aeronautics and Astronautics, Purdue University, West Lafayette, Indiana, Dec. 2019.

[72] J. Williams, D. E. Lee, R. L. Whitley, K. A. Bokelmann, D. C. Davis, and C. F. Berry, "Targeting Cislunar Near Rectilinear Halo Orbits for Human Space Exploration," in *Paper No. AAS 17-267, AAS/AIAA Spaceflight Mechanics Meeting*, San Antonio, Texas, Feb. 2017.

[73] C. P. Newman, D. C. Davis, R. J. Whitley, J. R. Guinn, and M. S. Ryne, "Stationkeeping, Orbit Determination, and Attitude Control for Spacecraft in Near Rectilinear Halo Orbits," in *Paper No. AAS 18-388, AAS Astrodynamics Specialist Conference*, Snowbird, Utah, Aug. 2018.

[74] D. E. Lee, "White Paper: Gateway Destination Orbit Model: A Continuous 15 Year NRHO Reference Trajectory," National Aeronautics and Space Administration, NASA Johnson Space Center, Houston, TX, Tech. Rep. Document ID: 20190030294, Aug. 2019.

[75] D. C. Davis, S. M. Phillips, K. C. Howell, S. Vutikuri, and B. P. McCarthy, "Stationkeeping and Transfer Trajectory Design for Spacecraft in Cislunar Space," in *Paper No. AAS 17-826, AAS/AIAA Astrodynamics Specialist Conference, Columbia River Gorge, Stevenson, Washington*, Aug. 2017.

[76] *Around the Moon with NASA's First Launch of SLS with Orion*, https://www.nasa.gov/feature/around-the-moon-with-nasa-s-first-launch-of-sls-with-orion, Editor: Kathryn Hambleton, NASA, Mar. 2018.

[77] T. Cichan, S. D. Norris, and P. Marshall, "Orion: Eft-1 flight test results and em-1/2 status," in *AIAA SPACE 2015 Conference and Exposition*, Pasadena, California, Aug. 2015, p. 4414.

[78] A. D. Cox, N. Bosanac, D. Guzzetti, K. Howell, D. Folta, and C. Webster, "An Interactive Trajectory Design Enviornment Leveraging Dynamical Structures in Multi-body Regimes," in *6th International Conference on Astrodynamics Tools and Techniques*, Darmstadt, Germany, Mar. 2016.

[79] D. Folta, N. Bosanac, D. Guzzetti, and K. Howell, "An Earth-Moon System Trajectory Design Reference Catalog," in *2nd AIAA Conference on Dynamics and Control of Space Systems*, Roma, Italy, Mar. 2014.

[80] D. Folta, C. Webster, N. Bosanac, A. D. Cox, D. Guzzetti, and K. Howell, "Trajectory Design Tools for Libration and Cislunar Environments," in *6th International Conference on Astrodynamics Tools and Techniques*, Darmstadt, Germany, Mar. 2016.

215

[81] D. Guzzetti, N. Bosanac, A. Haapala, K. Howell, and D. Folta, "Rapid Trajectory Design in the Earth-Moon Ephemeris System via an Interactive Catalog of Periodic and Quasi-Periodic Orbits," *Acta Astronautica*, vol. 126, pp. 439–455, Sep. 2016.

[82] D. E. Lee, R. J. Whitley, and C. Acton, *Sample Deep Space Gateway Orbit: NAIF Plantary Data System Navigation Node*, https://go.nasa.gov/3lGWUQX, NASA Jet Propulsion Laboratory, 2018.

[83] V. Muralidharan and K. C. Howell, "Stationkeeping in Earth-Moon Near Rectilinear Halo Orbits," in *AAS/AIAA Astrodynamics Specialist Conference*, Lake Tahoe, California (Virtual), Aug. 2020.

[84] D. C. Davis, R. J. Power, K. C. Howell, and J. P. Gutkowski, "Lunar Impact Probability for Spacecraft in Near Rectilinear Halo Orbits," in *31st AAS/AIAA Space Flight Mechanics Meeting*, Virtual, Feb. 2021.

[85] J. Williams, H. A. Kamath, R. A. Eckman, G. L. Condon, R. Mathur, and D. C. Davis, "Copernicus 5.0: Latest Advances in JSC's Spacecraft Trajectory Optimization and Design System," in *AAS/AIAA Astrodynamics Specialists Conference*, Portland, Maine, Aug. 2019.

[86] S. L. McCarty and M. L. McGuire, "Parallel Monotonic Basin Hopping for Low Thrust Trajectory Optimization," in *2018 Space Flight Mechanics Meeting*, Kissimmee, Florida, Jan. 2018.

[87] S. L. McCarty, L. M. Burke, and M. L. McGuire, "Analysis of Cislunar Transfers from a Near Rectilinear Halo Orbit with High Power Solar Electric Propulsion," in *AAS/AIAA Astrodynamics Specialist Conference*, Snowbird, Utah, Aug. 2018.

[88] M. Gupta, "Finding Order in Chaos: Resonant Orbits and Poincaré Sections," M.S. Thesis, School of Aeronautics and Astronautics, Purdue University, West Lafayette, Indiana, May 2020.

[89] T. M. V. Escribano, "Spacecraft Transfer Trajectory Design Exploiting Resonant Orbits in Multi-Body Environments," Ph.D. Dissertation, Purdue University, West Lafayette, Indiana, 2013.

A. INITIAL CONDITIONS FOR PERIODIC ORBIT FAMILIES

Tables of initial conditions for sample periodic orbit families used in this analysis are available in the following appendix. The initial conditions of select family members are provided along with the Jacobi constant value and orbital period of the family member. The state values in the tables are initial conditions in the barycenter-centered Earth-Moon rotating frame and are provided as nondimensional values. The characteristic quantities used to redimensionalize these values are defined as: characteristic length, $l^* = 384400$ km, and characteristic time, $t^* = 375190.25852$ sec. Since each initial condition is provided at a perpendicular crossing of the $y = 0$ plane, the values for y_0, $\dot{x}_0$, and $\dot{z}_0$ are equal to zero. A corrections scheme may still be necessary to solve for a precisely periodic solution due to differences in characteristic value, numerical integrator, or even differences between computers, however, the values in the tables provide useful initial guesses.

Table A.1. : Initial conditions for the L_2 halo orbit family

JC	Period	x_0	z_0	$\dot{y}_0$
3.0591	1.3632096570	1.0110350588	-0.1731500000	-0.0780141199
3.0493	1.4748399512	1.0192741002	-0.1801324242	-0.0971927950
3.0411	1.5872714606	1.0277926091	-0.1858044184	-0.1154896637
3.0341	1.7008482705	1.0362652156	-0.1904417454	-0.1322667493
3.0283	1.8155211042	1.0445681848	-0.1942338538	-0.1473971442
3.0236	1.9311168544	1.0526805665	-0.1972878310	-0.1609628828
3.0199	2.0474562565	1.0606277874	-0.1996480091	-0.1731020372
3.0171	2.1741533495	1.0691059976	-0.2014140887	-0.1847950147
3.0155	2.2915829886	1.0768767277	-0.2022559057	-0.1943508955
3.0152	2.4093619266	1.0846726654	-0.2022295078	-0.2027817501
3.0162	2.5273849254	1.0925906981	-0.2011567058	-0.2101017213
3.0188	2.6455248145	1.1007585320	-0.1987609769	-0.2162644440
3.0234	2.7635889805	1.1093498794	-0.1946155759	-0.2211327592
3.0313	2.8909903824	1.1194130163	-0.1873686594	-0.2246002627
3.0424	3.0073088423	1.1297344316	-0.1769810336	-0.2254855800
3.0584	3.1205655022	1.1413664663	-0.1612996515	-0.2229158600
3.0807	3.2266000495	1.1542349115	-0.1379744940	-0.2147411949
3.1085	3.3173903769	1.1669663066	-0.1049833863	-0.1984458292
3.1359	3.3833013605	1.1766385512	-0.0621463948	-0.1748356762
3.1521	3.4154433338	1.1808881373	-0.0032736457	-0.1559184478

Table A.2. : Initial conditions for the P2HO$_1$ orbit family

JC	Period	x_0	z_0	$\dot{y}_0$
3.0580	2.7486723000	1.0124213729	-0.1739463747	-0.0801103670
3.0638	2.8235719903	0.9686100061	-0.1684646845	-0.0555868296
3.0716	2.9470915455	0.9428902766	-0.1621459176	-0.0367463465
3.0778	3.0718373938	0.9280339523	-0.1570215893	-0.0278535009
3.0830	3.2098634414	0.9177532010	-0.1525284780	-0.0253346758
3.0866	3.3390119532	0.9116052635	-0.1492702168	-0.0275809790
3.0893	3.4781621508	0.9074818076	-0.1466452811	-0.0334316688
3.0907	3.6071172693	0.9053614223	-0.1449312614	-0.0411597104
3.0910	3.7456075513	0.9044951611	-0.1437576475	-0.0512886367
3.0905	3.8738428281	0.9047472035	-0.1431979716	-0.0619366228
3.0889	4.0115944839	0.9059473646	-0.1430690015	-0.0743674595
3.0867	4.1392474276	0.9077780758	-0.1433117179	-0.0865211750
3.0835	4.2765261366	0.9103912789	-0.1438936424	-0.0999906823
3.0800	4.4039019522	0.9133170339	-0.1446839313	-0.1126257931
3.0756	4.5410586110	0.9169169198	-0.1457671148	-0.1261483024
3.0710	4.6684708483	0.9206100089	-0.1469654829	-0.1384542728
3.0657	4.8057987675	0.9249032213	-0.1484447194	-0.1512842987
3.0605	4.9334592177	0.9291366414	-0.1499785567	-0.1627035911
3.0546	5.0711130707	0.9339173119	-0.1517856322	-0.1743951579
3.0485	5.2089533970	0.9388868141	-0.1537336561	-0.1854168651

Table A.3. : Initial conditions for the P4HO$_1$ orbit family

JC	Period	x_0	z_0	$\dot{y}_0$
3.0194	8.2676291788	1.0619393673	-0.1999741894	-0.1749961447
3.0189	8.3305139834	1.0681129545	-0.1976100673	-0.1868722998
3.0187	8.3392497293	1.0738246899	-0.1946216607	-0.1984738200
3.0183	8.3519917053	1.0786654098	-0.1919984087	-0.2083581121
3.0178	8.3693678945	1.0833295002	-0.1893927253	-0.2179310067
3.0173	8.3878867600	1.0871892065	-0.1871812140	-0.2258888455
3.0167	8.4096026243	1.0909131908	-0.1850039744	-0.2335944979
3.0161	8.4309304649	1.0940376079	-0.1831478491	-0.2400766927
3.0155	8.4547978250	1.0971075676	-0.1813014490	-0.2464568317
3.0149	8.4775801091	1.0997316965	-0.1797082140	-0.2519152440
3.0142	8.5026193458	1.1023550439	-0.1781043165	-0.2573726538
3.0136	8.5262347341	1.1046324969	-0.1767049403	-0.2621078568
3.0129	8.5519768095	1.1069405119	-0.1752821493	-0.2669009993
3.0123	8.5761129683	1.1089683638	-0.1740297442	-0.2711051374
3.0117	8.6023105873	1.1110450669	-0.1727463692	-0.2754011052
3.0111	8.6267952587	1.1128866230	-0.1716087730	-0.2792006165
3.0104	8.6533063618	1.1147879601	-0.1704357869	-0.2831115888
3.0098	8.6780368548	1.1164862743	-0.1693902247	-0.2865931191
3.0091	8.7047739081	1.1182510772	-0.1683067141	-0.2901975105
3.0085	8.7316043012	1.1199566179	-0.1672632043	-0.2936663490

Table A.4. : Initial conditions for the P2HO$_2$ orbit family

JC	Period	x_0	z_0	$\dot{y}_0$
3.0158	4.5243776465	0.9902279661	0.0392479429	0.7431504374
3.0176	4.3364693699	0.9913034068	0.0386425658	0.7476198379
3.0180	4.3344588357	0.9925765901	0.0404028452	0.7275812069
3.0186	4.3322427233	0.9936999422	0.0418211289	0.7119297395
3.0197	4.3274956856	0.9956999819	0.0440891033	0.6876036122
3.0225	4.3154119806	0.9997963248	0.0479397591	0.6474122281
3.0267	4.2966706889	1.0050420842	0.0517347036	0.6074272113
3.0343	4.2610464740	1.0135348381	0.0559827198	0.5575089518
3.0421	4.2236953788	1.0214960279	0.0583763748	0.5199524066
3.0446	4.2114971687	1.0239852380	0.0588603231	0.5093886860
3.0457	4.2066140086	1.0249716121	0.0590196996	0.5053259810
3.0462	4.2037569181	1.0255464522	0.0591042680	0.5029882761
3.0467	4.2014068389	1.0260181267	0.0591691271	0.5010860112
3.0472	4.1989300286	1.0265141820	0.0592329594	0.4991004650
3.0480	4.1953346327	1.0272324868	0.0593174846	0.4962518855
3.0495	4.1879862293	1.0286948426	0.0594609346	0.4905454113
3.0544	4.1645925208	1.0333161410	0.0596666029	0.4732448565
3.0711	4.0891753953	1.0483318888	0.0577756525	0.4227218693
3.1038	3.9680003798	1.0758753256	0.0417283774	0.3430241217
3.1247	3.9102015266	1.0926153718	0.0005492180	0.2990655449

Table A.5. : Initial conditions for the P4HO$_2$ orbit family

JC	Period	x_0	z_0	$\dot{y}_0$
3.0158	9.0487552928	1.0749349573	-0.2021215571	-0.1920690379
3.0167	9.0396341760	1.0578442875	-0.2047569352	-0.1678532831
3.0175	9.0542791209	1.0524484578	-0.2047233749	-0.1606194256
3.0178	9.0601028655	1.0505487899	-0.2045610040	-0.1581773718
3.0181	9.0646190673	1.0491368344	-0.2043821958	-0.1564064537
3.0186	9.0707205473	1.0472961590	-0.2040685317	-0.1541623227
3.0192	9.0786237393	1.0450028327	-0.2035390634	-0.1514838937
3.0202	9.0888613168	1.0421535217	-0.2026443039	-0.1483728351
3.0218	9.1037491359	1.0382266494	-0.2009270031	-0.1445796433
3.0252	9.1306372229	1.0319435819	-0.1968531223	-0.1401578788
3.0332	9.2021506431	1.0215863525	-0.1864218292	-0.1399647167
3.0419	9.3830140082	1.0126738542	-0.1723454500	-0.1560887631
3.0443	9.5440425474	1.0113733655	-0.1648460585	-0.1739113299
3.0444	9.6990195652	1.0129644895	-0.1593270671	-0.1918297866
3.0350	10.2961547121	1.0286792032	-0.1457428883	-0.2522546927
3.0040	11.7792576999	1.0624281188	-0.1343562748	-0.3275531781
2.9745	13.7831848966	1.0850769369	-0.1379181777	-0.3653699405
2.9502	16.0024825055	1.0955445136	-0.1591111395	-0.3767847569
2.9281	18.1058513583	1.0954718438	-0.1988427540	-0.3675757435
2.9017	20.0406128078	1.0829659022	-0.2591580427	-0.3388198392

Table A.6. : Initial conditions for the DRO orbit family

JC	Period	x_0	z_0	$\dot{y}_0$
3.3949	0.2230147974	0.9624690577	0	0.7184165432
3.1361	0.6166055596	0.9361690577	0	0.5420829797
3.0460	1.0873149322	0.9098690577	0	0.4861304073
2.9982	1.6036604892	0.8835690577	0	0.4704001643
2.9676	2.1456222060	0.8572690577	0	0.4752341941
2.9455	2.6935872117	0.8309690577	0	0.4931694567
2.9278	3.2259140152	0.8046690577	0	0.5206492176
2.9123	3.7214359005	0.7783690577	0	0.5556648548
2.8976	4.1639236713	0.7520690577	0	0.5969085865
2.8828	4.5451073473	0.7257690577	0	0.6434438745
2.8674	4.8656732383	0.6993690577	0	0.6947808121
2.8510	5.1282795896	0.6730690577	0	0.7500292555
2.8334	5.3419826389	0.6467690577	0	0.8090396816
2.8145	5.5150452938	0.6204690577	0	0.8716174367
2.7940	5.6550946637	0.5941690577	0	0.9376894311
2.7720	5.7686517772	0.5678690577	0	1.0072891703
2.7482	5.8610608744	0.5415690577	0	1.0805472211
2.7227	5.9366010546	0.5152690577	0	1.1576874834
2.6952	5.9986577916	0.4889690577	0	1.2390293886
2.6655	6.0500729893	0.4625690577	0	1.3253326531

Table A.7. : Initial conditions for the P4DRO$_1$ orbit family

JC	Period	x_0	z_0	$\dot{y}_0$
2.9968	6.4915502113	1.0956682452	0	-0.4609248208
2.9959	6.5485885660	0.8845107832	0	0.4743574248
2.9964	6.5290759463	0.8881739964	0	0.4803342276
2.9972	6.4957408939	0.8917748197	0	0.4865396058
2.9985	6.4431996078	0.8958372773	0	0.4940373523
2.9999	6.3863556127	0.8993742277	0	0.5010892078
3.0016	6.3206394402	0.9029247130	0	0.5087544394
3.0040	6.2358495848	0.9070375019	0	0.5185000486
3.0064	6.1540002137	0.9107184007	0	0.5281450983
3.0091	6.0656645085	0.9145075806	0	0.5391356431
3.0126	5.9575658739	0.9190089132	0	0.5538272990
3.0162	5.8575030844	0.9231303718	0	0.5691073969
3.0202	5.7531848587	0.9274537610	0	0.5873608931
3.0256	5.6300450982	0.9326814165	0	0.6130965586
3.0309	5.5202873810	0.9375419661	0	0.6414499043
3.0371	5.4103948974	0.9427019598	0	0.6774553305
3.0454	5.2877445017	0.9489909423	0	0.7322348510
3.0538	5.1873253393	0.9548106899	0	0.7978771935
3.0634	5.0999440508	0.9607749714	0	0.8876749392
3.0751	5.0270734064	0.8269820512	0	0.3380345610

Table A.8. : Initial conditions for the P3DRO orbit family

JC	Period	x_0	z_0	$\dot{y}_0$
3.0195	4.8679175854	1.1576212188	0	-0.3907560378
2.9792	5.9133796935	1.1441959072	0	-0.4404641249
2.9600	6.9624821495	1.1390387355	0	-0.4630132033
2.9466	8.0120878887	1.1375912558	0	-0.4777333824
2.9352	9.0618428978	1.1390736802	0	-0.4890310074
2.9243	10.1115680630	1.1441425709	0	-0.4989057158
2.9129	11.1609787955	1.1544825767	0	-0.5092275845
2.9005	12.2093637244	1.1727211087	0	-0.5231708538
2.8870	13.2550459522	1.2021281538	0	-0.5464595719
2.8718	14.2947674567	1.2465694880	0	-0.5879367258
2.8522	15.3306534698	1.3128760123	0	-0.6612357173
2.8211	16.3157251836	1.4134135214	0	-0.7871650440
2.7595	17.1460740884	1.5731240846	0	-1.0015000745
2.6545	17.6202334002	1.7745036512	0	-1.2771325275
2.5314	17.8163757586	1.9532058473	0	-1.5211892324
2.4128	17.8997982829	2.0924197498	0	-1.7106243445
2.3070	17.9400954058	2.1982877750	0	-1.8545519919
2.2159	17.9623481703	2.2791896940	0	-1.9646576348
2.1384	17.9762583596	2.3419296680	0	-2.0502288942
2.0720	17.9859903680	2.3918758002	0	-2.1185301990

Table A.9. : Initial conditions for the P4DRO$_2$ orbit family

JC	Period	x_0	z_0	$\dot{y}_0$
2.7180	23.7934787116	0.5108186768	0	1.1712159177
2.7112	23.8300666099	0.5227173792	0	1.1437277425
2.6874	23.9386902799	0.5172567104	0	1.1677579735
2.6477	24.0720507028	0.4943906436	0	1.2435274369
2.5930	24.1928487816	0.4588814278	0	1.3630406618
2.5287	24.2818292647	0.4178386954	0	1.5110422363
2.4550	24.3446949025	0.3738285512	0	1.6861067582
2.3764	24.3861756894	0.3307824483	0	1.8791318363
2.2922	24.4142408470	0.2888480972	0	2.0951784303
2.2094	24.4324468193	0.2514353687	0	2.3199711523
2.1291	24.4450141079	0.2184333643	0	2.5531228142
2.0581	24.4537258575	0.1917278556	0	2.7748346037
1.9971	24.4602141890	0.1704499552	0	2.9801804243
1.9500	24.4648793658	0.1550440166	0	3.1496032414
1.9143	24.4683183591	0.1439418395	0	3.2851849677
1.8889	24.4707559882	0.1363105019	0	3.3861627870
1.8698	24.4725912402	0.1307301340	0	3.4645757913
1.8555	24.4739697997	0.1266428911	0	3.5247106256
1.8439	24.4750910226	0.1233889126	0	3.5743480816
1.8344	24.4760216951	0.1207376000	0	3.6160189851

Table A.10. : Initial conditions for the 3D-DRO orbit family

JC	Period	x_0	z_0	$\dot{y}_0$
2.3696	6.2414231384	0.2689593272	0.0006672577	2.1828166312
2.3602	6.2434225752	0.2649822134	0.0175693816	2.2041844112
2.3356	6.2483056197	0.2548250233	0.0323714156	2.2603080609
2.3003	6.2545876454	0.2407344649	0.0442204946	2.3422243906
2.2581	6.2611662574	0.2245638951	0.0531132557	2.4429302528
2.2100	6.2676846688	0.2068771950	0.0595298525	2.5628871380
2.1613	6.2733959899	0.1897942813	0.0633491692	2.6907075793
2.1119	6.2784668880	0.1731927422	0.0651968022	2.8290458071
2.0630	6.2828952089	0.1574354301	0.0654044813	2.9766896162
2.0157	6.2867158632	0.1427695329	0.0643000252	3.1324321087
1.9690	6.2900955836	0.1288539333	0.0621073736	3.3013086773
1.9271	6.2928449438	0.1167800717	0.0592983499	3.4693335862
1.8883	6.2951612694	0.1059880731	0.0560713726	3.6412430258
1.8528	6.2971058252	0.0963997512	0.0526401974	3.8158174314
1.8203	6.2987363864	0.0879016117	0.0491654956	3.9921064269
1.7895	6.3001530766	0.0800938465	0.0456303067	4.1762786806
1.7624	6.3012974788	0.0734250592	0.0423695948	4.3542586163
1.7375	6.3022646428	0.0674737258	0.0392908859	4.5326130720
1.7145	6.3030859003	0.0621395988	0.0364137689	4.7112212469
1.6923	6.3038117254	0.0571622037	0.0336454587	4.8969134509

Table A.11. : Initial conditions for the 1:4 resonant orbit family

JC	Period	x_0	z_0	$\dot{y}_0$
1.7558	32.0015662490	2.6507804803	0	-2.4550718463
1.9195	32.0996425086	-4.3254333777	0	4.1536089989
2.1657	32.2768375035	2.3901635333	0	-2.0944883448
2.3991	32.4792517134	2.1927785365	0	-1.8235752680
2.6298	32.6897774836	1.9363173483	0	-1.4694105430
2.8085	32.6867254453	1.6572728522	0	-1.0760008741
2.8965	32.1839019112	-3.9800476556	0	3.6670271454
2.9371	31.4459145410	-3.9437572597	0	3.6226522593
2.9650	30.6922737366	1.3209512578	0	-0.5787448157
2.9930	29.9324950589	-3.8845692092	0	3.5513489154
3.0258	29.2080471096	1.2579501638	0	-0.4496423089
3.0660	28.5266544314	1.2409106471	0	-0.3828324281
3.1096	27.8886335124	1.2300229543	0	-0.3069993172
3.1480	27.2107341419	1.2244376145	0	-0.2273642598
3.1724	26.5016189250	-3.7075556621	0	3.3336723268
3.2041	25.8773775825	-3.6699105930	0	3.2877802802
3.2681	25.4912913687	1.4256274130	0	-0.4403998384
3.3534	25.3031747343	1.5964440759	0	-0.6807132603
3.4331	25.2177009704	1.7826637745	0	-0.9360286507
3.4968	25.1777028357	-3.0591542202	0	2.5526558549

Table A.12. : Initial conditions for the 3D 1:4 resonant orbit family

JC	Period	x_0	z_0	$\dot{y}_0$
2.9810	30.2072936419	1.2934087171	-0.0441431084	-0.5319876182
2.9753	30.1816646146	1.2814583147	-0.1059050611	-0.5165624317
2.9654	30.1256578508	1.2602222565	-0.1638270255	-0.4891137182
2.9529	30.0208682607	1.2316676708	-0.2138930890	-0.4521521050
2.9406	29.8297839892	1.1983346945	-0.2522355393	-0.4089226734
2.9341	29.6014553648	1.1726243911	-0.2704867936	-0.3753810046
2.9314	29.3556766373	1.1523347399	-0.2788562418	-0.3485617107
2.9308	29.1076189806	1.1353297673	-0.2829254308	-0.3256650646
2.9310	28.8397079297	1.1186296150	-0.2856944202	-0.3027275907
2.9313	28.5980003323	1.1040402609	-0.2880446019	-0.2823648266
2.9313	28.3604661746	1.0896461803	-0.2907913873	-0.2620968904
2.9308	28.1273965298	1.0752443721	-0.2941233947	-0.2417899380
2.9295	27.8787067426	1.0595145531	-0.2983501340	-0.2196846567
2.9280	27.6564029457	1.0451556861	-0.3025726255	-0.1994576201
2.9262	27.4396877371	1.0308312181	-0.3070910226	-0.1788304090
2.9239	27.2277295237	1.0163123034	-0.3122783780	-0.1568797002
2.9202	26.9993619025	0.9997374358	-0.3198366150	-0.1298758086
2.9139	26.7885076895	0.9831306874	-0.3305295465	-0.1004941520
2.9008	26.5693950202	0.9639039422	-0.3485629515	-0.0644109757
2.8695	26.3080728932	-4.0409627460	-0.3365763568	3.7354178029

Table A.13. : Initial conditions for the period-3 P2HO$_1$ orbit family

JC	Period	$\mathbf{x_0}$	$\mathbf{z_0}$	$\mathbf{\dot{y}_0}$
3.0856	9.8977281886	0.9132219196	-0.1501841067	-0.0265112348
3.0852	9.8898243966	0.9201970328	-0.1484368449	-0.0565406584
3.0844	9.8810771663	0.9265671655	-0.1463628718	-0.0829058222
3.0829	9.8691256030	0.9335749432	-0.1436892996	-0.1107812286
3.0797	9.8454695234	0.9444281115	-0.1391123040	-0.1513506676
3.0722	9.8036779374	0.9625127124	-0.1319817903	-0.2092427662
3.0595	9.8025480947	0.9870373049	-0.1264907851	-0.2616432018
3.0448	9.9452422307	1.0163389991	-0.1239244638	-0.2940266448
3.0358	10.1193693325	1.0378890327	-0.1219878427	-0.3076893119
3.0319	10.2196789262	1.0492499139	-0.1206913171	-0.3129897735
3.0299	10.2782233531	1.0557640701	-0.1198929655	-0.3155526115
3.0285	10.3234257420	1.0606863569	-0.1192923015	-0.3172661038
3.0272	10.3743986192	1.0659754030	-0.1186877260	-0.3188895242
3.0249	10.4819415132	1.0751732119	-0.1179559265	-0.3211607043
3.0142	11.3682201230	1.0962086516	-0.1232544003	-0.3273917152
2.9984	12.9232076043	1.1145803848	-0.1317486732	-0.3440964261
2.9910	13.7386762237	1.1243273036	-0.1350370641	-0.3548698346
2.9863	14.3013224753	0.8420263070	-0.1367090014	0.3579947942
2.9823	14.8280788526	0.8325176216	-0.1348148853	0.3723970129
2.9798	15.2712896533	0.8212280398	-0.1306979931	0.3891109249

B. BROUCKE STABILITY DIAGRAM

The parameters α and β are derived from the characteristic polynomial associated with the monodromy matrix. The characteristic polynomial is defined as $p(\lambda) = \det(\mathbf{\Phi}(t_0+P, t_0) - \lambda\mathbf{I})$ where $\det(\cdot)$ is the determinant operator and $\mathbf{I}$ is a 6×6 identity matrix. By definition, the roots of $p(\lambda)$ are the eigenvalues of $\mathbf{\Phi}(t_0 + P, t_0)$. Since the monodromy matrix is symplectic, the characteristic polynomial takes the form

$$p(\lambda) = (\lambda - 1)^2(\lambda - \lambda_1)\left(\lambda - \frac{1}{\lambda_1}\right)(\lambda - \lambda_2)\left(\lambda - \frac{1}{\lambda_2}\right) \tag{B.1}$$

or equivalently,

$$p(\lambda) = (\lambda - 1)^2(\lambda^2 + \sigma_1\lambda + 1)(\lambda^2 + \sigma_2\lambda + 1) \tag{B.2}$$

where $\sigma_1 = -\left(\lambda_1 + \frac{1}{\lambda_1}\right)$ and $\sigma_2 = -\left(\lambda_2 + \frac{1}{\lambda_2}\right)$. The characteristic polynomial is then rewritten as a function of α and β as

$$p(\lambda) = (\lambda - 1)^2(\lambda^4 + \alpha\lambda^3 + \beta\lambda^2 + \alpha\lambda + 1) \tag{B.3}$$

where $\alpha = \sigma_1 + \sigma_2$ and $\beta = 2 + \sigma_1\sigma_2$. Since the monodromy matrix, $\mathbf{\Phi}(t_0 + P, t_0)$, is diagonalizable and is equivalently written as $\mathbf{\Phi}(t_0 + P, t_0) = \mathbf{P}\mathbf{\Lambda}\mathbf{P}^{-1}$, the trace of the monodromy matrix is simply computed as

$$Tr(\mathbf{\Phi}(t_0 + P, t_0)) = Tr(\mathbf{\Lambda}) = 2 + \lambda_1 + \frac{1}{\lambda_1} + \lambda_2 + \frac{1}{\lambda_2}. \tag{B.4}$$

Thus, the equations for α and β are rewritten as

$$\alpha = \sigma_1 + \sigma_2 = -\left(\lambda_1 + \frac{1}{\lambda_1} + \lambda_2 + \frac{1}{\lambda_2}\right) = 2 - Tr\left(\mathbf{\Phi}(t_0 + P, t_0)\right) \tag{B.5}$$

and

$$\beta = 2 + \sigma_1\sigma_2 = \frac{1}{2}\left(\alpha^2 - \left(\lambda_1^2 + \frac{1}{\lambda_1^2} + \lambda_2^2 + \frac{1}{\lambda_2^2}\right)\right) = \frac{1}{2}\left(\alpha^2 + 2 - Tr\left(\mathbf{\Phi}(t_0 + P, t_0)^2\right)\right). \tag{B.6}$$

The parameters α and β fully define the orientation of the four nontrivial eigenvalues of the monodromy matrix with respect to the discrete-time stability bound, the unit circle.

The Broucke stability diagram in Figure B.1 offers insight into the eigenvalue configuration in the complex plane. In this figure, the small graphic in each region illustrates the unit circle and the general arrangement of the four nontrivial eigenvalues. By noting changes in the eigenstructure over the evolution of the family based solely on the values of (α, β), bifurcations are detected. The bifurcations of interest (and their relation to the Broucke stability diagram) are described in Table B.1. The derivations of the curves delineating the regions on the Broucke stability diagram in Figure B.1 and defining the bifurcations listed in Table B.1 follow. Considered in this investigation are the following bifurcation types:
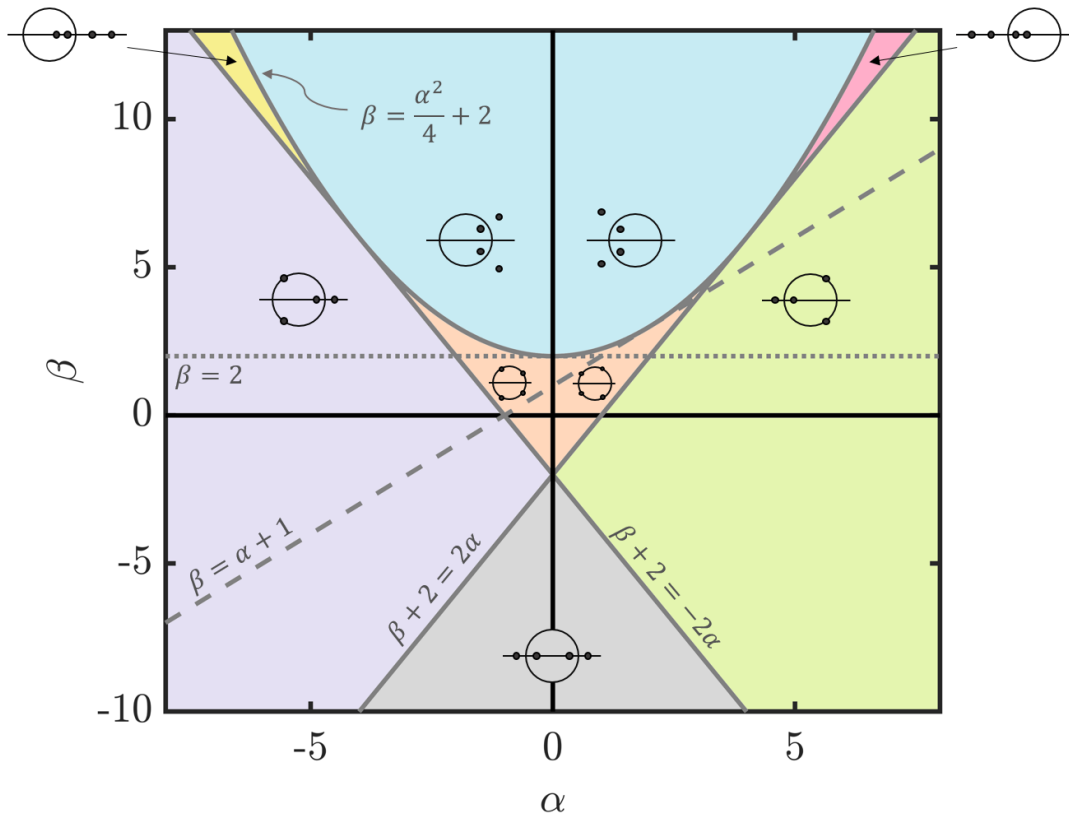

Figure B.1. : Broucke stability diagram [60]

Table B.1. : Classification of bifurcations of interest based on a Broucke stability diagram

Bifurcation Type	Eqn. of Line Crossed	Color Transitions	Stab. Change?
Tangent	$\beta + 2 = -2\alpha$	Orange $\leftrightarrow$ Purple Green $\leftrightarrow$ Grey Yellow $\leftrightarrow$ Purple	Yes
Period-Doubling	$\beta + 2 = 2\alpha$	Orange $\leftrightarrow$ Green Purple $\leftrightarrow$ Grey Pink $\leftrightarrow$ Green	Yes
Period-Tripling	$\beta = \alpha + 1$	N/A	No
Period-Quadrupling	$\beta = 2$	N/A	No
Secondary Hopf	$\beta = \frac{\alpha^2}{4} + 2$ $\alpha \in (-4, 4)$	Orange $\leftrightarrow$ Blue	Yes
Modified Secondary Hopf	$\beta = \frac{\alpha^2}{4} + 2$ $\alpha \in (-\infty, -4] \cup [4, \infty)$	Pink $\leftrightarrow$ Blue Yellow $\leftrightarrow$ Blue	No

1. **Tangent Bifurcation:** In the case of a change in family stability occurring simultaneously with two nontrivial eigenvalues of the monodromy matrix going to unity, a tangent bifurcation has occurred. Letting $\lambda_1 = \frac{1}{\lambda_1} = 1$, the value for $\sigma_1 = -2$. Then, $\alpha = \sigma_1 + \sigma_2 = \sigma_2 - 2$ and $\beta = 2 + \sigma_1\sigma_2 = 2 - 2\sigma_2$. Combining these expressions, the equation relating α and β at a tangent bifurcation is

$$\beta + 2 = -2\alpha. \tag{B.7}$$

2. **Period-Doubling Bifurcations:** At a period-doubling bifurcation, two nontrivial monodromy matrix eigenvalues collide at -1 and depart from the unit circle to the negative real line or vice versa [57]. Letting $\lambda_1 = \frac{1}{\lambda_1} = -1$, the value for $\sigma_1 = 2$. Then, $\alpha = \sigma_1 + \sigma_2 = \sigma_2 + 2$ and $\beta = 2 + \sigma_1\sigma_2 = 2 + 2\sigma_2$. Combining these expressions, the equation relating α and β at a period-doubling bifurcation is

$$\beta + 2 = 2\alpha. \tag{B.8}$$

3. **Period-Multiplying Bifurcations:** A period-multiplying bifurcation (of multiplying factor m where m is an integer greater than 2) occurs when two nontrivial monodromy matrix eigenvalues evolve such that $\lambda_j, 1/\lambda_j = \sqrt[m]{1} = \cos(2\pi/m) \pm i\sin(2\pi/m)$ [55]. Period-tripling and period-quadrupling bifurcations are considered in this analysis.

- **Period-Tripling Bifurcation:** At a period-tripling bifurcation, let $\lambda_1 = -0.5 + 0.866i$ and $\frac{1}{\lambda_1} = -0.5 - 0.866i$. The value for σ_1 is therefore unity. Then, $\alpha = \sigma_1 + \sigma_2 = \sigma_2 + 1$ and $\beta = 2 + \sigma_1\sigma_2 = 2 + \sigma_2$. Combining these expressions, the equation relating α and β at a period-tripling bifurcation is

$$\beta = \alpha + 1. \tag{B.9}$$

- **Period-Quadrupling Bifurcation:** At a period-quadrupling bifurcation, let $\lambda_1 = i$ and $\frac{1}{\lambda_1} = -i$. The value for σ_1 is therefore zero. Then, $\alpha = \sigma_1 + \sigma_2 = \sigma_2$ and $\beta = 2 + \sigma_1\sigma_2 = 2$. Combining these expressions, the equation relating α and β at a period-quadrupling bifurcation is

$$\beta = 2. \tag{B.10}$$

4. **Secondary Hopf and Modified Secondary Hopf Bifurcations:** A secondary Hopf bifurcation occurs when two eigenvalues collide on the unit circle and depart into the complex plane at a location other than ± 1 along the real axis. A modified secondary Hopf bifurcation is triggered when two eigenvalues collide on the real line and depart into the complex plane (other than at ± 1). At both a secondary and modified secondary Hopf bifurcation, the four nontrivial eigenvalues of the monodromy matrix are reduced to $\lambda_1 = \lambda_2$ and $\frac{1}{\lambda_1} = \frac{1}{\lambda_2}$, thus, $\sigma_1 = \sigma_2 = \sigma$. Then, $\alpha = \sigma_1 + \sigma_2 = 2\sigma$ and $\beta = 2 + \sigma_1\sigma_2 = 2 + \sigma^2$. Combining these expressions, the equation relating α and β at a secondary and modified secondary Hopf bifurcation is

$$\beta = \frac{\alpha^2}{4} + 2. \tag{B.11}$$

234

If the values of α and β that are computed for a particular member of an orbit family satisfy one of the above expressions, a bifurcation has occurred.

C. NRHOs OF INTEREST: FAST FACTS

This section is intended to serve as a quick reference guide for the L_2 southern 9:2 lunar synodic resonant NRHO and the L_2 southern 4:1 lunar synodic resonant NRHO. Both of these orbits are of interest for NASA's Gateway mission. The figures and tables are described below:

- **Figure C.1:** The L_2 southern 9:2 and 4:1 lunar synodic resonant NRHOs are plotted in a variety of rotating frames in orange and blue, respectively. The Earth-Moon rotating frame is the typical frame in which these orbits are viewed; the orbital geometry is relatively simple in this frame and is one-revolution periodic. The Moon-centered inertial frame illustrates that the NRHOs are non-Keplerian and are non-periodic in the inertial frame. The NRHOs are plotted in the Sun-Moon rotating frame to illustrate that they are periodic in this frame, albeit over 9 revolutions for the 9:2 NRHO and 4 revolutions for the 4:1 NRHO. The Moon's shadow is fixed in this frame, thus, the geometry of the synodic resonant NRHOs is one strategy to produce orbits that avoid lunar eclipse conditions. Similarly, the NRHOs are plotted in the Sun-Earth rotating frame. In this frame, the 9:2 NRHO geometry repeats after 9 revolutions while the 4:1 NRHO geometry repeats after 4 revolutions. The shadow of the Earth is fixed in this frame.

- **Figure C.2:** The 4:1 and 9:2 lunar synodic resonant NRHOs are plotted in the Earth-Moon rotating frame and colored by osculating Keplerian true anomaly computed with respect to the Moon in the Moon-centered inertial frame. Note the rapid transition through true anomaly values near perilune.

- **Figure C.3:** The distance to the Moon along the 9:2 and 4:1 lunar synodic resonant NRHOs is plotted as a function of time along the NRHOs. The 9:2 NRHO approaches the Moon more closely than the 4:1 NRHO.

- **Figure C.4:** The osculating Keplerian orbital elements computed with respect to the Moon (using Moon-centered inertial frame position and velocity values) are plotted

against time along the orbit and true anomaly for the CR3BP NRHOs of interest. Time = 0 days corresponds to apolune along each orbit.

- **Figure C.5:** One revolution along the L_2 southern 9:2 lunar synodic resonant NRHO is plotted in black in the Moon-centered inertial frame. The orbit is computed in the CR3BP. At 9 instants along the NRHO, equally spaced in time, the Keplerian orbital elements are used to compute an instantaneous conic orbit, plotted in colors. The red dot along the NRHO corresponds to the location at which the instantaneous Keplerian orbit is computed.

- **Figure C.6:** A view down the Moon-centered inertial Z-axis (a "top-down" view) is plotted. Each of the orbits in Figure C.5 are plotted in the corresponding color in this figure. The CR3BP 9:2 NRHO is plotted in black.

- **Figure C.7:** The osculating Keplerian orbital elements computed with respect to the Earth (using Earth-centered inertial frame position and velocity values) are plotted against time along the orbit and true anomaly for the CR3BP NRHOs of interest. Time = 0 days corresponds to apolune along each orbit. Note that near perilune along each orbit, the instantaneous conic orbit is hyperbolic.

- **Figure C.8:** A spatial view and "top-down" view (corresponding to looking down the Earth-centered inertial Z-axis) of the Earth-centered inertial 9:2 NRHO and instantaneous conic orbits are plotted. The position that each conic is computed corresponds to the identical locations in Figures C.5 and C.6. At perilune, the instantaneous Keplerian orbit is hyperbolic–this orbit is plotted in light blue. The 9:2 NRHO in this figure is plotted in black.

- **Table C.1:** This table contains reference values for the CR3BP L_2 9:2 lunar synodic resonant NRHO.

- **Table C.2:** This table contains reference values for the CR3BP L_2 4:1 lunar synodic resonant NRHO.

(a) Earth-Moon rotating frame

(b) Moon-centered inertial frame

(c) Moon-centered inertial frame

(d) Sun-Moon rotating frame

(e) Sun-Moon rotating frame

(f) Sun-Moon rotating frame

(g) Sun-Earth rotating frame

(h) Sun-Earth rotating frame
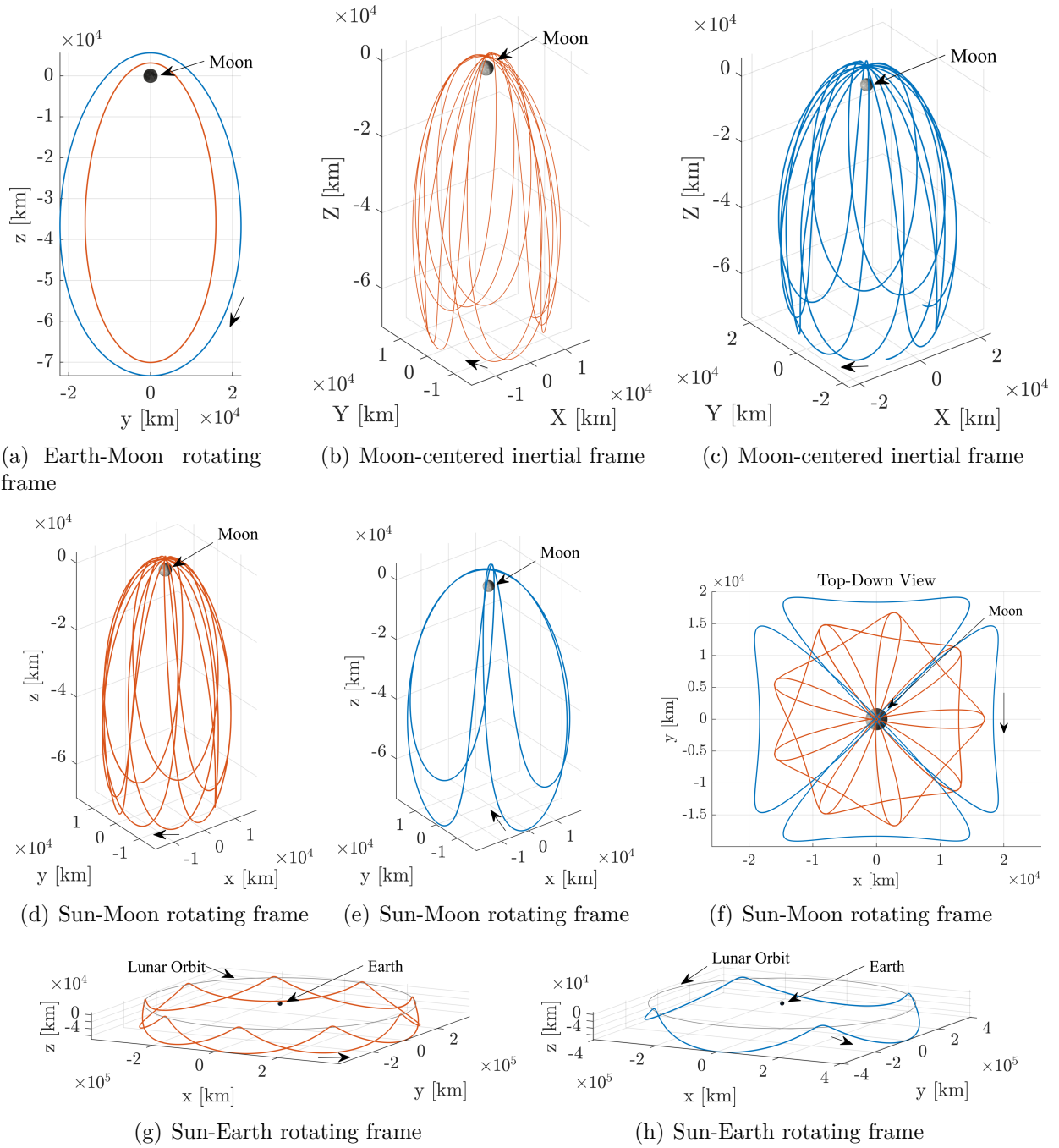
Figure C.1. : The 9:2 synodic resonant NRHO (orange) and the 4:1 synodic resonant NRHO (blue) computed in the CR3BP

238

(a) 4:1 lunar synodic resonant NRHO

(b) 9:2 lunar synodic resonant NRHO
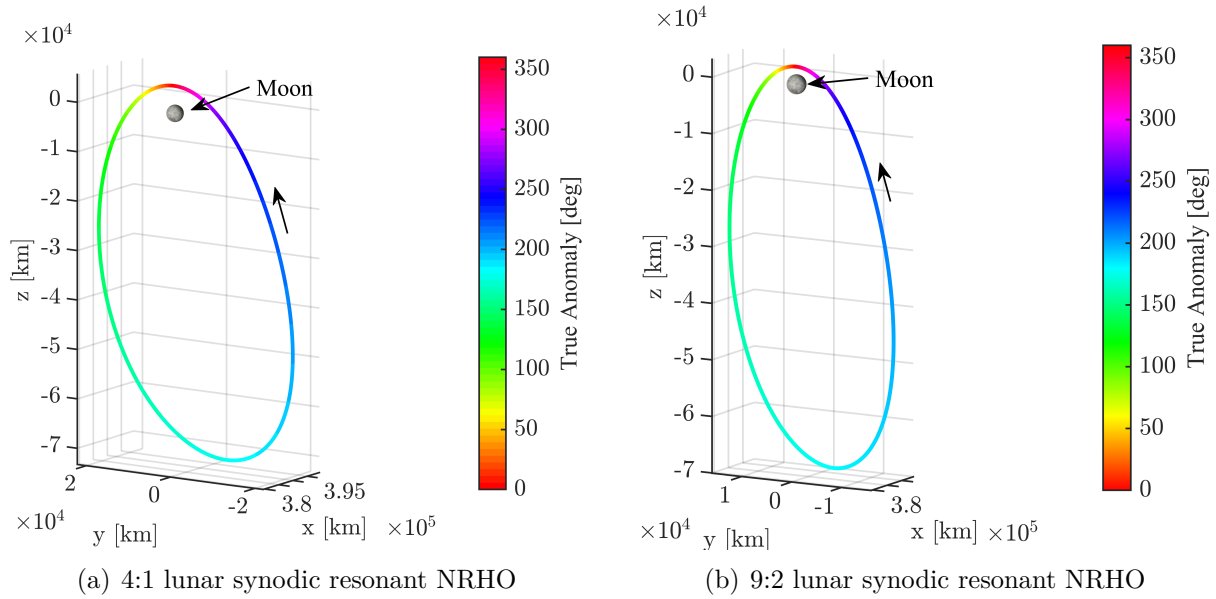
Figure C.2. : Osculating true anomaly (computed with respect to Moon) measured along the 9:2 synodic resonant NRHO and the 4:1 synodic resonant NRHO
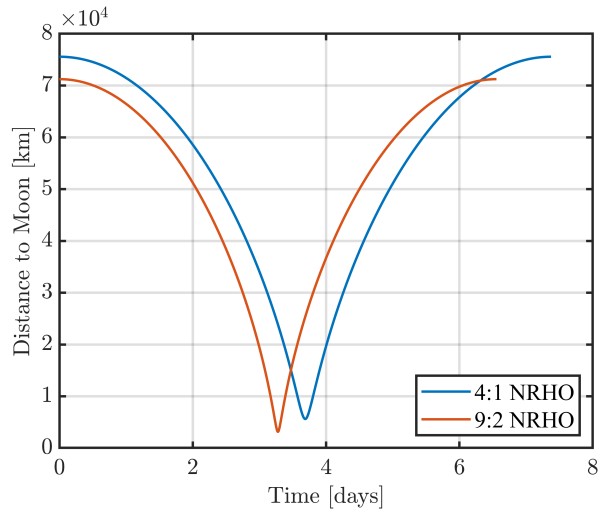

Figure C.3. : Distance to the Moon along the CR3BP 4:1 and 9:2 NRHOs
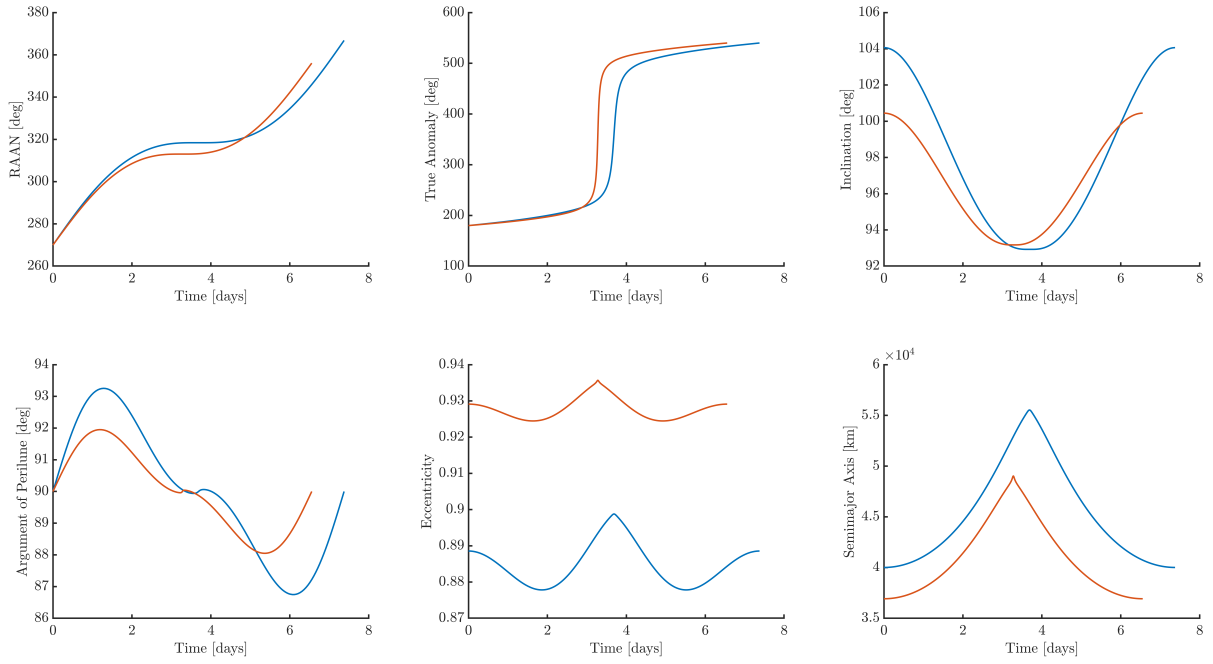
(a) Keplerian orbital elements vs time
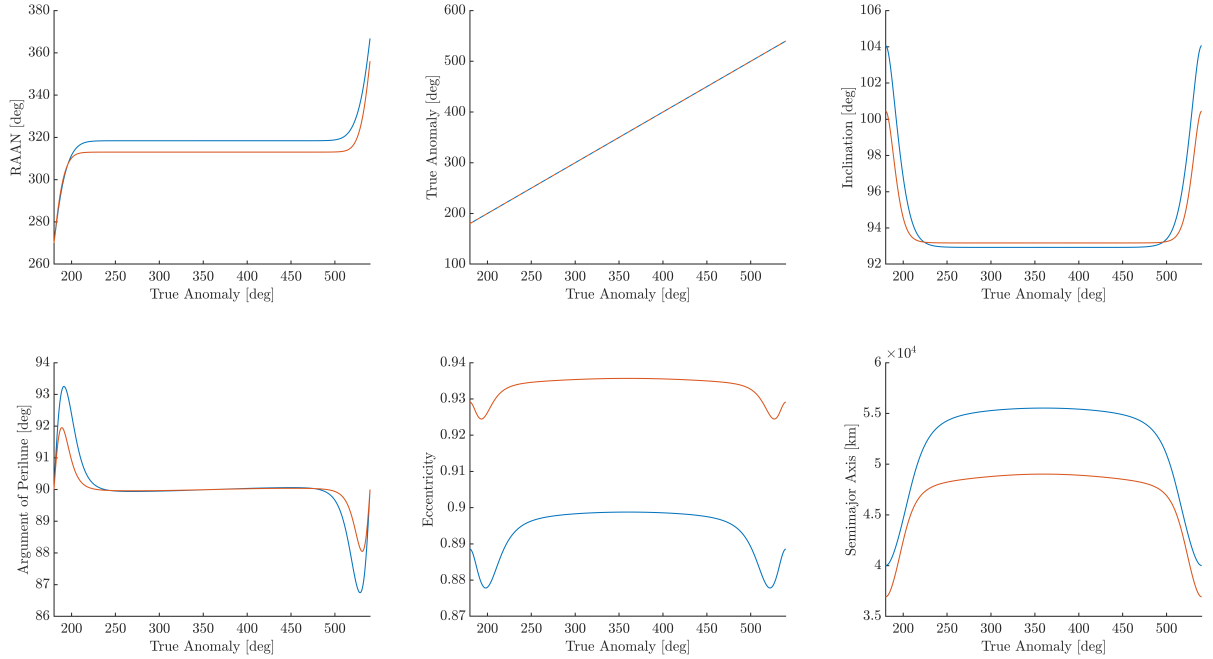
(b) Keplerian orbital elements vs true anomaly

Figure C.4. : Osculating Keplerian orbital elements (computed with respect to Moon) along the 9:2 NRHO (orange) and 4:1 NRHO (blue)

(a) Time = 0 days (apolune)

(b) Time = 0.819 days

(c) Time = 1.64 days

(d) Time = 2.46 days

(e) Time = 3.28 days (perilune)

(f) Time = 4.09 days

(g) Time = 4.917 days

(h) Time = 5.736 days

(i) Time = 6.556 days (apolune)
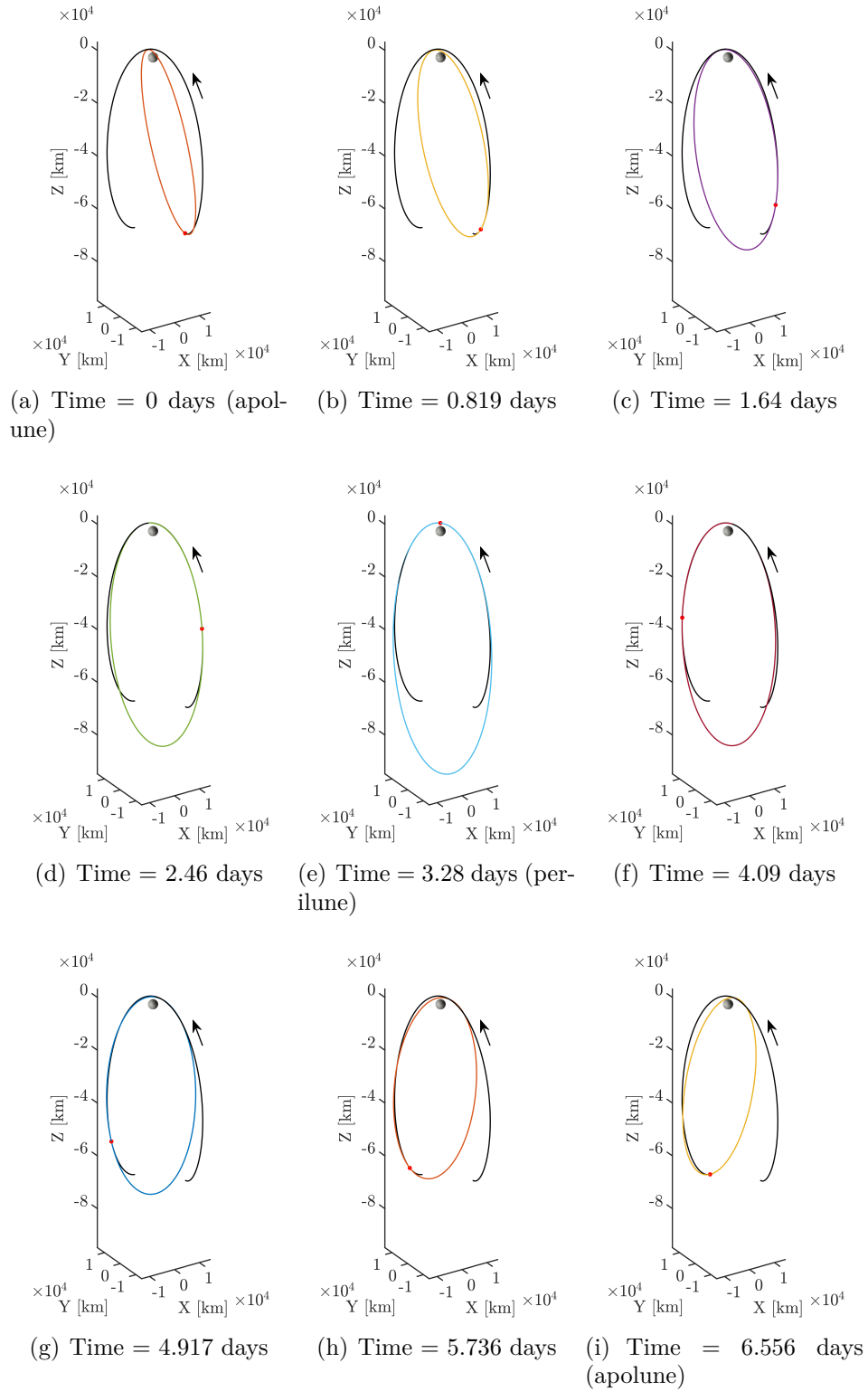
Figure C.5. : Instantaneous Keplerian orbits (computed with respect to Moon) at locations along the 9:2 NRHO, plotted in the Moon-centered inertial frame
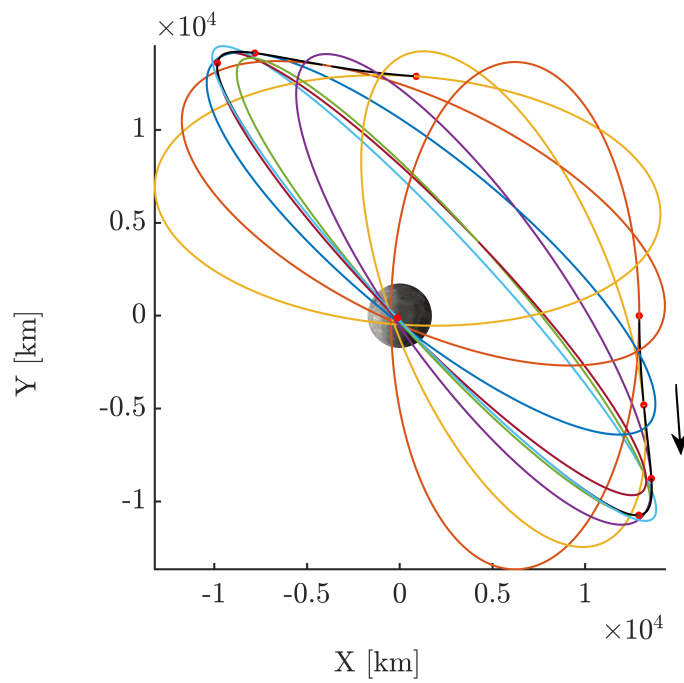
Figure C.6. : View down *Z*-axis of Keplerian orbits (computed with respect to Moon) at locations along the 9:2 NRHO from Figure C.5, plotted in the Moon-centered inertial frame
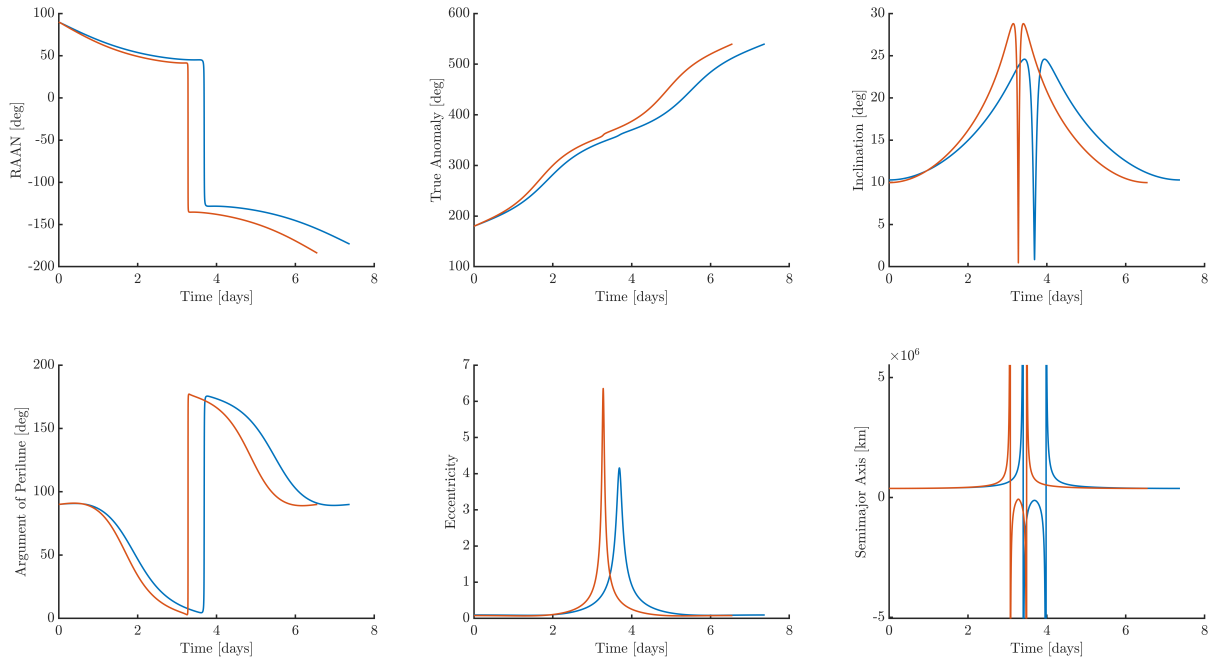
(a) Keplerian orbital elements vs time
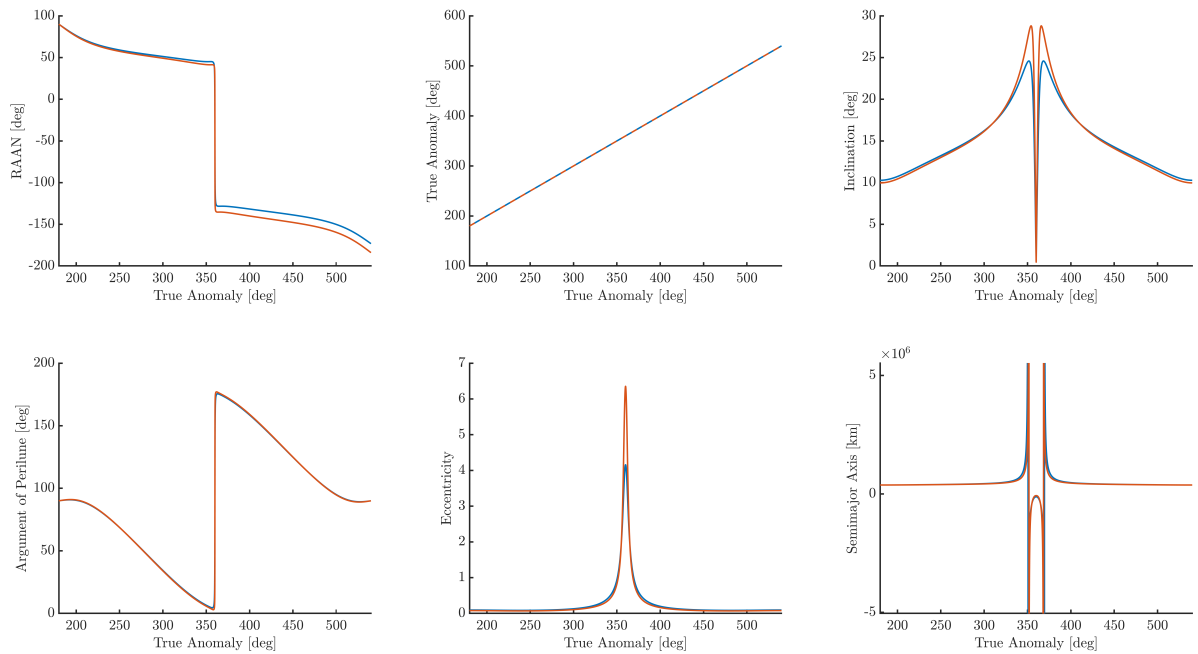

(b) Keplerian orbital elements vs true anomaly

Figure C.7. : Osculating Keplerian orbital elements (computed with respect to Earth) along the 9:2 NRHO (orange) and 4:1 NRHO (blue)
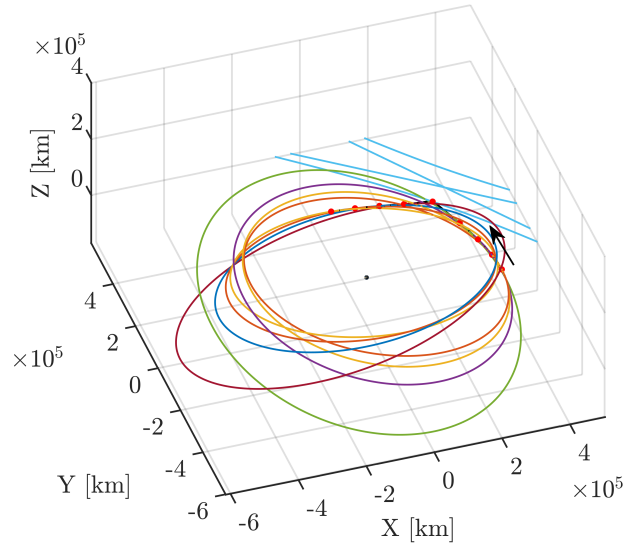
(a) Spatial view
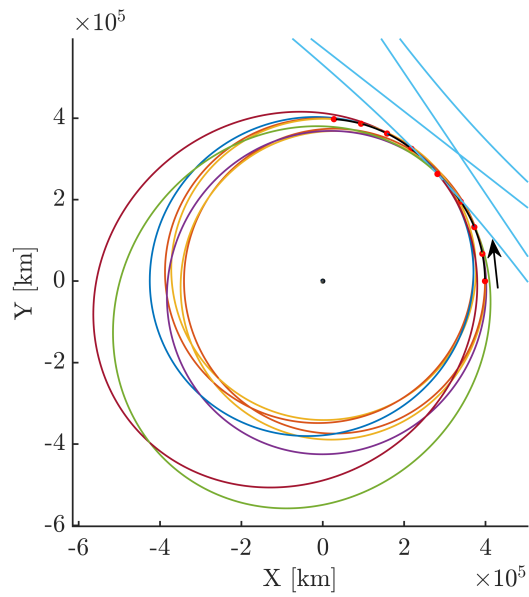
(b) View down Z-axis

Figure C.8. : Keplerian orbits (computed with respect to Earth) at locations along the 9:2 NRHO, plotted in the Earth-centered inertial frame

Table C.1. : CR3BP L_2 9:2 lunar synodic resonant NRHO information

Initial Conditions, $[x, y, z, \dot{x}, \dot{y}, \dot{z}]$	[1.02134, 0, -0.18162, 0, -0.10176, 9.76561e-07] nd
	= [393921.42, 0, -70049.20, 0, -0.10408, 9.98854e-07] km, km/s
Orbital Period	1.50206 nd = 6.5556 days
Eigenvalues of Monodromy Matrix	-2.13996, -0.46730,
	0.99999 + 0.00508i, 0.99999 - 0.00508i,
	0.68987 + 0.72394i, 0.68987 - 0.72394i
Stability Indices, ν_i	1.30363, 1, 1
Perilune Radius	0.00818 nd = 3153.06 km
Apolune Radius	0.18468 nd = 71229.88 km
Perilune Speed in Earth-Moon Rotating Frame	1.69614 nd = 1.73486 km/s
Apolune Speed in Earth-Moon Rotating Frame	0.10176 nd = 0.10408 km/s
Amplitude of Orbit, $[Amp_x, Amp_y, Amp_z]$	[0.03394, 0.08277, 0.18978] nd
	= [13089.84, 31924.81, 73197.43] km
Jacobi Constant	3.04719

Table C.2. : CR3BP L_2 4:1 lunar synodic resonant NRHO information

Initial Conditions, $[x, y, z, \dot{x}, \dot{y}, \dot{z}]$	[1.03545, 0, -0.19003, 0, -0.13071, 5.62991e-07] nd $= [399365.90, 0, -73294.05, 0, -0.13370, 5.75843e-07]$ km, km/s
Orbital Period	1.68981 nd = 7.375 days
Eigenvalues of Monodromy Matrix	-2.88383, -0.34676, 1.00423, 0.99578, 0.51535 + 0.85698i, 0.51535 - 0.85698i
Stability Indices, ν_i	1.61529, 1, 1
Perilune Radius	0.01457 nd = 5620.72 km
Apolune Radius	0.19590 nd = 75558.58 km
Perilune Speed in Earth-Moon Rotating Frame	1.25862 nd = 1.28735 km/s
Apolune Speed in Earth-Moon Rotating Frame	0.13071 nd = 0.13370 km/s
Amplitude of Orbit, $[Amp_x, Amp_y, Amp_z]$	[0.04835, 0.11460, 0.20459] nd $= [18647.01, 44200.51, 78907.40]$ km
Jacobi Constant	3.03476

VITA

Emily Marie Zimovan Spreen started her undergraduate studies at the University of Maryland, College Park in aerospace engineering in 2011. During her time at University of Maryland, Emily participated in the honors program and contributed to research at the Space Systems Laboratory. In the summers of 2012 and 2013, Emily interned at NASA Goddard Space Flight Center where she worked in attitude control systems. At Goddard Space Flight Center, Emily was selected as a John Mather Nobel Scholar–an award that recognizes high academic achievement and a strong interest in space. In 2013, after being awarded the NASA Aeronautics Scholarship, Emily transferred into the undergraduate aeronautical and astronautical engineering program at Purdue University where she focused on dynamics and control. Over the summer of 2014, as a part of the NASA Aeronautics Scholarship Program, Emily interned at NASA Langley Research Center. Emily graduated first in her class with her Bachelor's Degree in Aerospace Engineering, earning highest distinction from Purdue University in 2015. Emily received numerous scholarships during her undergraduate studies including the Peter Mueller Memorial Scholarship for Aeronautical and Astronatical Engineering, the Space Shuttle Memorial Scholarship, a Women in Aerospace Foundation Scholarship, multiple scholarships from the National Society of Professional Engineers, and a Purdue Industrial Roundtable Scholarship.

Emily remained at Purdue University to work with Professor Kathleen Howell after her Bachelor's degree to earn her Master of Science in aerospace engineering. The summer prior to starting graduate school, Emily began interning at NASA Johnson Space Center where she worked in guidance, navigation, and control (GN&C). Emily continued working in GN&C at NASA Johnson Space Center throughout her Master's degree. The research Emily conducted during her Master of Science degree focused primarily on characteristics and design strategies for near rectilinear halo orbits in the Earth-Moon system. Emily's M.S. degree was funded by the Charles C. Chappelle Fellowship and the Ross Fellowship through Purdue University; she earned her M.S. in August of 2017.

Emily continued in the Multi-Body Dynamics Research Group with Professor Kathleen Howell for her Doctor of Philosophy degree. Throughout her Ph.D., Emily has been funded as a NASA Space Technology Research Fellow. Emily also continued interning at NASA JSC, becoming a Pathways intern and civil servant in 2017. As a part of the Pathways program, she has worked on flight software for NASA's Orion spacecraft and has also contributed as a member of the Gateway Mission Design Team. Upon graduation, Emily will transition to full-time employment at NASA Johnson Space Center where she will work in the Flight Mechanics and Trajectory Design Branch.